UCLouvain
Institute for Information
and Communication Technologies,
Electronics and Applied Mathematics

Physics-based computational imaging for positron emission tomography and lensless endoscopy

Stéphanie Guérit

Thesis submitted in partial fulfillment
of the requirements for the degree of
Docteur en sciences de l'ingénieur et technologie

Dissertation committee:

Prof. John A. Lee (UCLouvain, advisor)
Prof. Laurent Jacques (UCLouvain, advisor)
Prof. Benoît Macq (UCLouvain)
Dr. Nelly Pustelnik (CNRS, ENS Lyon)
Dr. Hervé Rigneault (CNRS, Aix-Marseille Université)
Prof. Jean-Pierre Raskin (UCLouvain, chairman)

Version of June 17, 2021.

hier tu n'existais pas

tu étais un désir
tu étais une idée

hier tu n'existais pas

nous t'imaginions
nous rêvions de toi

et puis tu es là
tellement toi
que du temps d'hier
on ne se souvient pas

Marcella et Marie Poirier

À Pierre-Yves et Alice

Abstract

UNRAVELING the mysteries of life has fascinated humans for millenniums. The emergence of digital computers paved the way to new imaging modalities able to measure properties and signals coming from the inside of the body, without opening it. Computational imaging (CI) was born. CI acquires digital observations that are often not readily understandable (*e.g.*, returning echoes in ultrasound scans). A recovery step is thus necessary to extract useful information. To solve the so-called inverse problem, we resort to an optimization including knowledge about the acquisition process (emission and collection processes, noise corruption, etc.) and the expected properties of the final estimate (*e.g.*, piecewise-smoothness).

In this thesis, we focus on two modalities designed to image cellular processes in living organisms: positron emission tomography (PET) and lensless endoscopy (LE). PET imaging is widely used to get information about patient physiological activity. It suffers from blurring and high level of noise. LE exploits fluorescence phenomenon to capture biological information at a micrometer scale. A challenging task is to avoid tissue photobleaching.

The dissertation addresses two inverse problems related to PET and LE. First, we study the deblurring of reconstructed PET images polluted by a high level of noise in non-blind and blind contexts. Then, we explore acquisition and reconstruction strategies for LE that exploits nice properties of the sensing operator to collect far less observations as in a traditional scheme. This approach leads to both reduced acquisition time and light exposure.

Merci !

Le document que vous tenez dans les mains synthétise les résultats de plusieurs années de recherche passées au sein de l'institut ICTEAM et du département ELEN. Son contenu est le fruit de nombreuses discussions, interactions et collaborations avec d'autres chercheurs. Je tiens particulièrement à remercier :

mes promoteurs John et Laurent pour leur disponibilité, leurs commentaires pertinents sur mon travail et leurs conseils avisés. J'ai la chance d'avoir pu bénéficier de leurs approches complémentaires afin d'allier au mieux aspects théoriques et expérimentaux ;

Anne pour sa disponibilité et son aide précieuse lors des acquisitions d'images PET à Woluwe ;

Adriana pour les heures que nous avons passées ensemble, peu avant la fin de sa thèse, à travailler sur la déconvolution aveugle d'images PET, à réfléchir à l'implémentation de GFB et ADMM et à préparer un abstract pour iTWIST. Sérénité et efficacité qualifient bien cette collaboration qui a été un réel plaisir de mon côté ;

Camille, Siddharth et Hervé pour la collaboration fructueuse qui a donné lieu à la seconde partie de cette thèse ainsi que pour l'accueil chaleureux dans leur laboratoire de Marseille en novembre 2018 ;

Nelly, Hervé, Benoît et Jean-Pierre pour leur participation à mon jury de thèse et pour le temps consacré à la relecture du manuscrit.

En tant qu'assistante, les activités d'enseignement ont occupé la moitié (voire davantage) de mon temps. Elles ont été une grande source de joie et d'apprentissage dans mon quotidien de doctorante ! J'ai eu la chance de

faire partie d'équipes didactiques qui m'ont fait confiance en m'accordant une grande liberté d'enseignement. Je tiens à remercier :

tous les étudiants et les étudiantes dont j'ai croisé la route. Ces années auraient été bien plus fades sans eux. Les discussions et questions durant les séances m'ont poussée à aller chercher, m'informer, questionner,... et parfois reconnaître que je n'avais pas de réponse à leur proposer. J'ai également apprécié en retrouver certains comme collègues de thèse (petit clin d'œil à Estelle, Dounia, Cyril et Vincent) ;

Piotr qui m'a fait redécouvrir les APP lors du cours INGE1213 et qui m'a totalement convaincue du concept. Merci également à Laurent, Claude, Benoît, Pierre-Yves, Thomas et Roselien avec qui j'ai eu le plaisir d'encadrer ce cours plusieurs années ;

Luc, Michel, Vincent, Pierre-Antoine, Jean-Pierre et Stéphanie, qui ont été (et sont toujours) des titulaires de cours d'une grande qualité. Merci à vous pour l'accueil et la place que vous m'avez donnée au sein de vos enseignements, merci pour votre confiance et les échanges riches que nous avons eus à de nombreuses reprises ;

les super chercheurs et assistants avec qui préparer les TP, devoirs, coordinations,... et même corriger les examens sont devenus des moments de réel plaisir ! :-) Spéciale dédicace à Pyg, Emilie, Charles, Grégoire, DJ Beni et Vincent (dit 20Cents).

Mes remerciements s'adressent aussi à tous les tuteurs que j'ai côtoyés, aux membres du secrétariat EPL (particulièrement, Laurence et Pascale) dont l'aide précieuse aura permis d'organiser des TP et des événements sans stress logistique, ainsi qu'à tous les acteurs du monde académique avec qui j'ai travaillé plus ponctuellement.

Ces années n'auraient certainement pas été aussi belles sans l'ambiance sympathique et décontractée qui régnait dans l'institut et plus particulièrement, au sein du couloir du premier étage du bâtiment Stévin et de sa légendaire cafétéria pirate. Pour tout cela, je remercie :

les Dauphins du Stévin pour les heures de discussion à propos de tout et de rien, leurs histoires tantôt cocasses tantôt sérieuses, leurs encouragements et leur écoute dans les moments plus difficiles, leur imagination débordante lorsqu'il s'agit de mettre en place le compteur TGIF ou le blason de notre couloir, les *dolphin game nights* (DGN),

les midis et *compulsory coffee breaks* (CCB) autour d'Alice, les délicieux gâteaux et autres pâtisseries alléchantes pour fêter les passages d'années, les expériences impliquant du mycélium et du café, des œufs ou des gaufres et un four à micro-ondes, les séances de Mölkky ou une mémorable partie de cache-cache,... Merci à tous les brollègues [Beni2019] : Abolfazl, Amir, Anne-Sophie, Antoine, Beni, Cédric, Damien, François, Gabriel, Kévin, Maxime, Niels, Pyg, Simon, Valerio, Victor et Vincent ;

les membres de l'AsCII avec qui j'ai eu la chance de mettre en place séminaires, événements scientifiques et sociaux pendant trois années. Des cougnous pour la St-Nicolas aux tournois de badminton en passant par la projection des PhD Movies, on a passé des bons moments !

toute l'équipe administrative et technique de l'institut dont particulièrement Nathalie, Isabelle, Brigitte, François, Jean, Ludzzie, Patricia, Christel, Esther, Souley et David.

Finalement, un énorme merci aux personnes "de l'ombre" qui m'ont soutenue tout au long de ces années et m'ont parfois offert des échappatoires bienvenues. Merci à :

tous les membres de ma famille pour leur stabilité, leurs encouragements et leur intérêt pour mon travail. Merci à mes fantastiques sœurs Laure et Emilie, à mes parents aimants Yves et Françoise ainsi qu'à mes grands-parents attentifs et à l'écoute. Merci également à mon beau-frère Jérôme et ma belle-famille (Claude, Sabine, Annesoh, Yannick, Jif et Ophélie) qui m'entourent également depuis les prémices de ce travail ;

mes amis. Leur amitié est un don précieux que je veillerai à cultiver tout au long de ma vie. Un merci tout particulier à Anaïs, Charlotte, Julie, Sigrid, Marie, Fred et Tigrou d'être à mes côtés depuis si longtemps ;

Papa, Emilie et Pierre-Yves qui ont eu le courage de relire de multiples (voire toutes !) parties de cette thèse et m'ont fait des commentaires toujours très pertinents. Votre aide a été très précieuse pour finaliser sereinement ce document ;

Pierre-Yves et Alice pour leur amour inconditionnel, leur patience, leurs sourires et encouragements dans les moments plus difficiles. Partager ma vie avec vous est un bonheur quotidien.

Contents

Positron emission tomography

Lensless endoscopy

1

Introduction

WHAT does the body look like from the inside? How does it work? These questions are related to the structural and physiological aspects of the human body. They have fascinated humans for millenniums. Since the 4th century BC, physicians have acquired scientific knowledge in this field mainly through animal dissection. During the 16th century, the Belgian anatomist André Vésale promoted observations of human corpses [102]. Until the end of the 19th century, there was only one way to observe the inside of a human body: opening it and looking inside with naked eyes. It was pretty invasive. In 1895, the German physicist Wilhelm Röntgen discovered X-rays. In the wake of this, he produced the first image of anatomical structures (of his wife's hand) acquired in a non-invasive way using a planar radiograph [126].

Nowadays, imaging and exploring the human body for clinical purposes is so common that every newborn already experienced at least one imaging modality during its fetal development through ultrasound scans. During their life, most people will encounter medical issues and will possibly undergo physical examinations relying on imaging techniques like magnetic resonance imaging (MRI) or X-rays scanning.

These *in vivo* techniques do not provide the same nature of information. They are traditionally divided into two families. Structural techniques give access to specific characteristics of the tissues (*e.g.*, attenuation or reflective indices) while functional techniques observe specific physio-

logical processes occurring in the body (*e.g.*, blood flow, water diffusion or glucose uptake) [116]. Each modality exploits the interaction of a specific source of energy with the tissues. It captures specific information that is mainly invisible to human eyes, *e.g.*, hidden structures, signals out of the range of visible light, cellular processes, etc. [129].

To the question *What does the body look like from the inside?*, we could thus answer: *it depends on the way you look at it*.

1.1 Computational imaging

A better answer would probably be: *it depends on the way the imaging device looks at it*. Indeed, except for the conventional radiography, we cannot directly interpret the digital data provided by most of the current imaging techniques. For instance, ultrasound imaging captures information about the tissue composition (through their reflection and transmission coefficients) but its measurements consist of reflected sound waves. In positron emission tomography (PET), the accumulation of a radiotracer in the tissues leads to the emission of pairs of photons later detected by the imaging system. In this case, the signal of interest is a radiotracer density map (related to some biological process) and the acquired data are projections of this map gathered in a sinogram. Most of the time, a post-processing of the acquired data is necessary to recover an interpretable image. This makes those modalities strongly dependent on computational techniques.

Computational imaging (CI) is not limited to a medical context. In many other applications, imaging techniques allow us to go beyond the human eyes perception. For instance, hyperspectral imaging captures images of an object or a scene for a large number of wavelengths. Since it allows an accurate characterization of the composition of the imaged quantity, it would be useful in various real applications like chemistry or biology [47, 107, 133]. In astronomy, CI techniques are also used to recover blurry and noisy images from telescopes [69] or to detect celestial objects like planets or circumstellar disks [110].

CI can be described as a two-steps process (see Figure 1.1): an *acquisition* (or *forward*) step and a *recovery* step. First, an imaging device acquires a digital signal containing the (possibly not readily understandable) observations of a quantity of interest. After the acquisition, this quantity is recovered via computational methods. Unlike conventional imaging, the acquisition step in CI requires a sampling strategy to capture information that is then digitally represented. The emergence of compressive sensing

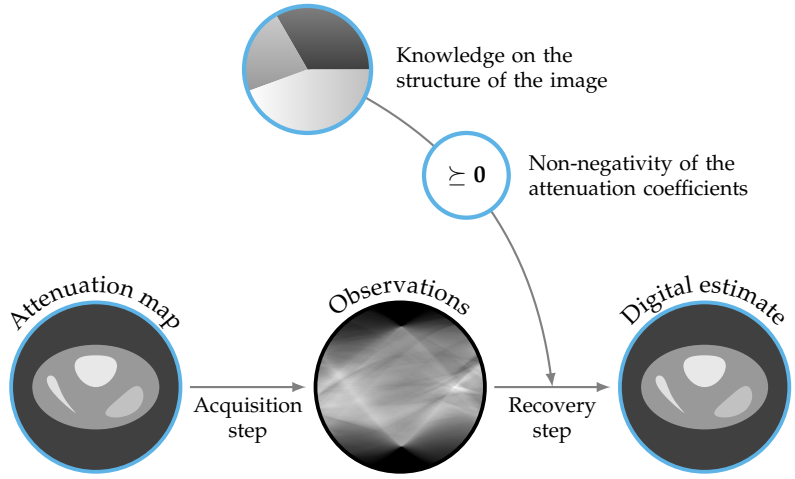

Figure 1.1 Computed tomography (CT) imaging as an example of computational imaging (CI). CT modality provides information about the attenuation of the tissues. In 2D CT, the signal of interest is a map of the attenuation coefficients of the tissues (left). The imaging device performs transmission scans for several orientations of the X-rays source. The measurements consist in 1D profiles that are gathered in a 2D sinogram (middle). Finally, a reconstruction algorithm is applied to recover a digital estimate of the original attenuation map (right). It includes prior knowledge on the structure or properties of the signal of interest (*e.g.*, non-negativity).

(CS) theory in the last decades opened new perspectives for CI: CS-based techniques aim at smartly designing both the acquisition device and the recovery method in order to reduce the amount of collected data while guaranteeing a good quality of the recovered estimate [33].

During the recovery step, we estimate the signal of interest from its measurements. This so-called *inverse* problem depends on the considered imaging process. For instance, denoising aims at removing the noise and outliers introduced in the observed data [128], inpainting tries to estimate the missing values in a signal [60], zooming consists in increasing the resolution of a signal, etc. [37, 60]. In this thesis, we focus on two estimation problems in biomedial imaging, more precisely in nuclear medicine and in fluorescence imaging. The first one is the *deblurring* of corrupted observations acquired with PET imaging (see Chapters 3 to 5). When the blurring operator is assumed to be spatially invariant, we talk about *de-*

convolution. The second estimation problem is the *reconstruction* of images from CS measurements acquired with an ultrathin endoscope (see Chapters 6 to 8).

Solving inverse problems faces two main challenges. First, we need to mathematically *formulate* the problem, *e.g.*, as a convex minimization problem. It requires an accurate knowledge of the acquisition step, preferentially approximated by a linear model. If this knowledge is unavailable, the corresponding problem is said to be *blind*. We also need some prior information on the signal of interest to be robust to distortion, noise or to approximation errors introduced by the modeling of the acquisition step. Second, we would like to *solve* the problem in a fast way with algorithms providing guarantees of convergence.

Recent techniques based on neural networks can bypass the first aforementioned challenge if they have access to a sufficiently large dataset during their training phase (see, *e.g.*, DeepPET in section 3.3 [85]). In this thesis, we rather focus on a mathematical formulation of the estimation problem based on the physics of the acquisition.

1.2 Imaging cellular processes

In the last decades, the increasing use of mouse models of disease in drug development led to the emergence of a new family of imaging techniques called *molecular imaging* [129]. Such techniques are able to image biological processes. Among them, we distinguish two main categories: (*i*) non-optical methods widely used in clinic (*e.g.*, PET and single-photon emission computed tomography (SPECT)) and (*ii*) optical approaches based on photonic methods that are still under research or only used for small animals imaging (*e.g.*, fluorescence molecular tomography or bioluminescence imaging) [109]. If suitable probes are available, modalities from both categories are able to provide *in vivo* images of very specific dynamic interactions occurring at the cellular scale, *e.g.*, showing the distribution of a drug and its target binding or allowing to observe the consequences of this binding on the target expression [129].

But the interest of molecular imaging is not restricted to the drug research area. In neuroscience, imaging neural activity in functionally connected regions of the brain at cellular scale is a long sought-after goal. Optical microscopy techniques such as two-photon fluorescence imaging of calcium activity—directly related to the propagation of the nerve impulses—have offered remarkable insight into the functional mapping of brain cir-

Technique	Resolution	Depth	Acquisition time
MRI	$10-100\ \mu$m	No limit	Minutes-hours
PET	$1-2$ mm	No limit	Minutes
SPECT	$1-2$ mm	No limit	Minutes
FRI	$2-3$ mm	<1 cm	Seconds-minutes
FMT	1 mm	<10 cm	Seconds-minutes
BLI	A few millimeters	A few centimeters	Minutes
IM	$1\ \mu$m	$<400\ \mu$m	Seconds-minutes

Table 1.1 Resolution, depth and acquisition time of the main molecular imaging systems for small animals (adapted from [129]): magnetic resonance imaging (MRI), positron emission tomography (PET), single-photon emission computed tomography (SPECT), fluorescence reflectance imaging (FRI), fluorescence-mediated molecular tomography (FMT), bioluminescence imaging (BLI) and intravital microscopy (IM). Optical techniques (FRI, FMT, BLI and IM) achieve high resolution but their imaging depth is limited compared to non-optical techniques (MRI, PET, SPECT).

cuits [64]. In clinic, PET imaging is widely used to obtain information about physiological processes in the patient body [16]. For instance, cardiologists use PET scanners to measure the myocardial perfusion. Neuropsychiatrists exploit this modality in the diagnosis of dementia or as an aid to plan the surgery of patients suffering from epilepsy. Finally, oncologists resort to PET imaging to assess tumor growth and treatment efficiency as well as for the follow-up of the patient after therapy [16].

The advantages of optical approaches based on microscopy over non-optical ones are that they are cheaper, faster and readily available (*e.g.*, they do not require radionuclides) [129]. However, they suffer from physical limitations. For instance, the scattering nature of brain tissue [146] has precluded the functional imaging at deep regions in the brain. This scattering phenomenon is amplified in the case of freely behaving animals interacting with their environment. Those physical limitations restrict either the spatial resolution or the imaging depth of such modalities compared to non-optical methods like MRI, PET or SPECT (see Table 1.1) [9, 109].

A solution to go beyond the depth limit of microscopy is to combine one of these optical techniques (*e.g.*, two-photon excited fluorescence microscopy) with a slightly invasive device playing the role of a waveguide.

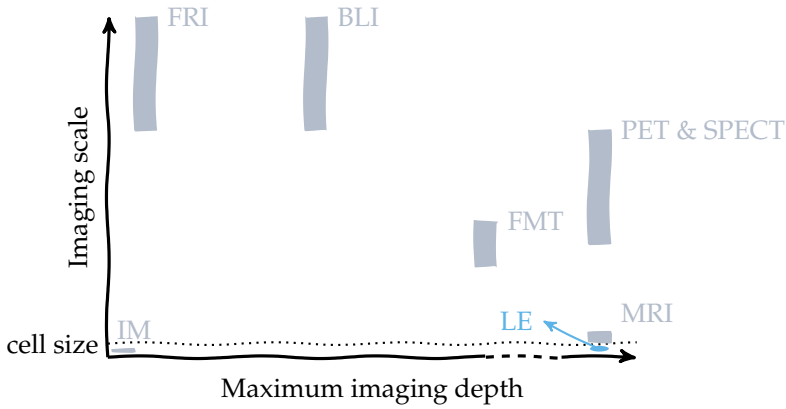

Figure 1.2 Current performances of molecular imaging devices for small animals. The development of lensless endoscopes (LE) will allow a deep imaging of biological processes at cellular scale (*i.e.*, a spatial scale around tens of micrometers). Figure drawn based on data from Table 1.1.

For instance, endomicroscopes, already used in clinical applications, use a fiber bundle as waveguide [113, 149]. Recent developments in adaptive optics, optical fibers and computational imaging techniques have opened a new class of imaging systems called *lensless endoscopes* (LE) [9, 24, 42, 117]. In these implementations, a *single* fiber in combination with wavefront shaping devices is employed as an ultrathin imaging system detecting the photons emitted by fluorescence. The extreme miniaturization of the imaging probe (diameter ≤ 200 μm) offers a minimally invasive route to imaging processes at cellular scale, deep in freely moving animals (see Figure 1.2).

Imaging challenges

The challenges encountered in PET and LE imaging share similarities driven by the *in vivo* context of those biomedical modalities. The first one is the *reduction of exposure* to the external agent necessary for the imaging process. In PET imaging, this agent is the radiotracer. For health reasons, we would like to minimize the dose injected into the patient body. In lensless endoscopy, this agent is the light. Fluorescent biological specimens are subject to photo-bleaching which is an irreversible damage leading to a complete loss of fluorescence due to an extended exposure to light. The second goal is the *reduction of the acquisition time*, either to minimize the

artifacts due to the patient's movements or, again, to reduce the light exposure during an acquisition with an LE. Those two challenges—specific to *in vivo* imaging—come in addition to the ones mentioned in section 1.1 concerning the formulation and the solving of inverse problems.

In this dissertation, we address two inverse problems subject to those additional constraints. First, we study the deconvolution of reconstructed PET images corrupted by a high level of noise that results from the short acquisition time and the low radioactive dose. Then, in the context of LE imaging, we explore acquisition and reconstruction strategies based on CS principles in order to reduce the number of measurements, directly related to the acquisition time and the light exposure. The tools that we use are general to a wide class of inverse problems but the mathematical formulation of each estimation problem is very specific since it is deeply related to the physics beyond the imaging process.

1.3 Contributions and outline

This thesis is divided into two parts: the first one concerns PET imaging and the second one is dedicated to lensless endoscopy. In the first chapter of each part, we describe the acquisition step of the imaging modality from the physical phenomena to the collection of observations by the device (see Chapters 3 and 6). Then, we propose a linear discrete forward model that is used in the inverse problem formulation. In PET imaging, we study the deconvolution problem in both a non-blind (see Chapter 4) and a blind (see Chapter 5) framework. We first characterize the noise in PET images reconstructed with linear algorithms and then, we formulate an inverse problem that accounts for this statistics and that includes prior information on the structure of the radiotracer density map. In LE imaging, the second chapter of the part (Chapter 7) is dedicated to a statistical analysis of the speckles which are used in Chapter 8 as illumination patterns. Chapter 8 presents two acquisition strategies based on such illumination and relying on CS principles as well as their associated reconstruction techniques. The CS approach allows to reduce the number of measurements and consequently, the light exposure and acquisition time.

The inverse problems corresponding to (blind) deconvolution and reconstruction from CS measurements are all expressed as *regularized* minimization problems, *i.e.*, as estimation problems including extra information on the signal to recover. In Chapter 2, we formally introduce the concepts of forward model and inverse problem in the context of imaging.

Then, we explain how regularization can help to formulate a *well-posed* inverse problem. Finally, we present tools of convex optimization as well as proximal algorithms designed to solve possibly non-smooth convex optimization problems.

Positron emission tomography

In Chapter 3, after the description of the acquisition step and its discrete approximation, we highlight some limitations of PET imaging. One of its major drawbacks is its low spatial resolution (equivalently, its high imaging scale, see Figure 1.2) compared to modalities like CT or MRI. It prevents, for instance, its use to accurately delineate tumors and to perform dose painting in radiotherapy. Indeed, even after tomographic reconstruction, PET images are still blurry and noisy. The following publication studies the deconvolution of synthetic images corrupted by Poisson noise. The assumption of piecewise-smoothness of the estimate is encoded in the total generalized variation (TGV) norm used as regularizer in the minimization problem.

> S. Guérit, L. Jacques, B. Macq, and J. A. Lee. "Post-reconstruction deconvolution of PET images by total generalized variation regularization". In: *23rd European Signal Processing Conference (EUSIPCO)*. 2015

In the perspectives of this paper, we mention that we should further investigate the nature of the noise after reconstruction in order to improve the formulation of the inverse problem. In Chapter 4, we show that the noise corruption in reconstructed PET images is far from being Poissonian. Instead, we demonstrate that under weak assumptions, this noise follows distribution showing two distinct behaviors: Gaussian and subexponential. In this chapter, we formulate an inverse problem taking into account this dual behavior. We validate our approach on PET images simulated with dPETSTEP software and on real PET data.

In Chapter 5, we assume that the blurring (or forward) operator considered as given in Chapter 4 is now unknown. The challenge is then to simultaneously estimate the density map and the blurring kernel. In collaboration with Adriana González, we show that a blind deconvolution technique similar to the one proposed in [71] can be applied to blind PET deconvolution up to minor modifications. This technique requires the knowledge of a region with constant activity in the patient body, typically the bladder. Most of the time, PET images are acquired with a combined

PET/CT scanner. The high resolution structural image obtained with computed tomography (CT) can be used to delineate such an organ.

> S. Guérit, A. González, A. Bol, J. A. Lee, and L. Jacques. "Blind deconvolution of PET images using anatomical priors". In: *the 3rd International Traveling Workshop on Interactions between Sparse models and Technology (iTWIST)*. 2016

Chapter 5 is based on this first proof of concept. It extends it in two directions: first, we replace the TV-norm by a TGV-norm in the minimization problem to promote piecewise-smoothness of the final image. Then, we validate the approach on simulated PET data instead of on synthetic observations generated by a (too) simple forward model.

Lensless endoscopy

The second part of this dissertation is mainly based on the following papers. The first one has been submitted to SIAM Journal in Imaging Sciences in March 2021,

> S. Guérit, S. Sivankutty, J. A. Lee, H. Rigneault, and L. Jacques. "Compressive lensless endoscopy with partial speckle scanning". 2021

> S. Guérit, S. Sivankutty, C. Scotté, J. A. Lee, H. Rigneault, and L. Jacques. "Compressive sampling approach for image acquisition with lensless endoscope". In: *the 4th International Traveling Workshop on Interactions between Sparse models and Technology (iTWIST)*. 2018

In Chapter 6, we describe the acquisition process in fluorescence imaging, from the illumination of the biological sample to the collection of the emitted signal. We also present the raster scanning, which is the traditional illumination and reconstruction scheme. It consists in scanning the sample with a focused light beam. This scheme provides a short acquisition time but is limited by a high sensitivity to perturbations during the calibration step and a poor quality of the final image.

When we get rid of the aforementioned calibration step, the produced light pattern is a speckle, *i.e.*, a pattern with multiple bright grains and dark regions. In Chapter 7, we study the possibility to estimate an image from observations acquired with such illumination patterns by first analyzing their statistical properties. We show that speckle fields follow a sub-exponential distribution that makes them good candidates to build efficient sensing operators.

In Chapter 8, we then justify the possibility to estimate an image with far fewer measurements compared to RS by establishing links with CS theory. We propose a CS acquisition scheme based on speckle illumination called partial speckle scanning (PSS). The first contribution of this chapter consists in characterizing an accurate linear sensing model of PSS. In particular, we deduce its equivalent sensing matrix from the discrete forward model derived in Chapter 6. The second contribution consists in optimizing the sampling trajectory parameters to get the best reconstruction quality for a given acquisition time or a prescribed number of measurements.

Other publications

For the sake of consistency, we did not include the following publications in this document.

> S. Guérit, L. Jacques, and J. A. Lee. "Image deconvolution by local order preservation of pixels values". In: *24th European Signal Processing Conference (EUSIPCO)*. 2016

> M. Kirkove, S. Guérit, L. Jacques, C. Loffet, F. Languy, J.-F. Vandenrijt, and M. Georges. "Determination of vibration amplitudes from binary phase patterns obtained by phase-shifting time-averaged speckle shearing interferometry". In: *Applied Optics* 57.27 (2018), pp. 8065–8077

The first paper proposes a deconvolution method that involves a new regularization term preserving local pixel value order relationships. In the paper, we investigate the theoretical properties of the proposed regularization and perform preliminary experiments on synthetic data. We could use this kind of constraint in Chapter 5. This extra prior would, for instance, assume that the pixel values of the kernel respect some ordering constraint, *e.g.*, a radial decay or a decay along one or several directions.

The second paper results from a collaboration with researchers in ULiège. It proposes a processing method to identify vibration modes based on binary phase patterns in shearography. Our contribution lies in the two-steps pre-processing of those binary patterns: (*i*) a phase rotation of the images and (*ii*) a denoising assuming piecewise-constant images.

2

Regularized inverse problems

The challenge, and art, in using convex optimization
is in recognising and formulating the problem.
S. Boyd and L. Vandenberghe

REGULARIZED inverse problems, and more generally, estimation problems, is a vast topic of research. Maybe a better title for this chapter would be "Elements of regularized inverse problems in imaging". Indeed, providing a complete overview of the field is obviously out of the scope of this thesis. Instead, we will introduce some key concepts and tools which are useful for the understanding of the following chapters.

The first question that arises when we talk of an *inverse* problem is: what is the *forward* model that we would like to invert? As mentioned in Chapter 1, medical imaging devices provide us with measurements (*e.g.*, X-rays intensity, returning echoes, count of photons, etc.) that depend on the physical process beyond the imaging modality. Those processes allow us to capture information about physiological activity—mostly invisible to the naked eye—occurring in the human body or about specific characteristics of the tissues. Those signals of interest, *e.g.*, organ perfusion, receptor binding or tissue reflectivity, can be seen as the inputs of imaging systems and the measurements as their outputs.

The forward (or acquisition) model mathematically relates the signal of interest f_0 to the measurement y acquired by an imaging device,

$$y = \mathcal{A}_\xi(f_0), \tag{2.1}$$

where $\mathcal{A}_\xi$ represents the mapping $f_0 \mapsto y$. This mapping can contain some randomness, indicated by ξ. Randomness can originate from the acquisition process but also from the intrinsic nature of the object of interest. In the last case, we consider f_0 as deterministic and representing a mean behavior. In this work, we assume that f_0 is a 2D object restricted to the field of view (FOV) of the device, denoted $\Omega \subset \mathbb{R}^2$, *i.e.*, $f_0 : \Omega \to \mathbb{R}$.

Knowing exactly the mapping $\mathcal{A}_\xi$ is impossible. Indeed, in addition to its intrinsic randomness, the accurate computation could be too demanding, *e.g.*, if $\mathcal{A}_\xi$ is non-linear. A solution consists in approximating the forward mapping by a simpler model generally made of a deterministic operator $\mathcal{A}$ (preferably linear) and a noise model accounting for all the noise sources (both physical and computational). In this case, (2.1) becomes

$$y = \mathcal{D}(\mathcal{A}f_0), \tag{2.2}$$

where $\mathcal{D}$ represents the degradation or noise model.

Computational image processing works with digital signals, in a discrete world. For this reason, we would like a discrete equivalent to (2.2). We suppose that f_0 can be represented in a finite set of $N = n^2$ orthogonal functions $\{\psi_i\}_{i=1}^N$ over Ω, *i.e.*, there exist coefficients $\{f_{0,i}\}_{i=1}^N$ such that

$$f_0(\boldsymbol{x}) \approx \textstyle\sum_{i=1}^N f_{0,i}\psi_i(\boldsymbol{x}).$$

In this work, we select a naive pixel representation $\psi_i(\boldsymbol{x}) \coloneqq \psi(\boldsymbol{x} - \boldsymbol{x}_i)$ with $\mathcal{X} \coloneqq \{\boldsymbol{x}_i\}_{i=1}^N$ evenly sampling Ω on N locations and $\psi(\boldsymbol{x})$ equals to $1/a^2$ if $\boldsymbol{x} \in [-a/2, a/2] \times [-a/2, a/2]$, and 0 otherwise. Assuming a square FOV, its side length is na. The discrete equivalent to f_0 is $\boldsymbol{f}_0 \coloneqq (f_{0,1}, \ldots, f_{0,N})^\top \in \mathbb{R}^N$, a vectorized version of the $n \times n$ discretized signal of interest.

We assume that $\mathcal{A}$ is a linear mapping and we define $\boldsymbol{A} \in \mathbb{R}^{M \times N}$ as its discrete equivalent which is commonly called *forward operator* or *sensing operator*. Depending on the application, $\boldsymbol{A}$ can be a convolution operator, a discrete Fourier transform, etc. The discrete forward model is then

$$\boldsymbol{y} = \mathcal{D}(\boldsymbol{A}\boldsymbol{f}_0), \tag{2.3}$$

where $\boldsymbol{y} \in \mathbb{R}^M$ is a vector containing the M observations of $\boldsymbol{f}_0$.

2.1 What is an inverse problem?

Model (2.3) explains how the observations $\boldsymbol{y}$ of a quantity of interest $\boldsymbol{f}_0$ are generated. However, to interpret the data and visualize the information it contains, we need to reconstruct $\boldsymbol{f}_0$ from its measurements. This estimation process requires a fine understanding of the acquisition model.

Given observations, we would like to *invert* the forward model to find $\boldsymbol{f}_0$, *i.e.*, we would like to find the mapping $\boldsymbol{y} \mapsto \boldsymbol{x}$. Finding such a mapping by direct inversion of (2.3) is unrealistic in most situations. For instance, this may be due to the randomness introduced by $\mathcal{D}$ or to the errors introduced when we approximate $\mathcal{A}_{\xi}$ by a deterministic, linear and discrete mapping $\boldsymbol{A}$ and a corruption operator $\mathcal{D}$.

A well-known solution to overcome this limitation is to find an estimate $\hat{\boldsymbol{f}}$ for $\boldsymbol{f}_0$ such that $\boldsymbol{y} \approx \boldsymbol{A}\hat{\boldsymbol{f}}$. We achieve this by minimizing a *distance* between the real observations, $\boldsymbol{y}$, and the estimated ones, $\boldsymbol{A}\hat{\boldsymbol{f}}$. The definition of a distance function is closely related to the concept of a *norm*.

Definition 2.1 (Norm) *[27, p. 634] A function $g : \mathbb{R}^N \to \mathbb{R}$ with $\operatorname{dom} g = \mathbb{R}^N$ is called a norm if it satisfies the following conditions:*

- *g is non-negative: $g(\boldsymbol{u}) \geq 0$, for all $\boldsymbol{u} \in \mathbb{R}^N$;*
- *g is definite: $g(\boldsymbol{u}) = 0$ only if $\boldsymbol{u} = \boldsymbol{0}$;*
- *g is homogeneous: $g(a\boldsymbol{u}) = |a|g(\boldsymbol{u})$, for all $\boldsymbol{u} \in \mathbb{R}^N$ and $a \in \mathbb{R}$;*
- *g satisfies the triangle inequality: $g(\boldsymbol{u} + \boldsymbol{v}) \leq g(\boldsymbol{u}) + g(\boldsymbol{v})$, for all $\boldsymbol{u}, \boldsymbol{v} \in \mathbb{R}^N$.*

Definition 2.2 (Distance) *[27, p. 634] The distance between two vectors $\boldsymbol{u}$ and $\boldsymbol{v}$ is defined as the length of their difference,*

$$\operatorname{dist}(\boldsymbol{u}, \boldsymbol{v}) := \|\boldsymbol{u} - \boldsymbol{v}\|,$$

where $\|\cdot\|$ represents any norm.

We write the following estimation problem,

$$\hat{\boldsymbol{f}} := \underset{\boldsymbol{u} \in \mathbb{R}^N}{\arg\min} \|\boldsymbol{A}\boldsymbol{u} - \boldsymbol{y}\|, \tag{2.4}$$

or equivalently,

$$\hat{\boldsymbol{f}} := \underset{\boldsymbol{u} \in \mathbb{R}^N}{\arg\min} \|\boldsymbol{A}\boldsymbol{u} - \boldsymbol{y}\|^2, \tag{2.5}$$

since a norm is always non-negative (see Definition 2.1). When we consider the ℓ_2-norm, this last problem is called the *least-squares minimization*. It is widely used in regression analysis, optimal control, data fitting, etc. [27]. From a Bayesian point of view, it corresponds to the negative log-likelihood of a Gaussian distribution (see Remark 2.1).

Objective functions of (2.4) and (2.5) are both *convex*, a highly desirable property in optimization, since every norm on $\mathbb{R}^N$ is convex [27].

Definition 2.3 (Convex set) *[27, p. 22] A set $\mathcal{Q}$ is convex if the line segment between any two points in $\mathcal{Q}$ lies in $\mathcal{Q}$,* i.e., *if for any $\boldsymbol{u}, \boldsymbol{v} \in \mathcal{Q}$ and any θ with $0 \leq \theta \leq 1$, we have*

$$\theta \boldsymbol{u} + (1 - \theta)\boldsymbol{v} \in \mathcal{Q}.$$

Definition 2.4 (Convex function) *[27, p. 67] A function $g : \mathbb{R}^N \to \mathbb{R}$ is convex if* $\operatorname{dom} g$ *is a convex set and if for all $\boldsymbol{u}, \boldsymbol{v} \in \operatorname{dom} g$ and any θ with $0 \leq \theta \leq 1$, we have*

$$g(\theta \boldsymbol{u} + (1 - \theta)\boldsymbol{v}) \leq \theta g(\boldsymbol{u}) + (1 - \theta) g(\boldsymbol{v}).$$

Any convex function g has a unique global minimum. It is *strongly* convex if it possesses a unique $\boldsymbol{u}^\star \in \operatorname{dom} g$ such that $g(\boldsymbol{u}^\star)$ is the minimum. The unicity of the solutions to (2.4) and (2.5) is directly related to the rank of the forward operator $\boldsymbol{A}$: if $\operatorname{rank}(\boldsymbol{A}) = N$ (only possible if $M \geq N$), there exists a unique solution while if $\operatorname{rank}(\boldsymbol{A}) < N$, the problem admits several minimizers. But even if $\operatorname{rank}(\boldsymbol{A}) = N$, a bad conditioning of $\boldsymbol{A}$ makes the minimization problems highly sensitive to errors in $\boldsymbol{y}$ resulting for instance in a noise amplification in the estimate. A small change in the observations greatly impacts the estimate $\hat{\boldsymbol{f}}$.

In many practical applications, problems (2.4) and (2.5) are thus considered as *ill-posed* due for instance to the presence of noise in the observations, to a badly conditioned sensing operator or to a number of measurements $M < N$. Consequently, we cannot guarantee the uniqueness or even the existence of a solution. Conversely, a *well-posed* problem was defined in 1902 by Hadamard as a problem admitting a unique solution that continuously depends on the observations [82, 83, 151].

In the next sections, we will focus on two key aspects of the estimation of a signal from its observations, namely the *formulation* of a well-posed inverse problem in section 2.2 and its computational *solving* in section 2.3.

2.2 How to formulate a well-posed inverse problem?

To address the issue described in section 2.1 and reduce the set of possible solutions, a widely used method[1] consists in adding extra objective functions ϕ_i with $i \in [I]$ in the minimization problem [27, 151]. Functions ϕ_i encode prior knowledge on the structure of the object of interest (*e.g.*, small energy of the signal, non-negativity, sparsity of the coefficients in some basis, etc. [27]). To solve the resulting multi-criterion problem, a common form of *regularization* is to minimize the weighted sum of the objective functions,

$$\hat{\boldsymbol{f}} \coloneqq \underset{\boldsymbol{u}\in\mathbb{R}^N}{\arg\min}\ \mathrm{dist}(\boldsymbol{A}\boldsymbol{u}, \boldsymbol{y}) + \sum_{i=1}^{I} \rho_i \phi_i(\boldsymbol{u}), \tag{2.6}$$

where $\rho_i > 0$ with $i \in [I]$ are *regularization parameters* making the trade-off between the data fidelity term and the regularization terms and not known *a priori* (see subsection 2.3.2). By abuse of notation, we denote the data fidelity term "dist" even when it is not a norm *stricto sensu* (*e.g.*, the squared ℓ_2-norm). The extra terms in the objective function encourage the estimate to respect a certain prior model of the original image. In this thesis, we restrict ourselfs to functions ϕ_i which are convex such that the objective function of (2.6) is also convex [27, p. 79]. In the following sections, we detail (*i*) the common functions used to enforce the consistency with the observations and (*ii*) several possible priors and their associate functions.

Remark 2.1. In some cases, formulation (2.6) can be seen as a maximum *a posteriori* probability (MAP) estimation problem. The Bayesian MAP estimate of $\boldsymbol{f}_0$ given observations $\boldsymbol{y}$ is

$$\hat{\boldsymbol{f}}_{\mathrm{MAP}} \coloneqq \underset{\boldsymbol{u}\in\mathbb{R}^N}{\arg\max}\ \log p_{\boldsymbol{y}|\boldsymbol{u}}(\boldsymbol{u}, \boldsymbol{y}) + \log p_{\boldsymbol{u}}(\boldsymbol{u}), \tag{2.7}$$

where p indicates a probability density function (pdf). From the Bayesian perspective, $\boldsymbol{f}_0$ is random while the classical point of view considers $\boldsymbol{f}_0$ as deterministic. Both approaches are similar: they seek an estimator that is close to $\boldsymbol{f}_0$ in expectation and that has small deviation [76]. The negative log-likelihood of the observations in (2.7), reflecting the statistics of the noise, can be associated with the data fidelity term in (2.6). For instance, when the noise on the observations is Laplacian (resp. Gaussian), the cor-

[1] If the forward operator is ill-conditioned, another (or complementary) solution is to apply preconditioning like in [37, 114, 115].

responding distance function is the ℓ_1-norm (resp. squared ℓ_2-norm). The second term in (2.7), related to the distribution of $\boldsymbol{u}$, can be seen as a regularization term penalizing the choices of $\boldsymbol{u}$ that are unlikely [27].

2.2.1 Data model

The data fidelity term mainly depends on the statistics of the noise corrupting the observations. A widely used distance function is the squared ℓ_2-norm [27, 53, 128], as in the least-squares problem,

$$\operatorname{dist}(\boldsymbol{Au}, \boldsymbol{y}) = \|\boldsymbol{Au} - \boldsymbol{y}\|_2^2.$$

The popularity of this quadratic function is probably due to its differentiability and the simple form of its gradient [27]. From a statistical perspective, this term is associated with the assumption of an i.i.d. Gaussian noise on the data. A weighted version of this norm could also include non i.i.d. possibly correlated Gaussian noise [27].

To deal with Poisson noise statistics, the squared ℓ_2-norm can still be used but requires first a variance-stabilizing transform (VST) of the observations such as proposed by Anscombe [10, 54] or a Gaussian approximation of the distribution [12]. We can also resort to the negative log-likelihood of the Poisson distribution for the distance function, called the *Kullback-Leibler divergence* [18, 118]. In this case, $\operatorname{dist}(\boldsymbol{Au}, \boldsymbol{y}) = \operatorname{KL}(\boldsymbol{Au}, \boldsymbol{y})$.

Definition 2.5 (Kullback-Leibler divergence) *The Kullback-Leibler divergence* $\operatorname{KL} : \mathbb{R}^N \to \mathbb{R}$ *is defined as*

$$\operatorname{KL}(\boldsymbol{u}; \boldsymbol{y}) = \sum_{i=1}^{N} (\boldsymbol{u} - \boldsymbol{y} \odot f(\boldsymbol{u}))_i + r(\boldsymbol{y}), \tag{2.8}$$

where $r(\boldsymbol{y})$ only depends on $\boldsymbol{y}$, f is applied componentwise on vector with $f(t) \coloneqq \log t$ if $t > 0$ and 0 otherwise and $\odot$ denotes the elementwise product.

Another possible data fidelity term is the ℓ_1-norm,

$$\operatorname{dist}(\boldsymbol{Au}, \boldsymbol{y}) = \|\boldsymbol{Au} - \boldsymbol{y}\|_1.$$

It used, for instance, to deal with noise having a heavy distribution tail (*e.g.*, Laplacian noise) or noise containing strong outliers like impulse noise [37]. Unlike the squared ℓ_2-norm, its non-differentiability prevents the use of gradient-based methods to solve the corresponding estimation problem.

The three aforementioned data fidelity terms are only a small part of the existing ones. For instance, we also mention the existence of fidelity terms related to a Poisson-Gaussian noise model [41, 100], the β-divergence that generalizes the squared ℓ_2-norm and the KL divergence [36] or a data fidelity term designed for multiplicative noise [53].

2.2.2 Prior information

The first use of regularization goes back to the early 60's. Tikhonov introduced the regularization of the least-squares problem based on (2.5) with a squared ℓ_2-norm [151], *i.e.*,

$$\phi_i(\boldsymbol{u}) = \|\boldsymbol{u}\|_2^2.$$

He showed that if operator $\boldsymbol{A}$ is bounded, this minimization problem has a unique solution given by a closed form expression [27]. This prior forces the estimate to keep small values, *i.e.*, to have a small energy. For instance, it prevents the spurious variations in the estimate due to noise amplification when $\boldsymbol{A}$ is badly conditioned.

In the following decades, researchers proposed and studied other regularizers [56], *e.g.*, terms promoting the smoothness of the estimate, a sparse representation in some basis (*e.g.*, wavelet basis), etc. We briefly introduce some of those priors below, with an emphasis on the TV- and TGV-norms that we extensively use in this thesis.

Belonging to a closed convex set

A first family of priors is the belonging of $\boldsymbol{f}_0$ to a closed convex set $\mathcal{Q}$, either explicitly defined or described through inequality constraints. For instance, a common assumption on $\boldsymbol{f}_0$ is the non-negativity, *i.e.*, $\mathcal{Q} = \mathbb{R}_+^N$. Other priors are ordering constraints [78], bounds on the minimum and/or maximum values of $\boldsymbol{f}_0$, norm ball constraint, etc. [27]

These priors can be expressed as contraints but, to match the formulation of (2.6), we consider the corresponding Lagrangian formulation. In this case, the function ϕ_i corresponding to the prior $\boldsymbol{u} \in \mathcal{Q}$ is the indicator function of the closed non-empty convex set $\mathcal{Q}$, defined as

$$\imath_{\mathcal{Q}}(\boldsymbol{u}) := \begin{cases} 0 & \text{if } \boldsymbol{u} \in \mathcal{Q} \\ +\infty & \text{otherwise.} \end{cases} \tag{2.9}$$

Notice that $\tau \imath_{\mathcal{Q}} = \imath_{\mathcal{Q}}$ for any $\tau > 0$, by definition of the indicator function.

Sparsity in some dictionary

Let $\boldsymbol{\Psi} \in \mathbb{R}^{N \times P}$ be a dictionary, either complete ($P = N$) or redundant ($P > N$) [142]. A signal $\boldsymbol{u} \in \mathbb{R}^N$ is said to be *sparse* in $\boldsymbol{\Psi}$ if it can be expressed as the linear combination of only a few columns of $\boldsymbol{\Psi}$, *i.e.*, if

$$\boldsymbol{c} = \boldsymbol{\Psi}^* \boldsymbol{u}$$

is a sparse vector.

Definition 2.6 (s-sparse signal) *Let $\boldsymbol{u} \in \mathbb{R}^N$. The vector $\boldsymbol{u}$ is said s-sparse if it has only s non-zeros entries,* i.e., *if the cardinality of $\boldsymbol{u}$ is equal to s.*

Natural images possess some intrinsic structure compared to signals like noise. We assume that there exist dictionaries in which they have a sparse representation or in which most of their coefficients is close to zero. There exist several functions ϕ_i promoting sparsity. In this work, we only consider the most widely used, namely the ℓ_1-norm,

$$\phi_i(\boldsymbol{u}) = \|\boldsymbol{\Psi}^* \boldsymbol{u}\|_1.$$

The priors promoting sparsity are barely used in this thesis. For this reason, we refer the reader to [29, 142] for a comprehensive understanding of sparsity in image processing.

Small total variation and small total generalized variation

Another possible assumption about the object of interest concerns its *piecewise smoothness*. The total variation (TV) and the total generalized variation (TGV) of an image are both quantities related to the first or higher order derivatives of this image. We first start by defining the discrete *gradient* operator, the *divergence* operator and the *symmetrized derivative* operator.

Definition 2.7 (Discrete gradient operator) *[79] The general discrete gradient operator $\boldsymbol{\nabla}$ applicable to $N \times k$ tensor fields is defined as*

$$\boldsymbol{\nabla} : \mathbb{R}^{N \times k} \to \mathbb{R}^{N \times 2k},\ \boldsymbol{u} \mapsto (\boldsymbol{\nabla} \boldsymbol{u}) \coloneqq (\boldsymbol{\nabla}_1 \boldsymbol{u}, \boldsymbol{\nabla}_2 \boldsymbol{u}),$$

with $k \in \mathbb{N}_0$ and $\boldsymbol{\nabla}_i \in \mathbb{R}^{N \times N}$ the first spatial derivative of the tensor field in direction $\boldsymbol{e}_i$, aligned with axis i of the 2D image.

In practice, discrete operators $\boldsymbol{\nabla}_1$, $\boldsymbol{\nabla}_2$ and their adjoints are approximated using forward and backward first-order finite differences with homogeneous Dirichlet boundary conditions, as described in [28]. When the

object is located at the center of a field of view (FOV) with zero background, $\boldsymbol{\nabla}_1$ and $\boldsymbol{\nabla}_2$ can be expressed as convolution operators with kernels $(-1, 1, 0)^\top$ and $(-1, 1, 0)$, respectively, and can be represented by circulant matrices. The adjoint of $\boldsymbol{\nabla}$ is equal to the negative of the *divergence* operator, *i.e.*, $\boldsymbol{\nabla}^* = -\mathrm{div}$.

Definition 2.8 (Divergence operator) *[79] The divergence operator* div *is defined as*

$$\mathrm{div} : \mathbb{R}^{N\times 2k} \to \mathbb{R}^{N\times k},\ \boldsymbol{u} = (\boldsymbol{u}_1, \boldsymbol{u}_2) \mapsto (-\boldsymbol{\nabla}_1^* \boldsymbol{u}_1 - \boldsymbol{\nabla}_2^* \boldsymbol{u}_2).$$

Definition 2.9 ($L_{p,q}$-norm) *Let $\boldsymbol{u} \in \mathbb{R}^{N\times k}$ and $\boldsymbol{u}_i \in \mathbb{R}^k$ be the i^{th} row of $\boldsymbol{u}$. The $L_{p,q}$-norm of $\boldsymbol{u}$ is defined as*

$$\|\boldsymbol{u}\|_{p,q} := \Big(\sum_{i=1}^{N} \|\boldsymbol{u}_i\|_p^q \Big)^{1/q}.$$

Definition 2.10 (TV-norm) *[37] The TV-norm of $\boldsymbol{u} \in \mathbb{R}^N$ is defined in a discrete setting as the ℓ_1-norm of the gradient magnitude of $\boldsymbol{u}$,*

$$\mathrm{TV} : \mathbb{R}^N \to \mathbb{R},\ \boldsymbol{u} \mapsto \mathrm{TV}(\boldsymbol{u}) := \|\boldsymbol{\nabla}\boldsymbol{u}\|_{2,1}. \tag{2.10}$$

The first use of the TV-norm dates back to early 90's. Rudin *et al.* proposed a denoising algorithm (*i.e.*, $\boldsymbol{A}$ is the identity operator) based on the minimization of a squared ℓ_2-norm (data fidelity term) and a TV-norm (regularization term) [128]. In many applications, frameworks based on TV are used to promote piecewise-constant images, *i.e.*, sparsity in the gradient domain [28]. However, as Knoll *et al.* [93] mentionned in the case of magnetic resonance imaging (MRI), this regularization is not well adapted to real images, *e.g.*, due to the heterogeneous nature of the tissues. Moreover, as in any other imaging modality, the borders of the true object do not perfectly match the pixel grid of the (discrete) reconstructed object. Consequently, we generally observe staircasing artifacts in smooth areas of images reconstructed with TV regularization [28, 93] (see Figure 2.1b).

To alleviate those limitations when working with real images, we can resort to the TGV-norm. This norm was introduced by Bredies *et al.* in 2010 and can be considered as the generalization of TV to higher-order image derivatives [28]. In this work, we only consider the second-order TGV, denoted TGV_α^2.

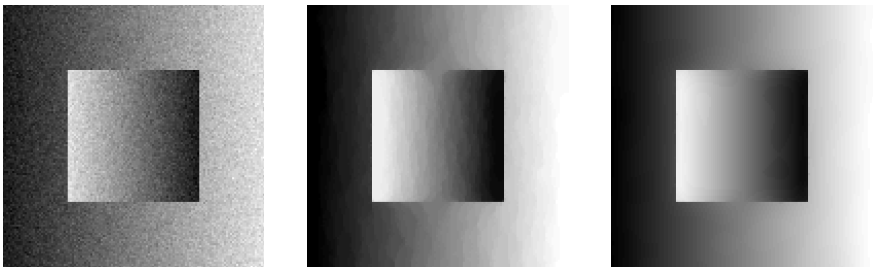

(a) (b) (c)

Figure 2.1 (a) Observations corrupted by additive white Gaussian noise, (b) estimate obtained after denoising with TV regularization, and (c) estimate obtained after denoising with TGV^2_α regularization. We observe an absence of staircasing effects in (c) compared to (b).

Definition 2.11 (Symmetrized derivative operator) *[79] The symmetrized derivative operator ε is*

$$\varepsilon : \mathbb{R}^{N\times 2} \to \mathbb{R}^{N\times 4},\ \boldsymbol{u} \mapsto \varepsilon(\boldsymbol{u}) := \frac{1}{2}\left((\boldsymbol{\nabla}\boldsymbol{u}) + (\boldsymbol{\nabla}\boldsymbol{u})S_{23}\right),$$

where $S_{23} \in \{0,1\}^{4\times 4}$ permutes the second and third columns of $\boldsymbol{\nabla}\boldsymbol{u}$.

Applying ε on the gradient of an image provides information about its second derivative. The concept of symmetrized tensors is detailed in [28].

Definition 2.12 (TGV^2_α-norm) *[28] The TGV^2_α-norm of $\boldsymbol{u} \in \mathbb{R}^N$ is defined in a discrete setting as*

$$\mathrm{TGV}^2_\alpha : \mathbb{R}^N \to \mathbb{R},\ \boldsymbol{u} \mapsto \mathrm{TGV}^2_\alpha(\boldsymbol{u}) := \min_{\boldsymbol{w}\in\mathbb{R}^{N\times 2}} \|\boldsymbol{\nabla}\boldsymbol{u} - \boldsymbol{w}\|_{2,1} + \alpha\|\varepsilon(\boldsymbol{w})\|_{2,1}, \tag{2.11}$$

where $\alpha > 0$ is a parameter making a trade-off between the edge-preserving term and the smoothness-promoting term.

Deriving $\mathrm{TGV}^2_\alpha(\boldsymbol{u})$ is not as easy as $\mathrm{TV}(\boldsymbol{u})$ because an additional minimization problem has to be solved. The optimal value of $\boldsymbol{w}$ in (2.11) depends on the features of image $\boldsymbol{u}$. Locally, in smooth areas, $\boldsymbol{w}$ is close to $\boldsymbol{\nabla}\boldsymbol{u}$ to give more importance to the smoothness-promoting term. In regions near image edges, $\boldsymbol{w}$ is close to $\mathbf{0}$ to preserve sharp edges like TV. These properties make TGV^2_α more adapted to real images than TV (see Figure 2.1c).

2.3 How to solve such problems?

Since we do not require the distance function or the ϕ_i's to be differentiable, we cannot use methods relying on the gradient or the Hessian of the objective function to solve (2.6) (*e.g.*, gradient descent method or Newton's method [27]). Instead, we resort to the family of *proximal algorithms* [111] that can deal with the optimization of non-differentiable functions like the ℓ_1-norm or the indicator functions of convex sets. The only requirement is that each function in (2.6) must be *lower semicontinuous* in addition to convex. For instance, the indicator function of a closed convex set defined in (2.9) is not continuous but is still lower semicontinuous.

Definition 2.13 (Lower semicontinuous function) *Let a function $g : \mathbb{R}^N \to \mathbb{R} \cup \{-\infty, +\infty\}$. A lower level set of g is defined as $\{\boldsymbol{u} \in \mathbb{R}^N | g(\boldsymbol{u}) \leq t\}$ for $t \in \mathbb{R}$. Function g is lower semicontinuous if and only if all its lower level sets are closed.*

The proximal algorithms are based on the notion of *proximal operator* introduced in 1962 by Moreau [43, 105]. The main advantage of this class of algorithms is that we do not need to compute the proximal operator of the whole objective function: we only need the expression of the proximal operators of each term in the sum. Some algorithms exploit the fact that some terms may be differentiable (*e.g.*, the proximal gradient method).

Definition 2.14 (Proximal operator) *Let g be a lower semicontinuous convex function from $\mathbb{R}^N$ to $\mathbb{R} \cup \{+\infty\}$ such that $\{\boldsymbol{u} \in \mathbb{R}^N | g(\boldsymbol{u}) < +\infty\}$ is non-empty. The proximal operator of $g : \mathbb{R}^N \to \mathbb{R}^N$ evaluated in $\tilde{\boldsymbol{u}} \in \mathbb{R}^N$ is unique and defined as*

$$\operatorname{prox}_g(\tilde{\boldsymbol{u}}) \coloneqq \underset{\boldsymbol{u} \in \mathbb{R}^N}{\arg\min} \frac{1}{2}\|\tilde{\boldsymbol{u}} - \boldsymbol{u}\|_2^2 + g(\boldsymbol{u}).$$

A proximal operator can be interpreted as a minimizer of the function g that stays close to $\tilde{\boldsymbol{u}}$ (see Figure 2.2). A lot of non-differentiable functions, like the ℓ_1-norm or the indicator function, have a closed-form proximal operator.

Functions in (2.6) possibly include linear operators in their expressions, *i.e.*, we can write $\phi_i(\boldsymbol{u}) = \phi_i'(\boldsymbol{L}_i\boldsymbol{u})$. If the operator $\boldsymbol{L}_i$ is *semi-orthogonal* and if the proximal operator of ϕ_i' is known, we can easily compute the proximal operator of ϕ_i with Property 2.15.

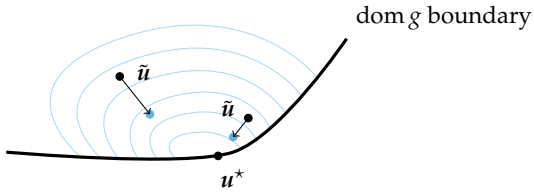

Figure 2.2 Illustration of the concept of proximal operator. Blue lines indicate the level sets of g. The minimizer of g is $\boldsymbol{u}^\star$.

Property 2.15 (Semi-orthogonal linear transform) *[43, 111] Let g be a function as defined in Definition 2.14. If $g(\boldsymbol{u}) = h(\boldsymbol{L}\boldsymbol{u})$ where $\boldsymbol{L} \in \mathbb{R}^{M\times N}$ is a semi-orthogonal linear operator,* i.e., *$\boldsymbol{L}\boldsymbol{L}^* = \nu \mathbf{Id}_M$ with $\nu > 0$, then*

$$\operatorname{prox}_{\lambda g}(\tilde{\boldsymbol{u}}) = \tilde{\boldsymbol{u}} + \nu^{-1}\boldsymbol{L}^*(\operatorname{prox}_{\nu\lambda h}(\boldsymbol{L}\tilde{\boldsymbol{u}}) - \boldsymbol{L}\boldsymbol{u}).$$

When $\boldsymbol{L}$ is orthogonal, it reduces to

$$\operatorname{prox}_{\lambda g}(\tilde{\boldsymbol{u}}) = \boldsymbol{L}^*\operatorname{prox}_{\nu\lambda h}(\boldsymbol{L}\tilde{\boldsymbol{u}}).$$

We rewrite (2.6) in a way making those operators visible,

$$\hat{\boldsymbol{f}} := \underset{\boldsymbol{u}\in\mathbb{R}^N}{\arg\min}\, G(\boldsymbol{u}) + \sum_{i=1}^{L} F_i(\boldsymbol{L}_i\boldsymbol{u}), \tag{2.12}$$

where $\boldsymbol{L}_i \in \mathbb{R}^{M_i\times N}$ and functions $G : \mathbb{R}^N \to \mathbb{R}$, $F_i : \mathbb{R}^{M_i} \to \mathbb{R}$ are convex lower semicontinuous functions for which the proximal operators are known or can be computed in a fast way. Function G does not necessarily correspond to the data fidelity term. In the following section, we describe the proximal algorithms used in this thesis (or that could be used) based on formulation (2.12).

2.3.1 Proximal algorithms

The algorithms described in this section aim at solving (2.12) for different assumptions on functions G and F_i's. For instance, the first two algorithms, the proximal gradient (PG) method and the generalized forward-backward (GFB) algorithm, assume that at least one term in the objective function is differentiable. The alternating direction method of multipliers (ADMM)

can deal with $L > 1$ but it requires $(\mathbf{Id}_N + \sum_{i=1}^{L} \boldsymbol{L}_i^* \boldsymbol{L}_i)$ to be easily invertible. The algorithm solving (2.12) with the weakest assumptions on the functions and the operators is the generalized version of the Chambolle-Pock (CP) primal-dual algorithm.

Proximal gradient method

The PG method, also known as the proximal forward-backward splitting [44], assumes that $L = 1$, $\boldsymbol{L}_1 = \mathbf{Id}_N$ and G is differentiable with a *Lipschitz continuous* gradient.

Definition 2.16 (Lispschitz continuity) *Function $g : \mathbb{R}^N \to \mathbb{R}$ is Lipschitz continuous if there exists a constant $\gamma > 0$ such that*

$$\|g(\boldsymbol{u}) - g(\boldsymbol{v})\|_2 \leq \gamma \|\boldsymbol{u} - \boldsymbol{v}\|_2$$

for all $\boldsymbol{u}, \boldsymbol{v} \in \mathbb{R}^N$.

One iteration of the algorithm is made up of two steps: a forward gradient step and a backward proximal step,

$$\boldsymbol{u}^{(n)} = \operatorname{prox}_{\mu F_1}(\boldsymbol{u}^{(n-1)} - \mu \nabla G(\boldsymbol{u}^{(n-1)})), \tag{2.13}$$

where $\mu > 0$ is a step-size. Parameter μ must verify the following condition to ensure the convergence of the method [111, section 4.2]: $\mu \in]0, 2/\gamma]$, where γ is the Lipschitz constant of ∇G. If γ is unknown, the parameter μ can be chosen by a line search [111]. Moreover, the step-size can change at each iteration. In this case, we replace μ by $\mu^{(n)}$ in (2.13).

Finally, let us mention two special cases of this method: (*i*) when G is the indicator function of a closed convex set, PG method reduces to a projected gradient method and (*ii*) when G is a ℓ_1-norm, the method is known as the iterative shrinkage/thresholding algorithm (ISTA), widely used to solve inverse problems promoting sparsity of the estimate [17, 111].

Generalized forward-backward algorithm

The GFB algorithm is a generalization of the PG method able to handle (2.12) with $L \geq 1$. It was recently proposed by Raguet *et al.* [120]. As for the PG method, it also assumes that G is differentiable with a Lipschitz continuous gradient. In their formulation, Raguet *et al.* assume that $\boldsymbol{L}_i = \mathbf{Id}_N$ for all $i \in [L]$ (see [120, Algorithm 1]).

Based on their work, we propose a formulation of the algorithm that make explicitly appear the operators $\boldsymbol{L}_i$'s like in (2.12). It assumes that

each operator is either semi-orthogonal or is such that $(\mathbf{Id}_N + \boldsymbol{L}_i^* \boldsymbol{L}_i)$ is easily invertible. We order the functions F_i such that the first L_{so} ones have semi-orthogonal operators and the last L_{inv} ones have operators with the property that $(\mathbf{Id}_N + \boldsymbol{L}_i^* \boldsymbol{L}_i)$ can be easily inverted. For these last functions, we introduce auxiliary variables $\boldsymbol{v}_i = \boldsymbol{L}_i \boldsymbol{u} \in \mathbb{R}^{M_i}$ for $i \in \{L_{\text{so}} + 1, L\}$. The projections onto these sets are denoted $\text{proj}_{\boldsymbol{L}_i}$, again for $i \in \{L_{\text{so}} + 1, L\}$. The steps are described in Algorithm 1.

Algorithm 1: Generalized forward-backward algorithm

initialization: choose $\lambda, \mu > 0$; $v_1, v_2, \omega_i \in]0,1[$ for $i \in [L]$ such that $v_1 + v_2 = 1$ and $\sum_{i=1}^{L} \omega_i = 1$; $\boldsymbol{z}_i^{(0)} \in \mathbb{R}^N$ for $i \in [L]$; $\boldsymbol{v}_i^{(0)}, \boldsymbol{p}_i^{(0)}, \boldsymbol{q}_i^{(0)} \in \mathbb{R}^{M_i}$ for $i \in \{L_{\text{so}} + 1, L\}$ and `maxIter`; set $\boldsymbol{u}^{(0)} = \sum_{i=1}^{L} \omega_i \boldsymbol{z}_i$;

for $n = 1$ **to** *maxIter* **do**

  for $i = 1$ **to** L_{so} **do**

$$\boldsymbol{z}_i^{(n)} = \boldsymbol{z}_i^{(n-1)} + \lambda\Big(\text{prox}_{\frac{\mu}{\omega_i} F_i \circ \boldsymbol{L}_i}\big(2\boldsymbol{u}^{(n-1)} - \boldsymbol{z}_i^{(n-1)} - \mu \nabla G(\boldsymbol{u}^{(n-1)})\big) - \boldsymbol{u}^{(n-1)}\Big);$$

  end

  for $i = 1$ **to** L_{so} **do**

$$\boldsymbol{p}_i^{(n)} = \boldsymbol{p}_i^{(n-1)} + \lambda\Big(\text{prox}_{\frac{\mu}{v_1} F_i}\big(2\boldsymbol{v}^{(n-1)} - \boldsymbol{p}_i^{(n-1)}\big) - \boldsymbol{v}^{(n-1)}\Big);$$

    `// Projection step`

$$(\tilde{\boldsymbol{z}}_i^{(n)}, \tilde{\boldsymbol{p}}_i^{(n)}) = \text{proj}_{\boldsymbol{L}_i}\Big(2\boldsymbol{u}^{(n-1)} - \boldsymbol{z}_i^{(n-1)} - \mu \nabla G(\boldsymbol{u}^{(n-1)}), 2\boldsymbol{v}^{(n-1)} - \boldsymbol{q}_i^{(n-1)}\Big);$$

$$\boldsymbol{z}_{L_{\text{so}}+i}^{(n)} = \boldsymbol{z}_{L_{\text{so}}+i}^{(n-1)} + \lambda(\tilde{\boldsymbol{z}}_i^{(n)} - \boldsymbol{u}^{(n-1)});$$

$$\boldsymbol{q}_i^{(n)} = \boldsymbol{q}_i^{(n-1)} + \lambda(\tilde{\boldsymbol{p}}_i^{(n)} - \boldsymbol{v}^{(n-1)});$$

$$\boldsymbol{v}_i^{(n)} = v_1 \boldsymbol{p}_i^{(n)} + v_2 \boldsymbol{q}_i^{(n)};$$

  end

$$\boldsymbol{u}^{(n)} = \sum_{i=1}^{L} \omega_i \boldsymbol{z}_i^{(n)};$$

  if *the stopping criterion is satisfied* **then**

    break;

  end

end

The proximal operators of $F_i \circ \boldsymbol{L}_i$ for $i \in \{1, L_{\text{so}}\}$ are computed using Property 2.15. To ensure the convergence of the algorithm, parameters λ

and μ are chosen such that $\lambda \in]0,1]$ and $\mu \in]0, 2/\gamma[$ where γ is the Lipschitz constant of ∇G [120]. GFB algorithm is very useful when the operators meet the aforementioned requirements. But in some cases, computing the projections related to the use of auxiliary variables can turn out to be very time consuming.

Alternating direction method of multipliers

ADMM, also called Douglas-Rachford splitting, can efficiently solve problem (2.12) for $L \geq 1$ when $(\mathbf{Id}_N + \sum_{i=1}^{L} \boldsymbol{L}_i^* \boldsymbol{L}_i)^{-1}$ can be easily computed for $i \in [L]$. As mentioned in [111], the main advantage of this method is that each term in the objective function is handled separately by the use of auxiliary variables ($\boldsymbol{v}$ in Algorithm 2). We detail the steps of ADMM for $L = 1$ and $\boldsymbol{L}_1 = \mathbf{Id}_N$ in Algorithm 2 and refer to [5] for a description of the more general case.

Algorithm 2: Alternating direction method of multipliers

initialization: choose $\tau > 0$, $\boldsymbol{u}^{(0)} \in \mathbb{R}^N$, $\boldsymbol{v}^{(0)} \in \mathbb{R}^N$, $\boldsymbol{s}^{(0)} \in \mathbb{R}^N$ and `maxIter`;

for $n = 1$ **to** *`maxIter`* **do**

$\boldsymbol{u}^{(n)} = \text{prox}_{\tau G}(\boldsymbol{v}^{(n-1)} - \boldsymbol{s}^{(n-1)})$;

$\boldsymbol{v}^{(n)} = \text{prox}_{\tau F_1}(\boldsymbol{u}^{(n)} + \boldsymbol{s}^{(n-1)})$;

$\boldsymbol{s}^{(n)} = \boldsymbol{s}^{(n-1)} + \boldsymbol{u}^{(n)} - \boldsymbol{v}^{(n)}$;

if *the stopping criterion is satisfied* **then**

break;

end

end

Chambolle-Pock primal-dual algorithm

In this work, we use a generalized version of the CP primal-dual algorithm introduced in 2010 by Chambolle and Pock in their seminal paper [37]. The original CP algorithm [37], described in Algorithm 3, is designed to solve the following saddle-point problem

$$\underset{\boldsymbol{u} \in \mathbb{R}^N}{\text{minimize}} \; \underset{\boldsymbol{p} \in \mathbb{R}^M}{\text{maximize}} \; G(\boldsymbol{u}) + \langle \boldsymbol{L}\boldsymbol{u}, \boldsymbol{p} \rangle - F^\star(\boldsymbol{p}), \tag{2.14}$$

where $\boldsymbol{L} \in \mathbb{R}^{M \times N}$ and $\boldsymbol{p} \in \mathbb{R}^M$ is a dual variable. Problem (2.14) is a primal-dual formulation of the primal problem: $\text{minimize}_{\boldsymbol{u} \in \mathbb{R}^N} \; G(\boldsymbol{u}) +$

$F(\boldsymbol{L}\boldsymbol{u})$. Function $F^\star : \mathbb{R}^M \to \mathbb{R}$ in (2.14) is the *convex conjugate function* (also called the Legendre-Fenchel conjugate) of F.

Definition 2.17 (Convex conjugate function) *[27] Let a function $g : \mathbb{R}^N \to \mathbb{R} \cup \{-\infty, +\infty\}$. The convex conjugate of g is $g^\star : \mathbb{R}^N \to \mathbb{R} \cup \{-\infty, +\infty\}$ and is defined as*

$$g^\star(\boldsymbol{p}) = \sup\{\boldsymbol{p}^\top \boldsymbol{u} - g(\boldsymbol{u}) | \boldsymbol{u} \in \mathbb{R}^N\}.$$

Algorithm 3: Chambolle-Pock primal-dual algorithm

initialization: choose $\tau, \sigma > 0, \theta \in [0,1], \boldsymbol{u}^{(0)} \in \mathbb{R}^N, \boldsymbol{p}^{(0)} \in \mathbb{R}^M$ and `maxIter`, set $\bar{\boldsymbol{u}}^{(0)} = \boldsymbol{u}^{(0)}$;

for $n = 1$ **to** *`maxIter`* **do**

$\boldsymbol{p}^{(n)} = \text{prox}_{\sigma F^\star}(\boldsymbol{p}^{(n-1)} + \sigma \boldsymbol{L}\bar{\boldsymbol{u}}^{(n-1)})$;

$\boldsymbol{u}^{(n)} = \text{prox}_{\tau G}(\boldsymbol{u}^{(n)} - \tau \boldsymbol{L}^* \boldsymbol{p}^{(n)})$;

$\bar{\boldsymbol{u}}^{(n)} = \boldsymbol{u}^{(n)} + \theta(\boldsymbol{u}^{(n)} - \boldsymbol{u}^{(n-1)})$;

if *the stopping criterion is satisfied* **then**

break;

end

end

In the rest of the thesis, parameter θ in Algorithm 3 is set to 1. The algorithm convergence is guaranteed when the primal and dual step-sizes, τ and σ, satisfy $\tau\sigma\|\boldsymbol{L}\|_2^2 \leq 1$ [37] where $\|\boldsymbol{L}\|_2$ is the ℓ_2 *operator norm* of $\boldsymbol{L}$.

Definition 2.18 (ℓ_2 operator norm) *[27] We define the ℓ_2 operator norm of $\boldsymbol{L} \in \mathbb{R}^{M \times N}$ as*

$$\|\boldsymbol{L}\|_2 = \sup\{\|\boldsymbol{L}\boldsymbol{u}\|_2 | \|\boldsymbol{u}\|_2 \leq 1\}.$$

If $\boldsymbol{u} \neq \boldsymbol{0}$, an equivalent formulation is

$$\|\boldsymbol{L}\|_2 = \sup_{\boldsymbol{u} \neq \boldsymbol{0}} \left\{ \frac{\|\boldsymbol{L}\boldsymbol{u}\|_2}{\|\boldsymbol{u}\|_2} \right\} =: \sigma_{\max}(\boldsymbol{L}),$$

where $\sigma_{\max}(\boldsymbol{L})$ is the largest singular value of matrix $\boldsymbol{L}$. The following inequality results from this second formulation,

$$\|\boldsymbol{L}\boldsymbol{u}\|_2 \leq \|\boldsymbol{L}\|_2 \|\boldsymbol{u}\|_2.$$

The ℓ_2 norm of the operator $\boldsymbol{L}$, $\|\boldsymbol{L}\|_2$, corresponds to its maximum singular value as mentioned in Definition 2.18. It is also equal to the square root of the maximum eigenvalue of $\boldsymbol{L}^*\boldsymbol{L}$ [27]. In practice, we compute the maximum eigenvalue of $\boldsymbol{L}^*\boldsymbol{L}$ using the power iteration [71].

The generalized CP (GCP) is appropriate when $L > 1$. It is derived in a product space using duality principles [71]. It can deal with (2.12) by first computing separately the proximal operators of $F_i^\star$'s and then, averaging them (see Algorithm 4).

Algorithm 4: Generalized Chambolle-Pock algorithm [71]

initialization: choose $\tau, \sigma > 0$, $\theta \in [0,1]$, $\boldsymbol{u}^{(0)} \in \mathbb{R}^N$, $\boldsymbol{p}_i^{(0)} \in \mathbb{R}^{M_i}$ for $i \in [L]$ and `maxIter`, set $\bar{\boldsymbol{u}}^{(0)} = \boldsymbol{u}^{(0)}$;

for $n = 1$ **to** *maxIter* **do**
  for $i = 1$ **to** L **do**
    $\boldsymbol{p}_i^{(n)} = \text{prox}_{\sigma F_i^\star}(\boldsymbol{p}_i^{(n-1)} + \sigma \boldsymbol{L}_i \bar{\boldsymbol{u}}^{(n-1)})$;
  end
  $\boldsymbol{u}^{(n)} = \text{prox}_{\tau G}(\boldsymbol{u}^{(n)} - \frac{\tau}{L} \sum_{i=1}^{L} \boldsymbol{L}_i^* \boldsymbol{p}_i^{(n)})$;
  $\bar{\boldsymbol{u}}^{(n)} = 2\boldsymbol{u}^{(n)} - \boldsymbol{u}^{(n-1)}$;
  if *the stopping criterion is satisfied* **then**
    break;
  end
end

The GCP algorithm only requires computing the proximal operators of G, the convex conjugates of each $F_i^\star$, as well as the adjoints of the operators $\boldsymbol{L}_i$'s. The following two properties are useful to compute $\text{prox}_{F_i^\star}$ when prox_{F_i} is known.

Definition 2.19 (Moreau decomposition) *[111] Let g be a function as defined in Definition 2.14. In this case, the following relation, called the Moreau decomposition, always holds*

$$\tilde{\boldsymbol{u}} = \text{prox}_g(\tilde{\boldsymbol{u}}) + \text{prox}_{g^\star}(\tilde{\boldsymbol{u}}).$$

Property 2.20 (Affine transformation) *[27] Let $g : \mathbb{R}^N \to \mathbb{R}$ and $a > 0, b \in \mathbb{R}$. The convex conjugate of $h(\boldsymbol{u}) = ag(\boldsymbol{u}) + b$ is $h^\star(\boldsymbol{p}) = ag^\star(\boldsymbol{p}/a) - b$. Suppose $\boldsymbol{L} \in \mathbb{R}^{N\times N}$ is non-singular and $\boldsymbol{b} \in \mathbb{R}^N$. Then, the conjugate of $h(\boldsymbol{u}) = g(\boldsymbol{L}\boldsymbol{u} + \boldsymbol{b})$ is*

$$h^\star(\boldsymbol{p}) = g^\star((\boldsymbol{L}^{-1})^\top \boldsymbol{p}) - \boldsymbol{b}^\top (\boldsymbol{L}^{-1})^\top \boldsymbol{p},$$

with $\operatorname{dom} h^\star = \boldsymbol{L}^\top \operatorname{dom} g^\star$.

In the next section, we present a few criteria designed (*i*) to automatically select the best value for the regularization parameter ρ (assuming there is only one balancing parameter) and (*ii*) to stop the internal iterations of the algorithms described below. Finally, in the (short) last section, we define the criteria used in this thesis to assess the quality of the estimate.

2.3.2 Regularization parameter and stopping criterion

As brought up in section 2.2, the optimal values of parameters ρ_i are unknown *a priori*. In this section, we consider problems similar to (2.6) but restricted to the ones with only one[2] regularization parameter ρ. Its optimal value, $\rho^\star$, depends on the associated regularization term and on the observations, directly related to the noise statistics.

Finding $\rho^\star$ theoretically is in general impossible. Ideally, it must be chosen such that the estimation error between $\boldsymbol{f}_0$ and $\hat{\boldsymbol{f}}_\rho$ is minimum, *i.e.*,

$$\rho^\star = \arg\min_{\rho>0} \operatorname{dist}(\hat{\boldsymbol{f}}_\rho, \boldsymbol{f}_0),$$

where dist can be, for instance, a squared ℓ_2-norm. As aforementioned, such a criterion is attractive but unrealistic: in real situations, we only have access to $\hat{\boldsymbol{f}}_\rho$ and $\boldsymbol{y}$. There exist a lot of methods in the literature to select a value for ρ, close to $\rho^\star$, *e.g.*, discrepancy principle, Stein's unbiased risk estimate, generalized cross-validatory criterion, whiteness of the residual, etc. [6, 18, 50, 99, 148]. A lot of criteria are based on the statistical properties of the noise and require an accurate knowledge of its distribution and its parameters (*e.g.*, the variance of the noise) [25].

In the next section, we describe several criteria based on the *residual* as well as a general principle that can be used to avoid *overfitting* of the data.

[2] The number of regularization terms L can still be ≥ 1 even if the problem involves only one regularization parameter, *e.g.*, if the problem includes one or several indicator functions.

Criteria based on the residual

The residual $\boldsymbol{r}$ is defined as the difference between the observations and the estimated observations, $\boldsymbol{A}\hat{\boldsymbol{f}}_\rho$,

$$\begin{aligned}\boldsymbol{r} \coloneqq \boldsymbol{y} - \boldsymbol{A}\hat{\boldsymbol{f}}_\rho &= \boldsymbol{A}\boldsymbol{f}_0 + \boldsymbol{n}_r - \boldsymbol{A}\hat{\boldsymbol{f}}_\rho \\ &= \boldsymbol{A}(\boldsymbol{f}_0 - \hat{\boldsymbol{f}}_\rho) + \boldsymbol{n}_r. \end{aligned} \tag{2.15}$$

Quantity $\boldsymbol{r}$ is a realization of the random vector $\boldsymbol{R} \coloneqq \boldsymbol{Y} - \boldsymbol{A}\hat{\boldsymbol{f}}_\rho$. The first term in (2.15) includes the details lost during the estimation process and the second one corresponds to the noise. For $\rho = \rho^\star$, we should have $\hat{\boldsymbol{f}}_\rho \approx \boldsymbol{f}_0$ and a residual only containing the noise. Consequently, we also expect the correlation of $\boldsymbol{R}$ to be similar to the one of $\boldsymbol{N}_r$.

Discrepancy principle. The discrepancy principle is based on the knowledge of the power of the noise, *e.g.*, the variance of the noise when $\mathcal{D}$ in (2.3) represents a corruption by an additive Gaussian noise. Intuitively, this criterion assumes that the distance (defined according to the noise model, see subsection 2.2.1) between $\boldsymbol{A}\boldsymbol{f}_0$ and $\boldsymbol{y}$ is well approximated by a quantity possibly depending on the noise model, namely $\text{dist}(\boldsymbol{A}\boldsymbol{f}_0, \boldsymbol{y}) \approx B_{\mathcal{D}}$. The discrepancy principle consists in finding an estimate $\hat{\boldsymbol{f}}_\rho$ such that $\text{dist}(\boldsymbol{A}\hat{\boldsymbol{f}}_\rho, \boldsymbol{y}) \approx B_{\mathcal{D}}$.

When the noise is assumed to be additive and Gaussian with variance σ^2, the Morozov discrepancy principle selects an estimate associated with parameter ρ such that [18, 106]

$$\|\boldsymbol{A}\hat{\boldsymbol{f}}_\rho - \boldsymbol{y}\|_2^2 \approx \sigma^2 M.$$

A discrepancy principle for Poisson noise was proposed in 2010 by Bertero *et al.* [18] and is given by

$$\text{KL}(\boldsymbol{A}\hat{\boldsymbol{f}}_\rho, \boldsymbol{y}) \approx \frac{M}{2}. \tag{2.16}$$

Carlavan *et al.* adapted (2.16) to images with null background [35],

$$\text{KL}(\boldsymbol{A}\hat{\boldsymbol{f}}_\rho, \boldsymbol{y}) \approx \frac{N_0}{2},$$

where $M = N$, $N_0 \leq N$ is the number of non-zero pixels and KL is the Kullback-Leibler divergence defined in Definition 2.5.

This criterion requires (*i*) to know the noise distribution and (*ii*) to estimate its parameter(s) from the observations [25]. In real applications with various sources of noise, those two requirements can be difficult to satisfy.

Whiteness of the residual. As for the discrepancy principle, we would like to find a stopping criterion related to the statistical properties of the residual (2.15). But here, we consider that we do not know precisely the distribution of the noise as well as its second-order (and higher) moments. We would like to avoid estimating such distribution or its parameters (*e.g.*, the variance in the Gaussian case).

In 2013, Almeida and Figueiredo introduced a criterion based on the spectral properties of the residual [6]. This approach is promising because it only needs minimal knowledge about the noise: if the noise on the observations—represented by operator $\mathcal{D}$ in (2.3)—is *additive* and *i.i.d.*, we could expect a residual that is spectrally *white*. A noise $\boldsymbol{N} \in \mathbb{R}^M$ is said to be a white vector when two conditions are met:

$$\mathbb{E}\boldsymbol{N} = \mathbf{0} \quad \text{and} \quad \Gamma_{\boldsymbol{N}} = \sigma^2 \mathbf{Id}_M,$$

where $0 < \sigma^2 < +\infty$ is possibly unknown and $\Gamma_{\boldsymbol{N}}$ is the diagonal autocorrelation matrix of $\boldsymbol{N}$. The second condition leads to a power spectral density that is constant over all the frequencies.

In the ideal case, the residual would perfectly correspond to the realization of the additive noise, $\boldsymbol{n}_r = \boldsymbol{n}$ in (2.15), *i.e.*, to a realization of a white vector. To assess if the residual has statistical properties close to those of a white vector, Almeida *et al.* define the following *whiteness measure* for blind and non-blind deblurring [6],

$$q(\hat{\boldsymbol{f}}_\rho) = \sum_{i,j=1, i\neq j}^{M} \frac{(\Gamma_{\boldsymbol{r}})_{ij}^2}{\sigma_{\boldsymbol{r}}^2}, \tag{2.17}$$

i.e., the sum of all the off-diagonal elements of the correlation matrix of the residual. Matrix $\Gamma_{\boldsymbol{r}}$ is the empirical estimation of $\Gamma_{\boldsymbol{R}}$ and $\sigma_{\boldsymbol{r}}^2$ is the variance of vector $\boldsymbol{r}$. The best value for ρ is the one minimizing (2.17). Unfortunately, $\hat{\boldsymbol{f}}_{\rho^\star} = \boldsymbol{f}_0$ is not the unique minimizer of (2.17). Indeed, since $\hat{\boldsymbol{f}}_\rho$ is estimated from (and thus, depends on) $\boldsymbol{y}$, the quantity $\boldsymbol{A}\hat{\boldsymbol{f}}_\rho$ could tend to match the noisy data leading to a residual equal to zero. In this limit case, the entries of $\Gamma_{\boldsymbol{r}}$ are all equal to zero, even the diagonal ones. This phenomenon is known as *data overfitting*.

Cross-validation

Overfitting results from the use of the same observations for both the estimation of f_0 and the evaluation of the quality criterion. An idea, already exploited by Boufounos *et al.* and Ward [25, 161] in the context of compressive sensing, is to use a technique based on cross-validation (CV) principle—widely used in the machine learning community—to avoid this pitfall. The observations y are divided into two distinct sets: an estimation set and a validation set, much smaller than the first one.

More formally, we randomly split the vector of observations y into an estimation vector y_{est} and a validation vector y_{val}, of sizes M_{est} and $M_{\text{val}} = M - M_{\text{est}}$, respectively. To do so, we define two restriction operators $R_{\text{est}} \in \{0,1\}^{M_{\text{est}} \times M}$ and $R_{\text{val}} \in \{0,1\}^{M_{\text{val}} \times M}$ such that $y_{\text{est}} = R_{\text{est}} y$ and $y_{\text{val}} = R_{\text{val}} y$, respectively. With CV approach, estimation problem (2.6) becomes

$$\hat{f}_\rho \coloneqq \underset{u \in \mathbb{R}^N}{\arg\min}\ \operatorname{dist}(R_{\text{est}} A u, R_{\text{est}} y) + \sum_{i=1}^{I} \rho_i \phi_i(u), \tag{2.18}$$

and the residual used in the quality criterion q is

$$r_{\text{val}} \coloneqq R_{\text{val}}(y - A\hat{f}_\rho).$$

The CV can be applied to any quality criterion, including the whiteness criterion proposed by Almeida *et al.* [6]. As suggested by [25], we can also use the *squared ℓ_2-norm of the residual* r_{val} as the criterion for stopping the internal iterations of the algorithms and selecting ρ,

$$q(\hat{f}_\rho) = \|R_{\text{val}}(y - A\hat{f}_\rho\|_2^2. \tag{2.19}$$

This last criterion shares similarity with the discrepancy principle for additive Gaussian noise. But unlike this one, (2.19) does not require any parameter estimation.

2.3.3 Quality of the estimate

In real applications, the (discretized) ground truth f_0 is obviously not available. However, when we perform *in silico* experiments, we often quantify the quality of the estimate $\hat{f}$ with respect to f_0, *e.g.*, to compare the performances of different numerical methods. There exist numerous quality metrics or indices, *e.g.*, *signal-to-noise ratio* (SNR), correlations coefficients, mutual information, structural similarity index measure (SSIM), etc. [130,

160] Even if they present some limitations (well explained in [159]), we use the SNR and the *increase in SNR* in the simulations reported in this thesis. The SSIM would be more appropriate since it compares the structure, independently of a change in contrast and luminance.

Definition 2.21 (Signal-to-noise ratio) *The signal-to-noise ratio (SNR) between an estimate $\hat{\boldsymbol{u}}$ and its ground truth $\boldsymbol{u}$ is defined as*

$$\mathrm{SNR}(\hat{\boldsymbol{u}}, \boldsymbol{u}) \coloneqq 20 \log_{10} \left(\frac{\|\hat{\boldsymbol{u}}\|_2}{\|\hat{\boldsymbol{u}} - \boldsymbol{u}\|_2} \right).$$

Definition 2.22 (Increase in signal-to-noise ratio) *Let $\boldsymbol{z} \in \mathbb{R}^N$ be a corrupted version of signal $\boldsymbol{u} \in \mathbb{R}^N$. Let $\hat{\boldsymbol{u}} \in \mathbb{R}^N$ be an estimate of $\boldsymbol{u}$ built from observations $\boldsymbol{z}$. The increase in signal-to-noise ratio (ISNR) compares the SNR of $\boldsymbol{z}$ with the SNR of $\hat{\boldsymbol{u}}$. It is defined as*

$$ISNR(\hat{\boldsymbol{u}}, \boldsymbol{u}, \boldsymbol{z}) = 10 \log_{10} \frac{\|\boldsymbol{z} - \boldsymbol{u}\|_2^2}{\|\hat{\boldsymbol{u}} - \boldsymbol{u}\|_2^2}.$$

Positron emission tomography

3

Basics of PET imaging

POSITRON emission tomography (PET) is one of the few medical imaging modalities providing information about physiological activity in the human body. Like for other nuclear imaging modalities, PET requires the use of a radiotracer, *i.e.*, a drug synthesized by the human body (*e.g.*, a glucose molecule) and labeled with a radionuclide. The observation of a specific metabolic process depends on the chosen radiotracer. The most frequent radiopharmaceuticals are ^{11}C, ^{13}N, ^{15}O, and ^{18}F, all short-lived isotopes of elements already present in our organism [116]. Due to its "long" half-life (about 110 min) and its versatility, ^{18}F-fluorodeoxyglucose (^{18}F-FDG) is widely used for clinical applications.

In clinic, PET imaging is mainly used in cardiology (*e.g.*, for coronary angiography), neuropsychiatry (*e.g.*, to help diagnose dementia) and oncology [16, chapter 1]. In radiotherapy, this modality permits to detect cells with abnormally high metabolic activity like cancer cells. Combined with structural imaging modalities, it has become essential for cancer diagnosis (*e.g.*, lung cancer or lymphoma), treatment planning, assessment of the tumor growth and of the patient's response, and follow-up after the end of the therapy [16, chapter 1]. This ability to assess the evolution of the response of a living organism to a treatment is also exploited in research—*e.g.*, to study a new drug or new cancer therapies.

Computational scientists can design algorithms that will help the physicians to interpret and exploit the information contained in PET images.

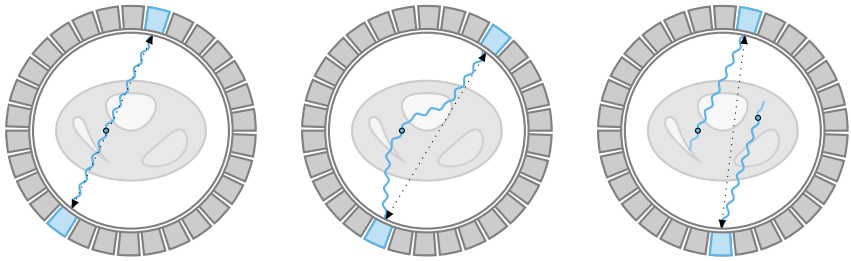

Figure 3.1 Illustration of (a) a true annihilation coincidence detection (ACD) occurring in a PET scanner (axial view), (b) a scattered ACD and (c) a random ACD. On each subfigure, a blue filled circle indicates an annihilation location. The emitted photons follow the blue trajectory and hit the corresponding detectors. The dotted line indicates the line of response associated with the event detection for the reconstruction.

Understanding the formation of PET images is then crucial to develop appropriate image processing techniques. In this chapter, we first briefly review the acquisition principle of PET modality in section 3.1. Then, in subsection 3.2.3, we describe a simplified continuous model underlying the generation of observations in the projected domain. It integrates the main phenomena having an impact on the quality of PET images—a low spatial resolution and a high level of noise. Finally, in section 3.3, we point out the imaging (and medical) challenges related to PET imaging such as accurate organ delineation.

3.1 Acquisition principle

First of all, the patient must ingest, inhalate or receive an injection of a drug labeled with a radionuclide. The radiotracer accumulates in tissues while constantly emitting positrons. After a short travel (around 0.5 to 0.6 mm for ^{18}F-FDG, see subsection 3.2.1), most of the positrons annihilate with electrons. This results in the emission of two 511 keV photons with anti-collinear trajectories (see Figure 3.1a). The simultaneous detection (in a timing window of 6 to 12 ns) of two photons by the scanner detectors is called a *coincidence event* or *annihilation coincidence detection* (ACD). From this observation, we assume that the annihilation—and not necessarily the positron emission—occurred somewhere along the line joining the two de-

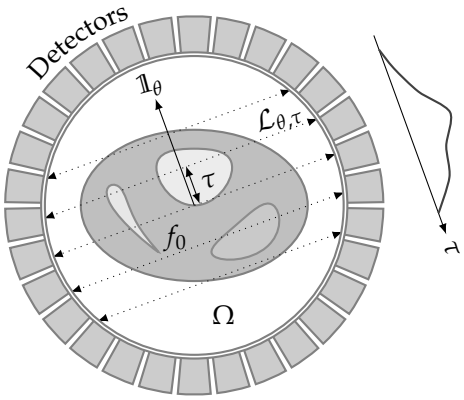

Figure 3.2 Tomographic acquisition of a quantity of interest f_0. For each discretized angle θ, the projection profile depends on τ and represents the coincidence events profile in this particular direction.

tectors. This line is called *line of response* (LOR). The number of ACD is stored for each pair of detectors, indexed by an angle θ and an affine parameter τ (see Figure 3.2). For θ fixed and τ varying, the resulting profile of photon counts is called *projection*. The collection of projections is called *sinogram* and can be seen as the discrete X-ray transform (or Radon transform) of the radioactivity map. After several correction steps (*e.g.*, to correct attenuation or random coincidence events), linear or iterative algorithms are used for the reconstruction [152].

In practice, the sinogram is far from being an ideal Radon transform of the radioactivity map. Indeed, several phenomena are responsible for degradation leading to (*i*) a low spatial resolution and (*ii*) a high level of noise in the reconstructed map. The poor spatial resolution of PET images is impacted by factors of four different origins [16, 97, 121]:

- the *physics* of the imaging modality (*e.g.*, non-zero positron range and imperfect collinearity of photons after annihilation with an electron);
- the *device* (*e.g.*, detectors geometry, depth of interaction of the photon in the detector, and stopping power of the crystal);
- the *patient* or the *object* (*e.g.*, patient motion during the acquisition);
- the *acquisition and reconstruction* (*e.g.*, sampling, rebinning, and parameters of the reconstruction algorithm).

We observe in practice a high level of noise in the projection space. This is mainly due to the low photon detection efficiency of the detectors and to the limitation of the injected tracer dose for obvious radio-protective reasons. Moreover, an ACD does not always result from the annihilation of a positron along the considered LOR. Scattered and random coincidences are also detected (see Figures 3.1b and 3.1c). If we do not correct them prior to the reconstruction, we will get a reconstructed image with poor contrast, *e.g.*, due to a background haze [116].

3.2 From radiotracer uptake to projections

We consider a sample—either a synthetic phantom or a living organism—that contains some biological compounds labeled with radionuclides. This sample is placed inside a PET scan with radius R and $2D$ detectors of width w. In this work, we only consider ACD in a transverse plane. Without loss of generality, we assume that the sample is restricted to a 2D circular FOV, also called object space $\Omega \subset \mathbb{R}^2$. A function $f : \Omega \times \mathbb{R} \to \mathbb{R}_+$ associates a radiotracer concentration $f(\boldsymbol{x}, t)$ with each location $\boldsymbol{x} \in \Omega$ at time t. According to the radioactive decay law [116], we write f as $f(\boldsymbol{x}, t) = f_0(\boldsymbol{x})e^{-\lambda t}$ where λ is the decay constant specific to the chosen radionuclide and f_0 is the concentration map at $t = 0$. This map is implicitly related to the metabolic activity: in areas with high radioactivity, we expect a high metabolic activity. Let us also define a discrete random field s that associates each pair of detectors with a number of ACD collected during acquisition time t_{acq}.

This section aims at describing a mathematical model relating the concentration map (f_0) to the acquired data (s). First, we will describe the emission model, *i.e.*, the expression of the ACD flux resulting from the radioactivity in the sample as a function of f_0. Then, we will propose a model for the flux collection by the scanner detectors leading to the measured quantity s. The final discrete model proposed in subsection 3.2.3 and based on subsections 3.2.1 and 3.2.2 only integrates the main factors of degradation that affect the quality of the reconstructed image. Since Chapters 4 and 5 concern post-reconstruction techniques, phenomena like Compton scattering or random coincidences are not detailed because they can be corrected before the reconstruction. For a comprehensive understanding of PET acquisition, we refer the reader to the books *Positron emission tomography* written by Bailey *et al.* [16] and *Medical Imaging: Signals and Systems* written by Prince and Links [116].

3.2.1 Emission model

As mentioned in section 3.1, radionuclides emit positrons that further annihilate with electrons and emit pairs of photons. Let us define a function $\varphi : [0, \pi] \times [-R, R] \times \mathbb{R}_+ \to \mathbb{N}_+$. The ACD flux $\varphi(\theta, \tau, t)$ is associated with a LOR parameterized by θ and τ and is denoted $\mathcal{L}_{\theta,\tau}$. The flux corresponds to the number of simultaneous detections observed at the ends of this LOR during the time window indexed by time t. $\mathcal{L}_{\theta,\tau}$ is defined as

$$\mathcal{L}_{\theta,\tau} \coloneqq \{\boldsymbol{x} \in \Omega | \mathbb{1}_\theta^\top \boldsymbol{x} - \tau = 0\},$$

where $\mathbb{1}_\theta \in \mathbb{S}$ is defined as $\mathbb{1}_\theta \coloneqq (\cos\theta, \sin\theta)$ in the Cartesian coordinate system.

Remark 3.1. Due to their finite width, a pair of detectors is associated with several LOR, called a *fan* of LOR. We will see how it affects the collected observations in subsection 3.2.2.

Flux φ can be seen as the sum of three main sources of flux: φ_T, φ_S and φ_R. Flux φ_T is related to the true coincidence events that actually occurred along the considered LOR, φ_S accounts for the scattered coincidences and φ_R represents the flux due to random coincidences. Function φ depends on f and on the chosen LOR but also on the nature of the encountered tissues and on instrumental parameters like detector efficiency. In this section, we derive the expression of $\varphi_T(\theta, \tau, t)$ at time t along $\mathcal{L}_{\theta,\tau}$ as a function of f, linear attenuation map $\mu : \Omega \to \mathbb{R}_+$ and instrumental parameters. We assume that μ is stationary, *i.e.*, that there is no change in the nature or position of the tissues during the acquisition process.

Let us assume that N_0 annihilations occurred at location $\boldsymbol{x}_0 \in \mathcal{L}_{\theta,\tau}$ at time t. The numbers of photons detected at each end of the LOR are [116]

$$N^+(\boldsymbol{f}_0, t) = N_0 e^{-\int_{\mathcal{L}^+_{\theta,\tau}} \mu(\boldsymbol{x};E)\,\mathrm{d}\boldsymbol{x}}$$
$$N^-(\boldsymbol{f}_0, t) = N_0 e^{-\int_{\mathcal{L}^-_{\theta,\tau}} \mu(\boldsymbol{x};E)\,\mathrm{d}\boldsymbol{x}},$$

where $\mathcal{L}^+_{\theta,\tau}$ and $\mathcal{L}^-_{\theta,\tau}$ are the shortest paths between $\boldsymbol{x}_0$ and each end of the LOR, and E is the photon energy (511 keV). The exponential factors model the attenuation due to tissues that the photons encounter on their way to the outside of the patient. An ACD requires a simultaneous detection of photons at each end of the LOR. If one of the two photons is absorbed, there is no detection. Consequently, the average number of ACD N_{av} depends on

the product of the attenuation factors and not anymore on the annihilation origin $\boldsymbol{x}_0$,

$$N_{\text{av}}(\boldsymbol{f}_0) = N_0 e^{-\int_\Omega \delta(\mathbb{1}_\theta^\top \boldsymbol{f} - \tau)\mu(\boldsymbol{x};E)\,\mathrm{d}\boldsymbol{x}}. \tag{3.1}$$

The total number of ACD resulting from all the annihilation events that occurred along $\mathcal{L}_{\theta,\tau}$ is given by the integral of (3.1) along this line,

$$\varphi_T(\theta,\tau,t) = e^{-\lambda t} c_E(\theta,\tau) \int_\Omega \delta(\mathbb{1}_\theta^\top \boldsymbol{f} - \tau) f_0(\boldsymbol{x})\,\mathrm{d}\boldsymbol{x},$$

where $c_E(\theta,\tau) := e^{-\int_\Omega \delta(\mathbb{1}_\theta^\top \boldsymbol{f} - \tau)\mu(\boldsymbol{x};E)\,\mathrm{d}\boldsymbol{x}} > 0$ accounts for the tissue attenuation along the considered LOR. An equivalent expression is

$$\varphi_T(\theta,\tau,t) = e^{-\lambda t} c_E(\theta,\tau) \mathcal{R} f_0(\theta,\tau), \tag{3.2}$$

where $\mathcal{R} f_0$ is the Radon transform of f_0. However, this model of positron emission is too ideal mainly for two reasons mentioned in section 3.1: (*i*) the annihilation and the emission of the positron do not occur at the same location and (*ii*) the two emitted photons are often not perfectly collinear. Consequently, we do not observe line integrals of f_0 but of a slightly different quantity. We describe those two physical phenomena before adapting expression (3.2).

Non-zero positron range. The radioactive decay that occurs in the patient body after radiotracer injection is responsible for the emission of particles α, β, and positrons. After emission, positrons have a non-zero initial kinetic energy. This energy decreases as the positron travels and interacts with the surrounding environment—*e.g.*, via (in)elastic collisions or scattering [16]. The distance covered by the particle before being at rest depends both on the initial kinetic energy, *i.e.*, on the radionuclide, and on the nature of encountered tissues. In the case of ^{18}F, the average range of positron in water—a medium with properties similar to those of human tissues—is 0.5 to 0.6 mm with a maximum distance of 2.4 mm [16, 97]. Monte-Carlo simulations of positron trajectories made by Levin *et al.* [97] show that the distribution of annihilation locations has an isotropic "cusp-like" shape. The impact of surrounding tissues heterogeneity on the trajectory is negligible for radionuclides with low energy such as ^{18}F [3]. Based on this observation, the effect of non-zero positron range is well approximated by a convolution in the spatial domain with a 3D biexponential kernel [97].

Studies [3, 121] consider the effect of non-zero positron range on the spatial resolution as negligible when the radiotracer is ^{18}F. Levin *et al.* observe however that in the case of scanners with small FOV (around 20 cm) and small detectors, this effect (independent of the scanner geometry) is dominant along with detector size (see subsection 3.2.2) [97].

Non-collinearity. The combination and annihilation of a positron and an electron at rest result in a radiation that generally consists in a pair of photons emitted in opposed directions. According to Bailey *et al.* [16], 65% of the photons emitted in the water are not perfectly collinear. This misalignement is due to the fact that the momentum is not always zero when positron and electron combine. The phenomenon of non-collinearity can be modeled by a convolution in the spatial domain with an isotropic Gaussian kernel [97]. The effects of non-collinearity do not depend on the radionucleide and are rather influenced by the system geometry—*e.g.*, FOV and detectors sizes. This factor is dominant in large scanners (FOV diameter around 80 cm) [97].

Considering those two phenomena, a better model for φ_T is

$$\varphi_T(\theta, \tau, t) = e^{-\lambda t} c_E(\theta, \tau) \mathcal{R}\{h_1 * f_0\}(\theta, \tau), \tag{3.3}$$

where $h_1 : \mathbb{R}^2 \to \mathbb{R}$ is a Gaussian kernel modeling the effects of non-zero positron range and non-collinearity.

3.2.2 Collection model

The scanners used for PET imaging have a finite number of detectors. Within the acquisition time t_{acq}, each pair of detectors collects the fluxes of a fan of LOR, acting like an operator of integration. Let us characterize each pair of detectors by the parameters of the LOR connecting their centers, (θ_i, τ_j) with $i, j \in [D]$. Due to the circular geometry of the device, angles θ_i are evenly sampled on $[0, \pi]$ while radial variables τ_j are non-uniformly sampled on $[-R, R]$.

At time t, the collection by a pair of detectors (θ_i, τ_j) with sensitivity $c_{i,j}$ can be modeled by an integral operator H_2 applied to the total flux φ followed by a sampling,

$$c_{i,j} \left[H_2 \varphi(\theta, \tau, t) \right]_{\substack{\theta=\theta_i \\ \tau=\tau_j}} := c_{i,j} \left[\int_{-R}^{R} h_2(\tau, \tau') \varphi(\theta, \tau', t) \, \mathrm{d}\tau' \right]_{\substack{\theta=\theta_i \\ \tau=\tau_j}}.$$

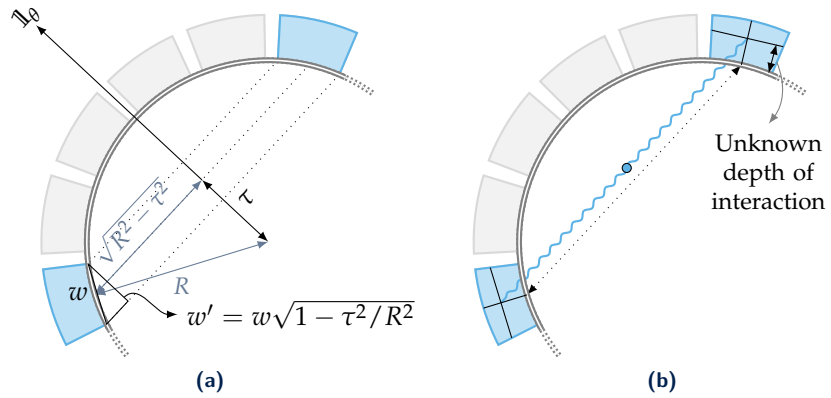

Figure 3.3 As we go away from the center of the field of view, (a) the effective width of collection $w' = w\sqrt{1-\tau^2/R^2}$ of a detector pair (highlighted in blue) gets smaller and (b) the parallax error, due to the finite depth of the detectors, gets larger. The dotted lines represent the lines of response associated to this pair of detectors for a given angle θ.

Constant $c_{i,j} > 0$ accounts among others for the detector efficiency and effects due to the geometry or to the (a)synchronicity of the considered detectors [16, chapter 5]. Kernel h_2 represents the effects due to the scanner and detector geometries. When $|\tau|$ increases, we observe two main phenomena: (*i*) the effective width of collection w' of a detector pair gets smaller due to the circular geometry of the device and (*ii*) the finite depth of the detectors leads to larger parallax errors (see Figure 3.3).

Within the acquisition duration t_{acq}, a number $s_{i,j} > 0$ of ACD are collected by the detectors pair (θ_i, τ_j). The randomness inherent to the disintegration process combined with the discrete nature of the detection process can be modeled by a Poisson random variable,

$$s_{i,j} \sim \mathcal{P}\left(c_{i,j} \int_0^{t_{\text{acq}}} [H_2 \varphi(\theta, \tau, t)]_{\substack{\theta=\theta_i \\ \tau=\tau_j}} \, \mathrm{d}t\right), \tag{3.4}$$

where the collection of $s_{i,j}$ with $i, j \in [D]$ is called *sinogram*. This multiplicative noise is common when we deal with photon counting processes.

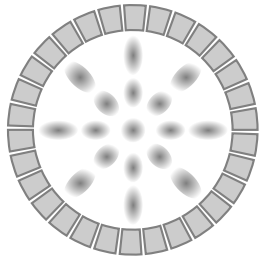

Figure 3.4 Simplified representation of the (circularly symmetric) blurring kernel $\tilde{h}_2$ at different locations $\boldsymbol{y}$ of the field of view. In first approximation, $\tilde{h}_2$ at each location can be seen as an anisotropic Gaussian kernel.

3.2.3 Discrete model for corrected projections

Before switching to a discrete framework, we first derive an alternate expression for $H_2\varphi_T(\theta,\tau,t)$. Using (3.3) and Fubini's theorem, we write

$$\begin{aligned} H_2\varphi_T(\theta,\tau,t) &= e^{-\lambda t}\int_\Omega\int_{-R}^{R} h_2(\tau,\tau')c_E(\theta,\tau')\delta(\mathbb{1}_\theta^\top\boldsymbol{x}-\tau')(h_1*f_0)(\boldsymbol{x})\,\mathrm{d}\tau'\mathrm{d}\boldsymbol{x} \\ &\approx e^{-\lambda t}c_E(\theta,\tau)\int_\Omega h_2(\tau,\mathbb{1}_\theta^\top\boldsymbol{x})(h_1*f_0)(\boldsymbol{x})\,\mathrm{d}\boldsymbol{x}, \end{aligned} \tag{3.5}$$

where we assumed that c_E is slowly varying inside the window defined by h_2 and is, in this case, well approximated by $c_E(\theta,\tau)$. Let us now write $h_2(\tau,\mathbb{1}_\theta^\top\boldsymbol{x})$ as the projection of a spatially variant kernel $\tilde{h}_2$ in Ω [58],

$$h_2(\tau,\mathbb{1}_\theta^\top\boldsymbol{x}) = \int_\Omega \delta(\mathbb{1}_\theta^\top\boldsymbol{y}-\tau)\tilde{h}_2(\boldsymbol{y},\boldsymbol{x})\,\mathrm{d}\boldsymbol{y}. \tag{3.6}$$

$\tilde{h}_2$ associates a function depending on $\boldsymbol{x}$ with each location $\boldsymbol{y}$ of the FOV. Since kernel h_2 does not depend on θ neither does $\tilde{h}_2$. Consequently, $\tilde{h}_2$ is circularly symmetric, *i.e.*, all the functions $\tilde{h}_2$ located at $\boldsymbol{y}$ such that $\|\boldsymbol{y}\|_2 = r \leq R$ are identical up to a rotation θ (see Figure 3.4). Combining (3.5) and (3.6) leads to

$$\begin{aligned} H_2\varphi_T(\theta,\tau,t) &\approx e^{-\lambda t}c_E(\theta,\tau)\int_\Omega \delta(\mathbb{1}_\theta^\top\boldsymbol{y}-\tau)\int_\Omega \tilde{h}_2(\boldsymbol{y},\boldsymbol{x})(h_1*f_0)(\boldsymbol{x})\,\mathrm{d}\boldsymbol{x}\,\mathrm{d}\boldsymbol{y} \\ &= e^{-\lambda t}c_E(\theta,\tau)\int_\Omega \delta(\mathbb{1}_\theta^\top\boldsymbol{y}-\tau)\tilde{H}_2\{h_1*f_0\}(\boldsymbol{y})\,\mathrm{d}\boldsymbol{y} \\ &= e^{-\lambda t}c_E(\theta,\tau)\mathcal{R}\left\{\tilde{H}_2(h_1*f_0)\right\}(\theta,\tau). \end{aligned}$$

Injecting this approximation in (3.4), we find

$$s_{i,j} \sim \mathcal{P}\left(c_{i,j}\int_0^{t_{\text{acq}}}\left[e^{-\lambda t}c_E(\theta,\tau)\mathcal{R}\left\{\tilde{H}_2(h_1 * f_0)\right\}(\theta,\tau) + H_2\{\varphi_S+\varphi_R\}(\theta,\tau,t)\right]_{\substack{\theta=\theta_i\\ \tau=\tau_j}} \mathrm{d}t\right). \quad (3.7)$$

Before the reconstruction, the sinogram usually undergoes different corrections along with a possible rebinning [16, chapter 5]: the weights $c_{i,j}$ are removed by normalization, the estimated counts of scattered and random coincidences are subtracted, the decay factor depending on t_{acq} is corrected and finally, the tissue attenuation is compensated. This last correction is based on a transmission scanner performed with a CT scan (monochromatic X-rays with energy equal to 511 keV). The CT projections are directly related to c_E and do not require a reconstruction. The expectation of corrected $s_{i,j}$ before rebinning is

$$\mathbb{E}s^c_{i,j} = \mathcal{R}\left\{\tilde{H}_2(h_1 * f_0)\right\}(\theta_i,\tau_j). \quad (3.8)$$

Due to data processing, $s^c_{i,j}$ is not a Poisson random variable anymore. Some authors consider that random variable $s^c_{i,j}$ follows a *shifted* Poisson distribution [16, chapter 4]. In Chapter 4, we show that corrected projections can be considered as sub-exponential random variables.

According to the framework described in Chapter 2, model (3.8) can be turned into the following discrete representation,

$$\mathbb{E}\boldsymbol{s}^c = \boldsymbol{\mathcal{R}}\tilde{\boldsymbol{H}}_2\boldsymbol{H}_1\boldsymbol{f}_0, \quad (3.9)$$

where $\boldsymbol{s}^c \in \mathbb{R}^M$ is the vector representation of the sinogram with $M \leq D^2$ ($M = D^2$ when there is no rebinning), $\boldsymbol{\mathcal{R}} : \mathbb{R}^N \to \mathbb{R}^M$ is the discrete Radon transform, $\tilde{\boldsymbol{H}}_2 \in \mathbb{R}^{N\times N}$ is a matrix close to a Toeplitz matrix but with smoothly varying rows[1], $\boldsymbol{H}_1 \in \mathbb{R}^{N\times N}$ is a circulant matrix, and $\boldsymbol{f}_0 \in \mathbb{R}^N$ is the vector representation of the discretized radiotracer concentration.

Recently, Berthon *et al.* developed a "dynamic PET simulator via tomographic emission projection" (dPETSTEP). This software uses a matrix representation of the imaging system to compute the projections of the object of interest in a fast way [19, 84]. The matrix representation, described in [19, p. 2], can be seen as the discrete equivalent to (3.7) with the extra

[1] $\tilde{\boldsymbol{H}}_2$ is well approximated by a sparse operator in the wavelet domain [58].

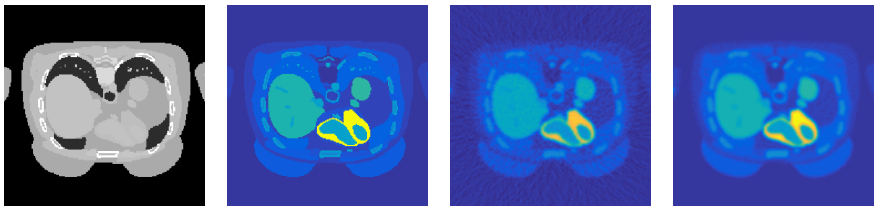

(a) CT scan **(b)** f_0 **(c)** $t_{\text{acq}} = 1\,\text{s}$ **(d)** $t_{\text{acq}} = 60\,\text{s}$

Figure 3.5 Zoom on simulations of a transaxial slice of the XCAT phantom [131] with dPETSTEP software: (a) attenuation map, (b) activity map, (c) observations for $t_{\text{acq}} = 1\,\text{s}$ and (d) observations for $t_{\text{acq}} = 60\,\text{s}$. Estimates are reconstructed from projections using filtered backprojection (FBP) algorithm, implemented in the software.

assumption of a spatially invariant kernel $\tilde{h}_2$. For a realistic scanner geometry, dPETSTEP simulations of projections are around 55,000 times faster than Monte Carlo simulations and the root mean square error (RMSE) between them differs only by 4% in average. In simulations of Chapters 4 and 5, we will use images reconstructed from projections generated by dPETSTEP (see *e.g.*, Figure 3.5).

3.3 Imaging challenges

One major drawback of PET images is their low spatial resolution causing for instance partial volume effects that prevent accurate delineation of small organs or precise uptake value estimation [96]. Several factors involved in this poor spatial resolution (see section 3.1) can be optimized with the design of the scanner [97]. First, the detectors can be designed to better detect scattered and random events, leading to a better correction of the projections. Secondly, there is a trade-off to be found in the choice of the depth of photon interaction in the crystal: a small depth limits the parallax error but reduces the detection efficiency at the same time. However, no matter the quality of the acquisition devices and the algorithms, the resolution of PET imaging systems will always be limited by (*i*) the non-zero positron range before annihilation, (*ii*) the imperfect collinearity between emitted photons, and (*iii*) the (finite) detector size [97].

Analytical reconstruction methods such as filtered backprojection (FBP)—a standard reconstruction algorithm in tomography—are based on the central section theorem [16, chapter 4]. Even if they offer good reconstruction

results, they are limited in the modeling of the degradation factors. Iterative algorithms such as maximum-likelihood expectation maximization (ML-EM) are powerful in the sense that they can include both the data model (including the noise statistics) and information on the structure of the radiotracer distribution. It requires however a good knowledge of the forward model. In 2019, Häggström *et al.* proposed a new reconstruction technique based on a deep convolutional network called DeepPET [85]. Their network reconstructs quantitative maps of radiotracer concentration in a very short time compared to the aforementioned methods. Moreover, an accurate knowledge of the forward model is not required since the optimization of the network parameters is automated. The training is based on more than 291,000 images. Whole-body images of patients were simulated with the XCAT phantom [131] (see subsection 4.5.1 for a more detailed description of the phantom) and dPETSTEP was then used to get realistic sinograms [84].

In the next two chapters, we present iterative algorithms designed to improve PET images in a post-processing and possibly blind context. In this case, observations vector $\boldsymbol{y} \in \mathbb{R}^N$ is the reconstructed image. Let $\mathcal{G} : \mathbb{R}^M \to \mathbb{R}^N$ be a reconstruction technique either linear (like FPB) or non-linear (like ML-EM). Observations $\boldsymbol{y}$ are related to $\boldsymbol{f}_0$ through

$$\boldsymbol{y} = \mathcal{G}(\boldsymbol{s}^c) \approx \tilde{\boldsymbol{H}}_2 \boldsymbol{H}_1 \boldsymbol{f}_0. \tag{3.10}$$

The proposed algorithms rely on the formulation of a minimization problem whose objective function includes several terms. A first term is related to the acquisition model and the noise statistics. The next ones encode the prior knowledge on the structure of the radioatracer concentration map and, in Chapter 5, on the blurring operator.

Based on (3.10), we define the *point spread function* (PSF) of an imaging device as the observation of an isolated (or point) source. In PET scanners, the PSF is generally spatially variant and depends on the reconstruction algorithm $\mathcal{G}$. In Chapters 4 and 5, the assumption of a spatially invariant PSF near the center of the FOV allows us to consider the deblurring of PET images as a *deconvolution* process.

4

Post-reconstruction deconvolution of PET images

IMPROVING the quality of PET images affected by low resolution and high level of noise is a challenging task in nuclear medicine and radiotherapy, as pointed out in section 3.3. In this chapter, we propose a restoration method achieved after tomographic reconstruction and targeting clinical situations where raw data are often not accessible. Our contribution introduces the recently developed TGV^2_α-norm to regularize the inverse problem (see subsection 2.2.1) as well as a data fidelity term mixing ℓ_1- and ℓ_2-norms to deal with the statistics of the noise. We stabilize this procedure with additional image constraints such as positivity and photometry invariance. To validate the method, experiments are conducted on both simulated data of XCAT phantom and real human PET images.

Context

A challenging step in radiotherapy treatment is the accurate delineation of the tumor volume based on PET images [96]. Some methods rely on visual interpretation or on activity threshold determination but suffer from methodological limitations [96]. The use of more complex segmentation algorithms is impeded by the two main drawbacks of PET imaging pointed out in section 3.1: low spatial resolution and high level of noise [155]. The first one is mainly due to the blur introduced by the random positron

travel, the photon diffusion in the patient tissues before annihilation and the large size of the scintillators required to detect high-energy photons (see subsection 3.2.3). The resulting point spread function (PSF) of the PET system is generally not uniform and can vary slightly in the field of view (FOV). The latter, *i.e.*, the noise in raw data, is due to low photon detection efficiency of the detectors and the limitation of the injected tracer dose in the patient body. The noise is Poissonian in the projection space, before reconstruction.

Improving the quality of PET images is essential before applying more advanced segmentation techniques. Deblurring and denoising can be applied either during the reconstruction process or in a post-processing phase. The second approach is more appropriate for clinical use since the access to raw data or to the reconstruction algorithm of the scanner is not always possible. After sinogram correction, images are reconstructed with standard iterative 3D algorithms like ML-EM or its accelerated version, ordered subset expectation maximization (OSEM) [152]. The statistics of the noise corrupting those reconstructed images are not well characterized [30, 36, 85]. An accurate, analytical, description of its distribution is in fact impossible since many factors influence the final distribution (*e.g.*, the pre-corrections applied to the raw sinogram, the choice of the reconstruction algorithm and its parameters, etc.). Some authors studied the noise distribution for specific algorithms like FBP or OSEM or proposed to consider a more general family of distributions, *e.g.*, the Tweedie distributions [36]. However, nowadays a classical Gaussian filter is still the most widely used tool in clinical denoising. Edge-preserving filters such as bilateral filters or M-smoothers are also used but, like the Gaussian filter, they are generally designed for additive noise [66]. For the deblurring step, classical deconvolution algorithms like Van Cittert's or Landweber's [66] are used. Other methods combine the denoising and deblurring steps, either in an iterative algorithm like Lucy-Richardson [125] or by solving an optimization problem [55, 68].

Contributions and outline

In this work, we choose the inverse problem approach in a post-processing phase and propose a problem formulation specific to the restoration of PET images. First, we theoretically show in section 4.2 that the noise statistics in a PET image reconstructed with a linear algorithm is well characterized by a mixture of two tails—a Gaussian tail for small intensities and

a sub-exponential tail for larger ones. Then, in section 4.3, we formulate the convex optimization problem that assumes that the PSF of the scanner is known. The objective function includes a Huber function as the data fidelity term. This loss function can indeed deal with the "mixed" behavior of the noise. It also introduces the TGV^2_α-norm as a regularization term [28] for PET deconvolution and considers specific properties of PET physics such as positivity and photometry invariance. Finally, we validate the deconvolution algorithm detailed in section 4.4 on PET images of the XCAT phantom simulated with dPETSTEP software (see section 4.5). We also show results obtained with our method on PET images of patients.

4.1 Discrete forward model and underlying assumptions

In this chapter, we work with the same notations as in Chapter 3. After tomographic reconstruction $\mathcal{G}$, the observed image $\boldsymbol{y} \in \mathbb{R}^N$ is associated with $\boldsymbol{f}_0 \in \mathbb{R}^N$ through the forward model (3.10) rewritten as

$$\boldsymbol{y} \approx \boldsymbol{H}\boldsymbol{f}_0, \tag{4.1}$$

where $\boldsymbol{H} \in \mathbb{R}^{N\times N}$ is a blurring operator accounting for both the physical and instrumental inaccuracies described in Chapter 3. Some assumptions on $\boldsymbol{H}$ lead to a simpler model. In first approximation, the PSF near the center of the FOV is uniform, Gaussian and isotropic in the 2D plane [66]. Consequently, blurred image $\boldsymbol{y}$ is assumed to result from the convolution of the original image with a kernel $\boldsymbol{h} \in \mathbb{R}^N$, the PSF of the scanner,

$$\boldsymbol{y} \approx \boldsymbol{h} * \boldsymbol{f}_0. \tag{4.2}$$

We make the assumption that the convolution kernel is known, either via direct measurement of an isolated source located at the center of the FOV or via the spec sheet of the considered imaging device. Operator $\boldsymbol{H}$ is the block-circulant operator[1] associated with kernel $\boldsymbol{h}$.

In both (4.1) and (4.2), we use the approximation symbol $\approx$ to account for the errors due for instance to the imperfect reconstruction, to the non ideal modeling of $\boldsymbol{h}$, and to the noise. In [79], we assumed that the observations are i.i.d. and follow a Poisson distribution. However, as explained in the introduction, the distribution of the noise in the reconstructed PET

[1] To be accurate, $\boldsymbol{H}$ should be a block-Toeplitz operator. However, the assumption of a block-circulant operator holds when the object to image and the PSF are small compared to the size of the FOV. In this case, both operators lead to the same observations $\boldsymbol{y}$.

images is not well characterized. Unlike the Poisson statistics observed in the raw sinogram, the post-reconstruction distribution depends on several factors. For instance, the entries of the corrected sinogram (3.8) are not Poisson distributed anymore. Furthermore, the reconstruction algorithm mixes the random variables of the sinogram in an unknown manner. With FBP, a Gaussian distribution seems to be a good fit for the noise while with ML-EM, a Gamma distribution could be a better choice [36]. In the next section, we show that when the reconstruction algorithm is linear, the noise on each element of $\boldsymbol{y}$ is characterized by a *sub-exponential* distribution [158], *i.e.*,

$$\mathbb{P}\{|y_i - (\boldsymbol{h} * \boldsymbol{f}_0)_i| \geq t\} \leq 2e^{-t/K_1},$$

for all $t \geq 0$ and $K_1 > 0$.

The physics of PET imaging suggests two additional constraints to model (4.1). The first property is the *positivity* since the original image $\boldsymbol{f}_0$ represents a non-negative activity map in a phantom or *e.g.*, the *in vivo* metabolic activity. Hence,

$$\boldsymbol{f}_0 \succeq \mathbf{0}.$$

The second property is *photometry invariance*. Total photometry preservation means that the total photon counts in the original and observed images are approximately the same. This property is particularly valuable for quantification aspects like the measurement of standardized uptake values (SUV) [155],

$$\sum_{i=1}^{N} (\boldsymbol{f}_0)_i \approx \sum_{i=1}^{N} y_i.$$

4.2 Noise statistics

As explained in subsection 3.2.3, the discrete sinogram which contains the observed projections of $\boldsymbol{f}_0$ undergoes several correction steps before the reconstruction. The corrected sinogram, $\boldsymbol{s}^c$, commonly writes [85]

$$s^c_{i,j} = \frac{s_{i,j} - \nu_{i,j}}{\varsigma_{i,j}},$$

where $\nu_{i,j} < s_{i,j}$ represents the correction of random events and $\varsigma_{i,j} > 0$ is a scaling factor that accounts, among others, for normalization, attenuation and delay correction. We consider that the correction of the random events is done in real-time, by counting the random ACD occurring during a de-

layed time window [16, 163]. Consequently, $\nu_{i,j}$ is also a Poisson random variable. If $\varsigma_{i,j}$ is properly estimated from the projections and the transmission scan, the expectation of $\boldsymbol{s}^c$ will be close to (3.9). We will then consider $\mathbb{E}\boldsymbol{s}^c = \boldsymbol{\mathcal{R}}(\boldsymbol{H}\boldsymbol{f}_0)$.

In this section, we show that the noise on the observations reconstructed from $\boldsymbol{s}^c$ with a linear algorithm follows a sub-exponential distribution. In other words, the residual $(\boldsymbol{y} - \boldsymbol{H}\boldsymbol{f}_0)_i$ is the realization of a random variable showing at least an exponential tail decay, *i.e.*,

$$\mathbb{P}\{|y_i - (\boldsymbol{H}\boldsymbol{f}_0)_i| \geq t\} \leq C_1 e^{-t/K_1},$$

for all $t \geq 0$ and $C_1, K_1 > 0$. This decay will motivate the choice of the data fidelity term in section 4.3. Our development is mainly based on the theoretical work of Vershynin [158] on non-asymptotic behavior of random variables and random matrices. It is divided into three statements:

1. A Poisson random variable is sub-exponential;
2. The difference of two Poisson random variables is sub-exponential;
3. If the reconstruction algorithm is linear, the noise on the resulting observations follows a sub-exponential distribution.

We first give the definition of a sub-exponential random variable.

Proposition 4.1 *[157, Proposition 2.7.1] Let X be a random variable. Then, the following properties are equivalent. The parameters $K_i > 0$ appearing in these properties differ from each other by at most an absolute constant factor.*

1. *The tails of X satisfy $\mathbb{P}\{|X| \geq t\} \leq C_1 e^{-t/K_1}$ for all $t \geq 0$.*
2. *The moments of X satisfy $\|X\|_p = (\mathbb{E}|X|^p)^{1/p} \leq pK_2$ for all $p \geq 1$.*
3. *The moment generating function of $|X|$ is bounded at some point,* i.e., *$\mathbb{E}e^{|X|/K_3} \leq C_3$.*

Factor C_1 in property 1 and upper bound C_3 in property 3 can be any finite positive value.

Definition 4.2 (Sub-exponential random variable) *[158, Definition 5.13] A random variable X that satisfies one of the equivalent properties of Proposition 4.1 is called a* sub-exponential *random variable. The* sub-exponential norm *of X, denoted $\|X\|_{\psi_1}$, is defined to be the smallest parameter K_2. In other words,*

$$\|X\|_{\psi_1} \coloneqq \sup_{p \geq 1} p^{-1} (\mathbb{E}|X|^p)^{1/p}.$$

Proposition 4.3 *Let X be a random variable following a Poisson distribution of parameter $\lambda \geq 0$,* i.e., *$X \sim \mathcal{P}(\lambda)$. Then, X is also a* sub-exponential *random variable with a sub-exponential norm bounded by*

$$\|X\|_{\psi_1} \leq 2C_3 \left[\ln\left(1 + \frac{\ln C_3}{\lambda}\right)\right]^{-1}, \tag{4.3}$$

with $C_3 > 1$.

Proof. Random variable X is sub-exponential if one of the three properties in Proposition 4.1 is satisfied. In this case, we check if the moment generating function (MGF) is bounded at some point, *i.e.*, if there exists $K_3 \in \mathbb{R}_0^+$ such that

$$\mathbb{E}e^{|X|/K_3} \leq C_3. \tag{4.4}$$

The MGF of Poisson random variable X with parameter λ is given by $\mathbb{E}e^{tX} = e^{\lambda(e^t-1)}$ [127]. Since such random variables are non-negative, expression (4.6) imposes

$$e^{\lambda(e^{1/K_3}-1)} \leq C_3. \tag{4.5}$$

This decreasing exponential function tends to 1 as K_3 tends to infinity. Consequently, for $C_3 > 1$, there exist K_3 values such that (4.6) is verified. X is a sub-exponential random variable.

Since the function on the left-hand side of (4.5) is continuous and strictly decreasing, the smallest K_2 value such that (4.6) is verified satisfies

$$e^{\lambda(e^{1/K_3}-1)} = C_3.$$

Hence,

$$K_3 = \left[\ln\left(1 + \frac{\ln C_3}{\lambda}\right)\right]^{-1},$$

with $C_3 > 1$. Since $K_2 = 2C_3K_3$ (see Appendix 4.A), an upper bound on the sub-exponential norm is given by

$$\|X\|_{\psi_1} \leq 2C_3 \left[\ln\left(1 + \frac{\ln C_3}{\lambda}\right)\right]^{-1}. \qquad \blacksquare$$

Regarding Proposition 4.3, the sub-exponential norm is roughly proportional to λ, the parameter of the Poisson distribution. Indeed, as λ in-

creases, the probability density function (pdf) of the distribution gets flatter. $\|X\|_{\psi_1}$ increases too as the decay rate of the bounding function (proportional to $1/\|X\|_{\psi_1}$) gets lower.

Proposition 4.4 *Let X_1 and X_2 be independent random variables following a Poisson distribution of parameters $\lambda_1 \geq 0$ and $\lambda_2 \geq 0$, respectively. Then, $Y := (X_1 - X_2)/b$ with $b > 0$ is also a* sub-exponential *random variable.*

Proof. According to Proposition 4.3, random variables X_1 and X_2 are sub-exponential. Their MGFs are then bounded by $C_1 > 1$ and $C_2 > 1$, respectively. Using the triangle inequality, the MGF of $|Y|$ is also bounded,

$$\mathbb{E}(e^{|X_1 - X_2|/K_3}) \leq \mathbb{E}(e^{(|X_1| + |X_2|)/K_3}) \leq C_1 C_2,$$

for $K_3 > 0$. Let $K_3' := K_3/b$. We get

$$\mathbb{E}e^{|Y|/K_3'} \leq C_1 C_2. \tag{4.6}$$

Random variable Y is then sub-exponential. ∎

From Proposition 4.4, we show that entries $s^c_{i,j}$ of the (non-negative) corrected sinogram follow a sub-exponential distribution. Finally, the next theorem allows us to characterize the distribution of the noise in PET images when the reconstruction algorithm $\mathcal{G}$ is linear, *e.g.*, FBP.

Theorem 4.5 *(from [157, Theorem 2.8.2]) Let $X_1, \ldots, X_N$ be independent, zero-mean, sub-exponential random variables, and $\boldsymbol{a} = (a_1, \ldots, a_N) \in \mathbb{R}^N$. Then, for every $t \geq 0$, we have*

$$\mathbb{P}\left\{\left|\sum_{i=1}^{N} a_i X_i\right| \geq t\right\} \leq 2\exp\left[-c\min\left(\frac{t^2}{K^2\|\boldsymbol{a}\|_2^2}, \frac{t}{K\|\boldsymbol{a}\|_\infty}\right)\right], \tag{4.7}$$

where $K = \max_i \|X_i\|_{\psi_1}$ and $c > 0$.

We denote $\boldsymbol{G} \in \mathbb{R}^{N \times M}$ the linear algorithm that is used for the reconstruction. Each pixel in the resulting PET image can be seen as a linear combination of the noisy projections contained in $\boldsymbol{s}^c$, *i.e.*, $\boldsymbol{y} = \boldsymbol{G}\boldsymbol{s}^c$. As explained at the beginning of the section, we assume that $\mathbb{E}\boldsymbol{s}^c = \boldsymbol{\mathcal{R}}(\boldsymbol{H}\boldsymbol{f}_0)$.

Let us rewrite (4.7) for $X_i = [\boldsymbol{s}^c - \boldsymbol{\mathcal{R}}(\boldsymbol{H}\boldsymbol{f}_0)]_i$ which is a zero-mean sub-

exponential random variable[2],

$$\mathbb{P}\left\{\left|\sum_{i=1}^{M} G_{ji}s_i^c - \sum_{i=1}^{M} G_{ji}[\boldsymbol{\mathcal{R}}(\boldsymbol{H}\boldsymbol{f}_0)]_i\right| \geq t\right\} \leq 2\exp\left[-c\min\left(\frac{t^2}{K^2\|\boldsymbol{G}_j\|_2^2}, \frac{t}{K\|\boldsymbol{G}_j\|_\infty}\right)\right],$$

where G_{ji} is the entry in the j-th row and i-th column of $\boldsymbol{G}$ and $\boldsymbol{G}_j \in \mathbb{R}^M$ is the j-th row of $\boldsymbol{G}$. If $\boldsymbol{G}$ is a good approximation of the inverse of the discrete Radon transform, we have

$$\sum_{i=1}^{M} G_{ji}[\boldsymbol{\mathcal{R}}(\boldsymbol{H}\boldsymbol{f}_0)]_i \approx (\boldsymbol{H}\boldsymbol{f}_0)_j.$$

Hence,

$$|\sum_{i=1}^{M} G_{ji}s_i^c - \sum_{i=1}^{M} G_{ji}[\boldsymbol{\mathcal{R}}(\boldsymbol{H}\boldsymbol{f}_0)]_i| \approx |y_j - (\boldsymbol{H}\boldsymbol{f}_0)_j|$$

corresponds to the deviation of observation j with respect to the original value at pixel j. We get

$$\mathbb{P}\left\{|y_j - (\boldsymbol{H}\boldsymbol{f}_0)_j| \geq t\right\} \leq 2\exp\left[-c\min\left(\frac{t^2}{K^2\|\boldsymbol{G}_j\|_2^2}, \frac{t}{K\|\boldsymbol{G}_j\|_\infty}\right)\right]. \quad (4.8)$$

Using $\|\boldsymbol{G}_j\|_\infty \leq \|\boldsymbol{G}_j\|_2$, we propose an alternative expression for (4.8) similar to [157, p. 37],

$$\mathbb{P}\left\{|y_j - (\boldsymbol{H}\boldsymbol{f}_0)_j| \geq t\right\} \leq \begin{cases} 2\exp(-\frac{ct^2}{K^2\|\boldsymbol{G}_j\|_2^2}) & \text{if } t \leq 1 \\ 2\exp(-\frac{ct}{K\|\boldsymbol{G}_j\|_2}) & \text{if } t > 1. \end{cases} \quad (4.9)$$

Regarding (4.9), the distribution of the noise in the restored PET image has a Gaussian behavior for small t but has a heavy tail—a sub-exponential behavior—for larger values of t.

[2] As mentioned in [157], centering a random variable does not affect its sub-exponentiality.

4.3 Inverse problem formulation

We are interested in finding an estimator $\hat{f}$ of the original image f_0 from observations $\boldsymbol{y}$ in (4.2). As explained in section 2.1, direct inversion is not possible and unicity of the solution is not guaranteed. To address this issue and reduce the set of possible solutions, we regularize the problem by adding a penalty term ϕ in the objective function (see section 2.2),

$$\begin{aligned} &\underset{\boldsymbol{u}\in\mathbb{R}^N}{\text{minimize}} \quad \operatorname{dist}(\boldsymbol{Hu}, \boldsymbol{y}) + \rho\phi(\boldsymbol{u}), \\ &\text{subject to} \quad \boldsymbol{u} \succeq \boldsymbol{0}, \quad \sum_{i=1}^{N} u_i \approx \sum_{i=1}^{N} y_i, \end{aligned} \tag{4.10}$$

where $\rho > 0$ is a regularization parameter. The two constraints come from the physics-based properties described in section 4.1.

4.3.1 Data fidelity term

The first term in the objective function (4.10) is the data fidelity term. Minimizing this term encourages $\boldsymbol{Hu}$ to be close to observations $\boldsymbol{y}$ according to a well chosen distance function. Usually, this function directly depends on the noise statistics. If we consider a Bayesian framework (see section 2.2), it coincides with the negative log-likelihood of the pdf of the noise.

In section 4.2, we showed that the noise on PET images reconstructed with linear algorithms exhibits two different behaviors. For small values of t in (4.9), the noise can be considered as Gaussian. For larger values of t, its behavior is closer to the behavior of, for instance, a Laplace random variable whose cumulative distribution function (CDF) presents the same exponential decay. We also adopt this noise model for images reconstructed with iterative algorithms such as ML-EM and we validate its relevance in section 4.5. To deal with this mixture of two tails, we propose the Huber function as the data fidelity term, similarly to Pairet's work [110].

Definition 4.6 (Huber function) *[111, section 3.1] The* Huber function h_δ *of parameter* $\delta > 0$ *is defined as the* infimal convolution, *denoted by* $\square$, *of the* ℓ_1*-norm with* $\frac{1}{2\delta}\|\cdot\|_2^2$, i.e.,

$$\begin{aligned} h_\delta : \mathbb{R}^N \to \mathbb{R}, \boldsymbol{u} \mapsto h_\delta(\boldsymbol{u}) &:= \left(\|\cdot\|_1 \square \frac{1}{2\delta}\|\cdot\|_2^2\right)(\boldsymbol{u}) \\ &= \inf_{\boldsymbol{w}\in\mathbb{R}^N} \left(\|\boldsymbol{w}\|_1 + \frac{1}{2\delta}\|\boldsymbol{w}-\boldsymbol{u}\|_2^2\right). \end{aligned} \tag{4.11}$$

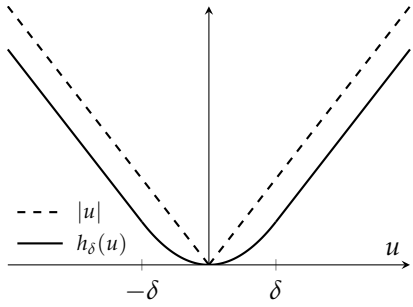

Figure 4.1 In 1D, Huber function with parameter δ (solid line) is a smooth approximation of the absolute value (dashed line). For $|u| < \delta$, its behaviour is quadratic. For $|u| \geq \delta$, it is a linear function.

For $N = 1$, it is given by

$$h_\delta(u) = \begin{cases} \frac{u^2}{2\delta} & \text{if } |u| \leq \delta \\ |u| - \frac{\delta}{2} & \text{if } |u| > \delta. \end{cases}$$

Interestingly, the Huber function is the Moreau envelope of the ℓ_1-norm, *i.e.*, a continuously differentiable approximation of $\|\cdot\|_1$ (see Figure 4.1).

Regarding (4.10), we define the distance function as

$$\text{dist}(\boldsymbol{Hu}, \boldsymbol{y}) = h_\delta(\boldsymbol{Hu} - \boldsymbol{y}), \tag{4.12}$$

with an appropriate choice of δ regarding (4.9), *e.g.*, $\delta = 1$.

To validate this choice in section 4.5, we also look at additional data fidelity terms that refer to other noise distributions. Typically, we consider Gaussian, Laplace and Poisson distributions. The negative log-likelihood of their pdf corresponds to the squared ℓ_2-norm, the ℓ_1-norm and the Kullback-Leibler (KL) divergence (see Definition 2.5), respectively. In [79], we considered this last statistics on synthetic data containing pure Poisson noise.

4.3.2 Regularization term

The second term in (4.10) is the regularization term promoting the respect of the *a priori* knowledge on the activity map structure. In this work, we consider a regularization term that forces the image to have a small TGV^2_α-norm, *i.e.*, to be piecewise-smooth. As explained in subsection 2.2.1, this

penality is more adapted than TV to natural images, including PET medical images. With TGV^2_α regularization[3], the constrained convex optimization problem reads

$$\begin{aligned} &\underset{\substack{\boldsymbol{u}\in\mathbb{R}^N,\\ \boldsymbol{w}\in\mathbb{R}^{N\times 2}}}{\text{minimize}} \quad \operatorname{dist}(\boldsymbol{H}\boldsymbol{u},\boldsymbol{y}) + \rho\|\boldsymbol{\nabla}\boldsymbol{u}-\boldsymbol{w}\|_{2,1} + \alpha\rho\|\varepsilon(\boldsymbol{w})\|_{2,1}, \\ &\text{subject to} \quad \boldsymbol{u}\succeq\boldsymbol{0}, \quad \sum_{i=1}^N u_i = \sum_{i=1}^N y_i. \end{aligned} \tag{4.13}$$

4.4 Numerical implementation

In this section, we describe how we numerically solve (4.13). To fit the framework described in subsection 2.3.1, we replace (4.13) with an equivalent, unconstrained, optimization problem with a unique optimization variable $\boldsymbol{z}$. Let $\mathcal{Q}$ be the set of images satisfying the property of photometry invariance, *i.e.*, $\mathcal{Q} \coloneqq \{\boldsymbol{u}\in\mathbb{R}^N | \boldsymbol{1}^\top\boldsymbol{u} = \boldsymbol{1}^\top\boldsymbol{y}\}$. We substitue the two constraints enforcing $\boldsymbol{u}$ to belong to the sets $\mathbb{R}^N_+$ and $\mathcal{Q}$ with two indicator functions $\iota_{\mathbb{R}^N_+}$ and $\iota_{\mathcal{Q}}$. They equal zero if $\boldsymbol{u}$ belongs to the convex sets and $+\infty$ otherwise. Equation (4.13) becomes

$$\begin{aligned} \hat{\boldsymbol{z}} \in \underset{\boldsymbol{z}\in\mathbb{R}^{N\times 3}}{\arg\min}\ &\operatorname{dist}(\boldsymbol{H}\boldsymbol{R}_u\boldsymbol{z},\boldsymbol{y}) + \rho\|(\boldsymbol{\nabla}\boldsymbol{R}_u - \boldsymbol{R}_w)\boldsymbol{z}\|_{2,1} \\ &+ \alpha\rho\|\varepsilon(\boldsymbol{R}_w\boldsymbol{z})\|_{2,1} + \iota_{\mathbb{R}^N_+}(\boldsymbol{R}_u\boldsymbol{z}) + \iota_{\mathcal{Q}}(\boldsymbol{R}_u\boldsymbol{z}), \end{aligned} \tag{4.14}$$

where $\boldsymbol{z} \coloneqq (\boldsymbol{u},\boldsymbol{w})$, $\boldsymbol{R}_u$ and $\boldsymbol{R}_w$ are restriction operators keeping only the first column of $\boldsymbol{z}$ and the last two columns of $\boldsymbol{z}$, respectively [71]. Estimated image $\hat{\boldsymbol{f}}$ is given by $\boldsymbol{R}_u\hat{\boldsymbol{z}}$. The convolution of the image with the blurring kernel is modeled by a circulant operator $\boldsymbol{H}$, easily applied to $R_u\boldsymbol{z}$ via a fast Fourier transform (FFT). A circulant operator assumes periodic boundaries in the original image. In our case, this assumption holds because (*i*) the object of interest is far enough from the borders of the FOV compared to the size of the blurring kernel and (*ii*) the background activity is zero. If this assumption does not hold, undesired border effects can be avoided using a "padding" method, *e.g.*, the one presented by Almeida *et al.* [5].

The presence of the two indicator functions in (4.14) leads to a nonsmooth in addition to a non-differentiable objective function. The use of

[3]The value $\alpha = 2$ is used in practice [93].

a proximal algorithm, *e.g.*, the generalized Chambolle-Pock (GCP) algorithm, is appropriate (see subsection 2.3.1). A compact formulation of (4.14) matching the notation of (2.12) is given by

$$\hat{\boldsymbol{z}} \in \underset{\boldsymbol{z}\in\mathbb{R}^{N\times 3}}{\arg\min}\, F_1(\boldsymbol{H}\boldsymbol{R}_{\boldsymbol{u}}\boldsymbol{z}) + F_2((\boldsymbol{\nabla}\boldsymbol{R}_{\boldsymbol{u}} - \boldsymbol{R}_{\boldsymbol{w}})\boldsymbol{z}) + F_3(\varepsilon(\boldsymbol{R}_{\boldsymbol{w}}\boldsymbol{z})) + G(\boldsymbol{z}), \quad (4.15)$$

with straightforward definitions of F_1, F_2, F_3 and G from (4.14).

4.4.1 Proximal operators of primal and dual functions

The implementation of GCP requires the proximal operator of primal function G as well as those of dual functions $F_1^\star$, $F_2^\star$ and $F_3^\star$. The proximal operator of $\imath_{\mathbb{R}_+^N} + \imath_{\mathcal{Q}}$ is given by a combination of positivity (max) and photometry invariance (average) proximal operators [111]. Since $\boldsymbol{R}_{\boldsymbol{u}}$ is tight frame, *i.e.*, $\boldsymbol{R}_{\boldsymbol{u}}\boldsymbol{R}_{\boldsymbol{u}}^* = \mathbf{Id}_N$, we use the property of semi-orthogonal transform to compute the proximal operator of G [43, Table 10.1],

$$\operatorname{prox}_{\tau G}(\tilde{\boldsymbol{z}}) = \tilde{\boldsymbol{z}} + \boldsymbol{R}_{\boldsymbol{u}}^*[\max(\boldsymbol{R}_{\boldsymbol{u}}\tilde{\boldsymbol{z}}, \boldsymbol{0}) - \frac{1}{N}\sum_{i=1}^{N}(\max(\boldsymbol{R}_{\boldsymbol{u}}\tilde{\boldsymbol{z}}, \boldsymbol{0})) - \boldsymbol{y})_i - \boldsymbol{R}_{\boldsymbol{u}}\tilde{\boldsymbol{z}}], \quad (4.16)$$

where τ is the primal step-size in GCP algorithm.

Functions F_2 and F_3 are $L_{2,1}$-norms. By conjugation, $F_2^\star$ and $F_3^\star$ are indicator functions [111, section 6.5]. Their proximal operators are projection operators onto the convex sets $\mathcal{Q}_2 := \{\tilde{\boldsymbol{q}} \in \mathbb{R}^{N\times 2} | \|\tilde{\boldsymbol{q}}\|_{2,\infty} \leq \rho\}$ and $\mathcal{Q}_3 := \{\tilde{\boldsymbol{r}} \in \mathbb{R}^{N\times 4} | \|\tilde{\boldsymbol{r}}\|_{2,\infty} \leq \alpha\rho\}$. They do not depend on the dual step-size σ (see section 2.3). Norm $\|\cdot\|_{2,\infty}$ is defined as

$$\|\tilde{\boldsymbol{q}}\|_{2,\infty} := \max_{i\in[N]} \|\tilde{\boldsymbol{q}}_i\|_2,$$

with $\tilde{\boldsymbol{q}}_i \in \mathbb{R}^2$ the i^{th} row of $\tilde{\boldsymbol{q}}$.

The proximal operator of $F_1^\star$ depends on the choice of the data fidelity term. We focus on Huber function but we also consider other terms as mentioned in subsection 4.3.1. When F_1 is the Huber function of parameter $\delta > 0$, the proximal operator of $F_1^\star$ is given by

$$\operatorname{prox}_{\sigma F_1^\star}(\tilde{\boldsymbol{p}}) = \mathcal{P}_{\mathcal{B}_\infty}\left(\frac{\tilde{\boldsymbol{p}} - \sigma\boldsymbol{y}}{1+\sigma\delta}\right), \quad (4.17)$$

where $\mathcal{P}_{\mathcal{B}_\infty}$ is the projection on the unit ball of the ℓ_∞-norm, *i.e.*, a box.

$\mathcal{P}_{\mathcal{B}_\infty}(\tilde{\boldsymbol{p}})$ is applied componentwise on $\tilde{\boldsymbol{p}}$,

$$\mathcal{P}_{\mathcal{B}_\infty}(\tilde{p}_i) \coloneqq \frac{\tilde{p}_i}{\max(|\tilde{p}_i|, 1)}.$$

The details of the computation—based on the fact that the infimal convolution is dual to addition [111]—are in Appendix 4.B.

Let us now mention the proximal operators of the alternative data fidelity terms. First, when F_1 is the squared ℓ_2-norm, $\operatorname{prox}_{\sigma F_1^\star}$ is given by

$$\operatorname{prox}_{\sigma F_1^\star}(\tilde{\boldsymbol{p}}) = \frac{\tilde{\boldsymbol{p}} - \sigma \boldsymbol{y}}{1 + \sigma}.$$

When the data fidelity term is the ℓ_1-norm, $\operatorname{prox}_{\sigma F_1^\star}$ is a projection operator onto the convex set $\mathcal{Q}_1 \coloneqq \{\tilde{\boldsymbol{p}} \in \mathbb{R}^N | \|\tilde{\boldsymbol{p}} - \sigma \boldsymbol{y}\|_\infty \leq 1\}$. Notice that when $\delta \to 0$, (4.17) tends to the the proximal operator of the conjugate of the ℓ_1-norm, that is coherent with the definition of the Huber function.

Finally, when the data fidelity term is the KL divergence (see Definition 2.5), *i.e.*, the negative log-likelihood of the Poisson distribution, the proximal operator of $F_1^\star$ is, for each component i of $\tilde{\boldsymbol{p}} \in \mathbb{R}^N$ [11],

$$\operatorname{prox}_{\sigma F_1^\star}(\tilde{p}_i) = \begin{cases} \frac{1}{2}\left(\tilde{p}_i + 1 - \sqrt{(\tilde{p}_i - 1)^2 + 4\sigma y_i}\right) & \text{if } y_i \neq 0 \\ 1 & \text{otherwise.} \end{cases}$$

4.4.2 Operators and their adjoints

The operator associated with F_1 is $\boldsymbol{L}_1 = \boldsymbol{H}\boldsymbol{R}_{\boldsymbol{u}} : \mathbb{R}^{N\times 3} \to \mathbb{R}^N$ and its adjoint is $\boldsymbol{R}_{\boldsymbol{u}}^* \boldsymbol{H}^*$. The adjoint of a restriction operator is a zero-padding operator. The operator associated with F_2 is $\boldsymbol{L}_2 = (\boldsymbol{\nabla}\boldsymbol{R}_{\boldsymbol{u}} - \boldsymbol{R}_{\boldsymbol{w}}) : \mathbb{R}^{N\times 3} \to \mathbb{R}^{N\times 2}$ and its adjoint is given by $(-\boldsymbol{R}_{\boldsymbol{u}}^* \circ \operatorname{div} - \boldsymbol{R}_{\boldsymbol{w}}^*)$ where the adjoint of the discrete gradient is given by the negative of the divergence (see Definition 2.8). Finally, the operator associated with F_3 is $\boldsymbol{L}_3 = (\varepsilon \circ \boldsymbol{R}_{\boldsymbol{w}}) : \mathbb{R}^{N\times 3} \to \mathbb{R}^{N\times 4}$. The adjoint operator is $(-\boldsymbol{R}_{\boldsymbol{w}}^* \circ \operatorname{div})$.

4.4.3 Parameters choice and stopping criterion

The algorithm for the deconvolution of PET images with TGV regularization is summarized in Algorithm 5. Variables $\boldsymbol{p} \in \mathbb{R}^N$, $\boldsymbol{q} \in \mathbb{R}^{N\times 2}$ and $\boldsymbol{r} \in \mathbb{R}^{N\times 4}$ are the dual variables (see subsection 2.3.1). To ensure the convergence of CP algorithm, we set $\tau = \sigma = 0.9/\|\boldsymbol{L}\|_2$ with $\|\boldsymbol{L}\|_2$ defined in

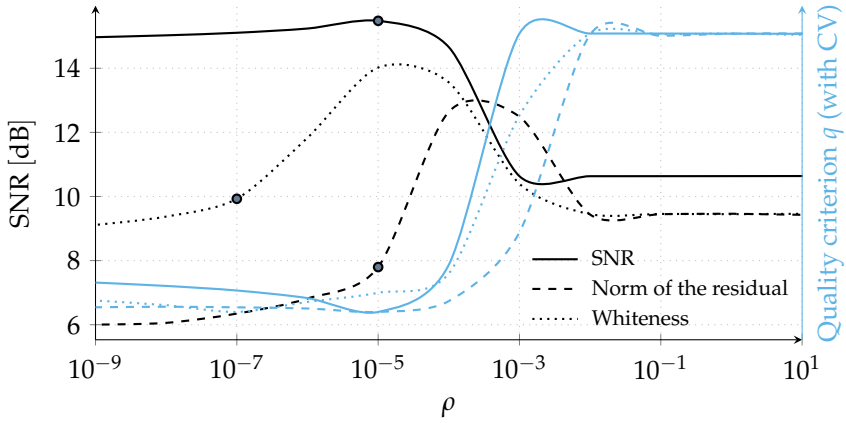

Figure 4.2 Left: mean SNR (over 10 trials) of a deconvolved image (with ℓ_1-norm as data fidelity term) of XCAT phantom as a function of ρ for three quality criteria q: SNR (solid black line), whiteness (dashed black line) and squared ℓ_2-norm of the residual (dotted black line). Quality function q is used both as stopping criterion for CP algorithm and as selection criterion for parameter ρ. Right: mean value of the criteria (over 10 trials) as a function of ρ. Blue lines correspond to the aforementioned criteria. Even with cross validation, neither the whiteness or the squared ℓ_2-norm of the residual succeeds to efficiently stop the internal iterations of CP algorithm (height of the dashed and dotted black curves with respect to the SNR one). Moreover, they also fail to find the value of ρ maximizing the SNR. The chosen value—corresponding to a minimal value of the criterion—is indicated by a filled circle. Projections were simulated with dPETSTEP for $t_{\text{acq}} = 5\,\text{s}$ and reconstructed with FBP.

p. 27. The maximum number of internal iterations `maxIter` of the CP algorithm is equal to 5000. However, if the quality q of the estimate is strictly monotonously decreasing during $q_{\text{it}} = 200$ iterations, internal iterations stop and the estimate with the best quality is selected.

As mentioned earlier in this chapter, the noise statistics is unknown and likely not white. For this reason, the criteria presented in subsection 2.3.2 in combination with CV fail to (*i*) provide an efficient stopping criterion for CP algorithm and (*ii*) select an appropriate value for parameter ρ (see Figure 4.2). Until we find a better criterion, we use the SNR as quality criterion q in the simulations. The initialization of the estimate is a null vector of size N. For $k > 1$, the initial guess of the algorithm is given by the previous es-

timate $\hat{f}_{\rho^{(k-1)}}$. Since we have no idea about the order of magnitude of ρ, we first run Algorithm 5 for 20 iterations on ρ with $\rho^{(1)} = 10^{10}$ and $\beta = 0.1$. The iteration providing the best estimate according to the SNR criterion is denoted $k^\star$. We run again Algorithm 5 with $\rho^{(1)}_{\text{new}} = \rho^{(k^\star-1)}$, $\beta_{\text{new}} = 0.8$ and a number of iterations `maxIterRho` equal to $\lceil \log(\beta^2)/\log\beta_{\text{new}} \rceil$ such that the last value of ρ_{new} is close to $\rho^{(k^\star+1)}$.

For the real experiments, internal iterations of CP algorithm stop when the relative error between two consecutive estimates goes beyond a user-defined threshold `Th`. In the experiments of this chapter, we set the threshold to 10^{-4}. We select the best regularization parameter by visual inspection. This lack for an efficient criterion is discussed in Chapter 9.

4.5 Experiments

In this section, we compare the proposed algorithm for different data fidelity terms (Huber function, ℓ_1, ℓ_2 and KL as described in section 4.3). We test different values for δ, the parameter of the Huber function (see Definition 4.6). We show that the Huber function with an appropriate choice for δ gives the best results in terms of SNR, no matter the reconstruction algorithm (FBP or OSEM). Data consist of simulated PET images of the XCAT phantom as well as experimental images collected from patients.

In both cases—simulated and experimental data—we compare the results of the proposed approach to a standard deblurring algorithm, the Lucy-Richardson (LR) deconvolution algorithm. This iterative deblurring technique was proposed independently by Leon Lucy and William Richardson [125] in the early seventies. The main iteration of the original LR deconvolution algorithm is

$$\boldsymbol{u}^{(n+1)} = \boldsymbol{u}^{(n)} \odot \left(\frac{\boldsymbol{H}^* \boldsymbol{y}}{\max(\boldsymbol{H}\boldsymbol{u}^{(n)}, \varepsilon)} \right), \tag{4.18}$$

where $\odot$ denotes the elementwise multiplication and ε is a small positive scalar needed to avoid division by zero. The Matlab implementation of this algorithm slightly differs from (4.18) due to some pre-processing of the image and the addition of a non-negativity constraint. We use this implementation in our experiments for state-of-the-art comparison. Several authors proposed other modified versions of this algorithm which are able, *e.g.*, to incorporate prior information on the image, to include wavelet-based denoising or to deal with a blind deconvolution framework [26, 63, 118].

Algorithm 5: TGV denoising and deblurring of PET images

input : a noisy and blurry image $\boldsymbol{y}$
output: a restored image $\hat{\boldsymbol{f}}$

initialization: $\boldsymbol{z}^{(0)} = \bar{\boldsymbol{z}}^{(0)} = \boldsymbol{0}_{N\times 3}$, $\boldsymbol{p}^{(0)} = \boldsymbol{0}_N$, $\boldsymbol{q}^{(0)} = \boldsymbol{0}_{N\times 2}$, $\boldsymbol{r}^{(0)} = \boldsymbol{0}_{N\times 4}$, $\rho = \rho^{(1)}$;
for $k = 1$ **to** *maxIterRho* **do**
  $q_{\text{it}} = 0$;
  for $n = 1$ **to** *maxIter* **do**
    $\boldsymbol{p}^{(n)} = \text{prox}_{\sigma F_1^\star}(\boldsymbol{p}^{(n-1)} + \sigma \boldsymbol{L}_1 \bar{\boldsymbol{z}}^{(n-1)})$;
    $\boldsymbol{q}^{(n)} = \text{prox}_{\sigma F_2^\star}(\boldsymbol{q}^{(n-1)} + \sigma \boldsymbol{L}_2 \bar{\boldsymbol{z}}^{(n-1)})$;
    $\boldsymbol{r}^{(n)} = \text{prox}_{\sigma F_3^\star}(\boldsymbol{r}^{(n-1)} + \sigma \boldsymbol{L}_3 \bar{\boldsymbol{z}}^{(n-1)})$;
    $\boldsymbol{z}^{(n)} = \text{prox}_{\tau G}(\boldsymbol{z}^{(n)} - \frac{\tau}{3}(\boldsymbol{L}_1^* \boldsymbol{p}^{(n-1)} + \boldsymbol{L}_2^* \boldsymbol{q}^{(n-1)} + \boldsymbol{L}_3^* \boldsymbol{r}^{(n-1)})$;
    $\bar{\boldsymbol{z}}^{(n)} = 2\boldsymbol{z}^{(n)} - \boldsymbol{z}^{(n-1)}$;
    if $q(\boldsymbol{R}_u \boldsymbol{z}^{(n)}) > q(\boldsymbol{R}_u \boldsymbol{z}^{(n-1)})$ **then**
      $\hat{\boldsymbol{z}} = \boldsymbol{z}^{(n)}$;
      $q_{\text{it}} = 0$;
    else
      $q_{\text{it}} = q_{\text{it}} + 1$;
    end
    if $n =$ *maxIter* **or** $q_{\text{it}} > 200$ **then**
      $\hat{\boldsymbol{z}} = \boldsymbol{z}^{(n)}$;
      break;
    end
  end
  $\hat{\boldsymbol{f}}_{\rho^{(k)}} = \boldsymbol{R}_u \hat{\boldsymbol{z}}$;
  if $k \neq$ *maxIterRho* **then**
    $\rho^{(k+1)} = \beta \rho^{(k)}$;
    $\boldsymbol{z}^{(0)} = \hat{\boldsymbol{z}}$;
  end
end
choose $k^\star$ such that $q(\hat{\boldsymbol{f}}_{\rho^{(k^\star)}}) \geq q(\hat{\boldsymbol{f}}_{\rho^{(k)}})$ for all k;
$\hat{\boldsymbol{f}} = \hat{\boldsymbol{f}}_{\rho^{(k^\star)}}$;

4.5.1 Synthetic data

Synthetic data is essential as a first step to validate the proposed approach and to quantitatively compare the different formulations. In this work, we use the second version of the 4D extended cardiac-torso (XCAT) phantom developed by Paul Segars and his team at Duke University Medical Center [131][4]. XCAT phantom includes thousands of highly detailed anatomical structures. Each of them is modeled by nonuniform rational B-spline (NURBS) and can be scaled or parameterized according to the user preferences. This phantom, designed for multimodality imaging, is very promising for research (including clinical research). Indeed, we can simulate a highly heterogeneous population of healthy people or of people with abnormalities like lesions or tumors.

In this work, we use the default XCAT female adult without heart or respiratory motion. The size of the whole body phantom is $350 \times 350 \times 850$ voxels with a voxel size equal to $0.2\,\text{mm} \times 0.2\,\text{mm} \times 0.2\,\text{mm}$. We generate two 3D maps (see Figure 4.3): (*i*) the attenuation map (CT scan) for an energy equal to 511 keV and (*ii*) the activity map. For the activity map, we set values for normal organs that are of the order of the SUV available in the literature [87, 122, 164]. Our aim is to simulate a plausible PET image and not to perfectly mimic a true ^{18}F-FDG distribution.

Prior to the simulations, we extract transaxial slices from attenuation and activity maps of the XCAT phantom. Then, we simulate 350×350 PET slices with dPETSTEP software with the parameters listed in Table 4.1. They correspond to the GE Discovery 690 PET/CT scanner described in [19]. The software simulate 10 different acquisition durations, *i.e.*, 10 levels of noise, from 1 to 10,000 s and take into account the radiotracer decay (6600 s for ^{18}F-FDG). Images are reconstructed without PSF correction either with FBP or iteratively with OSEM (20 iterations and 24 subsets). For algorithmic purposes, observations $\boldsymbol{y}$ (reconstructed images) are normalized by their ℓ_1-norm directly related to the total activity injected in the phantom.

To estimate the 2D blurring kernel, we run dPETSTEP for an isolated radioactive source located at the center of the FOV. We set the acquisition time to 10^6 s to assume a noiseless acquisition. We apply (4.18) and Algorithm 5 to the normalized simulated images using the estimated kernel. The quality of deconvolved images $\hat{\boldsymbol{f}}$ is quantified with the signal-to-noise ratio (SNR) (see Definition 2.21).

[4] I am grateful to Prof. Segars for giving me free access to this amazing phantom.

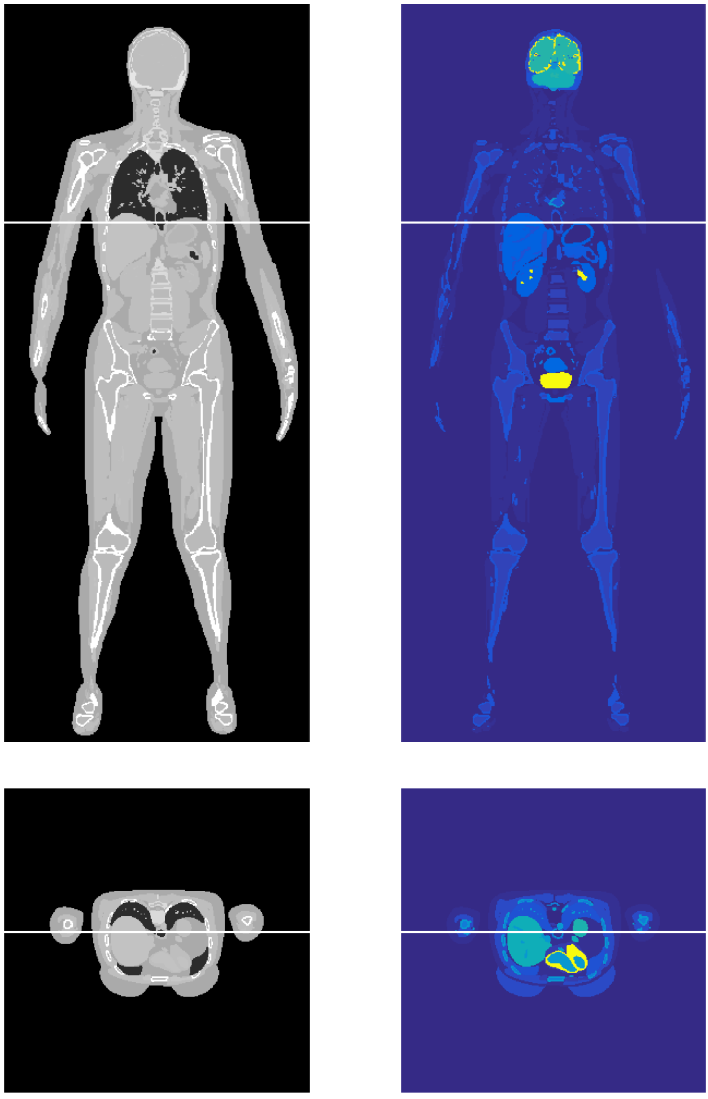

Figure 4.3 Coronal (above) and transaxial (below) slices of the XCAT average female phantom [131]: attenuation map (left) and activity map (right). The location of the transaxial (resp. coronal) slice is indicated by a white line on the coronal (resp. transaxial) slice. Coronal and transaxial slices of the activity map do not share the same intensity scale.

Table 4.1 Parameters used for simulations with dPETSTEP software.

FOV diameter	700 mm
Gantry diameter	810 mm
# Radial bins	381
# Angular bins	288
2D system PSF (FWHM)	4.9 mm
System sensitivity	33.4 cps/kBq
Total activity	10.63 MBq
Scatter fraction	0.37
Random fraction	0.07

Results

The results of the simulations are visible on Figures 4.4 to 4.7 for PET images reconstructed with both FBP and OSEM algorithms. In both cases, we observe that the Huber function (see Figures 4.4 and 4.6) provides good restoration results when its parameter δ is smaller or equal to 10^0 with a maximum for $\delta = 10^{-2}$. When $\delta \to 0$, the behavior of the corresponding curves tends to the one of the ℓ_1-norm (see Figures 4.5 and 4.7), as expected from the definition of the Huber function (see Definition 4.6). The poor quality of images deconvolved with a large parameter may be explained by the fact that the Huber function gets flatter as δ increases: the errors are less penalized and, in the limit, are not penalized at all. With FBP, such images seem blurred while with OSEM, they look rather noisy.

For FBP, the results obtained with the other data fidelity terms are of similar quality (see Figure 4.5). The ℓ_1-norm outperforms the other ones and reaches the best SNR achieved by the Huber function. Visually, the textures of the organs in the image estimated using the ℓ_1-norm seem smoother than those obtained with the squared ℓ_2-norm or the LR algorithm (which only assumes non-negativity). For an acquisition time equal to 1 s, none of those methods manage to recover the tiny structures present in Figure 4.3. KL divergence gives satisfactory results but the restoration is around four times slower compared to the ones based on the other data fidelity terms.

In the case of iterative OSEM algorithm, the best data fidelity term in Figure 4.7 is the squared ℓ_2-norm. Like the ℓ_1-norm for FBP, it also reaches the maximum SNR achieved by the Huber function with $\delta \in \{10^{-2}, 10^0\}$. We observe less artifacts in the flat regions of the images estimated with the squared ℓ_2-norm and the Huber function ($\delta = 10^0$) than in the images

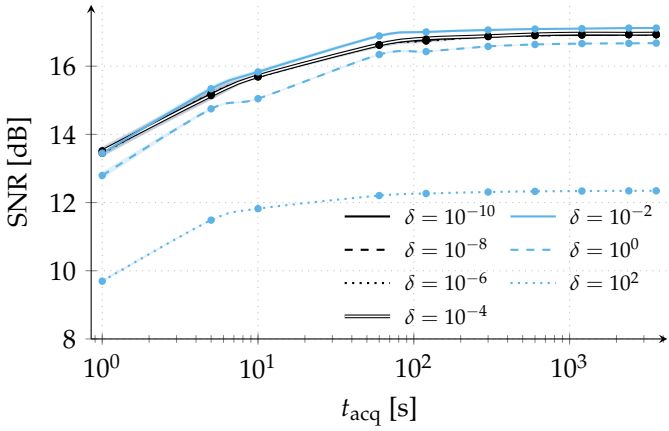

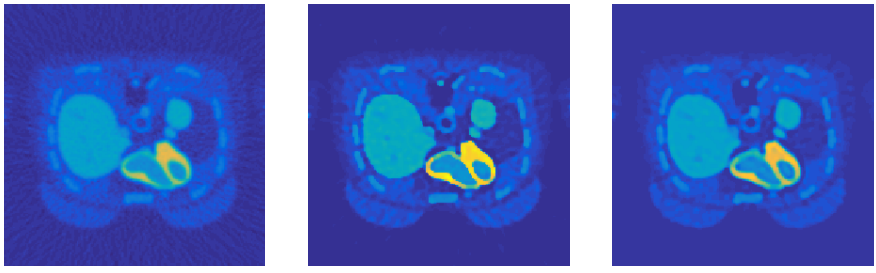

Observations y | Huber ($\delta = 10^{-2}$) | Huber ($\delta = 10^{2}$)

Figure 4.4 Synthetic data (FBP): Huber function. Above: mean SNR (over 10 trials) of the deconvolved XCAT phantom *versus* the acquisition time. The fidelity term is the Huber function, considered for different parameters δ from $\delta = 10^{-10}$ to $\delta = 10^{2}$. The (very thin) light areas around the curves represent the standard deviation. The observations were generated with dPETSTEP software and FBP reconstruction. The simulation parameters are described in section 4.5 and Table 4.1. Below: zoom on the ground truth, the observations and the estimate of f_0 obtained for $t_{\text{acq}} = 1\,\text{s}$ and $\delta \in \{10^{-2}, 10^{2}\}$. The images share the same intensity scale as the ones of Figure 4.5.

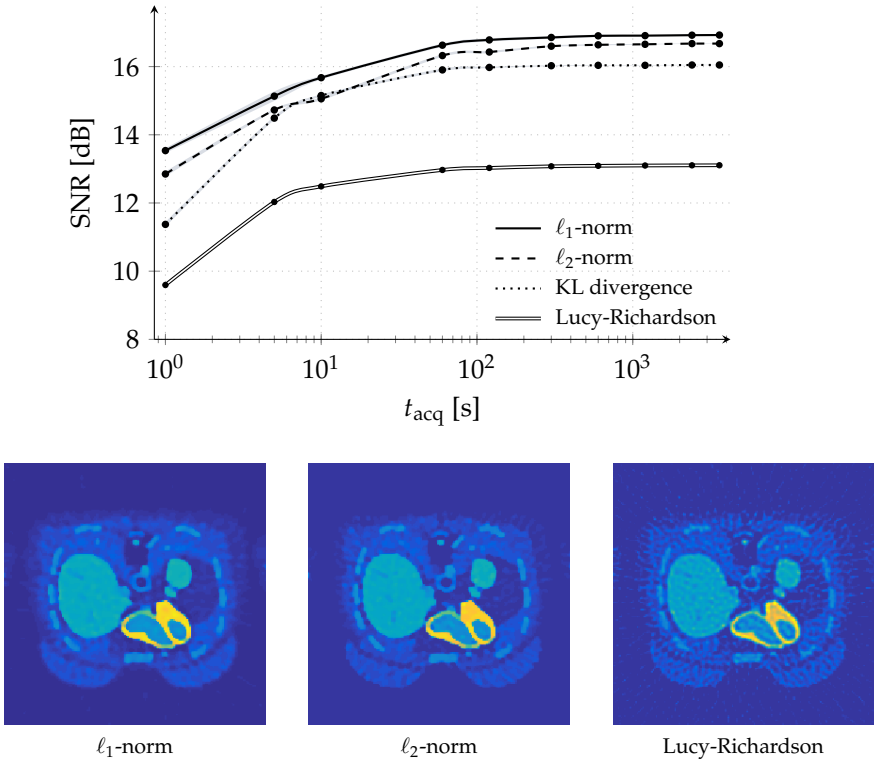

Figure 4.5 Synthetic data (FBP): comparison of fidelity terms. Above: mean SNR (over 10 trials) of the deconvolved XCAT phantom *versus* the acquisition time. Three different data fidelity terms (ℓ_1-norm, squared ℓ_2-norm and KL divergence) were considered for comparison along with the LR algorithm (4.18). The (very thin) light areas around the curves represent the standard deviation. The observations were generated with dPETSTEP software and FBP reconstruction. The simulation parameters are described in section 4.5 and Table 4.1. Below: zoom on estimates of f_0 obtained for $t_{\text{acq}} = 1\,\text{s}$. The images share the same intensity scale as the ones of Figure 4.4.

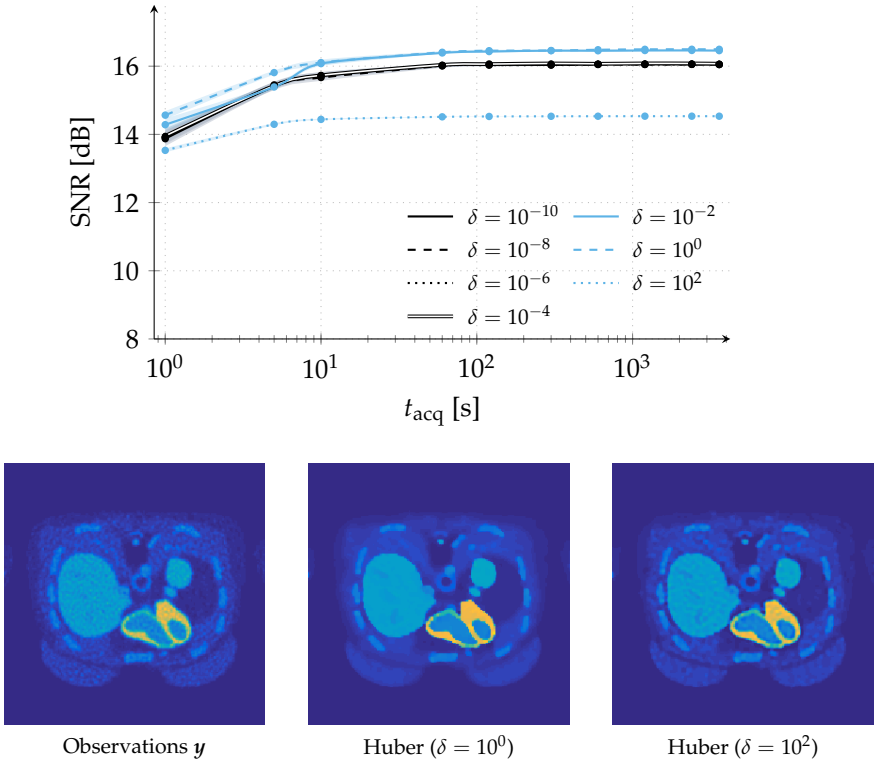

Figure 4.6 **Synthetic data (OSEM): Huber function.** Above: mean SNR (over 10 trials) of the deconvolved XCAT phantom *versus* the acquisition time. The fidelity term is the Huber function, considered for different parameters δ from $\delta = 10^{-10}$ to $\delta = 10^2$. The (very thin) light areas around the curves represent the standard deviation. The observations were generated with dPETSTEP software and OSEM reconstruction. The simulation parameters are described in section 4.5 and Table 4.1. Below: zoom on the observations and the estimates of f_0 obtained for $t_{\text{acq}} = 1\,\text{s}$ and $\delta \in \{10^0, 10^2\}$. The images share the same intensity scale as the ones of Figure 4.7.

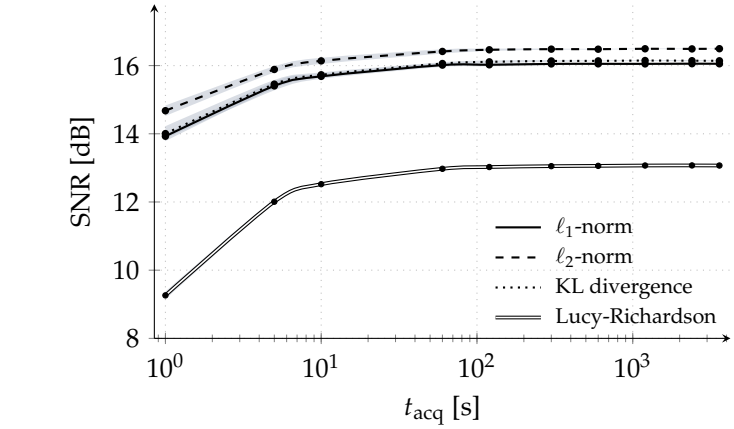

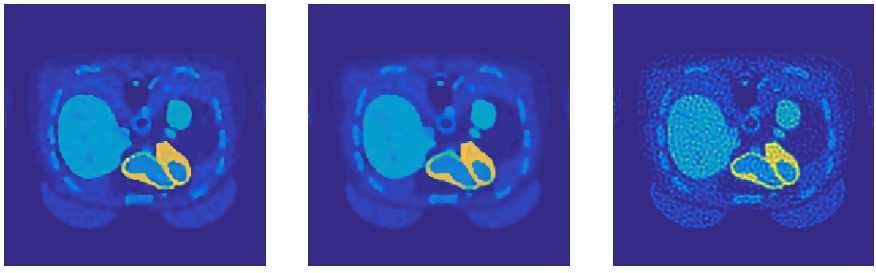

ℓ_1-norm ℓ_2-norm Lucy-Richardson

Figure 4.7 Synthetic data (OSEM): comparison of fidelity terms. Above: mean SNR (over 10 trials) of the deconvolved XCAT phantom *versus* the acquisition time. Three different data fidelity terms (ℓ_1-norm, squared ℓ_2-norm and KL divergence) were considered for comparison along with the LR algorithm (4.18). The (very thin) light areas around the curves represent the standard deviation. The observations were generated with dPET-STEP software and OSEM reconstruction. The simulation parameters are described in section 4.5 and Table 4.1. Below: estimates of f_0 obtained for $t_{\text{acq}} = 1\,\text{s}$. The images share the same intensity scale as the ones of Figure 4.6.

obtained with a ℓ_1-norm data fidelity term of with LR algorithm.

In both cases, linear and iterative algorithms, solving (4.13) with the Huber function gives the best results. However, it requires to properly tune the parameter δ. If such a search is not possible, the ℓ_1-norm and the squared ℓ_2-norm are proper substitutes. Further research could investigate if such a behavior, *i.e.*, a ℓ_1-norm for linear reconstruction algorithms and a squared ℓ_2-norm for iterative algorithms, generalizes.

We observe on the images sharp edges with smooth areas. Unfortunately, the XCAT phantom has uniform activity in all the anatomical structures. Consequently, we cannot measure the ability of the TGV regularization to restore tissue texture compared to a classical TV regularization. The introduction of tissue heterogeneity in the XCAT phantom is under work [23] and could be exploited in a future work.

4.5.2 Experimental data

We tested the deconvolution methods described in this chapter on a dataset of real PET images of patients with pharyngolaryngeal squamous cell carcinoma. The reader will find detailed explanations about the experimental setup and the acquisition parameters in [45]. Patients were injected with 185-370 MBq of ^{18}F-FDG and imaged 50 minutes post-injection for 20 minutes on a Siemens ECAT EXACT HR$^+$ scanner (Siemens/CTI, Knoxville, TN). After sinogram correction, images were reconstructed with the FBP algorithm. The size of the reconstructed volume is $128 \times 128 \times 47$ and the voxel size is $2.2\,\text{mm} \times 2.2\,\text{mm} \times 3.12\,\text{mm}$. The PSF was measured experimentally with a line source perpendicular to the axial slices in a diffusing material (water). In first approximation, the PSF at 100 mm from the center of the FOV was Gaussian and isotropic with 6 mm of FWHM.

Equation (4.18) and Algorithm 5 were used to deblur 128×128 transaxial slices of the PET volumes, normalized like described in subsection 4.5.1. We used a 2D isotropic Gaussian kernel with FWHM equal to 6 mm as PSF for the deblurring algorithm. Unlike described in Algorithm 5, we select the value of the regularization parameter by visual inspection. Since there is no original image available, main results consist of a visual comparison between the images deconvolved with the different data fidelity terms.

Results

Figure 4.8 shows the results of the patient slice deconvolution. As expected from the simulations, the image deblurred with LR has a poor quality and a lot of artifacts. The estimates obtained with the Huber function and the

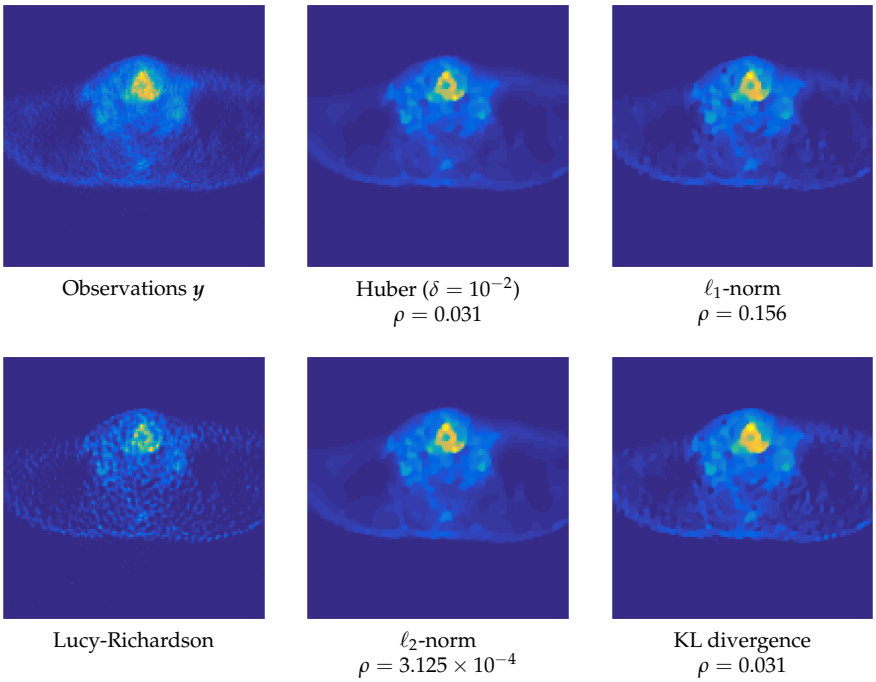

Figure 4.8 Estimates of a patient slice (A13). Patient slice was deconvolved from observations y with either (4.18) (LR) or Algorithm 5 with different data fidelity terms (Huber function, ℓ_1-norm, squared ℓ_2-norm and KL divergence). The estimates obtained with Algorithm 5 share the same intensity scale. Image owner: UCLouvain, Center of Molecular Imaging, Radiotherapy, and Oncology (MIRO) [45].

ℓ_2-norm are similar. Their background are smoother than the ones of KL divergence or ℓ_1-norm. Among the four data fidelity terms, KL divergence seems to give the worst estimate: in addition to the "noisy" body background, the tumor edges seem less sharp compared to the other images.

Appendix 4.A Relationship between K_2 and K_3

This appendix details the relationship between K_2 and K_3 constants in Proposition 4.1, namely $K_2 = 2C_3K_3$. The proof is based on [157, p. 32].

Proof. Let X be a random variable. We assume that $\mathbb{E}e^{|X|/K_3} \leq C_3$, with $C_3 > 1$. We will derive a bound on the moments of X. First, we show that $\forall x \in \mathbb{R}$,

$$|x| \leq e^x + e^{-x}.$$

Indeed, from Taylor series of the exponential function, the following inequalities hold

$$x \leq e^x - 1 \leq e^x, \quad x \geq 0 \qquad \text{and} \qquad -x \leq e^{-x} - 1 \leq e^{-x}, \quad x < 0.$$

Since $e^{-x} > 0$ (resp. $e^x > 0$) for all $x \in \mathbb{R}$, we add this term on the right-hand side of the inequality for $x \geq 0$ (resp. $x < 0$).

$$x \leq e^x + e^{-x}, \quad x \geq 0 \qquad \text{and} \qquad -x \leq e^{-x} + e^x, \quad x < 0.$$

Combining those inequalities, we get $|x| \leq e^x + e^{-x}$. Let $p > 0$. Hence,

$$\frac{|x|}{p} \leq e^{x/p} + e^{-x/p} \leq \left(e^x + e^{-x}\right)^{1/p},$$

where the last inequality holds again because e^x and e^{-x} take only positive values. Rearranging the inequality leads to

$$|x| \leq p\left(e^x + e^{-x}\right)^{1/p}. \tag{4.19}$$

Now, we replace x in (4.19) by random variable X and we express the expectation of $|X|^p$,

$$\mathbb{E}|X|^p \leq p^p(\mathbb{E}e^X + \mathbb{E}e^{-X}).$$

Similarly, by a simple change of variable,

$$\mathbb{E}|X|^p \leq (pK_3)^p(\mathbb{E}e^{X/K_3} + \mathbb{E}e^{-X/K_3}).$$

Since $\mathbb{E}e^{|X|/K_3} \leq C_3$ with $C_3 > 1$, we finally find

$$(\mathbb{E}|X|^p)^{1/p} \leq pK_3(2C_3)^{1/p} \leq p(2C_3K_3), \qquad \forall p > 0. \tag{4.20}$$

■

Appendix 4.B Proximal operator of the convex conjugate of the Huber function

Function F_1 in (4.15) is a shifted Huber function with parameter δ,

$$F_1(\boldsymbol{u}) = h_\delta(\boldsymbol{u}-\boldsymbol{y}) = \left(\|\cdot\|_1 \square \frac{1}{2\delta}\|\cdot\|_2^2\right)(\boldsymbol{u}-\boldsymbol{y}).$$

In this appendix, we derive the proximal operator of the convex conjugate of F_1 given by $\operatorname{prox}_{\sigma F_1^\star}(\tilde{\boldsymbol{p}}) = \mathcal{P}_{\mathcal{B}_\infty}\left(\frac{\tilde{\boldsymbol{p}}-\sigma\boldsymbol{y}}{1+\sigma\delta}\right)$.

Proof. First, we compute the convex conjugate of h_δ,

$$\begin{aligned} h_\delta^\star(\boldsymbol{p}) &= \left(\|\cdot\|_1 \square \frac{1}{2\delta}\|\cdot\|_2^2\right)^\star(\boldsymbol{p}) \quad \textit{(infimal convolution is dual to addition)} \\ &= \iota_{\mathcal{B}_\infty}(\boldsymbol{p}) + \frac{\delta}{2}\|\boldsymbol{p}\|_2^2, \end{aligned} \tag{4.21}$$

since the dual function of a norm is the indicator function of dual norm unit ball $\mathcal{B}$ (here, the ℓ_∞-norm). The second term is obtained knowing that $(\frac{1}{2}\|\boldsymbol{p}\|_2^2)^\star = \|\frac{1}{2}\boldsymbol{p}\|_2^2$ and applying Property 2.20 [27]. Using again Property 2.20, the convex conjugate of F_1 is given by

$$F_1^\star(\boldsymbol{p}) = h_\delta^\star(\boldsymbol{p}) + \boldsymbol{y}^\top\boldsymbol{p}.$$

The proximal operator of $F_1^\star$ is

$$\begin{aligned} \operatorname{prox}_{\sigma F_1^\star}(\tilde{\boldsymbol{p}}) &= \operatorname*{arg\,min}_{\boldsymbol{p}} \frac{1}{2}\|\tilde{\boldsymbol{p}}-\boldsymbol{p}\|_2^2 + \iota_{\mathcal{B}_\infty}(\boldsymbol{p}) + \frac{\sigma\delta}{2}\|\boldsymbol{p}\|_2^2 + \sigma\boldsymbol{y}^\top\boldsymbol{p} \\ &= \operatorname*{arg\,min}_{\boldsymbol{p}\in\mathcal{B}_\infty} \|\tilde{\boldsymbol{p}}-\boldsymbol{p}\|_2^2 + \sigma\delta\|\boldsymbol{p}\|_2^2 + 2\sigma\boldsymbol{y}^\top\boldsymbol{p} \\ &= \operatorname*{arg\,min}_{\boldsymbol{p}\in\mathcal{B}_\infty} (1+\sigma\delta)\|\boldsymbol{p}\|_2^2 + 2(\sigma\boldsymbol{y}-\tilde{\boldsymbol{p}})^\top\boldsymbol{p} + r_1(\tilde{\boldsymbol{p}},\boldsymbol{y}) \\ &= \operatorname*{arg\,min}_{\boldsymbol{p}\in\mathcal{B}_\infty} \|\sqrt{1+\sigma\delta}\boldsymbol{p} + \frac{\sigma\boldsymbol{y}-\tilde{\boldsymbol{p}}}{\sqrt{1+\sigma\delta}}\|_2^2 + r_2(\tilde{\boldsymbol{p}},\boldsymbol{y}), \end{aligned}$$

where r_1 and r_2 are functions that do not depend on the optimization variable $\boldsymbol{p}$. Since ℓ_2-norms are convex, we can first find $\boldsymbol{p}$ minimizing this quantity and then, project it onto the convex set $\mathcal{B}_\infty$. Hence,

$$\operatorname{prox}_{\sigma F_1^\star}(\tilde{\boldsymbol{p}}) = \mathcal{P}_{\mathcal{B}_\infty}\left(\frac{\tilde{\boldsymbol{p}}-\sigma\boldsymbol{y}}{1+\sigma\delta}\right). \qquad \blacksquare$$

5

Blind deconvolution of PET images using anatomical prior

The design of PET scanners can vary greatly between manufacturers and models and so do their imaging properties like, for instance, the point spread function (PSF). Measuring the PSF of a scanner with an isolated radioactive source requires a specific setup as well as the access to the scanner. In post-reconstruction restoration methods, the blurring function is often approximated by a spatially invariant Gaussian PSF characterized by a full width at half maximum (FWHM) given in the spec sheet of the device. Restoration of images acquired in the context of a multicentric study (with centralization of the reconstructed data) is then challenging: the raw data are not always accessible and the PSF cannot be directly measured. This context motivates the development of blind deconvolution (BD) techniques to jointly estimate the PSF and the PET image.

In this chapter, we propose a general BD technique that restores a low resolution blurry image using information from data acquired with another, high resolution, imaging modality. For instance, in a situation requiring whole body imaging, the bladder provides the method with an uniform radiotracer activity region, delineated based on high resolution images. We validate the proposed method on synthetic and actual phantoms. The results show the relevance of the BD approach, particularly useful when the device and/or the raw data are not accessible.

Context

In 1975, Stockham *et al.* employed the term *blind deconvolution* for the first time to characterize the task of estimating both the image and the blurring kernel from corrupted observations [144]. We encounter BD problem in many applications such as speech signal processing [144], estimation of complex blurred images [46], astronomy [70], medical imaging [101, 103], etc. *Blind* can also qualify other restoration or reconstruction techniques where several signals are unknown, *e.g.*, blind source separation [39, 150], blind reconstruction of PET images [98] or blind fluorescence imaging [20].

The BD problem is severly ill-posed since in general, only a few information on the observed image and on the imaging system is available [94]. Some authors use simple inverse filtering [15] to solve this problem. But most of the time, an iterative algorithm is used for the deconvolution: it alternates between the image and filter estimations. However, even if they provide satisfactory results, those algorithms lack of guarantees of convergence, stability, robustness to noise, etc. [15].

Stockham *et al.* point out the importance of including "distinguishing characteristics" of both signals in the deconvolution method but to keep them as simple as possible to address to a broad class of applications. Prior knowledge on the image can be as simple as non-negativity or known support [46, 63] but can also concern the image structure, *e.g.*, sparsity in some wavelet basis or sparse edges [4, 5, 70]. Some work consider weak assumptions on the blurring operator such as a small support or non-negativity [4, 144] while others assume a parametric PSF to reduce the number of unknowns to estimate [94, 101, 103]. This last approach considerably reduces the search space but is sensitive to errors in the PSF model [7].

Anatomical information can be useful to regularize such an ill-posed problem. For instance, Sroubek *et al.* developed a "structural TV" prior built from the anatomical images to regularize the (non-blind) reconstruction of PET images [141]. Due to its perfect dilution in the kidneys, ^{18}F-FDG uniformly accumulates in the patient bladder with high concentration (see Figure 5.1) [16]. This organ can be accurately delineated by physicists or by segmentation algorithms based on high resolution structural images. This provides a strong prior information that can be used to regularize the BD problem: inside this region, the intensity of the restored image must be constant (*i.e.*, the gradient is zero). González *et al.* used a similar prior for BD of astronomical images with a celestial transit [70]. Indeed, when a celestial body of known diameter moves in front of the sun, its extreme

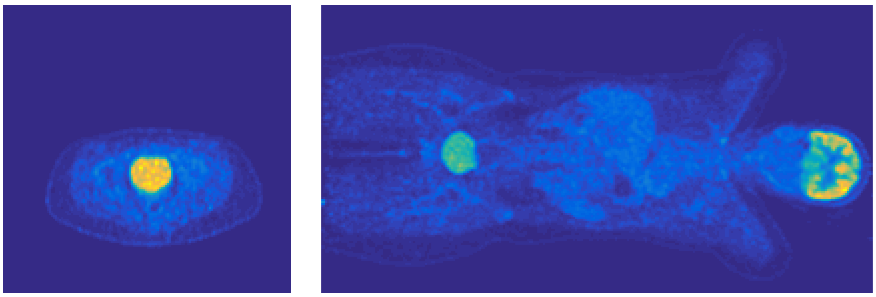

Figure 5.1 (a) Transaxial and (b) coronal PET images of a patient. Activity in the bladder is high and uniform. Source: Cliniques universitaires St-Luc.

ultraviolet emission is zero. In their work, the PSF is directly inferred from the observations without assuming a parametric model.

Contributions and outline

Following [70], we propose a BD framework to jointly estimate the PSF and the PET image using anatomical information provided by another imaging modality, *e.g.*, a transmission scan obtained by computed tomography (CT) [77]. We assume that the radiotracer concentration is uniform in some regions in the body, *e.g.*, in the bladder. Our method does not assume any parametric model for the blurring kernel and only relies on weak assumptions such as spatial invariance or non-negativity. The proposed BD method is general and can be applied to any restoration problem where a region of uniform intensity is known.

Like in Chapter 4, we start by describing the discrete model relating the observations to the object of interest, in this case the radiotracer activity map. We mention some properties of both the activity map and the blurring kernel. Then, in section 5.2, we formulate the biconvex optimization problem and we detail the constraints encoding the prior information on the image and the kernel, including the knowledge provided by the CT images. Like in [70], we solve this problem by using the alternating minimization algorithm presented in section 5.3. Each subproblem is solved independently with proximal algorithms. Finally, in section 5.4, we present the experiments conducted on both synthetic and experimental data.

5.1 Discrete forward model

In this chapter, we keep the same notations as in Chapters 3 and 4. Moreover, our next developments rely on the discrete forward model proposed in section 4.1, *i.e.*,

$$\boldsymbol{y} \approx \boldsymbol{H}\boldsymbol{f}_0, \tag{5.1}$$

where observations $\boldsymbol{y}$ reconstructed from the projections are corrupted by a noise with unknown distribution. If the reconstruction algorithm is linear, we showed in section 4.2 that the noise distribution is characterized by a double tail—Gaussian and sub-exponential. Unlike in Chapter 4, we now assume that the blurring operator $\boldsymbol{H}$ is *unknown*. We only consider weak assumptions on this operator, namely that $\boldsymbol{H}$ (*i*) preserves the photon counts, (*ii*) is non-negative, (*iii*) is linear and (*iv*) is spatially invariant over the whole field of view (FOV). This last feature allows us to write (5.1) as the discrete convolution product between a kernel $\boldsymbol{h} \in \mathbb{R}^N$, considered as the scanner PSF, and $\boldsymbol{f}_0$,

$$\boldsymbol{y} \approx \boldsymbol{h} * \boldsymbol{f}_0, \tag{5.2}$$

Like in Chapter 4, the physics of the imaging modality suggests to include several additional constraints on $\boldsymbol{f}_0$ and $\boldsymbol{h}$ in (5.2). First, the PET image represents the distribution of a non-negative radiotracer activity in the patient body, *i.e.*,

$$\boldsymbol{f}_0 \succeq \boldsymbol{0}.$$

Moreover, activity $\boldsymbol{f}_0$ is observed through a counting process. Observations $\boldsymbol{y}$ are consequently also non-negative.

Secondly, by definition, the PSF is the impulse response of the device, *i.e.*, the observation of a point source. It follows that

$$\boldsymbol{h} \succeq \boldsymbol{0}. \tag{5.3}$$

Finally, the last two constraints come from the property of photometry invariance mentioned in section 4.1. The original image satisfies $\sum_{i=1}^{N} (\boldsymbol{f}_0)_i = \sum_{i=1}^{N} y_i$. We also enforce this flux preservation by constraining the PSF to verify $\boldsymbol{1}_N^\top \boldsymbol{h} = 1$ that is equivalent to an unitary ℓ_1-norm since $\boldsymbol{h}$ is non-negative. We express the combination of this last constraint and (5.3) by forcing $\boldsymbol{h}$ to belong to the *probability simplex* ($\mathcal{PS}$) convex set [111],

$$\mathcal{PS} = \{\boldsymbol{u} \in \mathbb{R}^N | \boldsymbol{u} \succeq \boldsymbol{0}, \boldsymbol{1}_N^\top \boldsymbol{u} = 1\}. \tag{5.4}$$

5.2 Inverse problem formulation

We aim at finding the best estimators $\hat{f}$ and $\hat{h}$ of the original image f_0 and the original filter h using observations y and the knowledge of the forward model given by (5.2). This inverse problem can be expressed as a minimization problem with two optimization variables, u and v,

$$\underset{u,v\in\mathbb{R}^N}{\text{minimize}} \quad \frac{1}{2}\|v * u - y\|_2^2, \tag{5.5}$$

where we consider the squared ℓ_2-norm as the data fidelity term. This choice is motivated by (*i*) the results of subsection 4.5.1, especially when iterative algorithms are used to reconstruct PET images, and (*ii*) the need for a $\mathcal{C}^1$ function. This last requirement is one of the conditions ensuring that the alternating algorithm (presented in the following subsection 5.3.1) converges to a critical point of the objective function (5.8) [14]. The Huber function would be more polyvalent regarding the reconstruction algorithm but its performance strongly depends on the choice of its parameter δ, not studied in this blind context.

This naive minimization of a distance function leads to an ill-posed as explained in section 2.1. Solving such a deconvolution problem is known to amplify some high frequencies, which typically causes Gibbs ringing artifacts to appear. When we work in a blind context, ill-posedness is also related to the fact that we cannot distinguish $\hat{f}$ from $\hat{h}$[1] or that we could obtain the trivial solution, *i.e.*, $\hat{f} = y$ and $\hat{h}$ is the Kronecker delta.

Like in Chapter 4, we address this issue by regularizing the problem, *i.e.*, by adding extra information on the objects to estimate (see section 2.1). The following two sections describe the prior information that we consider (or not) for both the image and the filter.

5.2.1 Priors on the radiotracer density map

In addition to the non-negativity constraint inherent to the photon emission process, we add two extra information on f_0.

Structure. The first prior concerns the intrinsic structure of natural images. The choice of an appropriate basis (*e.g.*, Fourier, wavelets, curvelets,

[1] Since the convolution product is commutative.

etc.) to represent the image leads to interesting properties such as sparsity (see subsection 2.2.1). In this work and like in Chapter 4, we assume that the TGV^2_{α}-norm of the original image is small, *i.e.*, the image is well represented by piecewise linear areas.

Region with uniform intensity. As mentioned in the introduction, one of the contributions of this chapter is to use anatomical information contained in a CT scan as extra knowledge to solve the inverse problem. In the case of real clinical images, the radiotracer activity in some organs, *e.g.*, the bladder, is uniform. The background activity, assumed to be zero, can also be seen as an area with constant activity. Nuclear physicists can accurately delineate such areas based on high resolution CT images. Mathematically, let Ω_c be the set of pixels where the radioactivity is constant. The image gradient must, in this case, belong to the set $\mathcal{Q}_{\Omega_c}$ of signals with zero intensity in Ω_c, *i.e.*, $\mathcal{Q}_{\Omega_c} := \{\boldsymbol{u} \in \mathbb{R}^{N\times 2} | \boldsymbol{u}_i = \boldsymbol{0}, \forall i \in \Omega_c\}$ where $\boldsymbol{u}_i \in \mathbb{R}^2$ is the i^{th} row of $\boldsymbol{u}_i$. In PET images, Ω_c contains the pixels that represent the patient's bladder or the background.

5.2.2 Priors on the blurring kernel

As explained in the introduction, we would like to be as naive as possible about the shape of the PSF such that the method can be applied to any PET scanner (even to other imaging modalities). To this end, we do not use a parametric model for $\boldsymbol{h}$: we just formulate the weak and nonspecific constraint expressed by (5.4).

Another weak prior—not considered in this work—is the limited support of the PSF compared to the size of the FOV [4, 70]. In [4], the authors only consider this prior to be as agnostic as possible about $\boldsymbol{h}$. We could also consider stronger assumptions on the structure of the PSF, *e.g.*, a sparse representation in some wavelet (redundant) basis or a decay along one or several directions (or more generally, the respect of some ordering between the pixels [78]). The assumption of a radial decay is quite general to the family of blurring operators, as defined by Escande *et al.* [57].

5.2.3 Formulation of the blind deconvolution inverse problem

Now, we add the constraints and the priors described in section 5.1 and subsections 5.2.1 and 5.2.2 into (5.5). The formulation of the BD inverse prob-

lem writes

$$\begin{aligned} \underset{\boldsymbol{u},\boldsymbol{v}\in\mathbb{R}^N}{\text{minimize}} \quad & \frac{1}{2}\|\boldsymbol{v}*\boldsymbol{u}-\boldsymbol{y}\|_2^2+\rho\mathrm{TGV}_\alpha^2(\boldsymbol{u}), \\ \text{subject to} \quad & \boldsymbol{u}\succeq\mathbf{0},\ \sum_{i=1}^N u_i=\sum_{i=1}^N y_i,\ \ \boldsymbol{\nabla}\boldsymbol{u}\in\mathcal{Q}_{\Omega_c},\ \ \boldsymbol{v}\in\mathcal{PS}, \end{aligned} \tag{5.6}$$

where the positive regularization parameter ρ controls the trade-off between the data fidelity term and the regularization one.

5.2.4 Validation using non-blind deconvolution

Once the PSF has been estimated using the BD scheme (5.6), we would like to assess its quality. In the context of real acquisitions, we cannot compare the estimate to the (unknown) ground truth filter. However, we know that a "good" filter should be able to restore the uniform radioactivity in the bladder (or, similarly, uniform activity in the background). The validation framework is the following: (*i*) we deconvolve several images acquired with the same device using the estimate $\hat{\boldsymbol{h}}$ (in a non-blind framework), without enforcing uniform intensity in Ω_c, and (*ii*) we check if the region that corresponds to the bladder has a TV-norm close to zero. The non-blind deconvolution (NBD) formulation is

$$\begin{aligned} \underset{\boldsymbol{u}\in\mathbb{R}^N}{\text{minimize}} \quad & \frac{1}{2}\|\hat{\boldsymbol{h}}*\boldsymbol{u}-\boldsymbol{y}\|_2^2+\rho\mathrm{TGV}_\alpha^2(\boldsymbol{u}), \\ \text{subject to} \quad & \boldsymbol{u}\succeq\mathbf{0},\quad \sum_{i=1}^N u_i=\sum_{i=1}^N y_i. \end{aligned} \tag{5.7}$$

We highlight the fact that the NBD formulation must be solved for one or several blurred images $\boldsymbol{y}$ that have not been used in (5.6) for the PSF estimation. Minimization problem (5.7) is identical to (4.13) in Chapter 4.

5.3 Numerical implementation

In this section, we detail how we numerically solve the BD minimization (5.6). We refer the reader to section 4.4 for the solving of (5.7).

We first rewrite (5.6) as an unconstrained minimization problem,

$$(\hat{f}_{\mathrm{BD}}, \hat{h}) \in \operatorname*{arg\,min}_{u,v \in \mathbb{R}^N} \mathcal{M}(u,v) := \operatorname*{arg\,min}_{u,v \in \mathbb{R}^N} \frac{1}{2}\|v * u - y\|_2^2 + \rho \mathrm{TGV}_\alpha^2(u) + \iota_{\mathbb{R}_+^N}(u) + \iota_{\mathcal{Q}}(u) + \iota_{\mathcal{Q}_{\Omega_c}}(\nabla u) + \iota_{\mathcal{P}_S}(v), \quad (5.8)$$

where the indicator functions encode the constraints on u and v. The set $\mathcal{Q}$—related to the photometry invariance—is defined in section 4.4.

We cannot solve (5.8) using classical tools from convex optimization since the problem is non-convex with respect to both u and v. However, the problem is biconvex, *i.e.*, the objective function is convex over u when v is fixed and *vice versa*. Even without guarantee of convergence, such problems are often solved using algorithms alternating between two steps: (*i*) minimization over u for v fixed and (*ii*) minimization over v for u fixed.

5.3.1 Alternating minimization algorithm

The alternating minimization algorithm that we use to solve (5.8) has been proposed by Attouch *et al.* [14] and has already been used for BD in the context of astronomical imaging [70]. The algorithm is the following:

$$\begin{cases} \hat{f}_{\mathrm{BD}}^{(m)} := \operatorname*{arg\,min}_{u \in \mathbb{R}^N} \mathcal{M}(u, \hat{h}^{(m-1)}) + \frac{\varrho_u^{(m)}}{2}\|u - \hat{f}_{\mathrm{BD}}^{(m-1)}\|_2^2 \\ \hat{h}^{(m)} := \operatorname*{arg\,min}_{v \in \mathbb{R}^N} \mathcal{M}(\hat{f}_{\mathrm{BD}}^{(m)}, v) + \frac{\varrho_v^{(m)}}{2}\|v - \hat{h}^{(m-1)}\|_2^2, \end{cases} \quad (5.9)$$

where the ℓ_2-norms enforce the current estimates to stay close to the previous ones. Parameters $\varrho_u^{(m)}$ and $\varrho_v^{(m)}$ are non-negative scalars called *cost-to-move* parameters. Algorithm (5.9) does not guarantee the convergence to the global optimum of $\mathcal{M}$. However, if the objective function satisfies some mild conditions and if the sequences of the estimates are bounded, Theorem 9 in [13] provides a guarantee of convergence to a fixed point of $\mathcal{M}$. Based on Adriana's González's proof [69, Appendix 5.B], we know that $\mathcal{M}$ satisfies the conditions formulated in [13]. Moreover, the sequences of estimates are bounded:

- The sequence $\{\hat{f}_{\mathrm{BD}}^{(m)}\}$ is bounded: $\hat{f}_{\mathrm{BD}}^{(m)} \succeq \mathbf{0}$ as enforced by the non-negativity constraint and $\hat{f}_{\mathrm{BD}}^{(m)} \preceq \|y\|_\infty \mathbf{1}_N$ due to the photometry invariance constraint.

- The sequence $\{\hat{\boldsymbol{h}}^{(m)}\}$ is bounded: $\hat{\boldsymbol{h}}^{(m)} \succeq \mathbf{0}$ and $\hat{\boldsymbol{h}}^{(m)} \preceq \mathbf{1}_N$ since $\hat{\boldsymbol{h}}^{(m)}$ belongs to the probability simplex $\mathcal{PS}$.

Like in (4.14), the presence of non-differentiable terms in $\mathcal{M}$ (the indicator functions and the ℓ_1-norms) makes the subproblems in (5.9) difficult to solve with only gradient-based methods. The first subproblem is solved using the generalized Chambolle-Pock (GCP) algorithm described in subsection 2.3.1. In [77], we used the alternating direction method of multipliers (ADMM) generalized to objective functions involving more than two terms [62, 111] to solve a similar problem but involving TV regularization. We could also use ADMM here but the GCP formulation is more straightforward when we deal with TGV regularization. The second subproblem is solved with the proximal gradient (PG) algorithm (see subsection 2.3.1) since it involves two differentiable functions and one indicator function.

In the next sections, we describe the ingredients (proximal operators, gradients, operators, etc.) needed to solve each subproblem. Finally, in subsection 5.3.4, we explain how we choose the values of the parameters (including the cost-to-move parameters) and how we stop the internal iterations of both algorithms.

5.3.2 Estimating the image with GCP

To fit the framework described in subsection 2.3.1, we express the first subproblem in (5.9) as a sum of one primal and several dual functions,

$$\hat{\boldsymbol{z}} \in \underset{\boldsymbol{z}\in\mathbb{R}^{N\times 3}}{\arg\min}\, F_1(\hat{\boldsymbol{H}}^{(m-1)}\boldsymbol{R}_{\boldsymbol{u}}\boldsymbol{z}) + F_2((\boldsymbol{\nabla}\boldsymbol{R}_{\boldsymbol{u}} - \boldsymbol{R}_{\boldsymbol{w}})\boldsymbol{z}) + F_3(\varepsilon(\boldsymbol{R}_{\boldsymbol{w}}\boldsymbol{z})) + F_4(\boldsymbol{\nabla}\boldsymbol{R}_{\boldsymbol{u}}\boldsymbol{z}) + F_5(\boldsymbol{R}_{\boldsymbol{u}}\boldsymbol{z}) + G(\boldsymbol{z}), \quad (5.10)$$

where $\hat{\boldsymbol{H}}^{(m-1)} \in \mathbb{R}^{N\times N}$ is the convolution operator corresponding to the estimated kernel $\hat{\boldsymbol{h}}^{(m-1)}$. Function F_1 is the data fidelity term, $F_1 = 0.5\|\cdot - \boldsymbol{y}\|_2^2$. Functions F_2 and F_3 are related to the TGV_α^2-norm: $F_2 = \rho\|\cdot\|_{2,1}$ and $F_3 = \alpha\rho\|\cdot\|_{2,1}$. Function F_4 is the indicator function on the convex set $\mathcal{Q}_{\Omega_c}$. F_5 corresponds to the ℓ_2-norm introduced by Attouch *et al.*, $F_5 = 0.5\varrho_u^{(m)}\|\cdot - \hat{\boldsymbol{f}}_{\mathrm{BD}}^{(m-1)}\|_2^2$. Finally, the primal function is $G = (\imath_{\mathbb{R}_+^N} + \imath_{\mathcal{Q}}) \circ \boldsymbol{R}_{\boldsymbol{u}}$. The image estimate is given by $\hat{\boldsymbol{f}}_{\mathrm{BD}}^{(m)} = \boldsymbol{R}_{\boldsymbol{u}}\hat{\boldsymbol{z}}$.

Proximal operators of primal and dual functions

Like in the previous chapter, the use of GCP requires the knowledge of the proximal operators of the primal function G and the dual functions $F_1^\star, F_2^\star, F_3^\star, F_4^\star$ and $F_5^\star$.

The proximal operator of the primal function, which combines the projections onto the convex sets $\mathbb{R}_+^N$ and $\mathcal{Q}$, is given by (4.16) in Chapter 4.

The proximal operator of the conjugate of the data fidelity term F_1 is given by

$$\operatorname{prox}_{\sigma F_1^\star}(\tilde{\boldsymbol{p}}) = \frac{\tilde{\boldsymbol{p}} - \sigma \boldsymbol{y}}{1+\sigma},$$

where $\sigma > 0$ is the dual step-size in GCP algorithm. The proximal operator of $F_5^\star$ is similar since F_5 is also a squared ℓ_2-norm,

$$\operatorname{prox}_{\sigma F_5^\star}(\tilde{\boldsymbol{p}}) = \frac{\tilde{\boldsymbol{p}} - \sigma \hat{\boldsymbol{f}}_{\text{BD}}^{(m-1)}}{1+\sigma/\varrho_u^{(m)}}.$$

Like in section 4.4, functions F_2 and F_3 are ℓ_1-norms. The proximal operators of their conjugates are projection operators onto the convex sets $\mathcal{Q}_2 := \{\tilde{\boldsymbol{q}} \in \mathbb{R}^{N\times 2} | \|\tilde{\boldsymbol{q}}\|_{2,\infty} \leq \rho\}$ and $\mathcal{Q}_3 := \{\tilde{\boldsymbol{r}} \in \mathbb{R}^{N\times 4} | \|\tilde{\boldsymbol{r}}\|_{2,\infty} \leq \alpha\rho\}$.

The proximal operator of F_4 is the projection operator onto the convex set $\mathcal{Q}_{\Omega_c}$ defined in subsection 5.2.1. Using the Moreau decomposition (see Definition 2.19), the proximal operator of $F_4^\star$ is also a projection operator,

$$\operatorname{prox}_{\sigma F_4^\star}(\tilde{\boldsymbol{q}}_i) = \begin{cases} \tilde{\boldsymbol{q}}_i & \text{if } i \in \Omega_{\text{c}} \\ \boldsymbol{0} & \text{otherwise,} \end{cases}$$

where $\tilde{\boldsymbol{q}}_i \in \mathbb{R}^2$ is the i^{th} row of $\tilde{\boldsymbol{q}} \in \mathbb{R}^{N\times 2}$.

Operators and their adjoints

The operator associated with F_1 in (5.10) is $\boldsymbol{L}_1 = \hat{\boldsymbol{H}}^{(m-1)}\boldsymbol{R}_{\boldsymbol{u}} : \mathbb{R}^{N\times 3} \to \mathbb{R}^N$ and its adjoint is $\boldsymbol{R}_{\boldsymbol{u}}^* \hat{\boldsymbol{H}}^{*(m-1)}$. The operators associated with F_2 and F_3 are identical to the ones defined in subsection 4.4.2. Finally, $\boldsymbol{L}_4 = \boldsymbol{\nabla}\boldsymbol{R}_{\boldsymbol{u}} : \mathbb{R}^{N\times 3} \to \mathbb{R}^{N\times 2}$ and $\boldsymbol{L}_5 = \boldsymbol{R}_{\boldsymbol{u}} : \mathbb{R}^{N\times 3} \to \mathbb{R}^N$ are the operators associated with F_4 and F_5. Their adjoints are $\big(-\boldsymbol{R}_{\boldsymbol{u}}^* \circ \operatorname{div}\big)$ and $\boldsymbol{R}_{\boldsymbol{u}}^*$, respectively.

5.3.3 Estimating the filter with PG

The second subproblem of (5.9) is solved with the PG method. Since the non-differentiable term is the indicator function of a convex set, PG algo-

rithm reduces to a projected gradient method [111] whose iteration is

$$\boldsymbol{v}^{(n)} = \mathcal{P}_{\mathcal{PS}}\Big(\boldsymbol{v}^{(n-1)} - \mu^{(m)}\hat{\boldsymbol{F}}_{\mathrm{BD}}^{*(m)}(\hat{\boldsymbol{F}}_{\mathrm{BD}}^{(m)}\boldsymbol{v}^{(n-1)} - \boldsymbol{y}) \\ -\mu^{(m)}\varrho_h^{(m)}(\boldsymbol{v}^{(n-1)} - \hat{\boldsymbol{h}}^{(m-1)})\Big), \quad (5.11)$$

where $\mathcal{P}_{\mathcal{PS}}$ is the projection onto $\mathcal{PS}$, $\mu^{(m)} > 0$ is the step-size of the gradient descent and $\hat{\boldsymbol{F}}_{\mathrm{BD}}^{(m)} \in \mathbb{R}^{N\times N}$ is the circulant matrix corresponding to $\hat{\boldsymbol{f}}_{\mathrm{BD}}^{(m)}$.

The projection of $\boldsymbol{v} \in \mathbb{R}^N$ onto the probability simplex is given by [111]

$$\mathcal{P}_{\mathcal{PS}}(\boldsymbol{v}) = \max(\boldsymbol{v} - \nu\mathbf{1}_N, \mathbf{0}_N),$$

for some $\nu \in \mathbb{R}$. By definition, $\mathcal{P}_{\mathcal{PS}}(\boldsymbol{v})$ must satisfy $\mathbf{1}_N^\top \mathcal{P}_{\mathcal{PS}}(\boldsymbol{v}) = 1$. We use bisection method [27] to find $\nu^\star$ such that $\mathbf{1}_N^\top \max(\boldsymbol{v} - \nu^\star\mathbf{1}_N, \mathbf{0}_N) = 1$.

5.3.4 Parameters choice and stopping criterion

The algorithm for the blind deconvolution of PET images with TGV regularization is summarized in Algorithm 6. For the non-blind deconvolution problem, *i.e.*, the filter validation, we use Algorithm 5 with the appropriate data fidelity term (function F_1 is the squared ℓ_2-norm).

The step-sizes σ and τ of the CP algorithm are set as described in subsection 4.4.3. The step-size of the gradient descent in the second subproblem, $\mu^{(m)}$, must verify the following condition [111]: $\mu^{(m)} \in]0, 1/\gamma^{(m)}]$ where $\gamma^{(m)}$ is the Lipschitz constant of the gradient of the differentiable terms in the objective function (see Appendix 5.A). It is given by

$$\gamma^{(m)} = \|\hat{\boldsymbol{F}}_{\mathrm{BD}}^{*(m)}\hat{\boldsymbol{F}}_{\mathrm{BD}}^{(m)} + \varrho_v^{(m)}\mathbf{Id}_N\|_2.$$

In Algorithm 6, we choose $\mu^{(m)} = 1/\gamma^{(m)}$.

The cost-to-move parameters, $\varrho_u^{(m)}$ and $\varrho_v^{(m)}$ must be bounded to ensure the convergence of (5.9). They are initialized with the value of the regularization parameter ρ. Then, for $m > 1$, $\varrho_u^{(m)} = \kappa_u\varrho_u^{(m-1)}$ and $\varrho_v^{(m)} = \kappa_v\varrho_v^{(m-1)}$. In this work, we consider $\kappa_u = \kappa_v = 0.75$. If the maximum number of iterations of the alternating algorithm `maxIterAlt` is finite, the sequences of $\varrho_u^{(m)}$ and $\varrho_v^{(m)}$ are bounded. We set `maxIterAlt` to 10.

Algorithm 6: Blind deconvolution of PET images

input : a noisy and blurry image $\boldsymbol{y}$
output: a restored image $\hat{f}_{\mathrm{BD}}$ and an estimated filter $\hat{\boldsymbol{h}}$

initialization: $\boldsymbol{z}^{(0)} = \mathbf{0}_{N\times 3}$, $\boldsymbol{v}^{(0)} = \mathbf{0}_N$, $\hat{\boldsymbol{f}}_{\mathrm{BD}}^{(0)} = \hat{\boldsymbol{h}}^{(0)} = \mathbf{0}_N$, $\rho = \rho^{(1)}$;
For $k = 1$ **to** *maxIterRho* **do**
  $\varrho_u^{(1)} = \varrho_v^{(1)} = \rho^{(k)}$;
  for $m = 1$ **to** *maxIterAlt* **do**
    `// Image estimation`
    Compute $\hat{\boldsymbol{z}}$ using Algorithm 5 (and its initialization), lines 3 to 20 extended to five dual functions;
    $\hat{\boldsymbol{f}}_{\mathrm{BD}}^{(m)} = \boldsymbol{R}_{\boldsymbol{u}}\hat{\boldsymbol{z}}$;
    `// Filter estimation`
    $q_{\mathrm{it}} = 0$;
    $\mu^{(m)} = 1/\|\hat{\boldsymbol{F}}_{\mathrm{BD}}^{*(m)}\hat{\boldsymbol{F}}_{\mathrm{BD}}^{(m)} + \varrho_v^{(m)}\mathbf{Id}_N\|_2$;
    for $n = 1$ **to** *maxIter* **do**
      $\mathrm{Grad} = \hat{\boldsymbol{F}}_{\mathrm{BD}}^{*(m)}(\hat{\boldsymbol{F}}_{\mathrm{BD}}^{(m)}\boldsymbol{v}^{(n-1)} - \boldsymbol{y}) + \varrho_h^{(m)}(\boldsymbol{v}^{(n-1)} - \hat{\boldsymbol{h}}^{(m-1)})$;
      $\boldsymbol{v}^{(n)} = \mathcal{P}_{\mathcal{PS}}\left(\boldsymbol{v}^{(n-1)} - \mu^{(m)}\mathrm{Grad}\right)$;
      if $q(\boldsymbol{v}^{(n)}) > q(\boldsymbol{v}^{(n-1)})$ **then**
        $\hat{\boldsymbol{h}}^{(m)} = \boldsymbol{v}^{(n)}$;
        $q_{\mathrm{it}} = 0$;
      else
        $q_{\mathrm{it}} = q_{\mathrm{it}} + 1$;
      end
      if $n =$ *maxIter* **or** $q_{\mathrm{it}} > 200$ **then**
        $\hat{\boldsymbol{h}}^{(m)} = \boldsymbol{v}^{(n)}$;
        break;
      end
    end
    if $m \neq$ *maxIterAlt* **then**
      $\varrho_u^{(m+1)} = \kappa_u\varrho_u^{(m)}$;
      $\varrho_h^{(m+1)} = \kappa_h\varrho_h^{(m)}$;
    end
  end

Algorithm 6: Blind deconvolution of PET images (continued)

```
    choose m⋆ such that q(ĥ^(m⋆)) ≥ q(ĥ^(m)) for all m;
    f̂_{BD,ρ^(k)} = f̂_BD^(m⋆);
    ĥ_{ρ^(k)} = ĥ^(m⋆);
    if k ≠ maxIterRho then
        ρ^(k+1) = βρ^(k);
        z^(0) = ẑ;
        v^(0) = ĥ^(m);
    end
end
choose k⋆ such that q(ĥ_{ρ^(k)}) ≥ q(ĥ_{ρ^(k)}) for all k;
f̂_BD = f̂_{BD,ρ^(k⋆)};
ĥ = ĥ_{ρ^(k⋆)};
```

We set the maximum number of internal iterations `maxIter` (both for GCP and PG algorithms) to 5000. Internal iterations stop after $q_{\text{it}} = 200$ iterations of non-increasing quality of the estimate or when n reaches `maxIter`. Like in Chapter 4, the noise statistics is unknown and likely not white. For the reason detailed in subsection 4.4.3, we use the SNR as quality criterion q in the simulations. The initialization of the estimates is a null vector of size N. For $k > 1$, the initial guesses of the algorithm are given by the previous estimates $\hat{f}_{\text{BD},\rho^{(k-1)}}$ and $\hat{h}_{\rho^{(k-1)}}$. Similarly to subsection 4.4.3, we first run Algorithm 6 for 20 iterations on ρ with $\rho^{(1)} = 10^{10}$ and $\beta = 0.1$. The iteration providing the best estimate for $\boldsymbol{h}$ according to the SNR criterion[2] is denoted $k^\star$. We run again Algorithm 6 with $\rho^{(1)}_{\text{new}} = \rho^{(k^\star-1)}$, $\beta_{\text{new}} = 0.8$ and a number of iterations `maxIterRho` equal to $\lceil \log(\beta^2)/\log\beta_{\text{new}} \rceil$ such that the last value of ρ_{new} is close to $\rho^{(k^\star+1)}$.

For the BD of real data, internal iterations of both GCP and PG algorithms stop when the relative error between two successive estimates goes beyond a threshold `Th` set to 10^{-4}. We select the best regularization parameter by visual inspection.

[2] Ideally, the quality criterion must take into account both $\hat{f}_{\text{BD},\rho^{(k)}}$ and $\hat{h}_{\rho^{(k)}}$ like the criteria based on the residual (see subsection 2.3.2).

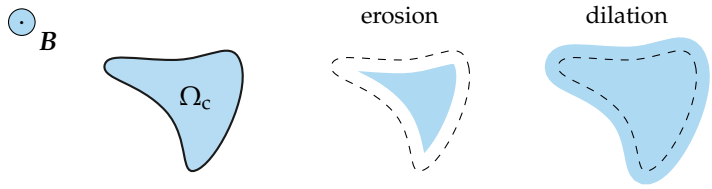

Figure 5.2 Illustration of the two main tools in morphological image processing: (middle) erosion and (right) dilation. Figures inspired from [139].

5.4 Experiments

In this last section, we present the results of studies conducted on synthetic and experimental data. They aim at (*i*) validating the BD framework (5.6) as well as its numerical implementation and (*ii*) measuring the influence of an accurate (or not) delineation of the region Ω_c. Every study includes the following two steps: (*i*) estimation of $\boldsymbol{f}_{0,\mathrm{BD}}$ and $\boldsymbol{h}$ via blind deconvolution, and (*ii*) estimation of $\boldsymbol{f}_{0,\mathrm{NBD}}$ via non-blind deconvolution, using kernel $\hat{\boldsymbol{h}}$.

In simulations, the quality of $\hat{\boldsymbol{f}}_{\mathrm{BD}}$ and $\hat{\boldsymbol{f}}_{\mathrm{NBD}}$ is measured with the increase in signal-to-noise ratio (ISNR) (see Definition 2.22). The quality of $\hat{\boldsymbol{h}}$ is measured with the signal-to-noise ratio (SNR) (see Definition 2.21).

5.4.1 Delineation of Ω_c

A crucial pre-processing step in our BD framework is the determination of the region Ω_c, *i.e.*, a region with uniform activity in $\boldsymbol{f}_{0,\mathrm{BD}}$. As explained in subsection 5.2.1, this area is delineated based on high resolution anatomical images which are subsequently downsampled to match the resolution of PET images. Since we work in a discrete setting with finite forward differences, some boundaries of Ω_c must be discarded. To this end, we consider a binary image $\boldsymbol{b}$ with $b_i = 1$ if $i \in \Omega_c$ and 0 otherwise. We first apply *erosion* on $\boldsymbol{b}$ by structuring element $(0,1,1)$ to obtain the mask for $\boldsymbol{\nabla}_1$. Then, we apply erosion on $\boldsymbol{b}$ with $(0,1,1)^\top$ to get the mask for $\boldsymbol{\nabla}_2$.

Definition 5.1 (Erosion) *[139] The erosion of a set Ω_c by a structuring element $\boldsymbol{B}$ is defined as the set of indices i such that $\boldsymbol{B}$ is included in Ω_c when its origin is located at i,* i.e., $\{i|\boldsymbol{B}_i \subseteq \Omega_c\}$ *(see Figure 5.2).*

To uniformly increase (resp. decrease) the size of Ω_c, *e.g.*, to study how the accuracy of the delineation impacts the quality of the estimated PSF, we apply *dilation* (resp. erosion) by structuring elements $(1,1,1)$ and $(1,1,1)^\top$.

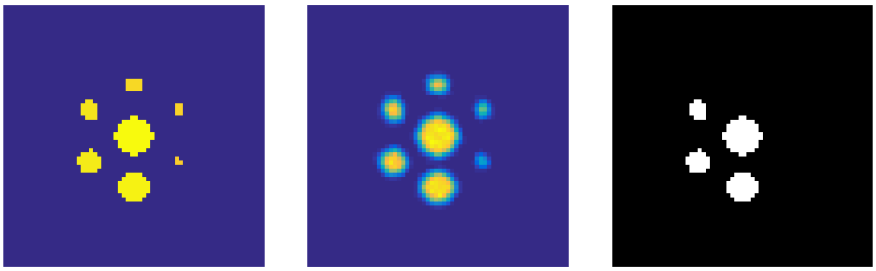

(a) (b) (c)

Figure 5.3 (a) Phantom with cylindrical holes corresponding to $f_{0,\mathrm{BD}}$ and $f_{0,\mathrm{NBD}}$, (b) observations simulated with dPETSTEP for $t_{\mathrm{acq}} = 10\,\mathrm{s}$ (see subsection 5.4.2), and (c) binary mask $\boldsymbol{b}$ corresponding to Ω_{c} (only used for blind deconvolution).

Definition 5.2 (Dilation) *[139] The dilation of a set Ω_{c} by a structuring element $\boldsymbol{B}$ is defined as the set of indices i such that $\boldsymbol{B}$ hits Ω_{c} when its origin is located at i,* i.e., $\{i|\boldsymbol{B}_i \cap \Omega_{\mathrm{c}} \neq \{\}\}$ *(see Figure 5.2).*

Erosion and dilation are the main tools in morphological image processing [139] (see Figure 5.2).

5.4.2 Synthetic data

The first study is carried out on simulations of a phantom with cylindrical holes of known diameters and filled with the same ^{18}F-FDG activity concentration (see Figure 5.3a). Its purposes are multiple. First, we compare the quality of $\hat{f}_{0,\mathrm{NBD}}$ obtained using $\hat{\boldsymbol{h}}$ with the one obtained using the true kernel $\boldsymbol{h}$. Second, we investigate the robustness of the method to an inaccurate delineation of Ω_{c}.

In this case, $f_{0,\mathrm{BD}}$ and $f_{0,\mathrm{NBD}}$ correspond to the same image. We generate independent observations for the BD and the NBD steps, as explained in subsection 5.2.4, using dPETSTEP and the parameters listed in Table 4.1 (see Figure 5.3b). The reconstruction is performed with OSEM algorithm (20 iterations and 24 subsets) to be coherent with the choice of the data fidelity term made in section 5.2. Like in subsection 4.5.1, the reconstructed blurred images $\boldsymbol{y}$ are normalized by their ℓ_1-norm. We estimate the ground truth of the 2D blurring kernel by running dPETSTEP for an isolated radioactive source located at the center of the FOV (see Figure 5.5). The acquisition time is set to 10^6 s to assume a noiseless acquisition.

In Chapter 4, the use of the attenuation map was restricted to the simulation of PET images. Here, it is employed to delineate the region with uniform activity, Ω_c. After this delineation step, we pre-process the binary image $\boldsymbol{b}$ containing Ω_c as explained in subsection 5.4.1 (see Figure 5.3c). From this binary image, we also generate two additional masks using dilation ($\Omega_{c,larger}$) and erosion ($\Omega_{c,smaller}$) by $(1,1,1)$ and $(1,1,1)^\top$.

Finally, we apply the two steps mentioned above. We estimate $\boldsymbol{f}_{0,BD}$ and $\boldsymbol{h}$ using Algorithm 6 with each of the three (pre-processed) binary masks: Ω_c, $\Omega_{c,larger}$ and $\Omega_{c,smaller}$. Then, we solve the NBD problem with an adapted version of Algorithm 5 for each of the three estimated filters (denoted $\hat{\boldsymbol{h}}$, $\hat{\boldsymbol{h}}_{larger}$ and $\hat{\boldsymbol{h}}_{smaller}$) and for the true blurring kernel $\boldsymbol{h}$.

Results

Figures 5.4 and 5.5 present the results of the simulations. In Figure 5.4, we see that the quality of both the estimated PSF $\hat{\boldsymbol{h}}$ and the corresponding $\hat{\boldsymbol{f}}_{NBD}$ increases as the acquisition time t_{acq} gets longer. When the size of the region with uniform intensity used in BD is overestimated, the SNR of the estimated PSF $\hat{\boldsymbol{h}}_{larger}$ reaches a plateau, here around 15 dB. The corresponding estimate $\hat{\boldsymbol{f}}_{larger}$ also suffers from the poor quality of $\hat{\boldsymbol{h}}_{larger}$. In contrast, the use of $\Omega_{c,smaller}$ leads to a quality similar to the one obtained when the entire region of uniform intensity, Ω_c, is used in the minimization problem. This is not surprising since the zero-gradient assumption is still valid in this smaller region. In Figure 5.5, we can visually assess the quality of the estimated PSFs. Due to a high level of noise in the simulated data, even the true PSF is not able to recover the flat area present in $\boldsymbol{f}_{0,NBD}$. The biggest variations are observed in the profile obtained with $\hat{\boldsymbol{h}}_{smaller}$.

5.4.3 Experimental data

Two experimental datasets were acquired to test the framework proposed in this chapter. Both of them include PET images. The first dataset also contains structural CT scans unlike the second one. Hopefully, the geometry of the phantom in the second dataset is perfectly known. It allows us to accurately define the region with uniform activity.

Phantom with cylindrical holes acquired on a human PET/CT scanner

The first one consists in observations of a phantom with cylindrical holes of known diameters filled with ^{18}F-FDG activity (1 mCi/100 mL). PET and CT images were acquired on a Philips GEMINI-TF PET/CT scanner with

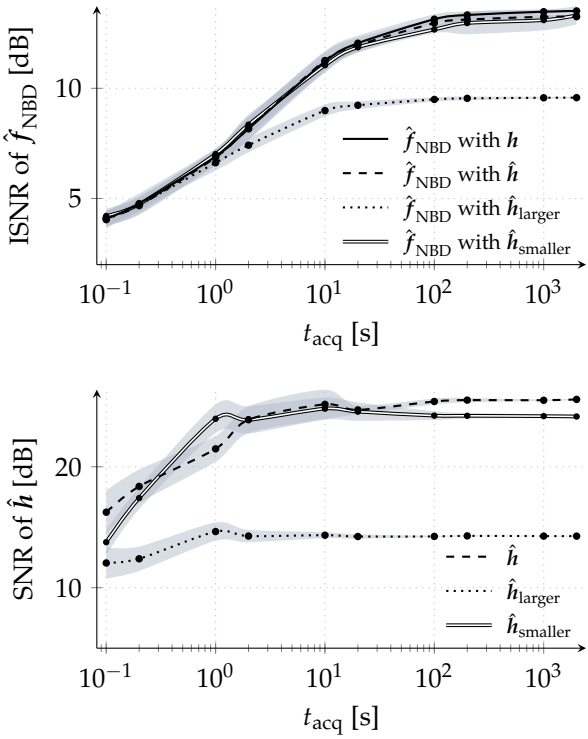

Figure 5.4 Simulations: quality of $\hat{f}_{\text{NBD}}$ and $\hat{h}$. Above: mean ISNR (over 10 trials) of the deconvolved phantom $f_{0,\text{NBD}}$ *versus* the acquisition time. The estimates are recovered in a non-blind deconvolution framework (NBD). The PSF used for the NBD is either the true PSF (h) or one of the PSFs estimated via blind deconvolution ($\hat{h}$, $\hat{h}_{\text{larger}}$ or $\hat{h}_{\text{smaller}}$). Below: mean SNR (over 10 trials) of the three estimated PSFs *versus* the acquisition time. The light areas around the curves represent the standard deviation. The observations were generated with dPETSTEP software. The simulation parameters are described in section 4.5 and Table 4.1.

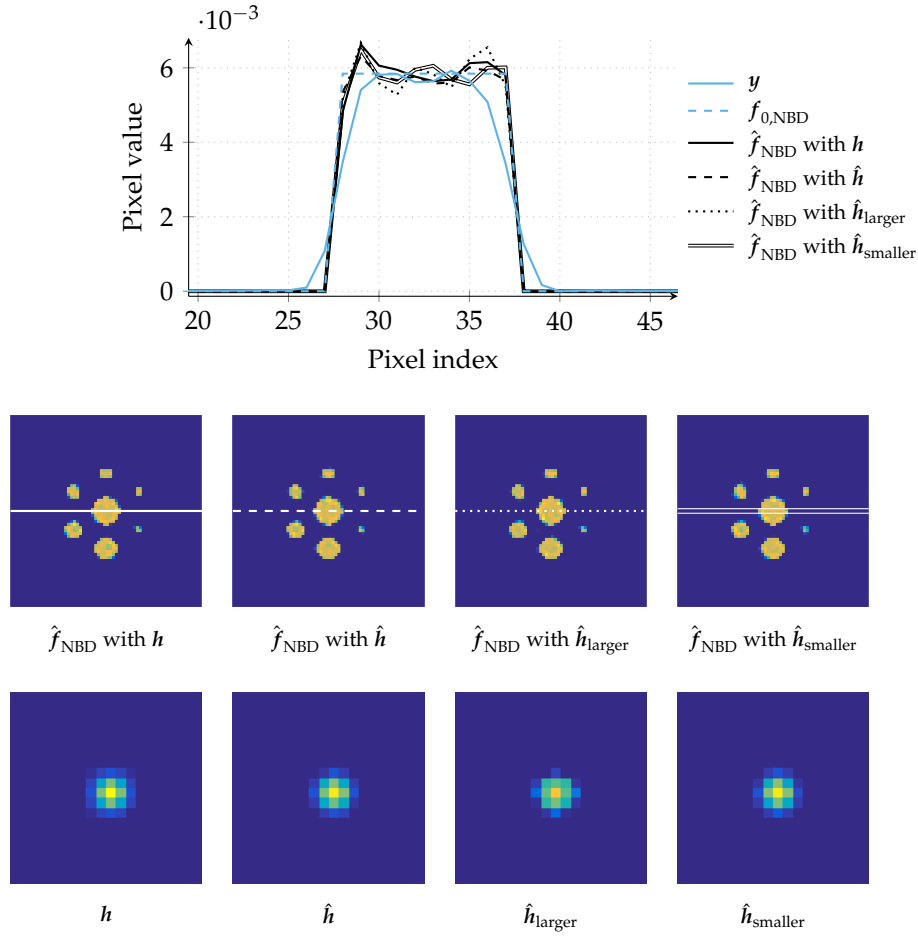

Figure 5.5 Simulations: estimates of $f_{0,\mathrm{NBD}}$ and h. The 64×64 estimates are recovered in a non-blind deconvolution (NBD) framework from observations generated with dPETSTEP software for $t_{\mathrm{acq}} = 10\,\mathrm{s}$. The simulation parameters are described in section 4.5 and Table 4.1. The PSF used for the NBD is either the true PSF (h) or one of the PSFs estimated via blind deconvolution ($\hat{h}$, $\hat{h}_{\mathrm{larger}}$ or $\hat{h}_{\mathrm{smaller}}$). Above: the 1D profiles correspond to sections of the observations and the ground truth (blue lines) and of the estimates (black lines). The location of the section is indicated by white horizontal lines in the figures below. The PSFs share the same intensity scale so do the estimates.

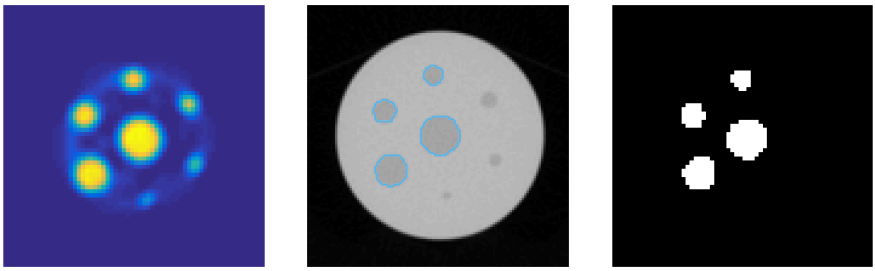

(a) (b) (c)

Figure 5.6 (a) Observation of a real phantom with cylindrical holes acquired on a combined PET/CT scanner ($t_{\text{acq}} = 900\,\text{s}$), (b) CT image of the phantom obtained on the same combined PET/CT scanner as (a), with the delineation of Ω_c in blue, and (c) binary mask extracted from (b).

an acquisition time of 900 s (see Figures 5.6a and 5.6b). The pixel size in the transaxial slices of PET volume is 2 mm × 2 mm. The images were cropped to 64 × 64. We also imaged a needle filled with the same radiotracer (3 mCi/mL). The needle observation, denoted $\boldsymbol{h}_{\text{needle}}$, can be seen as a ground truth for the PSF (see Figure 5.7). For the restoration, we consider that Ω_c is made of the four largest disks in the CT image (see Figure 5.6c).

In this study, we compare the estimate of the PSF obtained with our BD scheme with $\boldsymbol{h}_{\text{needle}}$ as well as the quality of their respective estimates in the NBD framework solved with an adapted version of Algorithm 5.

Figure 5.7 presents the results on this first dataset. The estimates $\hat{\boldsymbol{f}}_{\text{NBD}}$ obtained with $\boldsymbol{h}_{\text{needle}}$ and $\hat{\boldsymbol{h}}$, respectively, show a flat profile in the area where we expect uniform radioactivity. The main difference lies in the amplitudes of the restored image: the estimate obtained with $\boldsymbol{h}_{\text{needle}}$ shows a higher activity in the four biggest holes.

Spherical phantoms acquired on a small animals PET scanner

The last study is conducted on spherical phantoms imaged in a PET scanner for small animals. We used two spheres of known internal diameter (10 mm and 24.8 mm) filled with uniform ^{18}F-FDG activity concentration (1 mCi/100 mL and 2.14 mCi/100 mL). Phantoms were located at the center of the FOV (12.8 cm × 12 cm) of a Philips MOSAIC small animal PET scanner. The acquisition time of 3D images was 600 s. After reconstruction with the iterative algorithm 3D-RAMLA, the original image size was 128 × 128 × 120 voxels, cropped to 64 × 64 × 64. The voxel size is

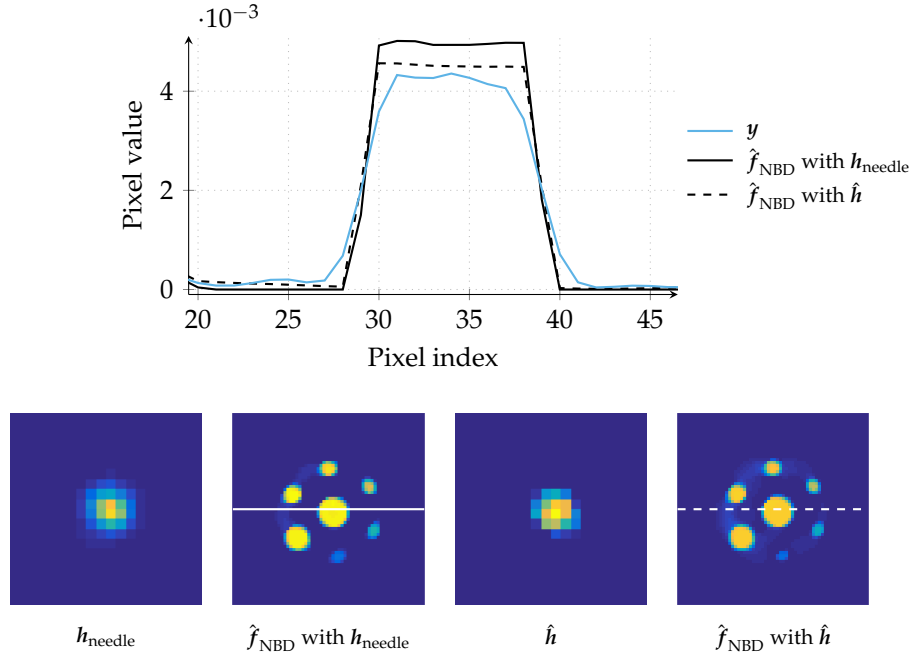

Figure 5.7 Experiments: estimates of $f_{0,\text{NBD}}$ and h. The 64×64 estimates are recovered in a non-blind deconvolution (NBD) framework from observations acquired as described in subsection 5.4.3. The PSF used for NBD is either the experimental PSF (h_{needle}) or the PSF estimated via blind deconvolution ($\hat{h}$). Above: the 1D profiles correspond to sections of the observations (blue line) and of the estimates (black lines). The location of the section is indicated by white lines in the figures below. The PSFs share the same intensity scale so do the estimates.

$1\,\text{mm} \times 1\,\text{mm} \times 1\,\text{mm}$. In this work, we only consider 2D transaxial slices.

The images of the smallest sphere are used for BD (see Figure 5.8a) and the ones of the biggest sphere are employed for validation (see Figure 5.8c). In the BD framework, region Ω_c corresponds to the entire sphere, delineated based on the knowledge of its internal diameter. This diameter is not an exact multiple of the pixel size. Regarding the results of simulations in subsection 5.4.2, we select a slightly smaller region for Ω_c (see Figure 5.8b).

Like for the first dataset, we use Algorithm 6 to estimate the filter and then, we validate it using a modified version of Algorithm 5. For comparison, we also deconvolve the NBD observation, *i.e.*, the imaged small

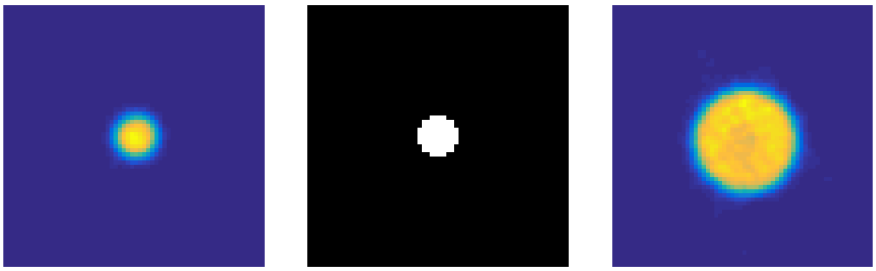

(a) (b) (c)

Figure 5.8 (a) Observations of a small sphere acquired on a small animals PET scanner ($t_{\text{acq}} = 600\,\text{s}$) and used for blind deconvolution, (b) binary mask extracted from (a), and (c) observations of a big sphere acquired like (a) and used for non-blind deconvolution.

sphere, with a Gaussian filter $\boldsymbol{h}_{\text{G}}$ whose the FWHM is equal to 2.7 mm [88].

In Figure 5.9, we observe the absence of a flat curve corresponding to the uniform activity in the sphere. Interestingly, we already see in the observations that the activity seems to be lower at the center of the sphere (see Figure 5.8c). Experimentally, we do not know how to justify this since the spheres were filled with uniform activity concentration. We also notice that the edges of the spheres are only a little bit sharper after the NBD but that there is still activity spitting out of the phantom. One possible explanation is related to the assumption that we made about spatial invariance of the PSF. The true PSF near the edges of the sphere spreads probably more compared to the Gaussian or the estimated ones.

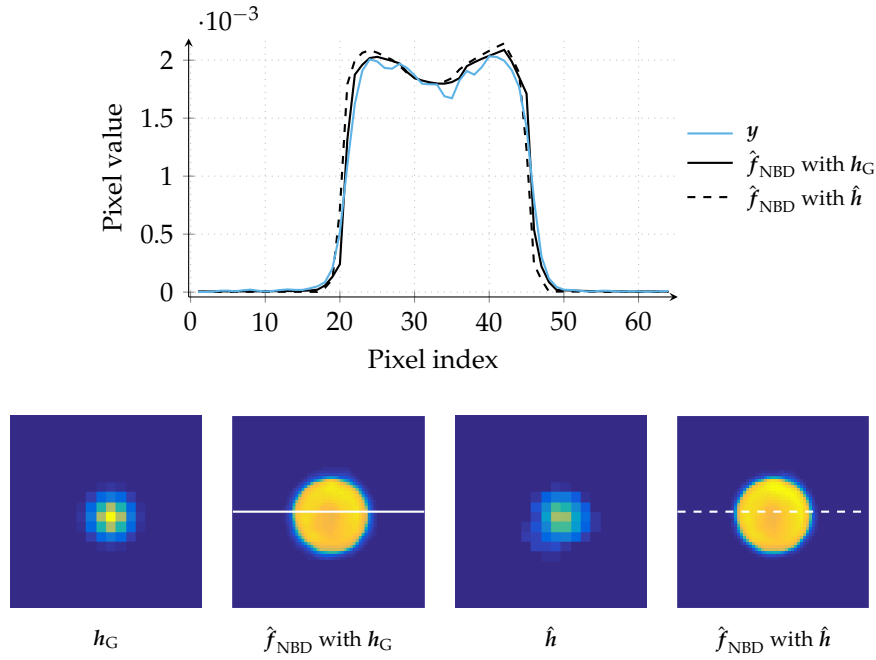

Figure 5.9 Experiments: estimates of $f_{0,\text{NBD}}$ and h. The 64×64 estimates are recovered in a non-blind deconvolution (NBD) framework from observations acquired as described in subsection 5.4.3. The PSF used for NBD is either a Gaussian PSF with a FWHM equal to 2.7 mm (h_{G}) or the PSF estimated via blind deconvolution ($\hat{h}$). Above: the 1D profiles correspond to sections of the observations (blue line) and of the estimates (black lines). The location of the section is indicated by white lines in the figures below. The PSFs share the same intensity scale so do the estimates.

Appendix 5.A Lipschitz constant in the PSF estimation

In this appendix, we compute the Lispschitz constant of the gradient of the differentiable terms in the objective function corresponding to the blurring kernel estimation (see (5.9)). The objective function is given by

$$\frac{1}{2}\|\hat{\boldsymbol{F}}_{\mathrm{BD}}^{*(m)}\boldsymbol{v}-\boldsymbol{y}\|_2^2+\frac{\varrho_v^{(m)}}{2}\|\boldsymbol{v}-\hat{\boldsymbol{h}}^{(m)}\|_2^2+\imath_{\mathcal{PS}}(\boldsymbol{v})=:\Lambda(\boldsymbol{v})+\imath_{\mathcal{PS}}(\boldsymbol{v}).$$

The gradient of Λ is

$$\nabla\Lambda(\boldsymbol{v})=\hat{\boldsymbol{F}}_{\mathrm{BD}}^{*(m)}(\hat{\boldsymbol{F}}_{\mathrm{BD}}^{(m)}\boldsymbol{v}-\boldsymbol{y})+\varrho_h^{(m)}(\boldsymbol{v}-\hat{\boldsymbol{h}}^{(m)}).$$

Let us check that $\nabla\Lambda$ is Lipschitz continuous with constant $\gamma^{(m)}>0$ (see Definition 2.16),

$$\begin{aligned}\|\nabla\Lambda(\boldsymbol{u})-\nabla\Lambda(\boldsymbol{v})\|_2&=\|\hat{\boldsymbol{F}}_{\mathrm{BD}}^{*(m)}\hat{\boldsymbol{F}}_{\mathrm{BD}}^{(m)}(\boldsymbol{u}-\boldsymbol{v})+\varrho_v^{(m)}(\boldsymbol{u}-\boldsymbol{v})\|_2\\&=\|(\hat{\boldsymbol{F}}_{\mathrm{BD}}^{*(m)}\hat{\boldsymbol{F}}_{\mathrm{BD}}^{(m)}+\varrho_v^{(m)})(\boldsymbol{u}-\boldsymbol{v})\|_2\\&\leq\|\hat{\boldsymbol{F}}_{\mathrm{BD}}^{*(m)}\hat{\boldsymbol{F}}_{\mathrm{BD}}^{(m)}+\varrho_v^{(m)}\|_2\|\boldsymbol{u}-\boldsymbol{v}\|_2,\end{aligned}$$

where the last inequality results from Definition 2.18. Consequently,

$$\gamma^{(m)}=\|\hat{\boldsymbol{F}}_{\mathrm{BD}}^{*(m)}\hat{\boldsymbol{F}}_{\mathrm{BD}}^{(m)}+\varrho_v^{(m)}\|_2.$$

Lensless endoscopy

6

Basics of lensless endoscopy

As mentioned in Chapter 1, the lensless endoscope (LE) is a promising device to acquire *in vivo* biological images at a cellular scale. In addition to its high resolution, the tiny size of the probe (diameter around 175 μm) allows a deep exploration of the tissues.

Andresen *et al.* define a LE as "a long waveguide, without any additional elements attached, capable of acquiring a multiphoton image of an object located at its tip" [9]. Particularly, when employed in conjunction with wavefront shaping devices such as liquid crystal spatial light modulators (SLM), fiber-based LE offers the ability to focus a light beam and scan the sample volume with no access to the distal end of the fiber. The main characteristic of LE compared to a conventional endoscope or an endomicroscope is the absence of optics or moving parts at their distal end [149]. It enables the design of ultrathin devices potentially capable to explore a new range of organs at depths unreachable in microscopy.

In this chapter, we first describe the main components of the entire device in section 6.1. Then, in section 6.2, we detail the linear mathematical model underlying the light collection by the fiber when we illuminate the biological sample with any light pattern. Finally, in section 6.3, we describe the traditional illumination scheme, called *raster scanning*, its reconstruction technique and the associated design and imaging challenges.

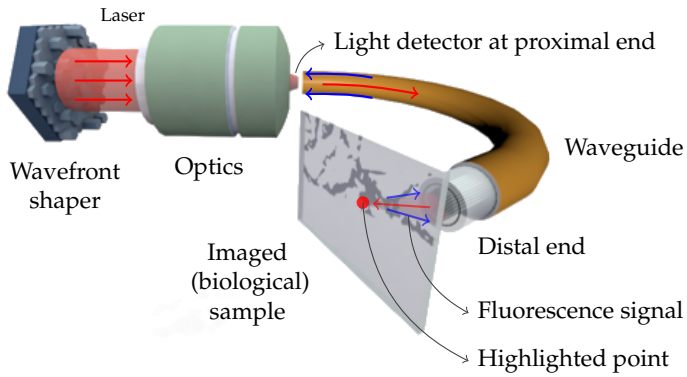

Figure 6.1 Lensless endoscope principle in raster scanning mode (*i.e.*, the light beam is shaped to focus on one point). Excitation signal is red and backscattered fluorescence signal is blue. Source: Institut Fresnel.

6.1 LE components

As illustrated in Figure 6.1, an LE consists of four main parts: a wavefront shaper, an optics part, a waveguide and a light detector. The role of the wavefront shaper is to appropriately shape the light beam to get specific illumination patterns at the distal end of the waveguide. The optics part is made of mirrors and lenses. It is used to focus the light from the wavefront shaper into the optical waveguide. In the context of lensless endoscopy where we are looking for a flexible device, the waveguide is a single optical fiber: it can be either a multicore fiber (MCF) or a multimode fiber (MMF). Its role is to carry the excitation signal to the biological sample and then to collect and guide the backscattered signal to an optical detector. Image is finally reconstructed either in a straightforward way (when a single pixel photodetector is used) or using more complex techniques based for instance on optical phase conjugation [135].

The LE considered in this work is designed as follows. The wavefront shaper is made of a liquid crystal SLM combined with a pair of galvanometric scan mirrors. The waveguide is a MCF with a section diameter of about 175 μm. In its inner part made of silica, 120 single mode cores conveying the excitation signal are arranged in a Fermat's golden spiral shape (see Figure 6.2a). Several cores arrangements were studied in the literature, both deterministic and stochastic (*e.g.*, pseudo-random or hexagonal arrangements). After calibration, Fermat's arrangement shows a low

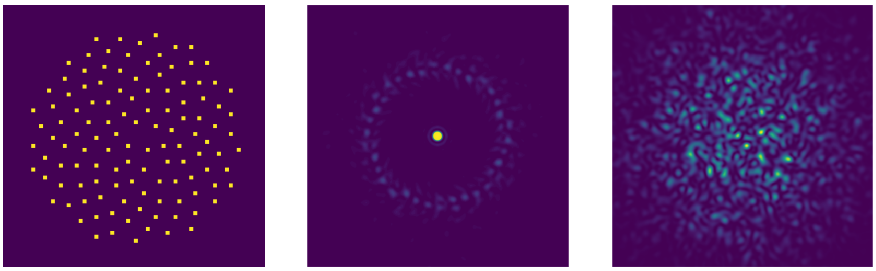

(a) (b) (c)

Figure 6.2 (a) Zoom on single mode cores arrangement in a Fermat's golden spiral shape, (b) simulated focused light beam (brightened for visualization purpose) and (c) one of the simulated speckle patterns obtained without fiber calibration. Images were simulated for a Fermat's golden spiral fiber core arrangement with $J = 120$, $D = 113\,\mu$m and $3\sigma_c = 3.2\,\mu$m. Experiment parameters are $\lambda = 1\,\mu$m, $z = 500\,\mu$m, and $a = 2\,\mu$m (see section 7.1 for the parameter definitions).

side lobes level (the dim ring in Figure 6.2b) and a very good contrast between the intensities of the central peak and the side lobes [138]. The first cladding is surrounded by an outer part made of air holes. This double cladding allows the entire silica surface to efficiently collect the backscattered fluorescent signal in the same way as a multimode waveguide. As a result, the excitation and the collection processes are decoupled [9]. Collected light is finally measured by a single pixel detector.

The considered LE presents two important features: it is *robust to fiber bending* [154] and, more importantly, it exhibits a *memory effect* that allows to scan the output illumination pattern by simply adding a phase tilt at the MCF entrance [149] (see section 7.3). The second acquisition strategy described in Chapter 8 mainly relies on this key property.

6.2 From illumination to photon collection

In this section, we first describe the fluorescence phenomenon, *i.e.*, the physical process underlying the generation of observations in lensless endoscopy. Secondly, we describe the model of photons collection by the MCF. Then, based on those previous models, we propose a discrete forward model explaining how the observations are related to the original fluorophore density map.

We consider a sample—either a synthetic phantom or a very thin slice of an *ex vivo* biological sample—containing some molecules of interest that have been tagged with fluorescent dyes. For the sake of simplicity, we assume that this sample is restricted to a 2D field of view (FOV), also called object space $\Omega \subset \mathbb{R}^2$. A function $f_0 : \Omega \times \mathbb{R} \to \mathbb{R}_+$ associates a fluorophore density $f_0(\boldsymbol{x}, t)$ with each location $\boldsymbol{x} \in \Omega$ at time instant t.

During the acquisition process, this continuous density map is turned into a finite set of observations, each of them being related to a particular configuration of the sensing device, *i.e.*, to a particular illumination pattern. Most of the time, the interpretation of the observations is not straightforward and a reconstruction process is necessary. In this case, we try to estimate the quantity of interest based on the acquired data. This inverse problem can be mathematically expressed as a minimization problem (see section 8.1). The formulation of the objective function to optimize requires a good knowledge (and modeling) of (*i*) the physics beyond the acquisition and (*ii*) the detection process.

6.2.1 Fluorescence model

Fluorescent molecules possibly absorb light and emit photons under illumination by a light pattern with static intensity S. The observed and measured photon flux $\varphi : \Omega \times \mathbb{R} \to \mathbb{R}$ depends on the intensity of the incident light but also on the fluorophore density f_0. In this section, we derive the expression of the photon flux $\varphi(\boldsymbol{x}, t)$ at time t emitted by the fluorophores located at $\boldsymbol{x} \in \Omega$ as a function of f_0, S and physical parameters. In the next section, we will relate this expression to the measurements obtained with the optical device.

The main phenomena controlling the number of emitted photons are singlet state and triplet state saturations, photo-bleaching, and background fluorescence [153].

Singlet state saturation. If light intensity $S(\boldsymbol{x})$ is high enough, *i.e.*, if the energy of incident photons is sufficient to bring an electron to an upper state, fluorophores absorb light. Due to this absorption, some molecules reach the excited singlet state $\mathcal{S}$ before progressively returning to the ground state. During this last process, some of them emit photons by fluorescence.

Triplet state saturation. Not all the fluorophores in the excited singlet state return to the ground state. Some of them cross to the excited triplet

state $\mathcal{T}$ at constant rate k_{isc} [140, 153]. The lifetime in $\mathcal{T}$ state is three to six orders of magnitude bigger than the excited singlet state lifetime. Molecules are then trapped in this state during microseconds to milliseconds and the photon emission decays substantially.

Photo-bleaching. Photo-bleaching is an irreversible photochemical damage caused when the biological specimen is exposed to light. The photo-bleached fluorophores permanently lose their ability to fluoresce. It occurs when the molecules are either in the singlet or in the triplet excited state. The rate constant depends on the incident light intensity, the number of excitation cycles, the environment, etc. As mentioned by Song *et al.* [140], the time scale of this process is of microseconds to minutes.

Background fluorescence. The background photon flux comes from two main sources: scattering and autofluorescence [153]. Rayleigh scattering can be efficiently blocked by optical filters and spontaneous Raman scattering is negligible since it is orders of magnitude weaker than the photon flux of interest. Autofluorescence arises from endogenous fluorophores absorbing and emitting photons in a frequency spectrum similar to those of the exogenous fluorescent probes but having higher saturation level [153]. The photon flux $\varphi_b(\boldsymbol{x}, t)$ induced by the background fluorescence in $\boldsymbol{x}$ is then assumed to be proportional to the illumination intensity $S(\boldsymbol{x})$.

In the context of LE, we formulate the following assumptions about the illumination duration and intensity, both tunable acquisition parameters: (*i*) illumination duration t_{acq} is short compared to the time needed to reach triplet excited steady state but long enough for singlet excited state to reach steady state, and (*ii*) intensity S at each $\boldsymbol{x}$ is low and, consequently, far from the saturation level. The first assumption allows us to consider only singlet excited state saturation and its corresponding flux (see Appendix 6.A for computation details) but also to expect no molecules displacement during the acquisition and to neglect the photo-bleaching of the sample. Those last two considerations make fluorophore density f_0 time invariant over the acquisition duration. The photon flux at location $\boldsymbol{x}$ is then given by

$$\varphi(\boldsymbol{x}) \approx Q_e k_d \frac{\sigma S(\boldsymbol{x})}{\sigma S(\boldsymbol{x}) + k_d} f_0(\boldsymbol{x}),$$

where quantum yield Q_e characterizes the efficiency of the emission process, k_d is the constant rate associated to the return to the ground state,

and σ is a parameter depending on laser wavelength λ and on the chosen dye [38, 153]. Taking into account the second assumption, typically $S(\boldsymbol{x}) \ll k_d/\sigma$, the photon flux depends linearly on the product of $S(\boldsymbol{x})$ and $f_0(\boldsymbol{x})$,

$$\varphi(\boldsymbol{x}) \approx Q_e \sigma S(\boldsymbol{x}) f_0(\boldsymbol{x}). \tag{6.1}$$

6.2.2 Photon collection model

Within the acquisition duration t_{acq}, the LE collects a non-negative number of photons Y, a fraction of those emitted by the sample. Neglecting for now any signal-independent noise term (*e.g.*, thermal or readout noise), this quantity is a Poisson random variable whose mean is

$$\mathbb{E}Y = \int_\Omega \int_0^{t_{\text{acq}}} c_0 \left(\varphi(\boldsymbol{x}) + \varphi_b(\boldsymbol{x})\right) \mathrm{d}t \, \mathrm{d}\boldsymbol{x}, \tag{6.2}$$

where φ and φ_b are the direct and the background photon fluxes generated by the object, and $0 < c_0 < 1$ is a constant accounting for the fraction of photons captured by the LE. In this work, we assume no sensitivity attenuation of the light collection closer to the periphery of the FOV (*i.e.*, c_0 does not depend on $\boldsymbol{x}$). This assumption relies on the large collection numerical aperture (NA) of the fiber (NA $= 0.5$) (see section 8.4).

6.2.3 Forward model and its discrete representation

Using (6.1) and (6.2), the continuous forward model relating the photon count Y to f_0 is

$$Y \sim \mathcal{P}\left(\int_\Omega S(\boldsymbol{x})[c_1 f_0(\boldsymbol{x}) + c_2] \, \mathrm{d}\boldsymbol{x}\right), \tag{6.3}$$

with constants $c_1, c_2 > 0$ depending on parameters c_0, Q_e, σ and t_{acq}. In this study, we are interested in the relative contrast between different regions of the object space Ω. Recovering f_0 up to a scaling factor and an offset is adequate. Defining $f \coloneqq c_1 f_0 + c_2$, model (6.3) becomes

$$Y \sim \mathcal{P}\left(\int_\Omega S(\boldsymbol{x}) f(\boldsymbol{x}) \, \mathrm{d}\boldsymbol{x}\right). \tag{6.4}$$

We simplify (6.4) by turning it into a discrete representation as explained in section 2.1. Combined with the corruption of any signal-independent noise sources (*e.g.*, electronic and readout noise) appearing in the measure-

ment process, the discrete version of continuous model (6.4) is then

$$Y \sim \mathcal{P}(\boldsymbol{s}^\top \boldsymbol{f}) + \mathcal{N}(0, \sigma^2),$$

where $\boldsymbol{s} \coloneqq (s_1, \dots, s_N)^\top$ and $\boldsymbol{f} \coloneqq (f_1, \dots, f_N)^\top$. All extra noise sources are modeled as a Gaussian noise with variance σ^2.

In practice, we do not collect only one but M observations y_i with $i \in [M]$, *i.e.*, M realizations of Y. Those distinct observations result from the illumination of the biological specimen with M (discretized) patterns $\boldsymbol{s}_j$ gathered in matrix $\boldsymbol{S} \coloneqq (\boldsymbol{s}_1, \dots, \boldsymbol{s}_M)$. We assume that we work in high photon counting regime where the Poisson noise is negligible compared to other noise sources. We then compactly represent the sensing model as

$$\boldsymbol{y} = \boldsymbol{S}^\top \boldsymbol{f} + \boldsymbol{n}, \tag{6.5}$$

where $\boldsymbol{n} \coloneqq (n_1, \dots, n_M)^\top$ contains M independent realizations of the noise.

To get observations $\boldsymbol{y}$ of collected photons, we need to set up an acquisition strategy. Each strategy is defined by the choice of (*i*) the illumination patterns $\boldsymbol{s}_j$, $j \in [M]$ and (*ii*) the number M of acquired observations. In section 8.3, we propose two acquisition frameworks and we detail the corresponding sensing matrices. Hereafter, we explain the traditional acquisition strategy and we highlight its limitations.

6.3 Traditional acquisition principle

We usually resort to raster scanning (RS) to acquire images with an LE [117, 137]. A similar strategy is used in laser scanning confocal microscopy. RS consists in scanning the FOV with a focused light beam (see Figure 6.2b) by applying a phase tilt at the MCF entrance. The focused beam follows a trajectory $\Omega_{\text{tr}} \subset \Omega$ made of evenly spaced parallel lines (see Figure 6.3). For each discrete position $\boldsymbol{p}_i \in \Omega_{\text{tr}}$ that belongs to the pixel grid $\mathcal{X}$ (see section 2.1), the fluorescence signal emitted by the biological sample travels back in the optical fiber and is measured by the single pixel detector. The number of observations is directly related to the total length of the trajectory and its sampling rate, *i.e.*, to the tunable parameters of the experiment.

The main advantage of this scanning method is that, for high photon counting regime, the reconstruction is trivial for basic inspection of the observations. Each measure can be associated with a specific scanning position and then, with a pixel location in the reconstructed image. An estimate

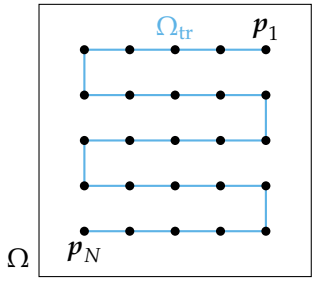

Figure 6.3 Raster scanning with a focused light beam. The focused spot scans each discrete position $\boldsymbol{p}_i \in \Omega_{\text{tr}} \subset \Omega$ with $i \in [N]$. The solid gray line represents the scanning trajectory Ω_{tr}. Black dots represent positions $\boldsymbol{p}_i$'s.

of $f(\boldsymbol{p}_i)$ is given by

$$\hat{f}(\boldsymbol{p}_i) = y_i \approx f(\boldsymbol{p}_i). \tag{6.6}$$

In other words, we consider that matrix $\boldsymbol{S}$ in (6.5) is well approximated by the identity operator over the FOV specified by $\{\boldsymbol{p}_i : i \in [M]\}$. However, even with a fiber arrangement optimized to produce point-like light beams (like Fermat's golden spiral shape [138]), distant side lobes in the light pattern (see Figure 6.2b) still limit the accuracy of this approximation.

This scanning technique requires a preliminary calibration of the SLM to generate a focused beam at the MCF output: specific sequences of proximal wavefronts are optimized to compensate the intrinsic mode scrambling in fibers and focus the light on specific positions of the FOV. This optimization needs an accurate estimation of the transmission matrix that relates the proximal wavefronts to the distal ones assuming that the fiber acts like a linear system.

6.4 Current challenges

RS acquisition provides fast image reconstruction but at the cost of some drawbacks, for instance: (*i*) the SLM needs to be calibrated to get a focused beam, (*ii*) imperfections of the focused beam are not corrected, and (*iii*) it is necessary to collect as many observations as the number of pixels in the discrete representation of the image. This last point forces the RS trajectory to visit each point of the pixel grid, or conversely, imposes a resolution of the final image directly related to the distance between two consecutive observations. These considerations highlight constraints on the usage of LE in realistic situations: (*i*) the device is sensitive to perturbations during

the calibration and imaging and (*ii*) the slow update rates of conventional SLMs limit the imaging speed [8]. This last challenge can be partly overcome by the use of scan mirrors (*e.g.*, galvanometric mirrors) combined with a fiber with a memory effect.

Hence, the core question of the second part of this thesis is the following: can we achieve accurate image reconstruction compared to RS using less measurements while keeping a short acquisition time? Without SLM calibration, the observed illumination pattern is a *speckle*, a pattern with multiple bright grains of light and dark regions with no well-defined global peak (see Figure 7.1a). Such a pattern results from the interference of multiple coherent light beams produced by each single mode cores when they are configured with arbitrary phases. It is similar to the pattern observed when laser light is reflected from or transmitted through an object or diffuser that is rough on the scale of the laser wavelength [74]. In some applications, *e.g.*, using coherent light like conventional holography or synthetic-aperture radar imaging, the presence of a speckle pattern is considered as an issue and methods were developed to suppress it or at least to minimize its effects [74]. But in some other imaging modalities, its random structure is appealing as it makes LE closer to recent compressive sensing and computational imaging procedures, *e.g.*, indirectly observing images with random sensing strategies [24, 33, 51, 117].

In Chapter 7, we mathematically introduce the formation of a speckle and its statistical properties, in a non-asymptotical framework. We show that despite their granular structure, an appropriate choice of the reconstruction parameters makes them good candidates to build efficient sensing matrices. In Chapter 8, we propose two acquisition strategies that rely on speckle illumination and that we validate through simulations and reconstruction of experimental data.

Appendix 6.A Fluorescence model

In this appendix, we detail the computation of the photon flux at steady-state when considering singlet state saturation and triplet state saturation.

Singlet state saturation

If light intensity is high enough, *i.e.*, if the energy of incident photons is sufficient to bring an electron to an upper state, fluorophores will absorb light with rate constant k_a defined as

$$k_a = \sigma S(\boldsymbol{x}) \propto \epsilon S(\boldsymbol{x}),$$

where σ is the attenuation cross-section and ϵ is the decadic molar attenuation coefficient depending on laser wavelength λ and on the chosen probe [38, 153]. Molecules in the ground state $\mathcal{S}_0$ reach an excited singlet state $\mathcal{S}$ of higher energy due to this absorption. They return then to their first state with a rate constant k_d by either emitting fluorescence or internal conversion. At each time instant t, a proportion $p_{\mathcal{S}}(t) \in [0,1]$ of fluorophores is in the excited singlet state. Temporal evolution of $p_{\mathcal{S}}(t)$ is given by

$$\frac{\mathrm{d}p_{\mathcal{S}}(t)}{\mathrm{d}t} = k_a[1 - p_{\mathcal{S}}(t)] - k_d p_{\mathcal{S}}(t), \tag{6.7}$$

and considering $p_{\mathcal{S}}(0) = 0$, we get

$$p_{\mathcal{S}}(t) = \frac{k_a}{k_a + k_d}\left(1 - e^{-(k_a+k_d)t}\right).$$

At steady-state, this proportion is equal to

$$\tilde{p}_{\mathcal{S}} = \frac{k_a}{k_a + k_d} = \frac{\sigma S(\boldsymbol{x})}{\sigma S(\boldsymbol{x}) + k_d}.$$

We observe that $\tilde{p}_{\mathcal{S}}$ saturates at 1 when $S(\boldsymbol{x})$ increases, as expected. Among all excited molecules returning to the ground state, only some of them will actually emit photons by fluorescence. The efficiency of this process is characterized by the emission quantum yield denoted by Q_e. The photon flux in $\boldsymbol{x}$ is finally given by

$$\begin{aligned} \varphi(\boldsymbol{x}, t) &= Q_e k_d \tilde{p}_{\mathcal{S}} f_0(\boldsymbol{x}, t) \\ &= Q_e k_d \frac{\sigma S(\boldsymbol{x})}{\sigma S(\boldsymbol{x}) + k_d} f_0(\boldsymbol{x}, t). \end{aligned} \tag{6.8}$$

Triplet state saturation

All of the fluorophores in the excited singlet state do not return to the ground state as explained in the previous section. Some of them cross to the excited triplet state $\mathcal{T}$ with a constant rate k_{isc} (*intersystem crossing*) [140, 153]. For fluorescein, rate $k_{isc} \ll k_d$ [140]. The lifetime in $\mathcal{T}$ state is three to six orders of magnitude bigger than the excited singlet state lifetime. Molecules are then trapped in this state during microseconds to milliseconds and the photon emission decays substantially. Expression (6.7) becomes

$$\frac{\mathrm{d}p_{\mathcal{S}}(t)}{\mathrm{d}t} = k_a p_{\mathcal{S}_0}(t) - k_d p_{\mathcal{S}}(t) - k_{isc} p_{\mathcal{S}}(t), \tag{6.9}$$

with $p_{\mathcal{S}_0}(t) + p_{\mathcal{S}}(t) + p_{\mathcal{T}}(t) = 1$. Considering the steady-state proportions $\tilde{p}_{\mathcal{S}_0}$, $\tilde{p}_{\mathcal{S}}$ and $\tilde{p}_{\mathcal{T}}$, the photon flux at $\boldsymbol{x}$ at time t is [140]

$$\varphi(\boldsymbol{x}, t) = Q_e k_d \frac{\sigma S(\boldsymbol{x}) k_1}{k_1(\sigma S(\boldsymbol{x}) + k_d + k_{isc}) + \sigma S(\boldsymbol{x}) k_{isc}} f_0(\boldsymbol{x}, t),$$

where k_1 is the rate constant for decay from triplet excited state to ground state. Since the lifetime in $\mathcal{T}$ state is long, this rate is very low.

7

The fascinating speckle phenomenon

THE astrophysical community discovered the speckle phenomenon at the end of the 19th century while observing stars with telescopes under different atmospheric conditions [59]. It was brought in the spotlight only a few decades after with the laser invention in the early 60's. In 1962 and 1963, several authors reported the observation of a granular pattern when the (coherent) light of a laser is scattered from a surface that is rough at the wavelength scale, *e.g.*, a piece of paper [75, 95]. The roughness of the surface introduces relative delays between the different scattered components leading to interferences on a distant observation plane. Goodman established the first basic statistical properties of this particular speckle structure in 1963 [73, 75]. Since then, a lot of research in this field has been and is still conducted. For a comprehensive book on the topic, we recommend *Speckle phenomena in optics: theory and applications* [74].

Before going into the details of acquisition strategies in Chapter 8, let us have a close look at the mathematics beyond the speckle formation in section 7.1. In the case of the lensless endoscope (LE) described in section 6.1, the spatial light modulator (SLM) plays the role of a rough surface or a diffuser by randomly modifying the phase of the excitation signal in each core. We study the main statistical properties of the resulting light pattern in section 7.2. Our main contribution is to show that the non-asymptotical

behavior of the tail of the speckle distribution is sub-exponential. The characterization of the speckle properties is essential to design appropriate sensing models. It will also bring useful insight on the spatial resolution we can hope to recover after imaging. Finally, in section 7.3, we mathematically explain the memory effect that is exploited in Chapter 8.

7.1 Speckle formation

Let us consider a laser beam of wavelength λ injected into a multicore fiber (MCF) with J cores. We denote by $\{\boldsymbol{q}_j\}_{j=1}^{J} \subset \mathbb{R}^2$ the J core locations in the 2D fiber endface $\mathcal{Z}_0$. With each core j, we associate a complex amplitude α_j representing the random delay introduced by the SLM. We assume i.i.d. delays. The field emitted by a single core is well described by its complex amplitude multiplied by a narrow envelope U_0. The field U_0 is approximately Gaussian with a maximum amplitude equal to 1 and a standard deviation σ_c that depends on the laser wavelength. The standard deviation is related to mode-field diameter d through $d = 2.35 \times \sigma_c$ [137].

The 2D speckle pattern is the intensity of the electromagnetic field E_z propagated on a plane $\mathcal{Z}$ parallel to $\mathcal{Z}_0$ at a distance $z > 0$. Fourier optics tells us that, at each location $\boldsymbol{x} \in \mathcal{Z} \subset \mathbb{R}^2$, E_z is obtained via the angular spectrum (AS) representation[1] [72],

$$E_z(\boldsymbol{x}) = (E_0 * H_z)(\boldsymbol{x}), \tag{7.1}$$

where E_0 is the electromagnetic field emanating from the MCF endface,

$$E_0(\boldsymbol{x}) = [U_0 * \sum_{j=1}^{J} \alpha_j \delta(\cdot - \boldsymbol{q}_j)](\boldsymbol{x}), \tag{7.2}$$

and H_z is the inverse Fourier transform of the AS propagator defined as

$$\hat{H}_z(\boldsymbol{k}) = \exp(-\mathrm{i}z\sqrt{k^2 - \|\boldsymbol{k}\|_2^2}), \tag{7.3}$$

with $k = 2\pi/\lambda$ and $\boldsymbol{k} = (k_x, k_y)^\top$ is the 2D-coordinate in the reciprocal space of $\boldsymbol{x}$. Let $U_z := U_0 * H_z$, the speckle pattern S on plane $\mathcal{Z}$ is therefore

$$S(\boldsymbol{x}) := |E_z(\boldsymbol{x})|^2 = \Big|\sum_{j=1}^{J} \alpha_j U_z(\boldsymbol{x} - \boldsymbol{q}_j)\Big|^2. \tag{7.4}$$

[1] Assuming optical field in homogeneous, isotropic, linear and source-free medium [72].

Remark 7.1 (Focused illumination). It is possible to create deterministic illumination patterns that do not present the speckle granular structure. Such an example is depicted in Figure 6.2b where we observe an illumination pattern focused on a narrow spot. This pattern, achieved for a Fermat's golden spiral core arrangement, is used for RS (see section 6.3). In this case, the complex amplitudes in (7.4) are set to 1 after a convenient calibration of the optical system [136]. This particular configuration ensures that all the components of the electromagnetic field constructively interfere in the origin of $\mathcal{Z}$. The expression of the light pattern focused at $\mathbf{0}$ in $\mathcal{Z}$ is

$$S_{\text{foc}}(\boldsymbol{x}) \coloneqq |\sum_{j=1}^{J} U_z(\boldsymbol{x} - \boldsymbol{q}_j)|^2. \tag{7.5}$$

Equation (7.4) can be simplified with the *far-field* assumption. This assumption considers that the illumination pattern is far from $\mathcal{Z}_0$, *i.e.*, $z \gg kD^2$ with D the diameter of the MCF endface. In this case, the Fraunhofer approximation holds [72]. Combined with the paraxial approximation which supposes small incidence angles with respect to the optical axis, we express E_z as a modulated scaling of the Fourier transform $\hat{E}_0$ [48, 72] (the full development is in Appendix 7.A),

$$E_z(\boldsymbol{x}) \approx -\frac{e^{-\mathrm{i}kz}}{\mathrm{i}\lambda z} e^{-\frac{\mathrm{i}k\|\boldsymbol{x}\|_2^2}{2z}} \hat{E}_0\left(-\frac{k\boldsymbol{x}}{z}\right). \tag{7.6}$$

Therefore, using (7.2) and the convolution theorem, the far-field approximation of S reads

$$S(\boldsymbol{x}) \approx \frac{1}{(\lambda z)^2} \left|\hat{U}_0\left(-\frac{k\boldsymbol{x}}{z}\right)\right|^2 \left|\sum_{j=1}^{J} \alpha_j e^{\frac{\mathrm{i}k\boldsymbol{q}_j^\top \boldsymbol{x}}{z}}\right|^2, \tag{7.7}$$

where the first factor is deterministic and the second one is random.

7.2 Statistical properties of speckles

Without loss of generality, we assume that $|\alpha_j| = 1$ and that the phases follow a uniform distribution on $[0, 2\pi]$, *i.e.*, $\alpha_j \sim_{\text{i.i.d.}} \exp(\mathrm{i}\mathcal{U}([0, 2\pi]))$. This configuration can be reached by properly shaping the laser beam. Indeed, due to the low coupling between the MCF cores, the phase of these amplitudes is strongly correlated with the phase of the light injected in the cores at the proximal end [9].

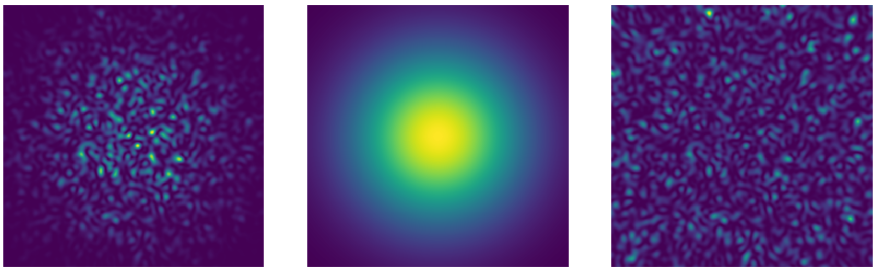

Figure 7.1 (a) One of the simulated speckle patterns obtained without fiber calibration, (b) mean speckle field $\bar{S}$ and (c) the residual field corresponding to (a). Images were simulated for a Fermat's golden spiral fiber core arrangement with $J = 120$, $D = 113\,\mu$m and $3\sigma_c = 3.2\,\mu$m. Experiment parameters are $\lambda = 1\,\mu$m, $z = 500\,\mu$m, and $a = 2\,\mu$m.

7.2.1 First- and second-order statistical properties

The intensity of S at location $\boldsymbol{x}$ is a random variable. Since $\mathbb{E}\{\alpha_j \alpha_k^*\} = \delta_{jk}$, the *mean speckle field* $\bar{S}$ is given by

$$\bar{S}(\boldsymbol{x}) := \mathbb{E}S(\boldsymbol{x}) = \sum_{j=1}^{J} |U_z(\boldsymbol{x} - \boldsymbol{q}_j)|^2 = [|U_z|^2 * \mathrm{AF}](\boldsymbol{x}), \tag{7.8}$$

where $\mathrm{AF}(\boldsymbol{x}) := \sum_{j=1}^{J} \delta(\boldsymbol{x} - \boldsymbol{q}_j)$ is the array factor (AF) related to the spatial arrangement of the cores. The mean field only depends on wavelength λ, the size of the cores and distance z (all included in $|U_z|^2$) as well as the cores arrangement. Figure 7.1b represents $\bar{S}$ for a Fermat's spiral core arrangement. Regarding (7.7) and since $\mathbb{E}\alpha_j = 0$, an approximation for the mean speckle field is

$$\bar{S}(\boldsymbol{x}) \approx \frac{J}{(\lambda z)^2} \left| \hat{U}_0 \left(-\frac{k\boldsymbol{x}}{z} \right) \right|^2. \tag{7.9}$$

We define the *residual field* $\tilde{R}$ such that $\tilde{R}(\boldsymbol{x}) := (S(\boldsymbol{x}) - \bar{S}(\boldsymbol{x}))/\bar{S}(\boldsymbol{x})$ and we write $S(\boldsymbol{x})$ as

$$S(\boldsymbol{x}) = \bar{S}(\boldsymbol{x}) \left(1 + \tilde{R}(\boldsymbol{x})\right), \tag{7.10}$$

where $\bar{S}(\boldsymbol{x})\tilde{R}(\boldsymbol{x})$ represents the variations of $S(\boldsymbol{x})$ around its mean. Those variations result from the (constructive and destructive) interferences be-

tween the individual fields emitted by the cores.

As shown by (7.10), $\bar{S}$ acts like a vignetting window while the randomness of the speckle field S comes from the residual field $\tilde{R}$ (see Figure 7.1). This field exhibits a spatial granular structure indicating that, for two points $\boldsymbol{x}, \boldsymbol{x}+\boldsymbol{\tau}$ close to each other, the two random variables $\tilde{R}(\boldsymbol{x})$ and $\tilde{R}(\boldsymbol{x}+\boldsymbol{\tau})$ are correlated. We show hereinafter that such a correlation exists as soon as $\|\boldsymbol{\tau}\|_2 \lesssim \lambda z/D$—the average size of a speckle grain scales like $\mathcal{O}(\lambda z/D)$. This is achieved by studying the second-order statistics of the residual field $\tilde{R}$, *i.e.*, the *autocorrelation* $\Gamma_{\tilde{R}}$ defined as

$$\Gamma_{\tilde{R}}(\boldsymbol{x}, \boldsymbol{x}+\boldsymbol{\tau}) \coloneqq \mathbb{E}(\tilde{R}(\boldsymbol{x})\tilde{R}^*(\boldsymbol{x}+\boldsymbol{\tau})), \tag{7.11}$$

with $\boldsymbol{\tau} \coloneqq (\tau_x, \tau_y)^\top$. Using approximations (7.7) and (7.9) to express $\tilde{R}$,

$$\tilde{R}(\boldsymbol{x}) \approx \frac{1}{J}\Big|\sum_{j=1}^{J} \alpha_j e^{\frac{\mathrm{i}k\boldsymbol{q}_j^\top \boldsymbol{x}}{z}}\Big|^2 - 1,$$

and remembering that $\mathbb{E}\{\alpha_j\alpha_k^*\alpha_l^*\alpha_m\} = \delta_{jk}\delta_{lm} + \delta_{jl}\delta_{km} - \delta_{jklm}$, we find

$$\begin{aligned}
\Gamma_{\tilde{R}}(\boldsymbol{x}, \boldsymbol{x}+\boldsymbol{\tau}) &\approx \frac{1}{J^2}\sum_{j,k,l,m=1}^{J} \mathbb{E}\{\alpha_j\alpha_k^*\alpha_l^*\alpha_m\} e^{\frac{\mathrm{i}k(\boldsymbol{q}_j-\boldsymbol{q}_k)^\top \boldsymbol{x}}{z}} e^{-\frac{\mathrm{i}k(\boldsymbol{q}_l-\boldsymbol{q}_m)^\top (\boldsymbol{x}+\boldsymbol{\tau})}{z}} - 1 \\
&\approx \frac{1}{J^2}\sum_{j,l=1}^{J} 1 + \frac{1}{J^2}\sum_{j,k=1}^{J} e^{-\frac{\mathrm{i}k(\boldsymbol{q}_j-\boldsymbol{q}_k)^\top \boldsymbol{\tau}}{z}} - \frac{1}{J^2}\sum_{j=1}^{J} 1 - 1 \\
&= \frac{1}{J^2}\Big|\mathcal{F}\Big(\sum_{j=1}^{J}\delta(\cdot - \boldsymbol{q}_j)\Big)\Big[-\frac{k\boldsymbol{\tau}}{z}\Big]\Big|^2 - \frac{1}{J} \\
&= \frac{1}{J^2}\Big|\mathcal{F}(\mathrm{AF})\Big[-\frac{k\boldsymbol{\tau}}{z}\Big]\Big|^2 - \frac{1}{J} \approx \Gamma_{\tilde{R}}(\boldsymbol{\tau}).
\end{aligned} \tag{7.12}$$

With the use of Fraunhofer approximation, this quantity does not depend on $\boldsymbol{x}$ anymore. Interestingly, the autocorrelation—and consequently the speckle size—is directly related to the Fourier transform of the array factor.

When we are far from $\mathcal{Z}_0$, an MCF with almost uniformly distributed core locations can be seen as a circular spot with diameter D and area A,

$$\frac{1}{J}\sum_{j=1}^{J}\delta(\boldsymbol{x}-\boldsymbol{q}_j) \approx \frac{1}{A}\mathrm{disk}\left(\frac{2\|\boldsymbol{x}\|_2}{D}\right) = \begin{cases} 1/A & \text{if } \|\boldsymbol{x}\|_2 \le D/2 \\ 0 & \text{otherwise} \end{cases}. \tag{7.13}$$

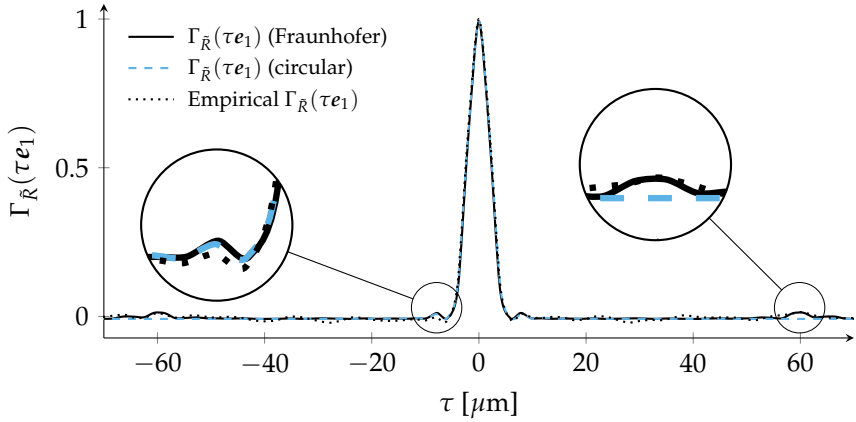

Figure 7.2 Autocorrelation of the residual field $\tilde{R}$ for three cases: (*i*) using Fraunhofer approximation (solid line), (*ii*) using Fraunhofer approximation and assumption of a circular aperture (dashed blue line), and (*iii*) by empirically computing the mean (over 25 trials) autocorrelation based on 1,000 realizations of $\tilde{R}$ (dotted line). The cores arrangement is a Fermat's golden spiral with $J = 120$ cores, diameter $D = 113\,\mu$m and $3\sigma_c = 3.2\,\mu$m. Experiment parameters are $\lambda = 1\,\mu$m, $z = 500\,\mu$m, and $a = 2\,\mu$m.

The Fourier transform of this function is the jinc function with unit value at the origin [72, 74]. Expression (7.12) becomes

$$\Gamma_{\tilde{R}}(\tau) \approx \left|2\Big(\frac{\pi D}{\lambda z}\tau\Big)^{-1} J_1\Big(\frac{\pi D}{\lambda z}\tau\Big)\right|^2 - \frac{1}{J}, \tag{7.14}$$

where $\tau := \|\boldsymbol{\tau}\|_2$, $k = 2\pi/\lambda$ and J_1 is the first-order Bessel function of the first kind. Following [74], we define the average area of a speckle grain as

$$A_\mathrm{s} := \iint_{-\infty}^{\infty} \Gamma_{\tilde{R}}(\boldsymbol{\tau})/\Gamma_{\tilde{R}}(\mathbf{0})\,\mathrm{d}\boldsymbol{\tau},$$

with $\Gamma_{\tilde{R}}(\mathbf{0}) = 1 - 1/J$. For a circular aperture as considered above, A_s is obtained via Parseval's identity and the average radius is $r := \sqrt{A_\mathrm{s}/\pi}$,

$$A_\mathrm{s} = \frac{(\lambda z)^2}{\pi(D/2)^2} \quad \text{and} \quad r = \frac{\lambda z}{\pi(D/2)}. \tag{7.15}$$

We thus get $r \propto \lambda z/D$. For the parameters of the simulation in Figure 7.2, the radius of a speckle grain is 2.8 μm.

Remark 7.2. Quantities (7.14) and (7.15) are easily computable since they only depend on the experiment parameters J, D, λ and z. Figure 7.2 shows $\Gamma_{\tilde{R}}$ as a function of $\boldsymbol{\tau}$ (with $\boldsymbol{\tau} = \tau \boldsymbol{e}_1$ and $\boldsymbol{e}_1$ the unit vector aligned with the horizontal axis of the 2D image) obtained with Fraunhofer approximation and the stronger assumption of a circular spot. Mean empirical estimations of $\Gamma_{\tilde{R}}$ based on 1,000 realizations of the residual field are also displayed for $\boldsymbol{x} = \boldsymbol{0}$. Both theoretical approximations explain well the main peak of the autocorrelation, which is similar to the peak observed when the light beam is focused (see Figure 6.2b). Even if distant side lobes are absent with the circular aperture assumption, (7.14) still provides a reliable closed form expression for the radius of a speckle grain.

Remark 7.3. With the Fraunhofer approximation, (7.5) becomes

$$\begin{aligned} S_{\text{foc}}(\boldsymbol{x}) &\approx \frac{1}{(\lambda z)^2} |\hat{U}_0 \mathcal{F}[\text{AF}]|^2 \left(-\frac{k\boldsymbol{x}}{z} \right) \\ &\approx \bar{S}(\boldsymbol{x})(J\Gamma_{\tilde{R}}(\boldsymbol{x}) + 1). \end{aligned}$$

Interestingly, $S_{\text{foc}}(\boldsymbol{x})$ is also vignetted and is directly related to the autocorrelation of the speckles.

7.2.2 Tail of the distribution

In [74], Goodman derives the probability density function (pdf) of a speckle with a large number of phasors (corresponding to the cores in our case). The use of the central limit theorem leads to an intensity $S(\boldsymbol{x})$ distributed according to an exponential law [74, chapter 3]. This is valid in the *asymptotic* case when the number of cores tends to infinity. In this section, we show that the (non-asymptotic) distribution of $S(\boldsymbol{x})$ is sub-exponential.

Figure 7.3 shows an empirical approximation of the pdf of $S(\boldsymbol{0})$ based on the generation of 10,000 discretized speckle patterns of size 128×128. The shapes of the histograms for other locations $\boldsymbol{x}$ are similar: we observe an exponential decay of the approximated pdf.

Proposition 7.1 *Let $S(\boldsymbol{x})$ be the intensity of a speckle pattern at location $\boldsymbol{x}$ in the field of view as defined in (7.4). The modulus of the complex amplitudes α_j's is equal to 1 and their phases follow a uniform distribution on $[0, 2\pi]$. Then, $S(\boldsymbol{x})$ is a* sub-exponential *random variable as defined in Definition 4.2 with a sub-exponential norm bounded by the mean intensity,* i.e.,

$$\|S(\boldsymbol{x})\|_{\psi_1} \leq \bar{S}(\boldsymbol{x}). \tag{7.16}$$

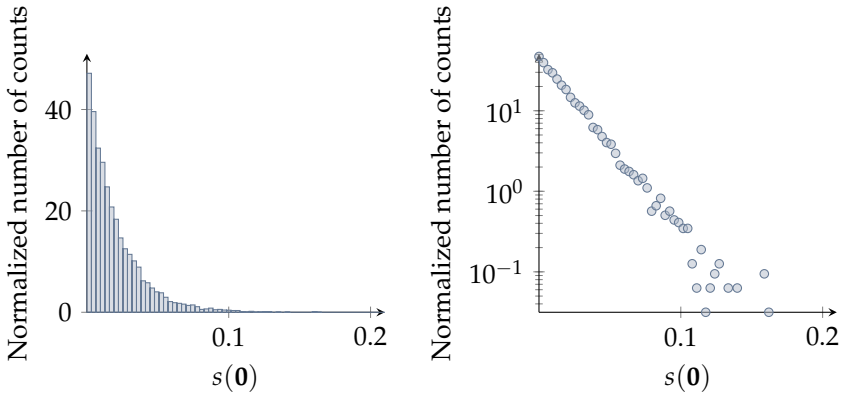

Figure 7.3 Estimation of the probability density function (pdf) of $S(\mathbf{0})$ based on the simulation of 10,000 speckle patterns of size 128×128. They were generated for a Fermat's spiral core arrangement ($J = 120$) and the following parameters: $\lambda = 1\,\mu$m, $z = 500\,\mu$m, $3\sigma_c = 3.2\,\mu$m and $a = 2\,\mu$m. Both figures show the same data but with a logarithmic scale for the y axis of the right graph. We observe an exponential decay of the estimated pdf.

Proof. According to Proposition 4.1, a random variable is sub-exponential if the moments of the distribution are bounded, *i.e.*, if there exists $K_2 \in \mathbb{R}_0^+$ such that $(\mathbb{E}|S(\boldsymbol{x})|^p)^{1/p} \leq pK_2$ is satisfied for all $p \geq 1$. The moments of $|S(\boldsymbol{x})| = S(\boldsymbol{x})$ (since $S(\boldsymbol{x}) \geq 0$) are given by

$$\begin{aligned}
\mathbb{E}S(\boldsymbol{x})^p &= \mathbb{E}\Big(\sum_{j,k=1}^{J} \alpha_j \alpha_k^* U_z(\boldsymbol{x}-\boldsymbol{q}_j) U_z^*(\boldsymbol{x}-\boldsymbol{q}_k)\Big)^p \\
&= \sum_{\substack{j_1,\dots,j_p=1 \\ k_1,\dots,k_p=1}}^{J} \mathbb{E}\{\alpha_{j_1}\alpha_{k_1}^* \dots \alpha_{j_p}\alpha_{k_p}^*\} U_z(\boldsymbol{x}-\boldsymbol{q}_{j_1}) U_z^*(\boldsymbol{x}-\boldsymbol{q}_{k_1}) \dots \\
&\qquad U_z(\boldsymbol{x}-\boldsymbol{q}_{j_p}) U_z^*(\boldsymbol{x}-\boldsymbol{q}_{k_p}).
\end{aligned}$$

Since $\mathbb{E}\alpha_j = 0$ and $\mathbb{E}\{\alpha_j \alpha_k^*\} = \delta_{jk}$, expectation $\mathbb{E}\{\alpha_{j_1}\alpha_{k_1}^* \dots \alpha_{j_p}\alpha_{k_p}^*\}$ is non-zero when each complex amplitude can be associated with its complex conjugate. For instance, the terms of the sum satisfying $j_1 = k_1, j_2 = k_2, \dots j_p = k_p$ are non-zero. There are $p!$ combinations of the indices that

lead to $\mathbb{E}\{\alpha_{j_1}^* \alpha_{k_1} \dots \alpha_{j_p}^* \alpha_{k_p}\} = 1$. We then have

$$\mathbb{E}S(\boldsymbol{x})^p \leq p! \sum_{j_1,\dots,j_p=1}^{J} |U_z(\boldsymbol{x}-\boldsymbol{q}_{j_1})|^2 \dots |U_z(\boldsymbol{x}-\boldsymbol{q}_{j_p})|^2 = p!\bar{S}(\boldsymbol{x})^p \leq p^p \bar{S}(\boldsymbol{x})^p.$$

The first inequality comes from the fact that some (non-negative) terms of the sum are considered multiple times (*e.g.*, the term corresponding to $j_1 = j_2 = \dots = j_p$). Finally,

$$(\mathbb{E}|S(\boldsymbol{x})|^p)^{1/p} \leq p\bar{S}(\boldsymbol{x}),$$

for all $p \geq 1$. The random variable $S(\boldsymbol{x})$ is consequently sub-exponential. A bound on its sub-exponential norm is given by

$$\|S(\boldsymbol{x})\|_{\psi_1} = \sup_{p\geq 1} p^{-1}(\mathbb{E}|S(\boldsymbol{x})|^p)^{1/p} \leq \bar{S}(\boldsymbol{x}). \tag{7.17}$$

An alternative proof[2] showing that $\|S(\boldsymbol{x})\|_{\psi_1} \lesssim \bar{S}(\boldsymbol{x})$ ($\lesssim$ instead of $\leq$) is based on the fact that $|\alpha_j|$ is bounded (see Appendix 7.B or [80]).

Proposition 7.2 *Following Proposition 7.1, $\tilde{R}(\boldsymbol{x})$ is a zero-mean sub-exponential random variable with a sub-exponential norm bounded by* 1.

Proof. The proof for the mean is straightforward. Since $S(\boldsymbol{x}) \geq 0$ and $\bar{S}(\boldsymbol{x}) > 0$, $\tilde{R}(\boldsymbol{x}) = S(\boldsymbol{x})/\bar{S}(\boldsymbol{x}) - 1$ is then lower and upper bounded by

$$-1 \leq \tilde{R}(\boldsymbol{x}) < S(\boldsymbol{x})/\bar{S}(\boldsymbol{x}).$$

The moments of $|\tilde{R}(\boldsymbol{x})|$ are bounded by

$$\begin{aligned} \mathbb{E}|\tilde{R}(\boldsymbol{x})|^p &< \max(1, \mathbb{E}S(\boldsymbol{x})^p/\bar{S}(\boldsymbol{x})^p) \\ &\leq \max(1, p^p) = p^p, \qquad \text{(from Proposition 7.1)} \end{aligned}$$

for all $p \geq 1$. Finally, $(\mathbb{E}|\tilde{R}(\boldsymbol{x})|^p)^{1/p} < p$. ∎

Proposition 7.2 informs us that the tail of the distribution of $\tilde{R}(\boldsymbol{x})$ decreases exponentially fast with a threshold $s \geq 0$, *i.e.*, for some universal constants $C, c > 0$,

$$\mathbb{P}\left(\left|\tilde{R}(\boldsymbol{x})\right| \geq s\right) \leq Ce^{-cs}.$$

[2] Credit to Laurent Jacques for it.

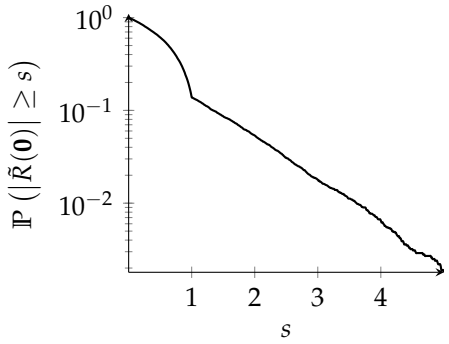

Figure 7.4 Estimation of $\mathbb{P}\left(\left|\tilde{R}(\mathbf{0})\right| \geq s\right)$ as a function of s based on the simulation of 10,000 speckle patterns of size 128×128. The fiber cores arrangement is a Fermat's spiral with $J = 120$, $D = 113\,\mu$m and $3\sigma_c = 3.2\,\mu$m. Experiment parameters are $\lambda = 1\,\mu$m, $z = 500\,\mu$m, and $a = 2\,\mu$m. We do observe an exponential decay of the tail of the distribution ($s \geq 1$).

Figure 7.4 shows an empirical approximation of $\mathbb{P}(|\tilde{R}(\mathbf{0})| \geq s)$ as a function of s based on the generation of 10,000 discretized speckle patterns of size 128×128. For $s \geq 1$ (corresponding to the tail), we do observe an exponential decay of the distribution.

7.3 Translation of an illumination pattern

One of the key properties of the MCF considered in this work is the low coupling between its J cores, *i.e.*, its *memory effect*. It expresses the fact that the phase of the light emitted from j^{th} core is roughly the same as the phase of the input light up to a constant term depending on intrinsic properties of the core [9]. A small change in the incident angle of the incoming light results in the same change in the phase of the output wavefront, and further in a translation of the illumination pattern (see Figure 7.5).

In this section, we explain how and under which conditions a modulation of the electric field in plane $\mathcal{Z}_0$, using for instance a galvanometer mirror, leads to a shift of the observed pattern in plane $\mathcal{Z}$. In particular, we can translate the residual field $\tilde{R}$ defined in (7.10) within the intensity vignetting imposed by the mean speckle field $\bar{S}$.

Let us apply a phase ramp $\boldsymbol{\theta}^\top \boldsymbol{x}$ to the complex amplitudes α_j's with $\boldsymbol{\theta} = (\theta_x, \theta_y)^\top$ the relative tilt imposed by the scan mirror. The new electro-

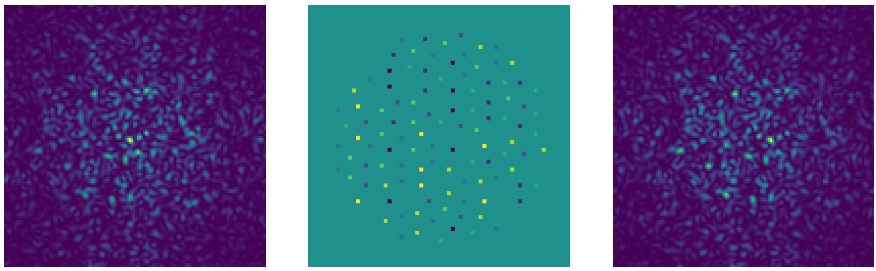

(a) (b) (c)

Figure 7.5 (a) Initial speckle pattern in $\mathcal{Z}$, (b) zoom on phase tilts applied on each complex amplitude and (c) the resulting shifted speckle in $\mathcal{Z}$. Images were simulated for a Fermat's spiral cores arrangement with $J = 120$, $D = 113\,\mu$m and $3\sigma_c = 3.2\,\mu$m. Experiment parameters are $\lambda = 1\,\mu$m, $z = 500\,\mu$m, and $a = 2\,\mu$m.

magnetic field $\tilde{E}_0$ and its Fourier spectrum $\hat{\tilde{E}}_0$ are given by

$$\tilde{E}_0(\boldsymbol{x}) = [U_0 * e^{\mathrm{i}\boldsymbol{\theta}^\top \cdot} \sum_{j=1}^{J} \alpha_j \delta(\cdot - \boldsymbol{q}_j)](\boldsymbol{x}) \quad \text{and} \quad \hat{\tilde{E}}_0(\boldsymbol{k}) = \hat{U}_0(\boldsymbol{k}) \sum_{j=1}^{J} \alpha_j e^{-\mathrm{i}\boldsymbol{q}_j^\top(\boldsymbol{k}-\boldsymbol{\theta})}.$$

The far-field approximation (7.7) for speckle $\tilde{S}$ writes in this case

$$\tilde{S}(\boldsymbol{x}) \approx \frac{1}{(\lambda z)^2} \Big| \hat{U}_0\Big(-\frac{k\boldsymbol{x}}{z} \Big) \Big|^2 \Big| \sum_{j=1}^{J} \alpha_j e^{\frac{\mathrm{i}k}{z} \boldsymbol{q}_j^\top (\boldsymbol{x} + \frac{z}{k}\boldsymbol{\theta})} \Big|^2 \tag{7.18}$$

$$= \bar{S}(\boldsymbol{x}) \Big[1 + \tilde{R}\Big(\boldsymbol{x} + \frac{z\boldsymbol{\theta}}{k} \Big) \Big]. \tag{7.19}$$

Thus, provided that $\|\boldsymbol{x}\|_2 \ll z$ and $z \gg kD^2$, a non-zero tilt $\boldsymbol{\theta}$ induces a shift $-z\boldsymbol{\theta}/k$ of the residual field, but the vignetting window remains unchanged. This effect is valid for any configuration of the complex amplitudes whether it is random or deterministic.

In this chapter, we analyzed the statistical properties of a speckle random field including its non-asymptotical distribution. In Chapter 8, this preliminary work will justify the possibility to estimate an image from observations acquired via speckle illumination, by establishing links with the compressive sensing theory. We will exploit the memory effect described in section 7.3 in one of the sensing strategies described in the next chapter.

Appendix 7.A Fraunhofer approximation

In the far-field, it is common to use the paraxial approximation which assumes only small incidence angles with respect to the optical axis [72]. In this case, $\|\boldsymbol{k}\|_2^2 \ll k^2$ and $\sqrt{k^2 - \|\boldsymbol{k}\|_2^2}$ is well approximated by its first-order Taylor expansion,

$$\sqrt{k^2 - \|\boldsymbol{k}\|_2^2} \approx \frac{k - \|\boldsymbol{k}\|_2^2}{2k}.$$

Regarding this last expression, an approximation for (7.3) is

$$\hat{H}_z(\boldsymbol{k}) \approx e^{-\mathrm{i}z\left(k - \frac{\|\boldsymbol{k}\|_2^2}{2k}\right)}.$$

The inverse Fourier transform of $\hat{H}_z$ is given by

$$H_z(\boldsymbol{x}) \approx -\frac{e^{-\mathrm{i}kz}}{\mathrm{i}\lambda z} e^{-\frac{\mathrm{i}k\|\boldsymbol{x}\|_2^2}{2z}}. \tag{7.20}$$

Introducing (7.20) in (7.1) leads to the Fresnel diffraction formula [48],

$$\begin{aligned} E_z(\boldsymbol{x}) &\approx -\frac{e^{-\mathrm{i}kz}}{\mathrm{i}\lambda z} e^{-\frac{\mathrm{i}k\|\boldsymbol{x}\|_2^2}{2z}} \iint_{-\infty}^{\infty} E_0(\boldsymbol{x}') e^{\frac{\mathrm{i}k\boldsymbol{x}^\top \boldsymbol{x}'}{z}} e^{-\frac{\mathrm{i}\|\boldsymbol{x}'\|_2^2}{2z}} \,\mathrm{d}\boldsymbol{x}' \\ &= -\frac{e^{-\mathrm{i}kz}}{\mathrm{i}\lambda z} e^{-\frac{\mathrm{i}k\|\boldsymbol{x}\|_2^2}{2z}} \mathcal{F}\left(E_0 e^{-\frac{\mathrm{i}\|\cdot\|_2^2}{2z}}\right)\left(-\frac{k\boldsymbol{x}}{z}\right). \end{aligned}$$

Moreover, if we assume $z \gg k\|\boldsymbol{x}'\|_{2,\max}^2$ with $\|\boldsymbol{x}'\|_{2,\max}^2$ the maximum value of $\|\boldsymbol{x}'\|_2^2$ such that $E_0(\boldsymbol{x}') \neq 0$, we get the Fraunhofer approximation [48][3],

$$E_z(\boldsymbol{x}) \approx -\frac{e^{-\mathrm{i}kz}}{\mathrm{i}\lambda z} e^{-\frac{\mathrm{i}k\|\boldsymbol{x}\|_2^2}{2z}} \hat{E}_0\left(-\frac{k\boldsymbol{x}}{z}\right).$$

Appendix 7.B Alternative proof for the sub-exponentiality of speckle fields

Following [157, 158], a *sub-exponential* (or *sub-Gaussian*) random variable $X \in \mathbb{C}$ is characterized by a finite sub-exponential (resp. sub-Gaussian) norm $\|X\|_{\psi_1}$ (resp. $\|X\|_{\psi_2}$) defined by

$$\|X\|_{\psi_p} := \sup_{q \geq 1} q^{-1/p} (\mathbb{E}|X|^q)^{1/q}, \quad p \in \{1, 2\}. \tag{7.21}$$

[3] In the context of LE, we assume $z \gg kD^2$ with D the diameter of the MCF distal end.

For instance, Gaussian and Laplacian random variables have finite sub-Gaussian and sub-exponential norms, respectively. For a bounded random variable both norms are finite, *i.e.*, if $|X| \leq C$, then $\|X\|_{\psi_p} \leq C$ for $p \in \{1,2\}$. For our complex amplitudes, $\|\alpha_j\|_{\psi_1} \leq 1$ and $\|\alpha_j\|_{\psi_2} \leq 1$ for $j \in [J]$.

These norms are totally equivalent to characterize the tail distribution of their random variables. In fact, for $p \in \{1,2\}$, the norm $K := \|X\|_{\psi_p}$ is finite *if and only if* the tail distribution of X satisfies $\mathbb{P}\{|X| \geq t\} \leq 2e^{-ct^p/K^p}$ for all $t \geq 0$, for some universal constant $c > 0$. This is similar to the known tail distributions of Gaussian or Laplacian random variables for $p = 2$ and $p = 1$, respectively.

Proposition 7.3 *Given a location $\boldsymbol{x}$ and J i.i.d. complex random amplitudes $\{\alpha_j, j \in [J]\}$ with unit modulus gathered in $\boldsymbol{\alpha} := (\alpha_1, \dots, \alpha_J)$, both the speckle intensity $S(\boldsymbol{x})$ and the residual field $\tilde{R}(\boldsymbol{x})$ are sub-exponential, and*

$$\|S(\boldsymbol{x})\|_{\psi_1} \lesssim \bar{S}(\boldsymbol{x}) \quad \textit{and} \quad \|\tilde{R}(\boldsymbol{x})\|_{\psi_1} \lesssim 1. \tag{7.22}$$

Proof. Defining $\boldsymbol{u}(\boldsymbol{x}) := \big(U_z(\boldsymbol{x}-\boldsymbol{q}_1), \cdots, U_z(\boldsymbol{x}-\boldsymbol{q}_J)\big)^* \in \mathbb{C}^J$, we can rewrite (7.4) as $S(\boldsymbol{x}) = |\langle \boldsymbol{\alpha}, \boldsymbol{u}(\boldsymbol{x})\rangle|^2$. From [158, Lemma 5.14], $\|X\|_{\psi_2}^2 \leq \|X^2\|_{\psi_1} \leq 2\|X\|_{\psi_2}^2$, therefore,

$$\big\||\langle \boldsymbol{\alpha}, \boldsymbol{u}(\boldsymbol{x})\rangle|^2\big\|_{\psi_1} \leq 2\|\langle \boldsymbol{\alpha}, \boldsymbol{u}(\boldsymbol{x})\rangle\|_{\psi_2}^2.$$

Moreover, from [158, Lemma 5.9], for J i.i.d. sub-Gaussian random variables X_j, we have the approximate *rotation invariance* $\|\sum_{j=1}^J X_j\|_{\psi_2}^2 \lesssim \sum_{j=1}^J \|X_j\|_{\psi_2}^2$. For $X_j := \alpha_j u_j^*(\boldsymbol{x})$, $\langle \boldsymbol{\alpha}, \boldsymbol{u}(\boldsymbol{x})\rangle = \sum_{j=1}^J X_j$, using $\|\alpha_j\|_{\psi_2} \leq 1$ and the fact that $\|\cdot\|_{\psi_2}$ is a norm, this property involves that

$$\|\langle \boldsymbol{\alpha}, \boldsymbol{u}(\boldsymbol{x})\rangle\|_{\psi_2}^2 \lesssim \sum_{j=1}^J \|X_j\|_{\psi_2}^2 = \sum_{j=1}^J \|\alpha_j\|_{\psi_2}^2 |u_j(\boldsymbol{x})|^2 \leq \sum_{j=1}^J |u_j(\boldsymbol{x})|^2 = \bar{S}(\boldsymbol{x}),$$

which proves the first inequality in (7.22). Regarding the second inequality, since $\|\cdot\|_{\psi_1}$ is a norm, it respects the triangular inequality, and from (7.10), we get

$$\begin{aligned}\|\tilde{R}(\boldsymbol{x})\|_{\psi_1} &= \|\bar{S}(\boldsymbol{x})^{-1}(S(\boldsymbol{x}) - \bar{S}(\boldsymbol{x}))\|_{\psi_1} \\ &\leq \|\bar{S}(\boldsymbol{x})^{-1}S(\boldsymbol{x})\|_{\psi_1} + 1 = \bar{S}(\boldsymbol{x})^{-1}\|S(\boldsymbol{x})\|_{\psi_1} + 1 \lesssim 1.\end{aligned}$$

■

8

Compressive acquisition schemes in lensless endoscopy

In this chapter, we investigate an acquisition strategy for lensless endoscopes (LE) based on compressive sensing (CS). Conversely to most optical microscopy techniques that rely on active illumination, our approach uses speckle illumination as previously mentioned in section 6.4. Consequently, it does not require to focus the excitation light beam on the observed sample. The goal is to reduce the acquisition time (*e.g.*, to preserve the biological sample of photo-bleaching) while achieving good reconstruction quality.

Context

Back to 1996, Bolshtyansky *et al.* studied an acquisition scheme very similar to ours [22] but involving a single multimode fiber (MMF). Pseudothermal ghost imaging also relies on a similar approach but uses a rotating diffuser to generate speckle patterns [90]. Speckles have also been extensively used to perform super-resolution fluorescence microscopy, most often in a blind context [91, 104, 108]. Such techniques (*e.g.*, structured illumination microscopy or super-resolution optical fluctuation imaging) allow to go beyond the diffraction limit and are then able to image structures at a sub-cellular scale. To compensate the fact that the patterns may be unknown, some works exploit the statistical properties of the speckles [91,

108] or consider weak assumptions on the original fluorophores distribution [104]. Bertolotti *et al.* studied a blind framework where the diffuser is completely opaque and prevents access to both the sample and the generated speckle [20]. To cover up this inaccessibility, they exploit the memory effect described in section 7.3. The vector of measurements can then be seen as a convolution product between the (unknown) speckle and the original image. In speckle scanning microscopy, Stasio *et al.* also took advantage of this effect with a multicore fiber (MCF) [143]. Except in super-resolution, the fluorescence signal in the aforementioned applications is measured with a single-pixel detector (or a similar device). The image of interest is estimated via a weighted sum of the speckle patterns [22], via the correlations of the observation vector with the illumination patterns [90, 132] or via the autocorrelation of the measurement vector [20, 143].

While the above-mentioned works consider a number of measurements M at least equal to the number of pixels in the final image, several authors reported the development of compressive optical imaging techniques requiring far fewer observations. These techniques are based on the seminal work of Candès *et al.* and Donoho on compressive sensing [33, 49]. The pseudo-randomness of the speckles and their easy generation make them interesting to build efficient sensing matrices. Katz *et al.* proposed a proof of concept for CS approach to pseudothermal ghost imaging including information about the image structure in the reconstruction algorithm [90]. A compressive approach was used in super-resolution microscopy [112] where the authors reach higher resolution by using saturated illumination with speckle patterns. CS was also exploited in experimental setups involving an MCF and/or an MMF, *e.g.*, in fluorescence microscopy [34, 134], optical photoacoustic [34] or microendoscopy [40]. Authors assume small total variation [134] or sparsity in some wavelet basis [40] as prior information on the image structure. In these three works, speckles patterns are recorded. This recording can be seen as a calibration step. As mentioned by [34], this step is simpler than conventional calibration via wavefront shaping since it only requires to measure the speckles intensities while beamforming requires field measurements before the experiment.

Remark 8.1. Most of these works do not provide theoretical links with the CS theory, *e.g.*, bounds on the number of measurements or properties of the sensing matrix. One counterexample is for instance the work of Valley *et al.*. In [156], they study the CS acquisition of sparse gigahertz-band signals with an MMF. The core of their paper is to empirically character-

ize the speckle-based sensing matrix. They compare it to an ideal sub-Gaussian sensing matrix through three features: the ability to recover different sparse signals, the coherence of the matrix, and the presence of a sharp phase transition.

Contributions and outline

The literature covered in the previous section shows that speckle illumination seems to be a promising way to face one of the main constraints preventing the use of LE: it removes the need for interferometric stability and costly calibration step before each acquisition, and it can possibly be used in a blind context. Experimental studies show that sensing matrices based on speckles patterns are valid candidates to acquire measurements in a compressive framework while still providing good reconstruction results. In fluorescence imaging, more than a low number of measurements, a short acquisition time is highly desirable to preserve the biological sample of photo-bleaching (see section 6.2). Such acquisition strategies would allow for high-speed imaging in a realistic setting. If the MCF fiber has a low coupling between the cores, the acquisition time can be substantially reduced by exploiting the memory effect of the MCF thanks to scan mirrors (*e.g.*, galvanometric mirrors). According to Andresen *et al.*, only strategies exploiting this effect will be able to satisfy the speed and resolution requirements for *in vivo* imaging, as moving such mirrors is much faster than changing an SLM configuration [9].

In this chapter, we study a novel acquisition strategy named *partial speckle scanning* (PSS). It combines elements of CS with the specific properties of the considered LE, namely its *robustness to spatial and temporal distortion*, its extremely *low coupling* between the cores of the fiber, and its *memory effect*. In particular, we generate only $P \leq M$ distinct speckles and we shift each of them $M_P = M/P \leq M$ times (see section 7.3), thus achieving a *partial* scanning of the object, to acquire a total of $M = PM_P$ observations. For $P = M$, we observe the sample with M different speckle illuminations while if $P = 1$, a unique speckle pattern is shifted M times.

The contribution of this chapter consists in designing and validating the acquisition strategy described above. It also includes the optimization of the sampling parameters (number of measurements M, M_P, shift induced by the mirrors, etc.) in order to get the best reconstruction quality (*e.g.*, for a given acquisition time).

The chapter is structured as follows. In section 8.1, we present a more general estimation problem compared to the raster scanning (RS) (see section 6.3). We formulate the imaging process as the solving of an inverse problem, *i.e.*, the minimization of an objective function made of a data fidelity term combined with regularizing priors on the expected fluorophore density map. A reconstruction based on this formulation can deal with a wide range of sensing matrices (*i.e.*, the light beam does not require a calibratione) and a number of observations $M \ll N$. We detail the algorithm to solve this inverse problem in section 8.2. The above-mentioned acquisition strategy (PSS), its formulation as inverse problem and the results of the simulations are presented in section 8.3. Finally, section 8.4 presents the experimental setup designed to compare different acquisition strategies on real fluorescent samples.

8.1 Inverse problem formulation

From observed data $\boldsymbol{y}$, we would like to estimate the original fluorescent response $\boldsymbol{f}$ of the sample, that is, we would like to *invert* the forward model given by (6.5) for a general sensing matrix $\boldsymbol{S}^\top$. As explained in section 2.2, the corresponding least-squares problem is often *ill-posed* mainly due to the noise corruption on the measurements but also because $\boldsymbol{S}^\top$ is not necessarily well conditioned, *e.g.*, if the number of observations M is smaller than the number of pixels N. Instead, we consider the following regularized and constrained minimization problem,

$$\begin{aligned} \underset{\boldsymbol{u}\in\mathbb{R}^N}{\text{minimize}} \quad & \text{dist}(\boldsymbol{S}^\top\boldsymbol{u}, \boldsymbol{y}) + \rho\phi(\boldsymbol{u}), \\ \text{subject to} \quad & \boldsymbol{u} \succeq \boldsymbol{0}, \end{aligned} \tag{8.1}$$

where $\rho > 0$ is a regularization parameter balancing between the data fidelity term and the regularization term, denoted by ϕ. The choice of a squared ℓ_2-norm as the distance function between $\boldsymbol{S}^\top\boldsymbol{u}$ and $\boldsymbol{y}$ is justified by the Gaussian assumption on the noise in (6.5). The constraint encodes the non-negativity of the original fluorophore density map, $\boldsymbol{f} \succeq \boldsymbol{0}$, that is implicit from the physics of fluorescence emission (see subsection 6.2.1).

Image structure. We assume that $\boldsymbol{f}$ is made of smooth areas separated by sharp boundaries (possibly corresponding to tissue interfaces or cellular membranes). This prior, encoded in function ϕ, corresponds either to the minimization of the TV-norm [128] or the TGV^2_α-norm [28, 93] (see sub-

section 2.2.2). Promoting a small TV-norm leads to piecewise constant images and is then well suited for the synthetic data used in the simulations. As for TGV, it can be seen as a generalization of TV to higher-order image derivatives. Minimizing the TGV^2_α-norm leads to piecewise linear estimates where parameter $\alpha > 0$ mades a trade-off between edge-preserving and smoothness-promoting terms (as suggested by [93], we set $\alpha = 2$). TGV^2_α is better suited for fluorescent samples used for the experiments or when we estimate a vignetted map.

The constraint in (8.1) can be replaced by adding a convex indicator function on the set $\mathbb{R}^N_+$ in the objective function. It is equal to zero if the constraint is satisfied and to $+\infty$ otherwise. The non-smooth convex estimation problems—with TV and TGV^2_α regularizations—finally write,

$$\hat{f} \in \operatorname*{arg\,min}_{u \in \mathbb{R}^N} \ \frac{1}{2}\|S^\top u - y\|_2^2 + \rho\|\nabla u\|_{2,1} + \imath_{\mathbb{R}^N_+}(u), \qquad \text{(TV)} \qquad (8.2)$$

$$\hat{f} \in \operatorname*{arg\,min}_{\substack{u \in \mathbb{R}^N, \\ w \in \mathbb{R}^{N\times 2}}} \ \frac{1}{2}\|S^\top u - y\|_2^2 + \rho\|\nabla u - w\|_{2,1} + \alpha\rho\|\varepsilon(w)\|_{2,1} + \imath_{\mathbb{R}^N_+}(u). \qquad \text{(TGV)} \qquad (8.3)$$

8.2 Numerical implementation

Like in section 4.4 for the deconvolution of PET images, we solve (8.2) and (8.3) with a generalized version of the Chambolle-Pock (GCP) primal-dual algorithm [37, 71]. This flexible algorithm allows for composing convex functions with linear operators in the minimization (see section 2.3).

A compact formulation of (8.2) matching the notation of (2.12) is

$$\hat{f} \in \operatorname*{arg\,min}_{u \in \mathbb{R}^N} F_1(S^\top u) + F_2(\nabla u) + G_{\mathrm{TV}}(u), \qquad (8.4)$$

with $G_{\mathrm{TV}} = \imath_{\mathbb{R}^N_+}$, $F_1 = 0.5\|\cdot - y\|_2^2$ and $F_2 = \rho\|\cdot\|_{2,1}$.

When the regularization term is the TGV^2_α-norm, a compact formulation for (8.3), similar to (4.15), is given by

$$\hat{z} \in \operatorname*{arg\,min}_{z \in \mathbb{R}^{N\times 3}} F_1(S^\top R_u z) + F_2((\nabla R_u - R_w)z) + F_3(\varepsilon(R_w z)) + G_{\mathrm{TGV}}(z), \qquad (8.5)$$

where we replaced u and w by a unique optimization variable $z := (u, w)$ like in section 4.4. Operators R_u and R_w are the same restriction operators

as in section 4.4. The first one keeps the first column of $\boldsymbol{z}$ and the second one keeps the last two columns of $\boldsymbol{z}$. The estimated map is $\hat{\boldsymbol{f}} = \boldsymbol{R}_{\boldsymbol{u}}\hat{\boldsymbol{z}}$. In this case, $G_{\mathrm{TGV}} = \iota_{\mathbb{R}_+^N} \circ \boldsymbol{R}_{\boldsymbol{u}}$, $F_1 = 0.5\|\cdot - \boldsymbol{y}\|_2^2$, $F_2 = \rho\|\cdot\|_{2,1}$ and $F_3 = \alpha\rho\|\cdot\|_{2,1}$.

8.2.1 Proximal operators of primal and dual functions

The GCP algorithm only requires computing the proximal operators of G_{TV}, G_{TGV} and of the Legendre-Fenchel conjugates of F_1, F_2 (and possibly F_3), as well as the adjoints of the operators, described in the next section.

The proximal operator of function G_{TV} is the projection onto $\mathbb{R}_+$,

$$\mathrm{prox}_{\tau G_{\mathrm{TV}}}(\tilde{\boldsymbol{u}}) = \max(\tilde{\boldsymbol{u}}, \boldsymbol{0}),$$

where $\tau > 0$ is the primal step-size in GCP algorithm. The proximal operator of G_{TGV} is $\mathrm{prox}_{\tau G_{\mathrm{TGV}}}(\tilde{\boldsymbol{z}}) = \tilde{\boldsymbol{z}} + \boldsymbol{R}_{\boldsymbol{u}}^*(\mathrm{prox}_{\tau G_{\mathrm{TGV}}}(\boldsymbol{R}_{\boldsymbol{u}}\tilde{\boldsymbol{z}}) - \boldsymbol{R}_{\boldsymbol{u}}\tilde{\boldsymbol{z}})$, using the property of semi-orthogonal linear transform (see Property 2.15).

The proximal operator of $F_1^\star$ is given by

$$\mathrm{prox}_{\sigma F_1^\star}(\tilde{\boldsymbol{p}}) = \frac{\tilde{\boldsymbol{p}} - \sigma\boldsymbol{y}}{1+\sigma},$$

where $\sigma > 0$ is the dual step-size in GCP algorithm.

Exactly like in section 4.4, functions F_2 and F_3 are ℓ_1-norms. The proximal operators of their conjugates are projection operators onto the convex sets $\mathcal{Q}_2 := \{\tilde{\boldsymbol{q}} \in \mathbb{R}^{N\times 2} | \|\tilde{\boldsymbol{q}}\|_{2,\infty} \leq \rho\}$ and $\mathcal{Q}_3 := \{\tilde{\boldsymbol{r}} \in \mathbb{R}^{N\times 4} | \|\tilde{\boldsymbol{r}}\|_{2,\infty} \leq \alpha\rho\}$.

8.2.2 Operators and their adjoints

The operator associated with F_1 in (8.4) (resp. (8.5)) is $\boldsymbol{L}_1 = \boldsymbol{S}^\top : \mathbb{R}^N \to \mathbb{R}^M$ (resp. $\boldsymbol{L}_1 = \boldsymbol{S}^\top\boldsymbol{R}_{\boldsymbol{u}} : \mathbb{R}^{N\times 3} \to \mathbb{R}^M$) and its adjoint is $\boldsymbol{S}$ (resp. $\boldsymbol{R}_{\boldsymbol{u}}^*\boldsymbol{S}$). In (8.4), the operator associated with F_2 is $\boldsymbol{L}_2 = \boldsymbol{\nabla} : \mathbb{R}^N \to \mathbb{R}^{N\times 2}$ and its adjoint is given by $\boldsymbol{\nabla}^* = -\mathrm{div}$ (see Definition 2.8). The operators associated with F_2 and F_3 in (8.5) are the same as those defined in subsection 4.4.2.

8.2.3 Regularization parameter and stopping criterion

As brought up earlier, the optimal value of parameter ρ in (8.2) and (8.3) is unknown *a priori*. We select a value for ρ based on the optimization of a quality criterion (see subsection 2.3.2). Following Boufounos and Ward [25, 161], we apply cross-validation (CV) principle to avoid the overfitting of noisy observations during the estimation process (see subsection 2.3.2). The set of M measurements is randomly divided into two subsets. The first

one contains M_{est} observations ($\boldsymbol{y}_{\text{est}}$) and is used for the image estimation. The second one contains $M_{\text{val}} = M - M_{\text{est}}$ measurements ($\boldsymbol{y}_{\text{val}}$) and is used to determine when to stop the iterative algorithm and/or to select the regularization parameter. In [161], Ward shows that provided a sensing operator $\boldsymbol{S}^\top$ satisfying the RIP, we can choose $M_{\text{val}} \ll M_{\text{est}}$.

With a CV approach, estimation problems (8.2) and (8.3) become

$$\hat{\boldsymbol{f}} \in \underset{\boldsymbol{u}\in\mathbb{R}^N}{\arg\min} \quad \frac{1}{2}\|\boldsymbol{R}_{\text{est}}(\boldsymbol{S}^\top\boldsymbol{u} - \boldsymbol{y})\|_2^2 + \rho\|\boldsymbol{\nabla}\boldsymbol{u}\|_{2,1} + \iota_{\mathbb{R}_+^N}(\boldsymbol{u}), \qquad \text{(TV)} \quad (8.6)$$

$$\hat{\boldsymbol{f}} \in \underset{\substack{\boldsymbol{u}\in\mathbb{R}^N,\\ \boldsymbol{w}\in\mathbb{R}^{N\times 2}}}{\arg\min} \quad \frac{1}{2}\|\boldsymbol{R}_{\text{est}}(\boldsymbol{S}^\top\boldsymbol{u} - \boldsymbol{y})\|_2^2 + \rho\|\boldsymbol{\nabla}\boldsymbol{u} - \boldsymbol{w}\|_{2,1} \qquad \text{(TGV)} \quad (8.7)$$
$$+ \alpha\rho\|\varepsilon(\boldsymbol{w})\|_{2,1} + \iota_{\mathbb{R}_+^N}(\boldsymbol{u}).$$

where $\boldsymbol{R}_{\text{est}} \in \{0,1\}^{M_{\text{est}}\times M}$ is a restriction operator such that $\boldsymbol{y}_{\text{est}} = \boldsymbol{R}_{\text{est}}\boldsymbol{y}$. The proximal operator of $F_1^\star$ becomes

$$\text{prox}_{\sigma F_1^\star}(\tilde{\boldsymbol{p}}) = \frac{\tilde{\boldsymbol{p}} - \sigma\boldsymbol{R}_{\text{est}}\boldsymbol{y}}{1+\sigma},$$

and $\boldsymbol{L}_1 = \boldsymbol{R}_{\text{est}}\boldsymbol{S}^\top$ in (8.4) and $\boldsymbol{L}_1 = \boldsymbol{R}_{\text{est}}\boldsymbol{S}^\top\boldsymbol{R}_{\boldsymbol{u}}$ in (8.5).

As in [25], we use the squared ℓ_2-norm of the residual to evaluate the quality of the estimate $\hat{\boldsymbol{f}}$. This is defined by

$$q(\hat{\boldsymbol{f}}) := \|\boldsymbol{R}_{\text{val}}(\boldsymbol{S}^\top\hat{\boldsymbol{f}} - \boldsymbol{y})\|_2^2,$$

where $\boldsymbol{R}_{\text{val}} \in \{0,1\}^{M_{\text{val}}\times M}$ is a restriction operator keeping only $M_{\text{val}} = M - M_{\text{est}}$ entries of a vector of size M and such that $\boldsymbol{y}_{\text{val}} = \boldsymbol{R}_{\text{val}}\boldsymbol{y}$. Quality function q is used, first, to stop the GCP algorithm when q reaches a minimum, and second, to select an appropriate value for ρ. This last operation is done by solving (8.6) and (8.7) for K values of ρ and ρ_{k^*} is considered as the best choice if $q(\hat{\boldsymbol{f}}_{\rho_{k^*}}) \leq q(\hat{\boldsymbol{f}}_{\rho_k})$, for all $k \in [K]$ (see Figure 8.1).

The algorithm for the reconstruction of images acquired with LE is summarized in Algorithm 7, for TV regularization. We solve (8.7) with Algorithm 5 with $\boldsymbol{p}^{(0)} = \boldsymbol{0}_{M_{\text{est}}}$ and the prox and operators defined above.

We choose the step-sizes σ and τ in GCP in the same way as we did in subsection 4.4.3. The maximum number of internal iterations `maxIter` is also equal to 5000. Internal iterations stop after $q_{\text{it}} = 200$ iterations of non-increasing quality of the estimate, $q(\boldsymbol{u}^{(n)})$, or when n reaches `maxIter`.

The initialization of the estimate is a null vector of size N. For $k > 1$,

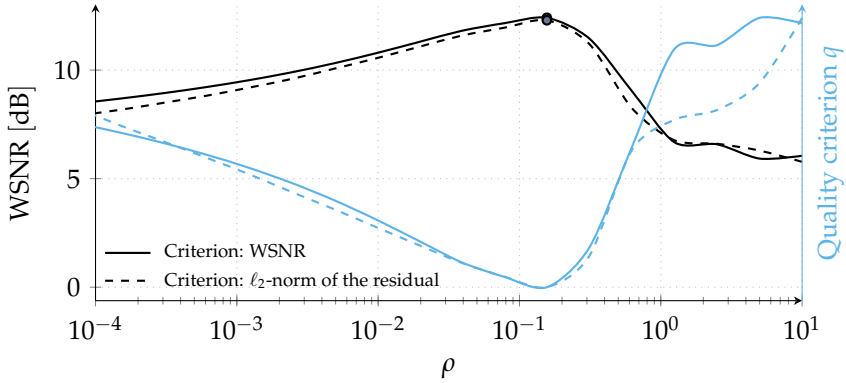

Figure 8.1 Mean WSNR (over 10 trials) of a restored USAF target as a function of ρ for two quality criteria q (black lines): WSNR (see (8.13)) and squared ℓ_2-norm of the residual. The blue lines represent the mean value of the criteria as a function of ρ. The chosen values—corresponding to a minimal value of the criterion—are indicated by a filled circle. The value selected by the norm of the residual is identical to the one selected by the (unrealistic) WSNR criterion. Observations were generated according to (6.5) with the SI strategy and $M/N = 0.3$ (see subsection 8.3.2).

the initial guess of the algorithm is given by the previous estimate $\hat{\boldsymbol{f}}_{\rho^{(k-1)}}$. The maximum number of iterations on ρ is 20. For CV, we set $M_{\text{val}} = 256$. In the simulations (see subsections 8.3.2 and 8.3.3), the initial value of the regularization parameter is $\rho^{(1)} = 10$ and $\beta = 0.5$. In the experiments (see subsection 8.4.2), $\rho^{(1)} = 2500$ for standard USAF transmission target, $\rho^{(1)} = 10^4$ for the fluorescent beads, and $\beta = 0.8$. In the experiments, we select the best regularization parameter by visual inspection.

8.3 Acquisition strategies based on CS

In this section, we describe how the LE forward model (6.5) can follow a CS scheme [33], *i.e.*, how we can capture and reconstruct images from a number of measurements $M < N$. Such CS frameworks also aim at removing the beamforming calibration of the RS method by using speckle illumination. We thus consider a sensing model where the patterns composing $\boldsymbol{S} \in \mathbb{R}_+^{N \times M}$ are associated with M random configurations $\{\boldsymbol{\alpha}_k\}_{k=1}^{M}$ of the MCF complex amplitudes.

In CS theory, the success of the estimation of a signal of interest mainly depends on the ability of the sensing matrix to capture information about

Algorithm 7: TV reconstruction of observations acquired with LE

input : observations $\boldsymbol{y}$ obtained after illumination of the sample by light patterns (deterministic or random)

output: a restored image $\hat{\boldsymbol{f}}$

initialization: $\boldsymbol{u}^{(0)} = \bar{\boldsymbol{u}}^{(0)} = \mathbf{0}_N$, $\boldsymbol{p}^{(0)} = \mathbf{0}_{M_{\text{est}}}$, $\boldsymbol{q}^{(0)} = \mathbf{0}_{N\times 2}$, $\tau = \sigma = 0.9/\|\boldsymbol{L}\|_2$, $\rho = \rho^{(1)}$;

for $k = 1$ **to** *maxIterRho* **do**
  $q_{\text{it}} = 0$;
  for $n = 1$ **to** *maxIter* **do**
    $\boldsymbol{p}^{(n)} = \text{prox}_{\sigma F_1^\star}(\boldsymbol{p}^{(n-1)} + \sigma \boldsymbol{R}_{\text{est}} \boldsymbol{S}^\top \bar{\boldsymbol{u}}^{(n-1)})$;
    $\boldsymbol{q}^{(n)} = \text{prox}_{\sigma F_2^\star}(\boldsymbol{q}^{(n-1)} + \sigma \boldsymbol{\nabla} \bar{\boldsymbol{u}}^{(n-1)})$;
    $\boldsymbol{u}^{(n)} = \text{prox}_{\tau G}(\boldsymbol{u}^{(n)} - \tau(\boldsymbol{S}\boldsymbol{R}_{\text{est}}^* \boldsymbol{p}^{(n-1)} - \text{div}[\boldsymbol{q}^{(n-1)}]))$;
    $\bar{\boldsymbol{u}}^{(n)} = 2\boldsymbol{u}^{(n)} - \boldsymbol{u}^{(n-1)}$;
    if $q(\boldsymbol{u}^{(n)}) > q(\boldsymbol{u}^{(n-1)})$ **then**
      $\hat{\boldsymbol{f}}_{\rho^{(k)}} = \boldsymbol{u}^{(n)}$;
      $q_{\text{it}} = 0$;
    else
      $q_{\text{it}} = q_{\text{it}} + 1$;
    end
    if $n =$ *maxIter* **or** $q_{\text{it}} > 200$ **then**
      $\hat{\boldsymbol{f}}_{\rho^{(k)}} = \boldsymbol{u}^{(n)}$;
      break;
    end
  end
  if $k \neq$ *maxIterRho* **then**
    $\rho^{(k+1)} = \beta \rho^{(k)}$;
  end
end
choose $k^\star$ such that $q(\hat{\boldsymbol{f}}_{\rho^{(k^\star)}}) \geq q(\hat{\boldsymbol{f}}_{\rho^{(k)}})$ for all k;
$\hat{\boldsymbol{f}} = \hat{\boldsymbol{f}}_{\rho^{(k^\star)}}$;

this signal during the acquisition process [123]. This theory offers tools to study the recovery of low-complexity signals (such as sparse images in a given basis) when the number of observations is much smaller than the number of pixels in the final image, *e.g.*, the restricted isometry property (RIP) and the null space property [33]. But as mentioned in [52, 123, 147], those two properties are difficult to verify directly (*e.g.*, for deterministic matrices) without extra assumptions on the sensing matrix. Most of the existing theoretical work in CS theory is about random matrices with zero-mean i.i.d. row entries, or random partial Fourier sampling. For instance, the behavior of a reconstruction based on observations acquired with sub-Gaussian or Bernoulli measurement matrices has been extensively studied from a theoretical point of view [33, 89]. However, those zero-mean random matrices with i.i.d. entries are too ideal for real-life applications where the physics often limits the choice of the sensing operator [52, 123].

In our case, the rows of $\boldsymbol{S}^\top$ in (6.5) correspond to the discrete representation of the illumination patterns. By definition, their entries are positive random variables with positive mean. Moreover, the rows exhibit some structure—they are correlated—mainly due to the spatial arrangement of the cores (see subsection 7.2.1).

In the following section, we introduce a slightly modified version of the acquisition model (6.5) including a zero-mean sensing matrix. In subsections 8.3.2 and 8.3.3, we study two compressive acquisition strategies for LE. We show how to make them, at least partially, compatible with CS theory. The first strategy, called *speckle imaging* (SI), observes the object with M distinct speckle patterns generated by M i.i.d. configurations $\{\boldsymbol{\alpha}_k\}_{k=1}^M$. The second, called *partial speckle scanning* (PSS), adopts a structured CS strategy: while observing the object, only a fraction of the M speckles are generated randomly, and the others consist of shifted copies of the first ones.

8.3.1 Debiased forward model

Using expression (7.10), we write the sensing matrix $\boldsymbol{S}^\top$ as

$$\boldsymbol{S}^\top = (\mathbf{1}_M \mathbf{1}_N^\top + \sqrt{M}\tilde{\boldsymbol{\Phi}})\bar{\boldsymbol{S}}, \tag{8.8}$$

where $\bar{\boldsymbol{S}} \coloneqq \operatorname{diag}(\bar{\boldsymbol{s}}) \in \mathbb{R}^{N\times N}$ with $\bar{\boldsymbol{s}} \coloneqq (\bar{s}_1, \dots, \bar{s}_N)^\top$ the positive coefficients of the discrete representation of the mean speckle field $\bar{S}$, and where $\tilde{\boldsymbol{\Phi}} \coloneqq (\tilde{\boldsymbol{r}}_1, \dots, \tilde{\boldsymbol{r}}_M)^\top / \sqrt{M} \in \mathbb{R}^{M\times N}$ is a zero-mean sub-exponential random matrix containing the M discretized residual fields $\tilde{R}_j$, $j \in [M]$, as defined in Proposition 7.2. The sub-exponential norm of its entries is bounded by

$1/\sqrt{M}$. Its row entries are not independent of each other as expected from the autocorrelation of $\tilde{\boldsymbol{r}}$, $\boldsymbol{\Gamma}_{\tilde{R}}$, that is the discrete representation of $\Gamma_{\tilde{R}}$.

Following [119, 145] and using (6.5) and (8.8), we consider the *debiased forward model*,

$$\boldsymbol{y}_{\text{deb}} \coloneqq \boldsymbol{y} - \mathbf{1}_M \mathbf{1}_N^\top \bar{\boldsymbol{S}} \boldsymbol{f} = \sqrt{M} \tilde{\boldsymbol{\Phi}} \bar{\boldsymbol{S}} \boldsymbol{f} + \boldsymbol{n}, \tag{8.9}$$

where $\tilde{\boldsymbol{\Phi}} = (\boldsymbol{S}^\top \bar{\boldsymbol{S}}^{-1} - \mathbf{1}_M \mathbf{1}_N^\top)/\sqrt{M}$. Quantity $\mathbf{1}_M \mathbf{1}_N^\top \bar{\boldsymbol{S}} \boldsymbol{f}$ is deterministic but unknown. In practice, when M is large enough, averaging observations y_i provides a good estimate of the (identical) entries of this vector,

$$\frac{1}{M} \sum_{i=1}^{M} y_i = \frac{1}{M} \sum_{i=1}^{M} (\boldsymbol{s}_i^\top \boldsymbol{f} + n_i) \approx \bar{\boldsymbol{s}}^\top \boldsymbol{f} = \mathbf{1}_N^\top \bar{\boldsymbol{S}} \boldsymbol{f},$$

where we assumed $\mathbb{E} n_i = 0 \; \forall i \in [M]$. Model (8.9) is then replaced by

$$\tilde{\boldsymbol{y}} \coloneqq \boldsymbol{y} - \frac{1}{M} \mathbf{1}_M \mathbf{1}_M^\top \boldsymbol{y} = \sqrt{M} \tilde{\boldsymbol{\Phi}} \bar{\boldsymbol{S}} \boldsymbol{f} + \tilde{\boldsymbol{n}}, \tag{8.10}$$

where $\tilde{\boldsymbol{n}} \in \mathbb{R}^M = \boldsymbol{n} + \mathbf{1}_M \mathbf{1}_N^\top \bar{\boldsymbol{S}} \boldsymbol{f} - \frac{1}{M} \mathbf{1}_M \mathbf{1}_M^\top \boldsymbol{y}$. The variance of each $\tilde{n}_i$ is equal to $(1 + \frac{1}{M})\sigma^2$ and tends to the variance of n_i for M large.

The modified minimization problems (8.6) and (8.7) read

$$\hat{\boldsymbol{f}} \in \operatorname*{arg\,min}_{\boldsymbol{u} \in \mathbb{R}^N} \; \frac{1}{2} \| \boldsymbol{R}_{\text{est}} (\sqrt{M} \tilde{\boldsymbol{\Phi}} \bar{\boldsymbol{S}} \boldsymbol{u} - \tilde{\boldsymbol{y}}) \|_2^2 + \rho \| \boldsymbol{\nabla} \boldsymbol{u} \|_{2,1} + \iota_{\mathbb{R}_+^N}(\boldsymbol{u}), \tag{TV}$$

$$\tag{8.11}$$

$$\hat{\boldsymbol{f}} \in \operatorname*{arg\,min}_{\substack{\boldsymbol{u} \in \mathbb{R}^N, \\ \boldsymbol{w} \in \mathbb{R}^{N \times 2}}} \; \frac{1}{2} \| \boldsymbol{R}_{\text{est}} (\sqrt{M} \tilde{\boldsymbol{\Phi}} \bar{\boldsymbol{S}} \boldsymbol{u} - \tilde{\boldsymbol{y}}) \|_2^2 + \rho \| \boldsymbol{\nabla} \boldsymbol{u} - \boldsymbol{w} \|_{2,1} \tag{TGV}$$

$$+ \alpha\rho \| \varepsilon(\boldsymbol{w}) \|_{2,1} + \iota_{\mathbb{R}_+^N}(\boldsymbol{u}). \tag{8.12}$$

and the quality criterion is

$$\tilde{q}(\hat{\boldsymbol{f}}) \coloneqq \| \boldsymbol{R}_{\text{val}} (\sqrt{M} \boldsymbol{\Phi} \bar{\boldsymbol{S}} \hat{\boldsymbol{f}} - \tilde{\boldsymbol{y}}) \|_2^2.$$

We can still use Algorithm 7 for the reconstruction: we only need to replace $\boldsymbol{S}^\top$ by $\sqrt{M} \tilde{\boldsymbol{\Phi}} \bar{\boldsymbol{S}}$ and $\boldsymbol{y}$ by $\tilde{\boldsymbol{y}}$.

In the following sections, we use the physical model (6.5) to simulate the data. For the reconstruction process, we consider the debiased observations $\tilde{\boldsymbol{y}}$ and the associated sensing matrix $\tilde{\boldsymbol{\Phi}}$. As explained in subsec-

tion 8.3.2, this choice leads to a quality of the final estimate similar to the one obtained with the biased model but achieved with a much shorter reconstruction time.

8.3.2 Speckle imaging

The first strategy (SI) acquires M observations by successively illuminating the biological sample with M different unstructured light patterns $\boldsymbol{s}_j$, each obtained from a random configuration of the SLM. Since we are in a compressive framework, the number of observations is much smaller than the number of pixels in the final image, *i.e.*, $M \ll N$.

Adamczak *et al.* showed that zero-mean sub-exponential matrices with i.i.d. entries satisfy the RIP with high probability when normalized by $\sqrt{M}$ [2]. They also demonstrated that robust reconstruction of s-sparse vectors can be achieved via ℓ_1-minimization or greedy methods when the number of (possibly noisy) measurements is $M = \mathcal{O}(s \ln^2(N/s))$. Foucart *et al.* showed that such matrices also satisfy a modified version of the RIP based on the ℓ_1-norm [65]. They propose a recovery algorithm able to recover s-sparse vectors with M in $\mathcal{O}(s \ln(N/s))$.

In our case, the sensing operator $\tilde{\boldsymbol{\Phi}}$ is a zero-mean sub-exponential random matrix which contains M realizations of the normalized random variable $\tilde{R}(\boldsymbol{x}_i)$. The rows of $\tilde{\boldsymbol{\Phi}}$ are independent as each illumination pattern is used for collecting one single observation. Unfortunately, the analysis of the autocorrelation of $\tilde{R}$ made in subsection 7.2.1 shows the entries of each row are (locally) correlated. It makes sense since only J parameters—the J random phases of the complex amplitudes $\alpha_1, \ldots, \alpha_J$—are used to generate a (discretized) speckle pattern of size $N \gg J$. Therefore, we cannot readily use the results of [2, 65]. The existence of the above-mentioned correlations does not prevent to satisfy the RIP. After all, random partial Fourier sensing matrices, made of M randomly sampled rows of a Fourier matrix, do present such correlations but respect the RIP under certain conditions [33]. Studying if our sensing matrix satisfies the RIP is an open question.

If we want to get closer to columns independency for $\tilde{\boldsymbol{\Phi}}$, *i.e.*, if we want to decrease the size of the speckle grains $r \propto \lambda z/D$, we can either decrease the distance z between the distal end of the fiber and the object (while still keeping the far-field regime valid) or increase D when designing the MCF. The pixel resolution a used to discretize f can be adjusted to the speckle grain size $\lambda z/D$ since a higher resolution cannot be achieved. We will follow this procedure in section 8.4 for actual LE fluorescence imaging.

Figure 8.2 (a) 128×128 ground truth $\boldsymbol{f}$ of standard USAF transmission target. (b) Vignetted ground truth $\bar{\boldsymbol{S}}\boldsymbol{f}$. (c) Acquisition with RS strategy as explained in section 6.3. Observations were generated according to (6.5) with focused illumination pattern (SNR of $\boldsymbol{\Phi}\boldsymbol{f}$ equal to 40 dB). The maximum intensity of the RS image is around three times lower than the one of the ground truth.

Simulations

We simulate observations $\boldsymbol{y}$ of 128×128 USAF transmission target $\boldsymbol{f}$ (see Figure 8.2a) according to (6.5) for $M/N \in \{0.1, 0.2, \ldots, 1\}$. Since synthetic USAF transmission target is piecewise constant, we choose TV regularization. We thus reconstruct estimates of $\boldsymbol{f}$ by first solving the original inverse problem (8.6) with $(\boldsymbol{\Phi}, \boldsymbol{y})$ and then the debiased model (8.11) with $(\tilde{\boldsymbol{\Phi}}, \tilde{\boldsymbol{y}})$. For comparison, we also simulate RS observations and measurements acquired with an ideal zero-mean Gaussian matrix $\boldsymbol{\Phi}_{\mathrm{G}}$.

The quality of an estimate $\hat{\boldsymbol{u}}$ is often measured with the signal-to-noise ratio (SNR) (see Definition 2.21). In our case, the vignetting $\bar{\boldsymbol{S}}$, intrinsic to the acquisition process, leads to a loss of information on the borders of the field of view (FOV). We would like a quality metric giving less weight to the pixels that are located far from the center of the FOV. We introduce the weighted SNR (WSNR),

$$\mathrm{WSNR}(\hat{\boldsymbol{u}}, \boldsymbol{u}) := \mathrm{SNR}(\bar{\boldsymbol{S}}\hat{\boldsymbol{u}}, \bar{\boldsymbol{S}}\boldsymbol{u}). \tag{8.13}$$

For each value of M/N above, M observations of $\boldsymbol{f}$ are generated according to model (6.5). The variance of the noise, σ^2, is set such that the SNR of $\boldsymbol{\Phi}\boldsymbol{f}$ is equal to 40 dB. For all the experiments, the illumination patterns were generated for a Fermat's spiral core arrangement ($J = 120$ cores and diameter $D = 113\,\mu$m) and the following parameters: $\lambda = 1\,\mu$m,

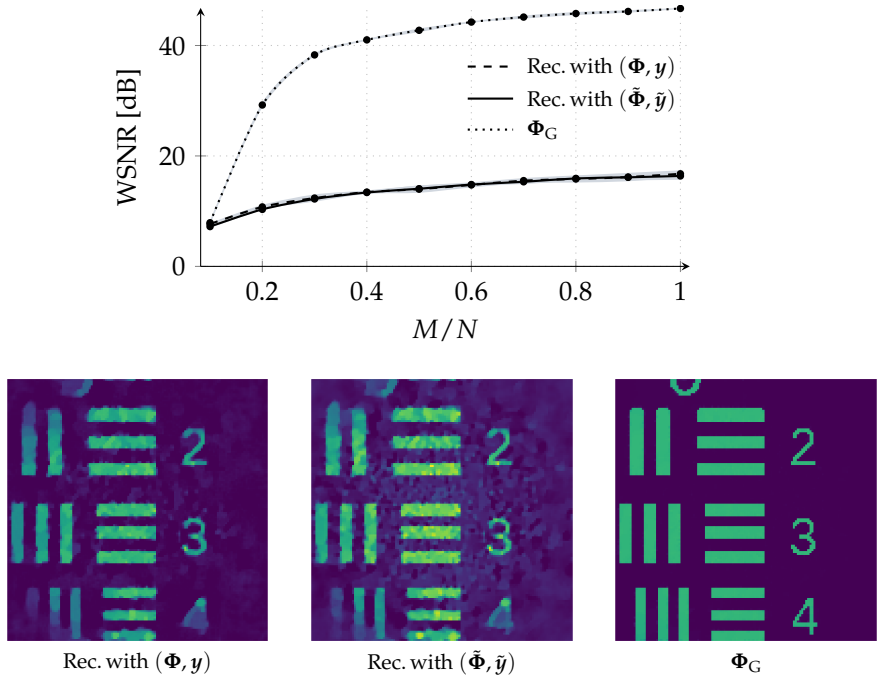

Figure 8.3 SI strategies. Above: mean WSNR (over 10 trials) of the restored USAF target *versus* M/N for three SI strategies: (*i*) acquisition and reconstruction with $(\boldsymbol{\Phi}, \boldsymbol{y})$ (dashed line), (*ii*) acquisition with $\boldsymbol{\Phi}$ and reconstruction with $(\tilde{\boldsymbol{\Phi}}, \tilde{\boldsymbol{y}})$ (solid line), and (*iii*) acquisition and reconstruction with ideal sensing matrix $\boldsymbol{\Phi}_{\mathrm{G}}$ (dotted line). The gray areas represent the standard deviations. Synthetic observations were generated according to (6.5) (SNR of $\boldsymbol{\Phi}\boldsymbol{f}$ equal to 40 dB). Below: estimates of $\boldsymbol{f}$ obtained for $M/N = 0.3$. They all share the same intensity scale.

$z = 500\,\mu$m, $3\sigma_c = 3.2\,\mu$m and $a = 2\,\mu$m. We perform the reconstruction with Algorithm 7 and the parameters described in subsection 8.2.3.

Comparison results

Simulation results are visible on Figure 8.3. Estimates of the fluorophore density map obtained with SI methods have a better quality compared to the estimate obtained with RS (WSNR equal to 1.68 dB with optimal normalization, see Figure 8.2c). However, unlike RS, SI requires to store M speckles patterns needed for the reconstruction.

Acquisition and reconstruction with Gaussian sensing matrix outper-

forms the other two frameworks involving speckle illumination. While unrealistic, such a Gaussian framework is useful as it sets an upper bound on the achievable reconstruction quality of LE imaging. For instance, it shows that the CS regime, where enough measurements are collected to ensure a reconstruction quality close to the measurement SNR of 40 dB, starts around $M/N = 0.3$ after a sharp transition in the curve. After this value, a further increase in the number of measurements does not lead to a significant gain in WSNR. The same behavior is observed for the reconstructions based on speckle acquisition even if the change in the curve rate is less outstanding. WSNR of images reconstructed with $(\tilde{\boldsymbol{\Phi}}, \tilde{\boldsymbol{y}})$ is similar to the one obtained for a reconstruction performed with $(\boldsymbol{\Phi}, \boldsymbol{y})$, despite the extra noise introduced in the debiased model. However, we observed significantly shorter reconstruction times for the debiased model when $M/N \leq 0.7$. We also noticed that, while the reconstruction with $(\boldsymbol{\Phi}, \boldsymbol{y})$ fails when we do not constraint the estimate to be non-negative, the debiased model performs almost as well without enforcing the positivity of the map (see Appendix 8.A). In the rest fo the paper, all reconstructions are performed with the debiased model.

8.3.3 Partial speckle scanning

SI strategy offers good reconstruction results but requires a long acquisition time. Unlike RS that can resort to scan mirrors to decrease the acquisition duration (see section 6.3), SI acquisition requires to change the SLM configuration for each observation. The rate of the SLM used in our setup is 1/60 s [86, see DVI frame rate] while the rate of galvanometric mirrors is around 1,000 times higher [32].

We propose a hybrid acquisition framework, called *partial speckle scanning* (PSS), which combines advantages of both techniques while keeping a high reconstruction quality. The proposed acquisition scheme strongly relies on two properties of the LE considered in this work: (*i*) we are able to easily generate speckles by randomly programming the SLM and (*ii*) we can exploit the MCF memory effect.

The PSS strategy acquires M observations but unlike the SI strategy, it collects $M_P \leq M$ observations with the same SLM configuration before changing it. For a fixed configuration, different tilts are applied to the input wavefront with the scan mirrors. This results in shifted copies of the original pattern as described in section 7.3.

Mathematically, given a set of $P = M/M_P$[1] complex amplitudes $\{\boldsymbol{\alpha}_j\}_{j=1}^{P}$ randomly generated as in the SI model, and M_P mirror tilts $\{\boldsymbol{\theta}_l\}_{l=1}^{M_P}$, the PSS sensing matrix $\tilde{\boldsymbol{\Phi}}$ used in model (8.10) corresponds to

$$\tilde{\boldsymbol{\Phi}} = [\tilde{\boldsymbol{\Phi}}_1^\top, \cdots, \tilde{\boldsymbol{\Phi}}_P^\top]^\top, \quad \text{with } \tilde{\boldsymbol{\Phi}}_j^\top = [\tilde{\boldsymbol{r}}_j^{(0)}, \tilde{\boldsymbol{r}}_j^{(1)}, \cdots, \tilde{\boldsymbol{r}}_j^{(M_P-1)}]^\top, \tag{8.14}$$

where $\tilde{\boldsymbol{r}}_j^{(l)}$ is the discrete representation of the shifted residual field for each $j \in [P]$, $l \in [M_P]$. We denote δ the shift between two consecutive speckle patterns $\tilde{\boldsymbol{r}}_j^{(l)}, \tilde{\boldsymbol{r}}_j^{(l+1)}$ in $\mathcal{Z}$, *i.e.*, $\delta \coloneqq z/k(\boldsymbol{\theta}_l - \boldsymbol{\theta}_{l+1})$.

In this work, we consider a single line scanning mode, *i.e.*, shifts are applied to the speckle patterns in only one (arbitrary) direction. Line scanning is fast and accurate because it only needs the rotation of one scan mirror.

When designing the PSS framework, the adjustment of the shift δ between two illumination faces two competing effects. First, if δ is too small compared to the size of a speckle grain, model (8.14) introduces a lot of redundant information, *i.e.*, correlations, between neighboring rows of the sensing matrix. Moreover, in addition to the column dependency mentioned in subsection 8.3.2, our sensing matrix further deviates from an ideal uncorrelated sub-exponential random matrix. Second, if we approximate $\tilde{\boldsymbol{\Phi}}$ by a block-circulant matrix (*e.g.*, to store less patterns), δ must be small enough such that approximation (7.19) still holds. This imposes us to respect the paraxial approximation for all translation steps, *i.e.*, we must have $M_P\delta \ll z$. Note that, while there exist sensing constructions based on subsampled random circulant matrices defined from sub-Gaussian random filters [52, 123], there are no known constructions for sub-exponential random filters. Despite this absence, our simulations below confirm that the PSS sensing compares favorably to the SI and the Gaussian schemes.

An advantage of the PSS scheme is that its scanning time t_{acq} is reduced compared to SI for the same number of measurements. Having a short acquisition time is highly desirable when working with biological samples subject to photo-bleaching (see subsection 6.2.1). Acquisition time is

$$t_{\text{acq}} = t_{\text{galva}}\left(\gamma\lceil M/M_P\rceil + M - \lceil M/M_P\rceil\right),$$

where $1/t_{\text{galva}}$ is the scan mirror rate and $\gamma \coloneqq t_{\text{SLM}}/t_{\text{galva}}$ with $1/t_{\text{SLM}}$ the SLM frame rate. If t_{SLM} is large compared to t_{galva}, *i.e.*, if γ is large, for a

[1] In practice, we do not require M to be a multiple of M_P. In all generality, $P = \lceil M/M_P\rceil$.

fixed M, t_{acq} can be kept small if we keep the number of distinct speckle patterns P small. In our setup, $\gamma \approx 10^3$.

Simulations

The first simulation aims to choose an appropriate shift δ between two consecutive speckles. We simulate M observations $\boldsymbol{y}$ of the 128×128 USAF transmission target $\boldsymbol{f}$ for $M/N = 0.3$. $M_P = 2$ observations are acquired before changing the configuration of the SLM. The shift δ is sequentially set to values in $\{0, 1, 2, 3, 4, 6, 8, 10\}$ [μm]. For each of them, we reconstruct estimates $\hat{\boldsymbol{f}}$ of $\boldsymbol{f}$ solving the debiased model (8.11) with $(\tilde{\boldsymbol{\Phi}}, \tilde{\boldsymbol{y}})$. Exactly like for the SI strategy, we consider the TV-norm as the regularization term.

We also conduct a second simulation where we compare the PSS strategies for different values of M_P. We simulate and reconstruct observations as described in the previous paragraph but with fixed value of δ (chosen according to the result of the first experiment), for $M/N \in \{0.1, 0.2, \dots, 1\}$ and $M_P \in \{1, 2, 4, 8, 16, 32, 64\}$. The value $M_P = 1$ corresponds to the SI strategy. We generate observations according to (6.5) with σ^2 such that the SNR of $\boldsymbol{\Phi f}$ is equal to 40 dB. The speckles are generated for a Fermat's spiral core arrangement ($J = 120$ cores and diameter $D = 113\,\mu$m) and the following parameters: $\lambda = 1\,\mu$m, $z = 500\,\mu$m, $3\sigma_c = 3.2\,\mu$m and $a = 2\,\mu$m. The time t_{SLM} is set to 100 ms, *i.e.*, slightly higher than the time given in the spec sheet [86], and t_{galva} is set to 100 μs [32].

We perform the reconstruction of both simulations like for the SI strategy, *i.e.*, with Algorithm 7 and the parameters described in subsection 8.2.3.

Results

Results of Figure 8.4 suggest to consider a shift $\delta \geq 4\,\mu$m. In this case, the spatial correlation between shifted patterns (related to the autocorrelation of field $\tilde{R}$ and to the speckle grain) is close to zero and the quality of the estimate is similar to the one obtained with the SI strategy.

Figure 8.5 shows the results of the second experiment performed with $\delta = 4\,\mu$m. Regarding Figure 8.4 and the choice of δ, it is not surprising to observe a reconstruction quality similar for all M_P values at fixed M/N. However, even if the reconstruction quality is similar for a given M/N ratio, we are more interested in considering the quality obtained for a fixed acquisition time t_{acq}. To minimize the photo-bleaching of the biological sample, we would like t_{acq} as small as possible while keeping high WSNR. In this case, the best choice is the PSS strategy with $M_P = 64$: we achieve high WSNR (around 17 dB) with an acquisition time around 30 s.

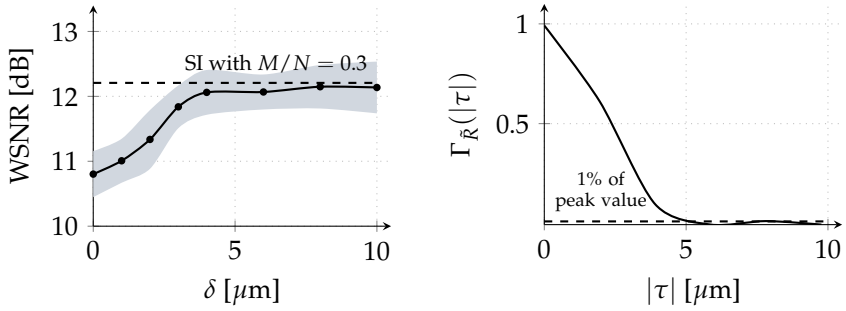

Figure 8.4 PSS strategy: choice of δ. (Left) Mean WSNR (over 25 trials) of the restored USAF target *versus* the shift between two consecutive replicas of the same speckle. The gray area represents the standard deviation. Synthetic observations were generated according to (6.5) (SNR of $\boldsymbol{\Phi} \boldsymbol{f}$ equal to 40 dB). Each illumination pattern was used twice and $M/N = 0.3$. (Right) Theoretical autocorrelation of the residual field $\tilde{R}$ defined in (7.12) as a function of $|\tau|$ (extracted from Figure 7.2).

Remark 8.2 (Approximation of the sensing matrix). Up to now, the proposed PSS strategy only decreases the acquisition time. Compared to SI for the same number of measurements, the number of speckles to be recorded to form the sensing matrix is identical. Moreover, the reconstruction time is similar between SI and PSS since the complexity (in $\mathcal{O}(MN)$) of the matrix-vector product involving $\tilde{\boldsymbol{\Phi}}$ is not optimized. By considering the translation rule (7.19), this can be potentially improved by approximating $\tilde{\boldsymbol{\Phi}}$ with a block-Toeplitz matrix $\tilde{\boldsymbol{\Phi}}_{\text{app}}$. Then, each matrix-vector product involving this new matrix can benefit from the FFT and the complexity is then reduced to $\mathcal{O}(N \log N)$. The previous storage of M speckle patterns is reduced to $\lceil M/M_P \rceil$ patterns. We test this matrix approximation in Figure 8.6. This figure is the same as Figure 8.5 but for a reconstruction performed with $\tilde{\boldsymbol{\Phi}}_{\text{app}}$. As expected, when M_P increases, $\|\boldsymbol{\theta}_{M_P}\|_2$ takes bigger values and the paraxial approximation is less respected. The error made by approximation (7.19) increases. This leads to a decrease in the reconstruction quality. However, for $M_P \leq 16$, the reconstruction quality is still similar to the one of the SI strategy (around 15 dB). Therefore, in this approximation of $\tilde{\boldsymbol{\Phi}}$ by $\tilde{\boldsymbol{\Phi}}_{\text{app}}$, one must find a trade-off between a fast acquisition time and the quality of the produced estimate. We therefore only consider the original matrix $\tilde{\boldsymbol{\Phi}}$ in our following experiments.

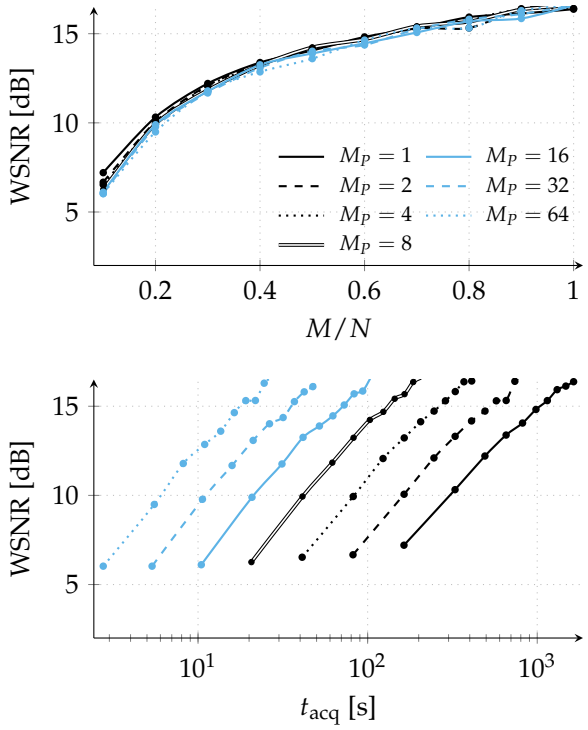

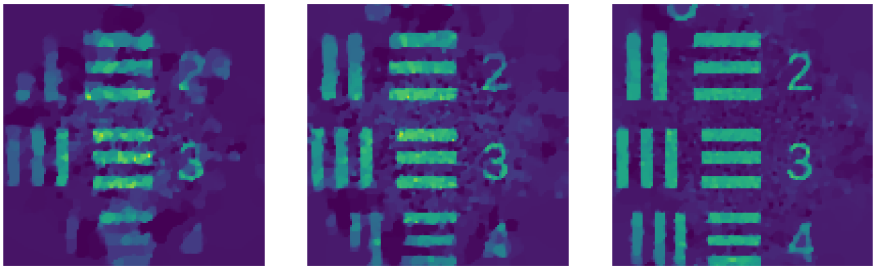

Figure 8.5 **PSS strategy.** Above: mean WSNR (over 10 trials) of the restored USAF target image *versus* M/N. Middle: same data as above but expressed as a function of t_{acq} instead of the M/N ratio. Synthetic observations were generated according to (6.5) (SNR of $\mathbf{\Phi} f$ equal to 40 dB). The number M_P of replicas of the same (shifted) speckle pattern belongs to $\{1, 2, 4, 8, 16, 32, 64\}$ and the shift δ between replicas is $4\,\mu$m. Below: estimates of f obtained for $M_P \in \{8, 16, 64\}$ and $t_{\text{acq}} \approx 20$ s. The PSS strategy with $M_P = 1$ corresponds to the SI strategy (see Figure 8.3). Estimates share the same intensity scale.

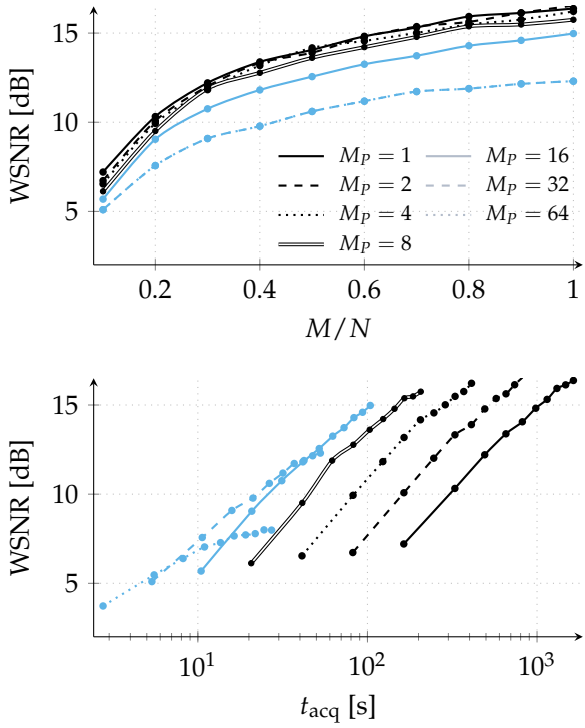

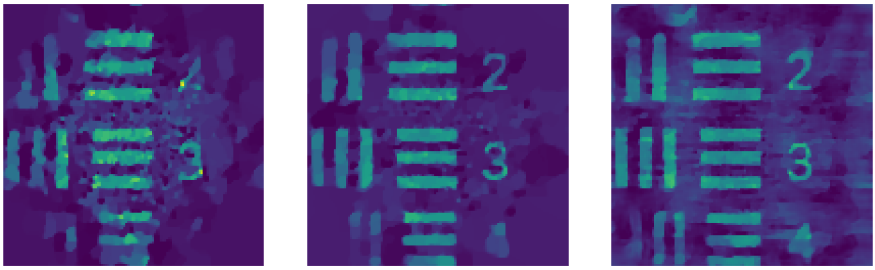

Figure 8.6 **PSS approximated strategy.** Above: mean WSNR (over 10 trials) of the restored USAF target image *versus* M/N. Middle: same data as above but expressed as a function of t_{acq} instead of the M/N ratio. Synthetic observations were generated according to (6.5) (SNR of $\mathbf{\Phi} f$ equal to 40 dB). The number M_P of replicas of the same (shifted) speckle pattern belongs to $\{1, 2, 4, 8, 16, 32, 64\}$ and the shift δ between replicas is $4\,\mu$m. Sensing matrix $\tilde{\mathbf{\Phi}}$ was approximated by a block-circulant operator $\tilde{\mathbf{\Phi}}_{\text{app}}$ (instead of a block-Toepliz operator since the FOV is limited) for the reconstruction. Below: estimates of $\boldsymbol{f}$ obtained for $M_P \in \{8, 16, 64\}$ and $t_{\text{acq}} \approx 20$ s. The PSS strategy with $M_P = 1$ corresponds to the SI strategy (see Figure 8.3). Estimates share the same intensity scale.

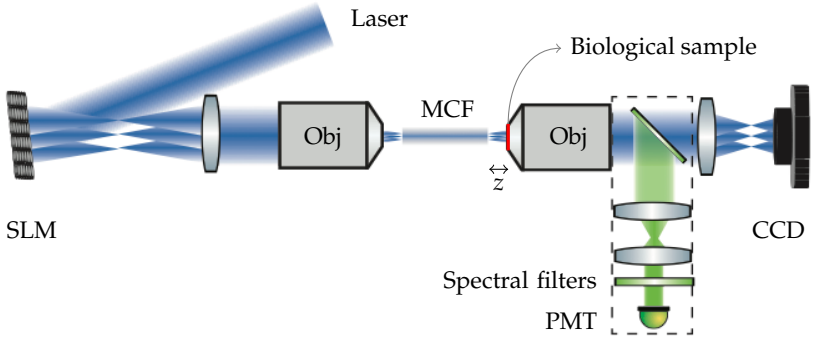

Figure 8.7 Simplified view of the experimental setup used to characterize the performance of the CS-based acquisition strategies. Relay optics (Obj) image the spatial light modulator (SLM) to the proximal endface of the multicore fiber (MCF). An imaging system with two channels is placed at a distance z of the MCF distal end. The main purpose of the first channel is to image the speckle patterns with a charge-coupled device (CCD) sensor. The second channel is dedicated to observations collection through a single pixel detector or photomultiplier tube (PMT).

8.4 Fluoresence imaging experiments

In this last section, we apply the SI and PSS methods to an actual LE in the context of fluorescence imaging. We first describe the experimental setup, material and methods, before explaining how these sensing strategies can improve the quality of the reconstructed images compared to the RS technique.

8.4.1 Experimental setup

A simplified view of the experimental setup is presented in Figure 8.7 and described below in functional blocks.

Spatial light modulator. A continous wave laser operating at 491 nm (Cobolt lasers, Sweden) is expanded and impinges upon a liquid crystal SLM (X10468-03, Hamamatsu, Japan). A set of relay optics, depicted by a single lens and objectives *Obj* in Figure 8.7, images the SLM to the proximal endface of the MCF. In order to maximize the injection of the light beams into the individual cores, a convex lenslet array whose centers are matched to the individual cores is displayed on the SLM. This results in a beamlet

array which is efficiently coupled into the MCF and whose relative phases can be tuned independently with the SLM.

Multicore fiber. Imaging through the MCF is analogous to phased arrays for beamforming where the relative phases between the cores (antennae) can be calibrated and tuned to generate and shift a focused beam. The cores of these fibers are single mode at the operating wavelength and exhibit an inter-core coupling term less than 20 dB [138]. These factors have two important advantages: (*i*) operations such as RS or defocusing can be performed with conventional optical elements at the distal end, and (*ii*) the resulting speckle patterns are highly resilient to external perturbations both thermal and mechanical (except for a global shift). These are significant advantages over single multimode fiber (MMF) where the significant off-diagonal coupling terms preclude stability and fast imaging with conventional optical elements. For a more comprehensive discussion of the imaging properties of the golden spiral MCFs, we refer the reader to [138].

Generation of the speckle patterns. Multiple illumination patterns are generated a few hundred microns away from the distal end as a combination of (*i*) randomizing the relative phase of the injected beamlets into the MCF resulting in a speckle pattern at the distal end of the fiber, and (*ii*) translations of the speckle pattern with a global tilt of the beamlets.

Calibration and imaging. The distal end of the MCF is placed at the focal plane of a second imaging system with two channels: one imaging the distal end onto the camera (CCD) and a second one detecting the signal of interest (PMT). The first channel serves for the recording of the sensing matrix, the visual inspection of the samples and the generation of an image close to the ground truth. The sensing matrix is populated by acquiring a multi-exposure image of each speckle pattern and fusing them to generate a synthetic high-dynamic range. The second channel employs a single pixel detector (PMT) (H7240-50, Hamamatsu, Japan) upon which the signal is detected. In the following experiments, the sample is either a standard USAF transmission target or fluorescent beads. In either case, we operate in a high photon count regime as assumed in section 6.2.

In the interest of maximum flexibility, we employ the SLM to function as a series of optical components such as a microlens array to maximize the coupling into the fiber, and as a galvanometric scanner. This also allows us to test and compare between the proposed imaging scheme and

USAF #1 USAF #2 Mean speckle field

Figure 8.8 Estimates of `USAF` ground truth. Images of standard USAF transmission target. They are estimated using the first channel of the imaging system (see Figure 8.7). The CCD sensor acquires M images of the product between a speckle and density map f. Their average divided by the mean speckle field (Gaussian fit estimated from the M light patterns) leads to the estimated ground truths.

conventional RS techniques. However, for the speckle illumination based compressive imaging proposed in the paper, the SLM can be replaced with conventional optical elements such as microlens arrays, mirror scanners and thin diffusers as in our earlier works [8].

8.4.2 Material and methods

The samples used for the experiments are either the standard `USAF` transmission target (see Figure 8.8) or or 5 μm fluorescent `Beads`. The `USAF` sample itself is not fluorescent: it is a layer of metal deposited on glass where the features (the bars) are transparent. To make it fluorescent, we apply a layer of highlighter on top of it. We use the setup depicted in Figure 8.7 and described in subsection 8.4.1 with a Fermat's golden spiral MCF containing $J = 118$ cores and with standard deviation $\sigma_c = 0.8\,\mu$m (or, equivalently, $d = 1.9\,\mu$m). The distance between the endface of the fiber and the sample plane is $z = 500\,\mu$m.

Acquisition and reconstruction

In all experiments, the data acquisition follows those two steps: (*i*) we record the speckle patterns with the CCD sensor to build and store the sensing matrix $\mathbf{\Phi}$ (pixel size equal to 2.2 μm), and (*ii*) we illuminate the sample with M speckles and measure the signal on the single pixel detector. Light patterns are either all different from each other (SI strategy)

or shifted versions of each other (PSS strategies) due to the application of global tilt terms on the SLM ($\delta = 1.1\,\mu$m).

The first experiment was designed to compare the SI and PSS strategies: $M = 4096$ measurements of `Beads #3` sample were acquired for $M_P = 1$ (SI) and then $M_P = 64$ (PSS). The second experiment acquired $M = 4096$ observations of two different parts of the `USAF` target (see Figure 8.8) with $M_P = 64$. Finally, $M = 4096$ observations of three other `Beads` samples were acquired with $M_P = 64$.

Unlike the number of observations M that is an acquisition parameter, the number of pixels N of the estimate (or equivalently, the pixel size a) can be chosen after the acquisition process. Ideally, a should match the diffraction limited point spread function of the device, *i.e.*, the speckle grain size. In this case, we can take full advantage of the CS-friendly statistical properties of the sensing matrix and we avoid spurious correlations in the estimate. For the considered experimental parameters, the average grain size is $r \approx 3.5\,\mu$m (see subsection 7.2.1). We thus set the pixel size $a = r$, and select $N = 80 \times 80$ for `USAF` samples and $N = 160 \times 160$ for `Beads` samples (the original sizes are 128×128 and 256×256, respectively).

We solve a problem slightly different from (8.12) giving better results,

$$\widehat{\bar{\boldsymbol{S}}\boldsymbol{f}} \in \underset{\substack{\boldsymbol{u}\in\mathbb{R}^N,\\ \boldsymbol{w}\in\mathbb{R}^{N\times 2}}}{\arg\min} \quad \frac{1}{2}\|\boldsymbol{R}_{\text{est}}(\sqrt{M}\tilde{\boldsymbol{\Phi}}\boldsymbol{u} - \tilde{\boldsymbol{y}})\|_2^2 + \rho\|\boldsymbol{\nabla}\boldsymbol{u} - \boldsymbol{w}\|_{2,1} + \alpha\rho\|\varepsilon(\boldsymbol{w})\|_{2,1} + \iota_{\mathbb{R}^N_+}(\boldsymbol{u}), \quad (8.15)$$

i.e., we estimate the *vignetted* fluorophore density map $\bar{\boldsymbol{S}}\boldsymbol{f}$ instead of $\boldsymbol{f}$. The regularization term is the TGV^2_α-norm. Indeed, this norm promotes piecewise linear images and is thus well adapted to our piecewise constant images multiplied by the smooth vignetting $\bar{\boldsymbol{s}}$. As for the simulations, we perform the reconstruction as described in subsection 8.2.3.

8.4.3 Results

Reconstruction results are visible in Figures 8.9 to 8.11. As expected, the SI strategy provides a better estimate for `Beads #3` sample: beads are better resolved and there are less artifacts in the background. However, this quality is obtained at the cost of an acquisition time 60 times longer compared to the PSS strategy. Middle and right images are again obtained with two different strategies (PSS and SI) but the same acquisition time $t_{\text{acq}} = 6.8\,$s. In this case, the SI strategy fails to reconstruct the beads.

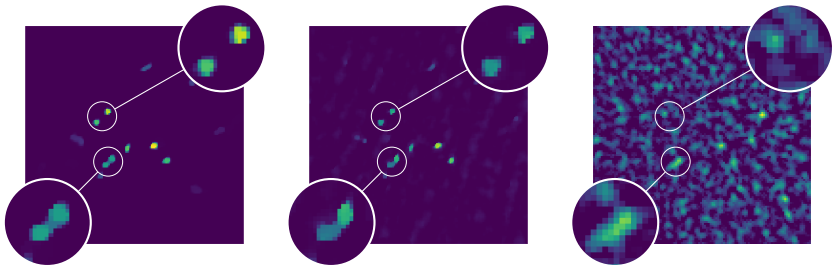

SI
$M = 4096$
$t_{\text{acq}} = 409.6\,\text{s}$

PSS
$M = 4096$
$t_{\text{acq}} = 6.8\,\text{s}$

SI
$M = 68$
$t_{\text{acq}} = 6.8\,\text{s}$

Figure 8.9 Vignetted estimates of `Beads #3` sample. Left and middle images are obtained with two different acquisition strategies (SI and PSS) but the same number of observations M ($\rho = 860$ and $\rho = 690$). Middle and right images are again obtained with two different strategies (PSS and SI) but the same acquisition time $t_{\text{acq}} = 6.8\,\text{s}$. Left and middle estimates share the same intensity scale. The intensity of the right estimate is 50 times lower compared to the other two images.

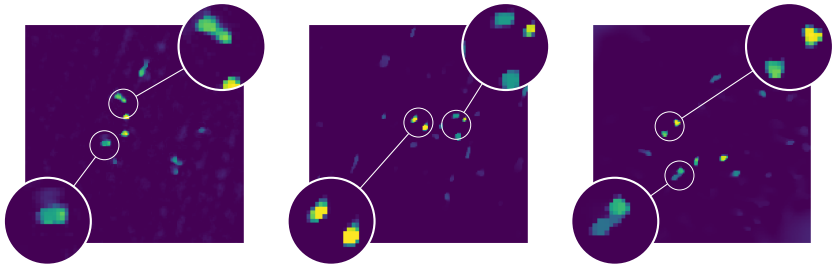

`#1`
$\rho = 440$

`#2`
$\rho = 440$

`#4`
$\rho = 100$

Figure 8.10 Vignetted estimates of `Beads` samples (`#1`, `#2` and `#4`). All the 160×160 estimates are reconstructed from $M = 4096$ observations acquired with the PSS strategy ($M_P = 64$). It corresponds to $M/N = 0.16$.

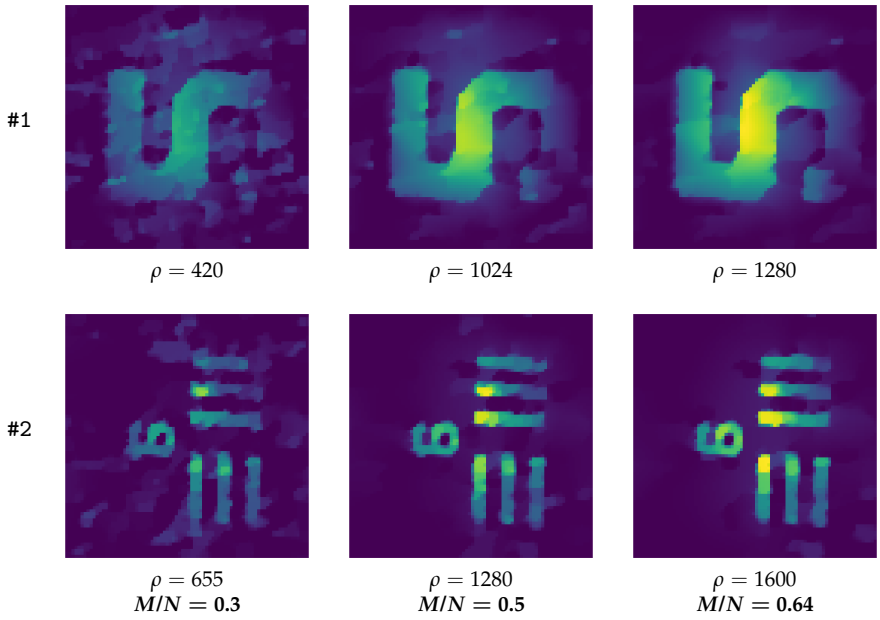

Figure 8.11 **Vignetted estimates of `USAF` samples with PSS strategy.** All the 80×80 estimates are reconstructed from $M = 4096$ observations (corresponding to $M/N = 0.64$) acquired with the PSS strategy ($M_P = 64$). The estimates of each sample share the same intensity scale.

For `USAF` samples and `Beads #1`, `#2` and `#4`, we performed the image reconstruction from the observations acquired with PSS strategy for M/N ratios in $\{0.3, 0.5, 0.64\}$ (see Figures 8.10 and 8.11). We note that in order to minimize photo-bleaching, we keep the incident laser power extremely low (few 100 s of μW over the entire FOV). This precludes us from acquiring ground truth fluorescence images of the beads since the sensitivity of a standard camera is much lower than the single pixel detector.

Appendix 8.A Inverse problem without the non-negativity constraint

Figure 8.12 is similar to Figure 8.3 but is obtained when we do not enforce the non-negativity of the estimate. In this case, we observe that the performance of the biased model is worse than the one of the debiased model. Even if the debiased model leads to negative values in the final image, the edges of the lines and the numbers are sharper (see, *e.g.*, the number 2).

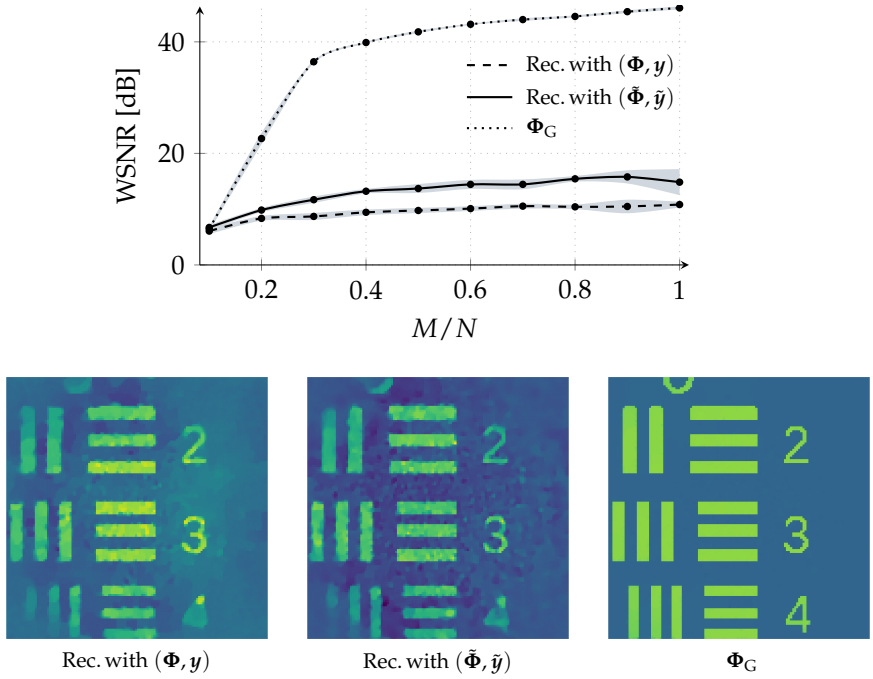

Figure 8.12 SI strategies without non-negativity constraint. Above: mean WSNR (over 10 trials) of the restored USAF target *versus* M/N for three SI strategies: (*i*) acquisition and reconstruction with $(\boldsymbol{\Phi}, \boldsymbol{y})$ (dashed line), (*ii*) acquisition with $\boldsymbol{\Phi}$ and reconstruction with $(\tilde{\boldsymbol{\Phi}}, \tilde{\boldsymbol{y}})$ (solid line), and (*iii*) acquisition and reconstruction with ideal sensing matrix $\boldsymbol{\Phi}_{\mathrm{G}}$ (dotted line). The gray areas represent the standard deviations. Synthetic observations were generated according to (6.5) (SNR of $\boldsymbol{\Phi f}$ equal to 40 dB). Below: estimates obtained for $M/N = 0.3$. They share the same intensity scale.

9

Summary and perspectives

Don't adventures ever have an end? I suppose not.
Someone else always has to carry on the story.
Bilbo Baggins

SEVERAL challenges were presented in Chapters 1, 3 and 6. This last chapter sums up how they were tackled. As the journey is not finished, we propose some directions for the next steps of this research.

9.1 The thesis in a nutshell

Chapter 2 introduced regularized inverse problems as well as important tools in convex optimization used throughout the thesis. Chapter 3 and Chapter 6 presented the general framework of PET and LE acquisition, respectively. They do not included contributions but they highlight imaging challenges related to each modality and are necessary in the formulation of the inverse problems. In the following, we thus focus on Chapters 4, 5, 7 and 8.

Positron emission tomography

In Chapter 4, we investigated the nature of the noise in PET images. First, we showed that under weak hypotheses on the sinogram correction, the

noise on the projections, before the reconstruction, is well characterized by a sub-exponential distribution. Assuming a linear (unknown) reconstruction algorithm, we demonstrated that the distribution of the noise in PET images has two behaviors. Around zero, the noise behaves like a Gaussian random variable but the tail of the distribution is sub-exponential.

Based on this, we proposed a formulation for the estimation problem that includes a data fidelity term showing this same dual behavior, namely the Huber function. Its change of behavior is controlled by a parameter δ (see Figure 4.1, p. 56). We regularized the inverse problem with a TGV^2_α-norm that promotes the piecewise-smoothness of the estimate. The criteria described in subsection 2.3.2 failed to efficiently stop the internal iterations of the GCP algorithm and to select an appropriate regularization parameter (see Figure 4.2, p. 60). For this reason, we used a criterion involving the original image. Even if unrealistic, it provides an upper bound on the quality that we can expect with another criterion.

The simulations showed that the Huber function, for an appropriate choice of the parameter δ, performs as well as the ℓ_1-norm (resp. squared ℓ_2-norm) when the linear FBP (resp. iterative OSEM) algorithm is used for the reconstruction (see Figures 4.4 to 4.7, pp. 66-69). The Huber function is polyvalent regarding the type of the reconstruction algorithm (linear or iterative) but it requires a possibly costly estimation of its parameter δ. In this chapter, we did not develop a rule to automatically set the parameter. In practical applications, where the ground truth is not available, it may bthus e better to choose the ℓ_1-norm or the squared ℓ_2-norm as the data fidelity term, depending on the nature of the reconstruction algorithm.

Chapter 5 extends Chapter 4 to a situation where the blurring operator is unknown, *i.e.*, to a blind context. Following [71], we formulated an inverse problem integrating prior information on both the image and the PSF. Unlike many works in the literature that deal with parametric models for the point spread function (PSF), we only considered weak priors on the PSF, namely its non-negativity and its flux preservation. We also included the knowledge of a region with uniform activity, in order to avoid the trivial solution or shifted estimates [71, 77].

Under the hypothesis of a spatially invariant kernel, we solved this new non-smooth and biconvex minimization problem using an alternating proximal algorithm. Simulations show the importance of an accurate delineation of the region with uniform activity (see Figure 5.4, p. 91). The results obtained on experimental data are encouraging: in the first dataset, the recovered PSF is close to the one measured experimentally with a nee-

dle. The activity in the main hole of the restored image is flat (see Figure 5.7, p. 94).

Lensless endoscopy

In Chapter 8, we proposed new sensing methods to image fluorescent samples in the context of lensless endoscopy. The two acquisition strategies are based on speckle illumination, namely speckle imaging (SI) and partial speckle scanning (PSS). Our work relies on showing that these speckles are random fields following a sub-exponential distribution (see Chapter 7). After normalization and discretization, they are good candidates to build efficient sensing matrices in a compressive framework [2].

The use of speckle illumination to collect observations raises a lot of challenges with regard to the design of the fiber, to the acquisition strategy and to the reconstruction scheme.

First, the arrangement of the single mode cores must be optimized to achieve narrow autocorrelation of the speckle field (see subsection 7.2.1), *i.e.*, a grain size as small as possible, and to minimize the magnitude of the side lobes. Fermat's golden spiral shape shows a low side lobes level and a very good contrast between the intensities of the central peak and the side lobes [138]. A small grain size combined with an appropriate choice of the resolution of the final image leads to a sensing matrix with nearly independent columns, a desirable property in compressed sensing.

Then, the acquisition strategy must be thought to minimize the acquisition time. This is necessary to avoid as far as possible the loss of fluorescence of the sample and to reach a frame rate suitable for *in vivo* imaging of cellular processes (*e.g.*, the propagation of nerve impulses). The SI strategy offers good reconstruction quality for far fewer measurements compared to raster scanning (RS) (see Figure 8.3, p. 140). However, the corresponding acquisition time is unrealistic for real biological applications. We overcome this limitation using the PSS strategy which exploits the memory effect of the multicore fiber (MCF) via the use of scan mirrors. Their response rate is around 1,000 times higher compared to a change of the spatial light modulator (SLM) configuration. With an appropriate speckle shift δ (see Figure 8.4, p. 144), we reach a reconstruction quality similar to that of SI (see Figure 8.5, p. 145).

Finally, the reconstruction scheme must encode prior information on the structure of the fluorophore density map. We proposed a debiased formulation including the minimization of TV or TGV^2_α-norm. We showed

that the sensing matrix can be approximated by a block-circulant matrix to reduce the number of stored patterns. When a same (shifted) speckle is used $M_P \leq 16$ times, the reconstruction quality is still close to the one of SI (see Figure 8.6, p. 146).

9.2 Perspectives for future work

The work presented in this document is only a small increment to the existing research in PET and LE imaging. In this section, we would like to mention some interesting directions for future work. Regarding Figure 1.1, we can mainly act on two aspects: the acquisition step and/or the recovery step. The first one is directly related to the sampling strategy implemented to acquire observations. The second one includes the formulation of the inverse problems—based on the knowledge of a forward model—as well as the reconstruction scheme.

Positron emission tomography

In this work, we focused on PET imaging in a post-processing phase. From this perspective, we can only act on the second step in Figure 1.1, *i.e.*, the recovery step.

A first improvement, and not the least, would be to consider a spatially varying blurring operator in the deconvolution problem. As shown in [1] and due to circular symmetry of the blurring kernel (see subsection 3.2.3), the PSF can be considered as isotropic only at the center of the field of view (FOV): as we move away from it, the difference between the radial and the tangential full width at half maximum (FWHM) of the PSF increases (*e.g.*, in a Siemens ECAT EXACT HR$^+$ scanner, at 100 mm of the center, the radial FWHM is around 7 mm and the tangential FWHM is around 5 mm). There exist several approaches to deal with such varying operators, *e.g.*, the use of diffeomorphisms and convolutions, separable approximations of the blurring kernel and its spatial variations, approximation of the blurring operator by a diagonal operator using wavelets or Gabor transforms, the use of windowed convolutions, etc. [57]. A few years ago, several authors proposed to approximate such an operator by a sparse matrix in the wavelet domain allowing in this way a fast matrix-vector product [57, 58, 162]. In a blind framework, this sparse representation could also be used as a prior on the blurring operator. Recent work makes use of trendy neural networks to learn the blurring operator expressed as an alternating product of diagonal and block-circulant matrices [31].

From a computational point of view, several improvements can be considered. First, we would like to select a value for the parameter of the Huber function based, for instance, on the blurry observed image. Second, we would like to find a criterion to stop the internal iterations of the deconvolution algorithm and to select the regularization parameter. This criterion will depend, for instance, on the distribution of the residual rather than on the ground truth—like our (unrealistic) criterion. This automatic selection of the final estimate is particularly necessary in the post-processing of real PET images. Third, we could extend Algorithms 5 and 6 to 3D PET volumes. This extension is quite straightforward since it basically only requires to modify our implementation of TGV^2_α. The challenge in this case will be to develop fast methods able to deal with the dramatic increase in the size of the optimization variable, especially when TGV^2_α is used.

Finally, it would be interesting to perform more comparisons with other (blind) deconvolution techniques. For instance, DeepPET combined to dPETSTEP for the training part seems to be very promising to reconstruct and deblur PET images in one single step [84, 85]. A main advantage of the deep convolutional networks is that they get rid of the formulation step required when we solve inverse problems via minimization; they learn the forward model from their training set.

Lensless endoscopy

The first research direction for LE imaging concerns the acquisition step and more specifically, the sampling scheme. In Chapter 8, we only considered line scanning for the PSS strategy. However, if we use two scan mirrors, other scanning trajectories could be considered to further minimize the number of measurements compared to traditional RS. If the mirrors are driven parallely, there would be no increase in the acquisition time. In this case, we could perform speckle scanning in a way similar to RS: a single speckle would scan $M \leq N$ positions in the FOV. In addition, recent advances in ultrafast scanners employing acousto-optic deflectors [124] and resonant galvanometers [8, 61] will serve to speed up the acquisitions both in the case of focused or speckle illumination. Faster SLM such as digital micromirror devices [67] and deformable mirrors [21] could also provide a massive speedup to SI, at the cost of experimental integration.

The 2D setup presented in this work is quite unrealistic for real *in vivo* imaging: (*i*) in practice, the LE will be required to image 3D volumes and (*ii*) we will not have access to the fiber endface to image the speckle pattern.

Regarding those challenges, we would like to highlight two interesting research directions. The first one is the design of a 3D acquisition and reconstruction framework. One of the challenges will be to deal with the depth dependency of the speckle autocorrelation [112] and with the scattering induced by the non-homogeneous propagation medium. The second one is the study of blind imaging taking advantage of the memory effect like in [20, 143]. In this case, the estimation is based on the autocorrelations of the measurements vector and of the discretized speckle field (known *a priori*). Another solution to deal with the inaccessibility to the fiber endface would be to perform a single initial calibration of the field (like in RS) and then, to compute it. Given the high resilience of the fiber to bending, this would alleviate the tedious calibration of multiple intensity patterns.

Developping speckle imaging in LE seems to be promising to further bring this new technology towards *in vivo* applications.

Bibliography

[1] L.-E. Adam, J. Zaers, H. Ostertag, H. Trojan, M. E. Bellemann, and G. Brix. "Performance evaluation of the whole-body PET scanner ECAT EXACT HR following the IEC standard". In: *IEEE Transactions on Nuclear Science* 44.3 (1997), pp. 1172–1179.

[2] R. Adamczak, A. E. Litvak, A. Pajor, and N. Tomczak-Jaegermann. "Restricted isometry property of matrices with independent columns and neighborly polytopes by random sampling". In: *Constructive Approximation* 34.1 (2011), pp. 61–88.

[3] A. M. Alessio and L. MacDonald. "Spatially variant positron range modeling derived from CT for PET image reconstruction". In: *IEEE Nuclear Science Symposium Conference Record*. 2008, pp. 3637–3640.

[4] M. S. C. Almeida and L. B. Almeida. "Blind and semi-blind deblurring of natural images". In: *IEEE Transactions on Image Processing* 19.1 (2010), pp. 36–52.

[5] M. S. C. Almeida and M. A. T. Figueiredo. "Deconvolving images with unknown boundaries using the alternating direction method of multipliers". In: *IEEE Transactions on Image Processing* 22.8 (2013), pp. 3074–3086.

[6] M. S. C. Almeida and M. A. T. Figueiredo. "Parameter estimation for blind and non-blind deblurring using residual whiteness measures." In: *IEEE Transactions on Image Processing* 22.7 (2013), pp. 2751–2763.

[7] M. S. C. Almeida. "Blind separation and blind deblurring of natural images". PhD thesis. Universidade Técnica de Lisboa, 2010.

[8] E. R. Andresen, G. Bouwmans, S. Monneret, and H. Rigneault. "Toward endoscopes with no distal optics: video-rate scanning microscopy through a fiber bundle". In: *Optics Letters* 38.5 (2013), p. 609.

[9] E. R. Andresen, S. Sivankutty, V. Tsvirkun, G. Bouwmans, and H. Rigneault. "Ultrathin endoscopes based on multicore fibers and adaptive optics: status and perspectives". In: *Journal of Biomedical Optics* 21.12 (2016), p. 121506.

[10] F. J. Anscombe. "The transformation of Poisson, binomial and negative-binomial data". In: *Biometrika* 35.3 (1948), pp. 246–254.

[11] S. Anthoine, J.-F. Aujol, Y. Boursier, and C. Mélot. "Some proximal methods for CBCT and PET tomography". In: *Inverse Problems and Imaging* 6.4 (2012).

[12] S. R. Arridge, K. Ito, B. Jin, and C. Zhang. "Variational Gaussian approximation for Poisson data". In: *Inverse Problems* 34 (2018).

[13] H. Attouch, J. Bolte, P. Redont, and A. Soubeyran. "Proximal alternating minimization and projection methods for nonconvex problems: an approach based on the Kurdyka-Lojasiewicz inequality". In: *Mathematics of Operations Research* 35.2 (2010), pp. 438–457.

[14] H. Attouch, P. Redont, and A. Soubeyran. "A new class of alternating proximal minimization algorithms with costs-to-move". In: *SIAM Journal on Optimization* 18.3 (2007), pp. 1061–1081.

[15] G. R. Ayers and J. C. Dainty. "Iterative blind deconvolution method and its applications". In: *Optics Letters* 13.7 (1988), p. 547.

[16] D. Bailey, D. Townsend, P. Valk, and M. Maisey. *Positron emission tomography*. 2005.

[17] A. Beck and M. Teboulle. "A fast iterative shrinkage-thresholding algorithm for linear inverse problems". In: *SIAM Journal on Imaging Sciences* 2.1 (2009), pp. 183–202.

[18] M. Bertero, P. Boccacci, G. Talenti, R. Zanella, and L. Zanni. "A discrepancy principle for Poisson data". In: *Inverse Problems* 26.10 (2010), p. 105004.

[19] B. Berthon, I. Häggström, A. Apte, B. J. Beattie, A. S. Kirov, J. L. Humm, C. Marshall, E. Spezi, A. Larsson, and C. R. Schmidtlein. "PETSTEP: Generation of synthetic PET lesions for fast evaluation of segmentation methods". In: *Physica Medica* 31.8 (2015), pp. 969–980.

[20] J. Bertolotti, E. G. Van Putten, C. Blum, A. Lagendijk, W. L. Vos, and A. P. Mosk. "Non-invasive imaging through opaque scattering layers". In: *Nature* 491.7423 (2012), pp. 232–234.

[21] T. G. Bifano, J. Perreault, R. Krishnamoorthy Mali, and M. N. Horenstein. "Microelectromechanical deformable mirrors". In: *IEEE Journal on Selected Topics in Quantum Electronics* 5.1 (1999), pp. 83–89.

[22] M. A. Bolshtyansky and B. Y. Zel'dovich. "Transmission of the image signal with the use of a multimode fiber". In: *Optics Communications* 123.4-6 (1996), pp. 629–636.

[23] J. Bond, D. Frush, E. Samei, and W. P. Segars. "Simulation of anatomical texture in voxelized XCAT phantoms". In: *Medical Imaging 2013: Physics of Medical Imaging*. Ed. by R. M. N. Hoeschen, B. R. Whiting, and Christoph. Vol. 8668. SPIE, 2013, pp. 155–160.

[24] V. Boominathan, J. K. Adams, M. S. Asif, B. W. Avants, J. T. Robinson, R. G. Baraniuk, A. C. Sankaranarayanan, and A. Veeraraghavan. "Lensless imaging: A computational renaissance". In: *IEEE Signal Processing Magazine* 33.5 (2016), pp. 23–35.

[25] P. T. Boufounos, M. F. Duarte, and R. G. Baraniuk. "Sparse signal reconstruction from noisy compressive measurements using cross validation". In: *2007 IEEE/SP 14th Workshop on Statistical Signal Processing*. 2007, pp. 299–303.

[26] N. Boussion, C. Cheze Le Rest, M. Hatt, and D. Visvikis. "Incorporation of wavelet-based denoising in iterative deconvolution for partial volume correction in whole-body PET imaging". In: *European Journal of Nuclear Medicine and Molecular Imaging* 36.7 (2009), pp. 1064–1075.

[27] S. Boyd and L. Vandenberghe. *Convex Optimization*. Cambridge: Cambridge University Press, 2004.

[28] K. Bredies, K. Kunisch, and T. Pock. "Total generalized variation". In: *SIAM Journal on Imaging Sciences* 3.3 (2010), pp. 492–526.

[29] A. M. Bruckstein, D. L. Donoho, and M. Elad. "From sparse solutions of systems of equations to sparse modeling of signals and images". In: *SIAM Review* 51.1 (2009), pp. 34–81.

[30] I. Buvat. "A non-parametric bootstrap approach for analysing the statistical properties of SPECT and PET images". In: *Physics in Medicine and Biology* 47.10 (2002), pp. 1761–1775.

[31] J. Calbert. "Learning integral operators from diagonal-circulant neural networks". Master thesis. Université catholique de Louvain, 2020.

[32] Cambridge Technology Inc. *62XXH Series Galvanometer Scanners*. Tech. rep. 2019.

[33] E. J. Candès and M. Wakin. "An introduction to compressive sampling". In: *IEEE Signal Processing Magazine* 25.2 (2008), pp. 21–30.

[34] A. M. Caravaca-Aguirre, S. Singh, S. Labouesse, M. V. Baratta, R. Piestun, and E. Bossy. "Hybrid photoacoustic/fluorescence microendoscopy through a multimode fiber using speckle illumination". In: *APL Photonics* 4 (2019), pp. 1–10.

[35] M. Carlavan and L. Blanc-Féraud. "Regularizing parameter estimation for Poisson noisy image restoration". In: *Proceedings of the 5th International ICST Workshop on New Computational Methods for Inverse Problems* (2011).

[36] Y. C. Cavalcanti, T. Oberlin, N. Dobigeon, C. Févotte, S. Stute, M. J. Ribeiro, and C. Tauber. "Factor analysis of dynamic PET images: Beyond Gaussian noise". In: *IEEE Transactions on Medical Imaging* 38.9 (2019), pp. 2231–2241.

[37] A. Chambolle and T. Pock. "A first-order primal-dual algorithm for convex problems with applications to imaging". In: *Journal of Mathematical Imaging and Vision* 40.1 (2010), pp. 120–145.

[38] P. C. Cheng. "The contrast formation in optical microscopy". In: *Handbook of Biological Confocal Microscopy: Third Edition*. 2006. Chap. 8, pp. 162–206.

[39] S. Choi, A. Cichocki, H.-M. Park, and S.-Y. Lee. "Blind source separation and independent component analysis: a review". In: *Neural Information Processing* 6.1 (2005).

[40] D. Choudhury, D. K. McNicholl, A. Repetti, I. Gris-Sánchez, T. A. Birks, Y. Wiaux, and R. R. Thomson. "Computational optical imaging with a photonic lantern". In: *Nature Communications* 11 (2020), p. 5217.

[41] E. Chouzenoux, A. Jezierska, J.-c. Pesquet, and H. Talbot. "A convex approach for image restoration with exact Poisson-Gaussian likelihood". In: *SIAM Journal on Imaging Sciences* 8.4 (2015), pp. 2662–2682.

[42] T. Cizmar and K. Dholakia. "Exploiting multimode waveguides for pure fibre-based imaging". In: *Nature Communications* 3 (2012), p. 1027.

[43] P. L. Combettes and J.-C. Pesquet. "Proximal splitting methods in signal processing". In: *Fixed-Point Algorithms for Inverse Problems in Science and Engineering*. Ed. by H. H. Bauschke, R. S. Burachik, P. L. Combettes, V. Elser, D. R. Luke, and H. Wolkowicz. Vol. 49. Springer Optimization and Its Applications. New York, NY: Springer New York, 2011. Chap. 10, pp. 185–212.

[44] P. L. Combettes and V. R. Wajs. "Signal recovery by proximal forward-backward splitting". In: *Multiscale Modeling & Simulation* 4.4 (2005), pp. 1168–1200.

[45] J.-F. Daisne, T. Duprez, B. Weynand, M. Lonneux, M. Hamoir, H. Reychler, and V. Grégoire. "Tumor volume in pharyngolaryngeal squamous cell carcinoma: comparison at CT, MR imaging, and FDG PET and validation with surgical Specimen 1". In: *Radiology* 1 (2004), pp. 93–100.

[46] B. L. Davey, R. G. Lane, and R. H. Bates. "Blind deconvolution of noisy complex-valued image". In: *Optics Communications* 69.5-6 (1989), pp. 353–356.

[47] K. Degraux. "Methods for solving regularized inverse problems : from non- Euclidean fidelities to computational imaging applications". PhD thesis. Université catholique de Louvain, 2017.

[48] C. A. DiMarzio. *Fourier Optics*. Tech. rep. 2020, pp. 359–384.

[49] D. L. Donoho. "Compressed sensing". In: *IEEE Transactions on Information Theory* 52.4 (2006), pp. 1289–1306.

[50] D. L. Donoho and I. M. Johnstone. "Adapting to unknown smoothness via wavelet shrinkage". In: *Journal of the American Statistical Association* 90.432 (1995), pp. 1200–1224.

[51] M. F. Duarte, M. A. Davenport, D. Takhar, J. N. Laska, T. Sun, K. F. Kelly, and R. G. Baraniuk. "Single-pixel imaging via compressive sampling". In: *IEEE Signal Processing Magazine* 25.2 (2008), pp. 83–91.

[52] M. F. Duarte and Y. C. Eldar. "Structured compressed sensing: From theory to applications". In: *IEEE Transactions on Signal Processing* 59.9 (2011), pp. 4053–4085.

[53] F.-X. Dupé, J. Fadili, and J.-L. Starck. "Linear inverse problems with various noise models and mixed regularizations". In: *Proceedings of the 5th International ICST Conference on Performance Evaluation Methodologies and Tools* (2012), pp. 621–626.

[54] F.-X. Dupé, J. Fadili, and J. Starck. "A proximal iteration for deconvolving Poisson noisy images using sparse representations". In: *IEEE Transactions on Image Processing* 18.2 (2009), pp. 310–321.

[55] F.-X. Dupé, J. Fadili, and J. Starck. "Deconvolution under Poisson noise using exact data fidelity and synthesis or analysis sparsity priors". In: *Statistical Methodology* 9.1-2 (Jan. 2012), pp. 4–18.

[56] M. Elad. "Sparse and redundant representation modeling-What next?" In: *IEEE Signal Processing Letters* 19.12 (2012), pp. 922–928.

[57] P. Escande and P. Weiss. "Sparse wavelet representations of spatially varying blurring operators". In: *SIAM Journal on Imaging Sciences* 8.4 (2015), pp. 2976–3014.

[58] P. Escande, P. Weiss, and F. Malgouyres. "Image restoration using sparse approximations of spatially varying blur operators in the wavelet domain". In: *Journal of Physics: Conference Series* 464.1 (2013).

[59] K. Exner and W. Villiger. "The "optical power" of the atmosphere and its measurement". In: *The Astrophysical Journal* 21 (1905), pp. 368–370.

[60] M. J. Fadili, J. L. Starck, and F. Murtagh. "Inpainting and zooming using sparse representations". In: *Computer Journal* 52.1 (2009), pp. 64–79.

[61] G. Y. Fan, H. Fujisaki, A. Miyawaki, R. K. Tsay, R. Y. Tsien, and M. H. Ellisman. "Video-rate scanning two-photon excitation fluorescence microscopy and ratio imaging with cameleons". In: *Biophysical Journal* 76.5 (1999), pp. 2412–2420.

[62] M. A. T. Figueiredo and J. M. Bioucas-Dias. "Frame-based deconvolution of Poissonian images using alternating direction optimization". In: *IEEE Transactions on Image Processing* 19.12 (2010), pp. 3133–3145.

[63] D. A. Fish, J. G. Walker, A. M. Brinicombe, and E. R. Pike. "Blind deconvolution by means of the Richardson–Lucy algorithm". In: *Journal of the Optical Society of America* 12.1 (1995), p. 58.

[64] B. A. Flusberg, E. D. Cocker, W. Piyawattanametha, J. C. Jung, L. Eunice, M. Cheung, and M. J. Schnitzer. "Fiber-optic fluorescence imaging". In: *Nature Methods2* 2.12 (2005), pp. 941–950.

[65] S. Foucart and G. Lecue. "An IHT algorithm for sparse recovery from subexponential measurements". In: *IEEE Signal Processing Letters* 24.9 (2017), pp. 1280–1283.

[66] X. Geets, J. A. Lee, A. Bol, M. Lonneux, and V. Grégoire. "A gradient-based method for segmenting FDG-PET images: methodology and validation." In: *European journal of nuclear medicine and molecular imaging* 34.9 (2007), pp. 1427–38.

[67] Q. Geng, C. Gu, J. Cheng, and S.-c. Chen. "Digital micromirror device-based two-photon microscopy for three-dimensional and random-access imaging". In: *Optica* 4.6 (2017), p. 674.

[68] P. Getreuer. "Total variation deconvolution using split Bregman". In: *Image Processing On Line* 2.2 (2012), pp. 158–174.

[69] A. González. "Solving inverse problems in imaging using robust and regularized optimization". PhD thesis. Université catholique de Louvain, 2016.

[70] A. González, V. Delouille, and L. Jacques. "Non-parametric PSF estimation from celestial transit solar images using blind deconvolution". In: *Journal of Space Weather and Space Climate* 6 (2016), A1.

[71] A. González, L. Jacques, C. De Vleeschouwer, and P. Antoine. "Compressive optical deflectometric tomography: A constrained total-variation minimization approach". In: *Inverse Problems and Imaging* 8.2 (2014), pp. 421–457.

[72] J. W. Goodman. *Introduction to Fourier optics*. Roberts and Company Publishers, 2005.

[73] J. W. Goodman. "Some fundamental properties of speckle". In: *Optical Society of America* 66.11 (1976), pp. 1145–1150.

[74] J. W. Goodman. *Speckle phenomena in optics: Theory and applications*. Roberts and Company Publishers, 2007.

[75] J. W. Goodman. *Statistical properties of laser speckle patterns*. Tech. rep. Defense documentation center for scientific and technical information, 1963.

[76] S. Guérit. *Lecture notes: Computational inverse problems (Laurent Demanet)*. Tech. rep. Louvain-la-Neuve, 2019.

[77] S. Guérit, A. González, A. Bol, J. A. Lee, and L. Jacques. "Blind deconvolution of PET images using anatomical priors". In: *the 3rd International Traveling Workshop on Interactions between Sparse models and Technology (iTWIST)*. 2016.

[78] S. Guérit, L. Jacques, and J. A. Lee. "Image deconvolution by local order preservation of pixels values". In: *24th European Signal Processing Conference (EUSIPCO)*. 2016.

[79] S. Guérit, L. Jacques, B. Macq, and J. A. Lee. "Post-reconstruction deconvolution of PET images by total generalized variation regularization". In: *23rd European Signal Processing Conference (EUSIPCO)*. 2015.

[80] S. Guérit, S. Sivankutty, J. A. Lee, H. Rigneault, and L. Jacques. "Compressive lensless endoscopy with partial speckle scanning". 2021.

[81] S. Guérit, S. Sivankutty, C. Scotté, J. A. Lee, H. Rigneault, and L. Jacques. "Compressive sampling approach for image acquisition with lensless endoscope". In: *the 4th International Traveling Workshop on Interactions between Sparse models and Technology (iTWIST)*. 2018.

[82] J. Hadamard. "Les problèmes aux limites dans la théorie des équations aux dérivées partielles". In: *Journal de Physique Théorique et Appliquée* 6.1 (1907), pp. 202–241.

[83] J. Hadamard. "Sur les problèmes aux dérivées partielles et leur signification physique". In: *Princeton University Bulletin* 13.4 (1902).

[84] I. Häggström, B. J. Beattie, and C. R. Schmidtlein. "Dynamic PET simulator via tomographic emission projection for kinetic modeling and parametric image studies". In: *Medical Physics* 43.6 (2016), pp. 3104–3116.

[85] I. Häggström, C. R. Schmidtlein, G. Campanella, and T. J. Fuchs. "DeepPET: A deep encoder–decoder network for directly solving the PET image reconstruction inverse problem". In: *Medical Image Analysis* 54 (2019), pp. 253–262.

[86] Hamamatsu. *LCOS-SLM (Liquid Crystal on Silicon-Spatial Light Modulator): X10468/X13267/X13138 series*. Tech. rep., pp. 1–13.

[87] P. Huet, S. Burg, D. Le Guludec, F. Hyafil, and I. Buvat. "Variability and uncertainty of 18F-FDG PET imaging protocols for assessing inflammation in atherosclerosis: Suggestions for improvement". In: *Journal of Nuclear Medicine* 56.4 (2015), pp. 552–559.

[88] M. C. Huisman, S. Reder, A. W. Weber, S. I. Ziegler, and M. Schwaiger. "Performance evaluation of the Philips MOSAIC small animal PET scanner". In: *European Journal of Nuclear Medicine and Molecular Imaging* 34.4 (2007), pp. 532–540.

[89] L. Jacques and P. Vandergheynst. "Compressed Sensing:"When sparsity meets sampling"". In: *Optical and Digital Image Processing: Fundamentals and Applications*. Wiley-Blackwell, 2010. Chap. 23.

[90] O. Katz, Y. Bromberg, and Y. Silberberg. "Compressive ghost imaging". In: *Applied Physics Letters* 95.13 (2009), pp. 93–96.

[91] M. K. Kim, C. H. Park, C. Rodriguez, Y. K. Park, and Y. H. Cho. "Superresolution imaging with optical fluctuation using speckle patterns illumination". In: *Scientific Reports* 5 (2015), pp. 1–10.

[92] M. Kirkove, S. Guérit, L. Jacques, C. Loffet, F. Languy, J.-F. Vandenrijt, and M. Georges. "Determination of vibration amplitudes from binary phase patterns obtained by phase-shifting time-averaged speckle shearing interferometry". In: *Applied Optics* 57.27 (2018), pp. 8065–8077.

[93] F. Knoll, K. Bredies, T. Pock, and R. Stollberger. "Second order total generalized variation (TGV) for MRI." In: *Magnetic resonance in medicine* 65.2 (2011), pp. 480–491.

[94] D. Kundur and D. Hatzinakos. "Blind image deconvolution". In: *IEEE Signal Processing Magazine* 13 (1996), p. 43.

[95] R. V. Langmuir. "Scattering of laser light". In: *Applied Physics Letters* 2.2 (1963), pp. 29–30.

[96] J. A. Lee. "Segmentation of positron emission tomography images: some recommendations for target delineation in radiation oncology". In: *Radiotherapy and oncology : journal of the European Society for Therapeutic Radiology and Oncology* 96.3 (2010), pp. 302–307.

[97] C. S. Levin and E. J. Hoffman. "Calculation of positron range and its effect on the fundamental limit of positron emission tomography system spatial resolution." In: *Physics in medicine and biology* 44.3 (1999), pp. 781–799.

[98] H. Li, O. R. Mawlawi, R. X. Zhu, and Y. Zheng. "Blind deblurring reconstruction technique with applications in PET imaging". In: *International Journal of Biomedical Imaging* (2009), p. 718157.

[99] F. Lucka, K. Proksch, C. Brune, N. Bissantz, M. Burger, H. Dette, and F. Wübbeling. "Risk estimators for choosing regularization parameters in ill-posed problems-properties and limitations". In: *Inverse Problems and Imaging* 12.5 (2018), pp. 1121–1155.

[100] M. Mäkitalo and A. Foi. "Optimal inversion of the generalized Anscombe transformation for Poisson-Gaussian noise". In: *IEEE Transactions on Image Processing* 22.1 (2013), pp. 91–103.

[101] J. Markham and J.-A. Conchello. "Parametric blind deconvolution: A robust method for the simultaneous estimation of image and blur". In: *Optical Society of America* 16.10 (1999), pp. 2377–2391.

[102] P. Mazliak. *Brève histoire de l'anatomie de l'Antiquité à André Vésale*. ADAPT-SNES, 2018.

[103] O. Michailovich and A. Tannenbaum. "Blind deconvolution of medical ultrasound images: A parametric inverse filtering approach". In: *IEEE Transactions on Image Processing* 16.12 (2007), pp. 3005–3019.

[104] J. Min, J. Jang, D. Keum, S. W. Ryu, C. Choi, K. H. Jeong, and J. C. Ye. "Fluorescent microscopy beyond diffraction limits using speckle illumination and joint support recovery". In: *Scientific Reports* 3 (2013), pp. 1–6.

[105] J.-J. Moreau. "Fonctions convexes duales et points proximaux dans un espace hilbertien". In: *Comptes rendus hebdomadaires des séances de l'Académie des sciences* 255 (1962), pp. 2897–2899.

[106] V. A. Morozov. *Methods for solving incorrectly posed problems*. Springer Science and Business Media, 1984.

[107] A. Moshtaghpour. "Computational interferometry for hyperspectral imaging". PhD thesis. Université catholique de Louvain, 2019.

[108] E. Mudry, K. Belkebir, J. Girard, J. Savatier, E. Le Moal, C. Nicoletti, M. Allain, and A. Sentenac. "Structured illumination microscopy using unknown speckle patterns". In: *Nature Photonics* 6.5 (2012), pp. 312–315.

[109] V. Ntziachristos. "Going deeper than microscopy: The optical imaging frontier in biology". In: *Nature Methods* 7.8 (2010), pp. 603–614.

[110] B. Pairet. “Signal processing methods for high-contrast observations of planetary systems”. Ph.D. thesis. Université catholique de Louvain, 2020.

[111] N. Parikh and S. Boyd. “Proximal algorithms”. In: *Foundations and Trends in optimization* 1.3 (2013), pp. 123–231.

[112] M. Pascucci, S. Ganesan, A. Tripathy, O. Katz, V. Emiliani, and M. Guillon. “Compressive three-dimensional super-resolution microscopy with speckle-saturated fluorescence excitation”. In: *Nature Communications* 10.1 (2019), pp. 1–8.

[113] A. Perperidis, K. Dhaliwal, S. McLaughlin, and T. Vercauteren. “Image computing for fibre-bundle endomicroscopy: A review”. In: *Medical Image Analysis* 62 (2020).

[114] M. Piana and M. Bertero. “Projected Landweber method and preconditioning”. In: *Inverse Problems* 13 (1997), pp. 441–463.

[115] T. Pock and A. Chambolle. “Diagonal preconditioning for first order primal-dual algorithms in convex optimization”. In: *IEEE International Conference on Computer Vision*. IEEE, 2011, pp. 1762–1769.

[116] J. L. Prince and J. M. Links. *Medical Imaging: Signals and Systems*. Pearson Prentice Hall Bioengineering, 2006.

[117] D. Psaltis and C. Moser. “Imaging with multimode fibers”. In: *Optics and Photonics News* 27.1 (2016), pp. 24–31.

[118] N. Pustelnik, C. Chaux, and J.-C. Pesquet. “Hybrid regularization for data restoration in the presence of Poisson noise”. In: *17th European Signal Processing Conference* (2009), pp. 2–6.

[119] M. Raginsky, R. M. Willett, Z. T. Harmany, S. Member, and R. F. Marcia. “Compressed sensing performance bounds under Poisson noise”. In: *IEEE Transactions on Signal Processing* 58.8 (2010), pp. 3990–4002.

[120] H. Raguet, J. Fadili, and G. Peyré. “Generalized forward-backward splitting”. In: *SIAM Journal on Imaging Sciences* 6.3 (2013), pp. 1199–1226.

[121] A. Rahmim, J. Qi, and V. Sossi. “Resolution modeling in PET imaging: theory, practice, benefits, and pitfalls.” In: *Medical physics* 40.6 (2013), p. 064301.

[122] C. D. Ramos, Y. E. Erdi, M. Gonen, E. Riedel, H. W. D. Yeung, H. A. Macapinlac, R. Chisin, and S. M. Larson. "Original article FDG-PET standardized uptake values in normal anatomical structures using iterative reconstruction segmented attenuation correction and filtered back-projection". In: *European Journal of Nuclear Medicine* 28.2 (2001).

[123] H. Rauhut, J. Romberg, and J. A. Tropp. "Restricted isometries for partial random circulant matrices". In: *Applied and Computational Harmonic Analysis* 32.2 (2012), pp. 242–254.

[124] G. D. Reddy, K. Kelleher, R. Fink, and P. Saggau. "Three-dimensional random access multiphoton microscopy for functional imaging of neuronal activity". In: *Nature Neuroscience* 11.6 (2008), pp. 713–720.

[125] W. H. Richardson. "Bayesian-based iterative method of image restoration". In: *Journal of the Optical Society of America* 62.1 (1972), pp. 55–59.

[126] W. C. Röntgen. "On a New Kind of Rays". In: *Science* 3.59 (1896), pp. 227–231.

[127] S. M. Ross. *Initiation aux probabilités*. 7th ed. Lausanne: Presses polytechniques et universitaires romandes, 2007.

[128] L. Rudin, S. Osher, and E. Fatemi. "Nonlinear total variation based noise removal algorithms". In: *Physica D: Nonlinear Phenomena* 60 (1992), pp. 259–268.

[129] M. Rudin and R. Weissleder. "Molecular imaging in drug discovery and development". In: *Nature Reviews Drug Discovery* 2.2 (2003), pp. 123–131.

[130] M. P. Sampat, Z. Wang, S. Gupta, A. C. Bovik, and M. K. Markey. "Complex wavelet structural similarity: A new image similarity index". In: *IEEE Transactions on Image Processing* 18.11 (2009), pp. 2385–2401.

[131] W. P. Segars, G. Sturgeon, S. Mendonca, J. Grimes, and B. M. Tsui. "4D XCAT phantom for multimodality imaging research". In: *Medical Physics* 37.9 (2010), pp. 4902–4915.

[132] J. H. Shapiro and R. W. Boyd. "The physics of ghost imaging". In: *Quantum Information Processing* 11.4 (2012), pp. 949–993.

[133] G. Shaw and D. Manolakis. "Signal processing for hyperspectral image exploitation". In: *IEEE Signal Processing Magazine* 19.1 (2002), pp. 12–16.

[134] J. Shin, B. T. Bosworth, and M. A. Foster. "Compressive fluorescence imaging using a multi-core fiber and spatially-dependent scattering". In: *Optics letters* 42.1 (2017), pp. 109–112.

[135] V. V. Shkunov and B. Y. Zel'dovich. "Optical phase conjugation". In: *Scientific American* 253.6 (1985), pp. 54–59.

[136] S. Sivankutty, D. Kogan, V. Tsvirkun, G. Bouwmans, E. Andresen, M. Guillon, M. Alonso, D. Oron, and H. Rigneault. "Non-interferometric calibration of the phase transmission matrix in lensless endoscopy (conference presentation)". In: *Adaptive Optics and Wavefront Control for Biological Systems V*. International Society for Optics and Photonics, 2019.

[137] S. Sivankutty, V. Tsvirkun, G. Bouwmans, D. Kogan, D. Oron, E. R. Andresen, and H. Rigneault. "Extended field-of-view in a lensless endoscope using an aperiodic multicore fiber". In: *Optics Letters* 41.15 (2016), p. 3531.

[138] S. Sivankutty, V. Tsvirkun, O. Vanvincq, G. Bouwmans, E. R. Andresen, and H. Rigneault. "Nonlinear imaging through a Fermat's golden spiral multicore fiber". In: *Optics Letters* 43.15 (2018), p. 3638.

[139] P. Soille. *Morphological image analysis*. 2004.

[140] L. Song, E. J. Hennink, I. T. Young, and H. J. Tanke. "Photobleaching kinetics of fluorescein in quantitative fluorescence microscopy". In: *Biophysical Journal* 68.6 (1995), pp. 2588–2600.

[141] F. Sroubek, M. Sorel, J. Boldys, and J. Sroubek. "PET image reconstruction using prior information from CT or MRI". In: *16th IEEE International Conference on Image Processing (ICIP)*. 2009, pp. 2493–2496.

[142] J.-L. Starck, F. Murtagh, and J. M. Fadili. *Sparse image and signal processing: wavelets, curvelets, morphological diversity*. Cambridge University Press, 2010.

[143] N. Stasio, C. Moser, and D. Psaltis. "Calibration-free imaging through a multicore fiber using speckle scanning microscopy". In: *Optics Letters* 41.13 (2016), p. 3078.

[144] T. G. Stockham, R. B. Ingebretsen, and T. M. Cannon. "Blind deconvolution through digital dignal processing". In: *Proceedings of the IEEE* 63.4 (1975), pp. 678–692.

[145] P. Sudhakar, L. Jacques, X. Dubois, P. Antoine, and L. Joannes. "Compressive imaging and characterization of sparse light deflection maps". In: *SIAM Journal on Imaging Sciences* 8.3 (2015), pp. 1824–1856.

[146] L. O. Svaasand and R. Ellingsen. "Optical properties of human brain". In: *Photochemestry and Photobiology* 38.3 (1983), pp. 293–299.

[147] T. Tanaka. "Performance analysis of L1-norm minimization for compressed sensing with non-zero-mean matrix elements". In: *IEEE International Symposium on Information Theory*. IEEE, 2018, pp. 401–405.

[148] A. M. Thompson, J. C. Brown, J. W. Kay, and D. M. Titterington. "A study of methods of choosing the smoothing parameter in image restoration by regularization". In: *IEEE Transactions on Pattern Analysis and Machine Intelligence* 13.4 (1991), pp. 326–339.

[149] A. J. Thompson, C. Paterson, M. A. A. Neil, C. Dunsby, and P. M. W. French. "Adaptive phase compensation for ultracompact laser scanning endomicroscopy". In: *Optics Letters* 36.9 (2011), p. 1707.

[150] O. Tichý and V. Smídl. "Bayesian blind separation and deconvolution of dynamic image sequences using sparsity priors". In: *IEEE Transactions on Medical Imaging* 34.1 (2015), pp. 258–266.

[151] A. N. Tikhonov, A. V. Goncharsky, V. V. Stepanov, and A. G. Yagola. *Numerical methods for the solution of ill-posed problems*. Ed. by S. S. M. Dordrecht. Kluwer Academic Publishers, 1995.

[152] S. Tong, A. M. Alessio, and P. E. Kinahan. "Image reconstruction for PET/CT scanners: past achievements and future challenges". In: *Imaging in medicine* 2.5 (2010), pp. 529–545.

[153] R. Y. Tsien, L. Ernst, and A. Waggoner. "Fluorophores for confocal microscopy: Photophysics and Photochemistry". In: *Handbook of Biological Confocal Microscopy: Third Edition*. 2006. Chap. 16, pp. 267–279.

[154] V. Tsvirkun, S. Sivankutty, K. Baudelle, R. Habert, G. Bouwmans, O. Vanvincq, E. R. Andresen, and H. Rigneault. "Flexible lensless endoscope with a conformationally invariant multi-core fiber". In: *Optica* 6.9 (2019).

[155] P. Valk, D. Bailey, D. Townsend, and M. Maisey. *Positron emission tomography: basic science and clinical practice*. Springer, 2004.

[156] G. C. Valley, G. A. Sefler, and T. Justin Shaw. "Multimode waveguide speckle patterns for compressive sensing". In: *Optics Letters* 41.11 (2016), p. 2529.

[157] R. Vershynin. *High-dimensional probability: An introduction with applications in data science*. Cambridge University Press, 2018.

[158] R. Vershynin. "Introduction to the non-asymptotic analysis of random matrices". In: *Compressed Sensing, Theory and Applications*. Ed. by Y. Eldar and G. Kutyniok. Cambridge University Press, 2012. Chap. 5, pp. 210–268.

[159] Z. Wang and A. C. Bovik. "Mean Squared Error : Love It or Leave It ?" In: *IEEE Signal Processing Magazine* 26.1 (2009), pp. 98–117.

[160] Z. Wang, A. C. Bovik, H. R. Sheikh, and E. P. Simmoncelli. "Image quality assessment: from error visibility to structural similarity". In: *IEEE Transactions on Image Processing* 13.4 (2004), pp. 600–612.

[161] R. Ward. "Compressed sensing with cross validation". In: *IEEE Transactions on Information Theory* 55.12 (2009), pp. 5773–5782.

[162] J. Wei, C. A. Bouman, and J. P. Allebach. "Fast space-varying convolution using matrix source coding with applications to camera stray light reduction". In: *IEEE Transactions on Image Processing* 23.5 (2014), pp. 1965–1979.

[163] M. Yavuz and J. A. Fessler. "New statistical models for randoms-precorrected PET scans". In: *Biennial International Conference on Information Processing in Medical Imaging*. Heidelberg: Springer Berlin, 1997, pp. 190–203.

[164] E. Zincirkeser, E. Sahin, M. Halac, and S. Sager. "Standardized uptake values of normal organs on 18F-fluorodeoxyglucose positron emission tomography and computed tomography imaging". In: *The Journal of International Medical Research* 35 (2007), pp. 231–236.

Acronyms, notations and quantities

Acronyms

ACD — Annihilation coincidence detection

ADMM — Alternating direction method of multipliers

AF — Array factor

BD — Blind deconvolution

BLI — Bioluminescence imaging

CCB — Compulsory coffee break

CCD — Charge-coupled device

CDF — Cumulative distribution function

CI — Computational imaging

CP — Chambolle-Pock

CS — Compressive sensing

CT — Computed tomography

CV — Cross-validation

DGN — Dolphin game night

dPETSTEP — Dynamic PET simulator via tomographic emission projection

F-FDG — F-fluorodeoxyglucose

FBP — Filtered backprojection

FFT — Fast Fourier transform

FMT — Fluorescence-mediated molecular tomography

FOV — Field of view

FRI — Fluorescence reflectance imaging

FWHM — Full width at half maximum

GCP — Generalized Chambolle-Pock

GFB — Generalized forward-backward

IM — Intravital microscopy

ISNR — Increase in signal-to-noise ratio

ISTA — Iterative shrinkage/thresholding algorithm

KL — Kullback-Leibler

LE — Lensless endoscope

LOR — Line of response

LR — Lucy-Richardson

MAP — Maximum *a posteriori* probability

MCF — Multicore fiber

MGF — Moment generating function

ML-EM — Maximum-likelihood expectation maximization

MMF — Multimode fiber

MRI — Magnetic resonance imaging

NBD — Non-blind deconvolution

OSEM — Ordered subset expectation maximization

pdf — Probability density function

PET — Positron emission tomography

PG — Proximal gradient

PMT — Photomultiplier tube

PS — Probability simplex

PSF — Point spread function

PSS — Partial speckle scanning

RIP — Restricted isometry property

RMSE — Root mean square error

RS — Raster scanning

SI — Speckle Imaging

SLM — Spatial light modulator

SNR — Signal-to-noise ratio

SPECT — Single-photon emission computed tomography

SSIM — Structural similarity index measure

SUV — Standardized uptake values

TGV — Total generalized variation

TV — Total variation

VST — Variance-stabilizing transform

WSNR — Weighted signal-to-noise ratio

XCAT phantom — Extended cardiac-torso phantom

Notations and conventions

$\|\boldsymbol{u}\|_p$ — ℓ_p-norm or p-norm of a vector $\boldsymbol{u} \in \mathbb{R}^N$

$\|\boldsymbol{u}\|_{p,q}$ — $L_{p,q}$-norm of $\boldsymbol{u} \in \mathbb{R}^{N \times k}$

$[N]$ — Set of the N first integers, *i.e.*, $[N] = \{1, \dots, N\}$

$\boldsymbol{u}$ — Vector in $\mathbb{R}^N$

$\boldsymbol{u}^\top$ — Transpose of vector $\boldsymbol{u}$

$g^\star$ — Conjugate function of g

$\odot$ — Elementwise product

$\boldsymbol{L}$ — Matrix in $\mathbb{R}^{M\times N}$

$\boldsymbol{L}^*$ — Adjoint of operator $\boldsymbol{L}$

$\|\boldsymbol{L}\|_2$ — ℓ_2 operator norm of $\boldsymbol{L}$

$\sigma_{\max}(\boldsymbol{L})$ — Largest singular value of matrix $\boldsymbol{L}$

$\mathbb{E}$ — Expectation operator

Γ_N — Correlation matrix of random vector N

$\iota_{\mathcal{Q}}$ — Indicator function of the closed non-empty convex set $\mathcal{Q}$

Quantities

f_0 — Signal of interest

$\boldsymbol{f}_0$ — Discrete representation of f_0

$\hat{\boldsymbol{f}}$ — Estimate of $\boldsymbol{f}_0$

$\hat{\boldsymbol{f}}_\rho$ — Estimate of $\boldsymbol{f}_0$ with explicit dependency to parameter ρ

$\boldsymbol{y}$ — Vector of observations in $\mathbb{R}^M$

$\mathcal{A}_\xi$ — Continuous forward mapping $f_0 \mapsto y$

$\mathcal{A}$ — Deterministic part of $\mathcal{A}_\xi$

$\boldsymbol{A}$ — Operator in $\mathbb{R}^{M\times N}$, discrete equivalent to $\mathcal{A}$

ρ — Regularization parameter

Ω — 2D Field of view

$\mathcal{D}$ — Degradation operator

N — Number of pixels in the final image

M — Number of observations

a — Pixel size

∇ — Gradient operator

$\boldsymbol{\nabla}$ — Discrete gradient operator

div — Divergence operator

ε — Symmetrized derivative operator

$\mathrm{prox}_{\lambda g}$ — Proximal operator of the function λg with $\lambda > 0$

$\mathbf{Id}_N$ — Identity matrix of size $N \times N$

γ — Lipschitz constant of ∇G in PG method

μ — Step-size in PG method

τ — Primal step-size in CP algorithm

σ — Dual step-size in CP algorithm

q — Quality criterion

$\boldsymbol{R}$ — Restriction operator with entries in $\{0, 1\}$